Analysis and Improvement of Supercritical CO2 Power and Refrigeration Cycles

MOJTABA, PURJAM
九州大学大学院総合理工学府環境エネルギー工学専攻

出版情報：九州大学, 2020, 修士, 修士
バージョン：
権利関係：

九州大学
KYUSHU UNIVERSITY

Analysis and Improvement of Supercritical CO_2 Power and Refrigeration Cycles

A Master Thesis

By

MOJTABA PURJAM

Submitted in Partial Fulfilment for the Degree of Master of Engineering

In the

Interdisciplinary Graduate School of Engineering Sciences

Department of Energy and Environment Engineering

Under Supervision of

Associate Professor	Professor
KYAW THU	TAKAHIKO MIYAZAKI

February 2021

interdisciplinary Graduate School of Engineering Sciences IGSES

Department of Energy and Environmental Engineering

Thermal Energy Conversion Systems Laboratory

熱エネルギー変換システム学研究室

九州大学　KYUSHU UNIVERSITY

Declaration

I declare that this thesis was composed by myself to be presented for the master's degree in Energy and Environmental Engineering Department Kyushu University. This work contained herein is my own except where explicitly stated in the text, and this project has not been submitted for any other degree or professional qualification except as specified.

Parts of this work have been published and other parts have the protentional to be published in the future.

- Purjam, M., Thu, K., & Miyazaki, T. (2021). Thermodynamic Modelling of an Improved Transcritical Carbon Dioxide Cycle with Ejector: Aiming Low-Temperature Refrigeration. *Applied Thermal Engineering*, 116531.
- Purjam, M., Thu, K., & Miyazaki, T. (2020). Development of an improved transcritical refrigeration system using natural refrigerants for low-temperature applications. In *14th IIR Gustav-Lorentzen Conference on Natural Fluids, GL 2020 - Proceedings* (pp. 116-121). (Refrigeration Science and Technology; Vol. 2020-December). International Institute of Refrigeration. https://doi.org/10.18462/iir.gl.2020.1213

Mojtaba Purjam

February 7th, 2021

ACKNOWLEDGEMENTS

Throughout the writing of this dissertation, I have received a great deal of support and assistance.

I first would like to express my gratitude to my kind and knowledgeable supervisor Professor Takahiko Miyazaki for his comments and teachings through the learning process of this master thesis. Furthermore, I would like to deeply thank my co-supervisor Professor Kyaw Thu for his remarks, experience sharing, engagements, and tireless efforts to support me during my master course.

I would like to thank Dr. František Mikšík. I was lucky that he was my tutor, my senior, and my dearest friend. I always have something to learn from him.

I would also like to thank all TECS lab members and staff for their kindness, friendship, and scientific collaboration during my master's degree.

A special thank my senior Dr. Indri Yaningsih for her teachings and support.

I send my best regards to the readers and referees of this thesis.

In addition, I would like to thank my parents and my siblings for their wise counsel and sympathetic care. You are always there for me.

Finally, I thank Japan Student Service Organization for JASSO scholarship and Interdisciplinary Graduate School of Engineering Sciences (IGSES) for their research support fund.

پیشکش فرزندان سرزمین اهورایی

Summary

This dissertation was prepared in two parts which both are mainly about thermodynamic analysis of CO_2 cycles. **Part I** focuses on proposing and analyzing a novel trans-critical CO_2 refrigeration cycle for low-temperature refrigeration application and **part II** investigates the feasibility of coupling a lithium bromide absorption refrigeration cycle with a CO_2 supercritical power cycle, aiming to enhance the total performance of the system.

Part I:

Low-temperature refrigeration (aka, deep-freezing) has an essential role in the food and pharmaceutical industries. Considering environmental and economic concerns, Carbon Dioxide (R744) has presented itself as a competent refrigerant. Even though many researchers performed extensive investigations on the performance of the low-temperature refrigeration cycles, the innovations in this field still exist, and refinement and examination of new layouts remain a hot topic, among which coupling an ejector with the cycle is a popular method that has shown promising results. This article proposes a new layout for low-temperature refrigeration together with the thermodynamic studies on the effects of changing pressures before and after the ejector by introducing an additional compressor, gas cooler, and turboexpander to the conventional layout of the transcritical CO_2 ejector cycle. The coefficient of performance (COP) around 1.4 was obtained for evaporation at -45°C. The first law analysis of the cycle was conducted, and optimal values for pressures before and after the ejector were identified. It was found that using a compressor and a gas cooler before the secondary entrance of the ejector is beneficial to COP, and the expansion process right after the ejector will affect the COP. It was discovered that the instant expansion after the ejector is unnecessary at optimum conditions, and the phase condition of the ejector's discharge has a huge impact on the performance. Optimization and parametric analysis of the cycle was conducted, and the effects of efficiencies of the cycle's components on COP were investigated. A simple and comprehensive second Law analysis of the proposed system is included, and the performance of the setup was briefly compared with other cycles in low-temperature refrigeration. It was revealed that this single-refrigerant proposed cycle not only can reach a reasonable performance for deep-freezing applications but also has a 10% less compression ratio than its R744 counterparts. Finally, an organic Rankine cycle was a couple with the R744 cycle to increase the performance. It is observed that the current hybrid cycle delivers the coefficient of performance up to 1.5.

Keywords: Low-Temperature Refrigeration; Ejector; Transcritical CO_2; Expansion device with work recovery; Optimization; Second Law analysis; Natural Refrigerants; ORC.

Part II:

Supercritical Carbon Dioxide Power Cycle (SCDC) has numerous advantages that make it a suitable candidate for versatile applications. Nowadays environmental disasters, climate changes, shrinking resources and ever-growing energy demand and applications for a new area of human society urge the scientist to rethink the global energy structure. SCDC has high flexibility and tolerance for new types of energy resources like fusion, high-temperature reactors, and high-temperature concentrated thermal solar receivers. SCDC is also the best candidate for pre-combustion and the only candidate for oxy-fuel combustion systems.

Using refrigeration cycles to improve the performance of the power cycle is an accepted method. Absorption refrigeration cycles are renowned systems for this purpose. However, until now the research about coupling an absorption refrigeration cycle to an SCDC for efficiency improvement is unknown. In order to bridge this gap, two SCDC layouts were selected and integrated with Lithium Bromide-Water refrigeration cycles (LiBr). Layout A is a modified intercooler single reheat cycle that shows great potential for an efficiency boost. Layout be is a recompression cycle with single reheat which did not show a great improvement, but the results illustrated that coupling LiBr with recompression cycle may have co-benefits for oxy-fuel combustion and carbon capture and storage.

A brief 1st law parametric analysis was conducted. It was found that LiBr usually reduces the mass flow rate of the single cycle and at a lower temperature of heat source the room for improvement is larger. The calculation and optimization of data were done by linearized methods.

Keywords: Supercritical CO_2 power cycle; Lithium Bromide absorption refrigeration; hybridization; performance improvement: optimization: 1st law of thermodynamics.

Contents

Introduction

1. The earth

“Our Green Planet” supports life. Until the time of writing down this thesis, there have **not** been any bullet-proof findings that show our planet is **not** the only place in the universe to be able to sustain life. Many controversial theories suggest different sources for the initiation of life on this planet. Meteors from mars, carbon-based asteroids, chemically active hot springs, and hydrothermal vents are among the suggested sources.

From the statistics point of view, there are billions of stars and hundreds of billions of planets orbiting them. By suggesting the proper characteristics of a planet like its distance from the sun, its sun, existence, and abundance of water, etc., early mathematician predicted that not only extraterrestrial life is possible but also there are hundreds of alien civilizations who are broadcasting their radio signals to us or preparing their invading forces to exterminate the humankind. The conclusion was led to even more interesting pseudoscientific ideas like ancient astronauts.

However, when other factors like the time and unpredicted mass extinctions were brought to the equation, the model shows that life in this vast galaxy over the earth is only a miracle and the life on earth perhaps is the only biomass in the universe which is only an inch away from extinction. According to geologists and archaeobiologists, there were five major and numerous minor mass extinction events in the history of the planet and the next time maybe we are not going to be lucky.

Fig. 1: A polar bear is desperately trying to rest over a block of melting ice. Source: Twitter @jenapratap66

2. Human race and pollution

Thanks to their brainpower, innovation, and teamwork, humankind managed to consolidate itself over the earth more than any species and made a safe and comfortable zone for itself. The more the living quality is improved, the more pressure is exerted on the environment. Additionally, the population growth also adds quantity to this complex destructive equation. Humans are gathering resources at a pace that cannot replenish by the earth and are producing more waste than it can be safely absorbed by the environment.

Gaseous waste (aka Pollutants) has the most impact on the environment and because of this, they are at the center of attention. Among those impacts, greenhouse and ozone-depleting effects make the biggest concerns.

The greenhouse effect is the process by which radiation from a planet's atmosphere warms the planet's surface to a temperature above what it would be without this atmosphere[1]. Greenhouse gases (i.e., Radiatively active gases) in a planet's atmosphere radiate infrared in all directions. Part of this radiation is directed towards the surface, thus warming it. The intensity of downward radiation (that is, the strength of the greenhouse effect, in other words, GWP) depends on the quantity of greenhouse gases that the atmosphere contains[2]. The temperature rises until the intensity of upward radiation from the surface, thus cooling it, balances the downward flow of energy. Earth's natural greenhouse effect is crucial to supporting life and initially caused moving life forms out of the ocean. Human activities, mainly the burning of fossil fuels and deforestation, have increased the greenhouse effect[3].

Global warming potential (GWP) is the heat absorbed by any greenhouse gas in the atmosphere, as a multiple of the heat that would be absorbed by the same mass of carbon dioxide. GWP is 1 for CO_2. For other gases, it depends on the gas and the time frame. Some gases, like methane, have large GWP since a ton of methane absorbs much more heat than a ton of CO_2. Some gases, again like methane, break down over time, and their heat absorption, or GWP, over the next 20 years is a bigger multiple of CO_2 than their heat absorption will be over 100 or 500 years. Values of GWP are estimated and updated for each time frame as methods improve[4][5].

The ozone depletion potential (ODP) of a chemical compound is the relative amount of degradation to the ozone layer it can cause, with trichlorofluoromethane (R-11) being fixed at an ODP of 1.0. Chlorodifluoromethane (R-22), for example, has an ODP of 0.05. R-11 has the maximum potential amongst chlorocarbons because of the presence of three chlorine atoms in the molecule. The first proposal of ODP came from Wuebbles in 1983. It was defined as a measure of destructive effects of a substance compared to a reference substance[6].

Table 1: Latest report of GWP of refrigerants

Species	Chemical formula	Lifetime (years)	GWP 100 years
Carbon Dioxide (R-744)	CO_2	variable	1
Methane (R50)	CH_4	12±3	21
Nitrous oxide (R-744A)	N_2O	120	310
R-23	CHF_3	264	11700
R-32	CH_2F_2	5.6	650
R-41	CH_3F	3.7	150
R-125	C_2HF_5	32.6	2800
R-134	$C_2H_2F_4$	10.6	1000
R-134a	CH_2FCF_3	14.6	1300
R-152a	$C_2H_4F_2$	1.5	140
R-143	$C_2H_3F_3$	3.8	300
R-143a	$C_2H_3F_3$	48.3	3800
R-227ea	C_3HF_7	36.5	2900
R-236fa	$C_3H_2F_6$	209	6300
R-245ca	$C_3H_3F_5$	6.6	560
Propylene (R-1270)	C_3H_6	12±3	1.8
Water (R-718)	H_2O	0.026	0.2±0.2
Ammonia (R-717)	NH_3	0.019	0
R-1234yf	$C_3H_2F_4$	0.07	3.7

3. Heat pumps and global warming

A heat pump is a device that transfers thermal energy from a source of heat to what is called a thermal reservoir. Heat pumps move heat in the opposite direction of spontaneous heat transfer, by absorbing heat from a cold space and releasing it to a warmer one. A heat pump uses an external power to accomplish the work of transferring energy from the heat source to the heat sink. The most common design of a heat pump involves four main processes: Pressurizing, Heat Release, Depressurizing, Heat Absorption. The heat transfer medium circulated through these processes is called refrigerant[7]. Air conditioners, refrigerators, and freezers are familiar examples.

Montreal protocol of 1987[8] was a successful step toward retirements of ODP refrigerants and nowadays those refrigerants became a part of history.

However, most of the manufactures preferred to replace zero ODP refrigerants with high-GWP ones. It was due to the fact that environmental laws against global warming were young and the new refrigerants were economic and high-performance. The explosion of high-GWP refrigerants (such as R134a in small-sized cycles) rings the bells in academic and environmental protection societies. Kyoto protocol 1997[9] was another breakthrough for solving environmental issues by international collaboration. New strict rules have limited the production of greenhouse gases. Researchers started working on new refrigerants and modifying heat pump components.

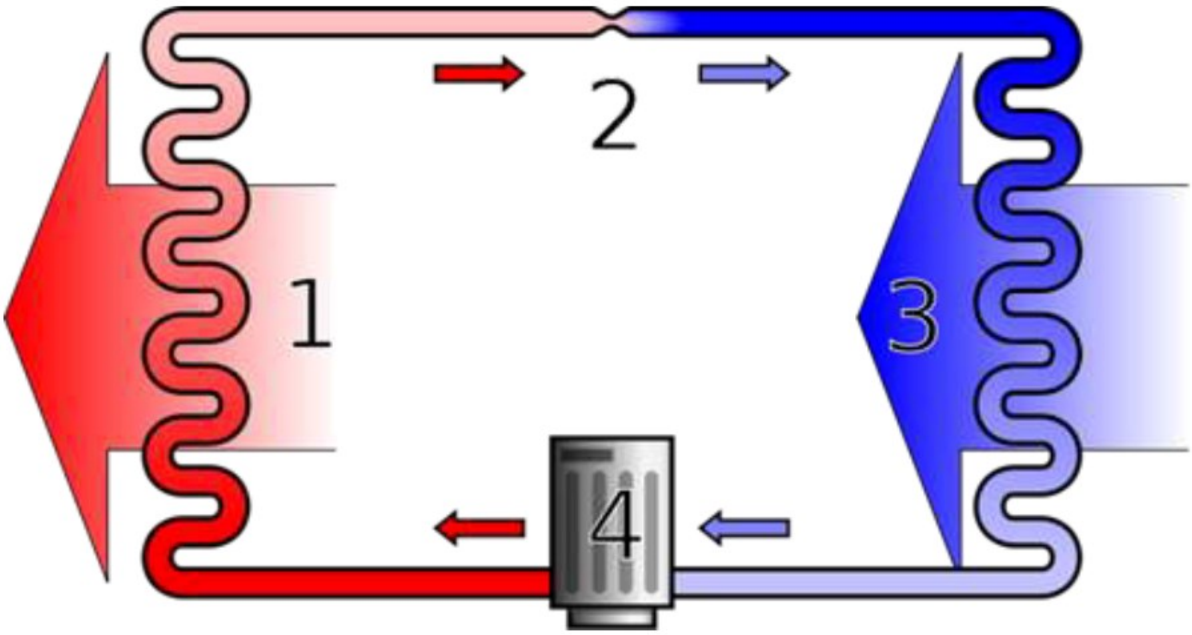

Fig. 2: A simple diagram of a heat pump cycle and its main processes[10]. 1) Heat Dissipation 2) Depressurizing 3) Heat Absorption 4) Pressurizing

Fig. 3: 1956 advertisement for AMANA Stor-Mor domestic R12 refrigerators

Some researchers suggested moving back to natural refrigerants such as CO_2, ammonia, water, and hydrocarbons. These substances are environmentally friendly but make them user and pocket-friendly was not easy. This issue became a real engineering challenge, especially for CO_2. Despite mechanical advantages, CO_2 cycles were energy-intensive. This phenomenon led to the analysis of direct and indirect environmental impacts of the refrigerants.

Direct impacts are the consequences of leakage from the cycle to the atmosphere. Indirect impacts were done by the amount of pollution which are released into the air to provide electricity for the cycle. This pair also called direct and indirect emissions and direct and indirect GWP[11].

CO_2 was extensively used before the 1950s but it was abandoned in favor of the halocarbons[12]. This phase-out was not because CFC refrigerants are better. It was mostly due to the low performance of the heat pump component, especially the compressor. In those days the metallurgy and computer-aided design were not as advanced as today. Now high-quality cycle parts are available, but it does not mean that replacing high-GWP with low-GWP fluids became easy. Conventional refrigerants naturally have better performance and the new high-tech parts were also available for them. Natural refrigerant cycles must reach a minimum performance to be considered as a proper environmental, mechanical, and economical replacement for their counterparts.

4. Heat engines and global warming

A heat engine is a system that converts heat to mechanical energy, which can then be used to do mechanical work (Like a gasoline car) or produce electricity (like power plants). It does this by bringing a working fluid from higher temperature to lower state temperature. A heat source generates thermal energy that brings the working fluid to a high-temperature state. The working fluid generates work in the working body of the engine (piston or turbine) while transferring heat to the colder sink until it reaches a low-temperature state. During this process, some of the thermal energy is converted into work by exploiting the properties of the working fluid[7]. There are two types of heat engines: close and open cycle. In open cycles, the working fluid is added to the cycle, and after the work, the production is released to the atmosphere. In a closed cycle, the working fluid is circulated in the cycle. Automobile and jet engines are examples of open cycles and the steam cycle in power plants is an example of close cycles.

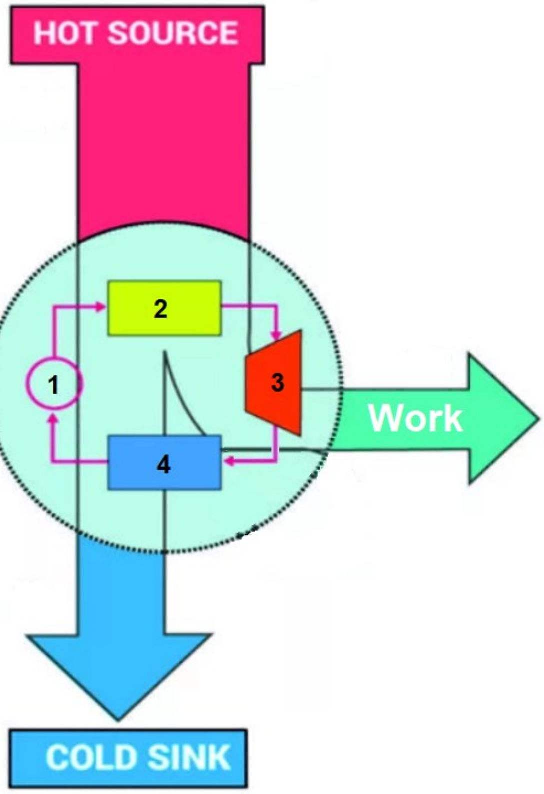

Fig. 4: A simple diagram of a heat engine cycle and its main processes. 1) Pressurizing 2) Heating 3) Work production 4) Cooling. Picture from [13] with some edition.

Energy sources for the heat engines are fossil fuels and combustible materials (such as biomass, biofuels, and waste), nuclear, solar receivers, geothermal heat, and waste heat.

Fossil fuels are the main energy source for humankind also the heat engines. In 2019, 73.11% of the world's electricity production comes from fossil fuels. Land transportation has 98% dependence on fossil fuel. This share for marine and air transportation is almost 100%[14]. World energy consumption is still increasing, and CO_2 emission is reaching critical values and human society is still far from the targets of the Kyoto protocol.

To address this issue numerous ideas were suggested by the scientist. Suggestion for reducing and reversing global warming is revising the national and international logistical and trade networks, managing the energy consumption, increase the efficiency of devices, increase the efficiency of electricity production, managing the electricity grid peaks and valleys, switching to renewable and sustainable energies, rethinking of nuclear power technologies, capturing CO_2, etc.

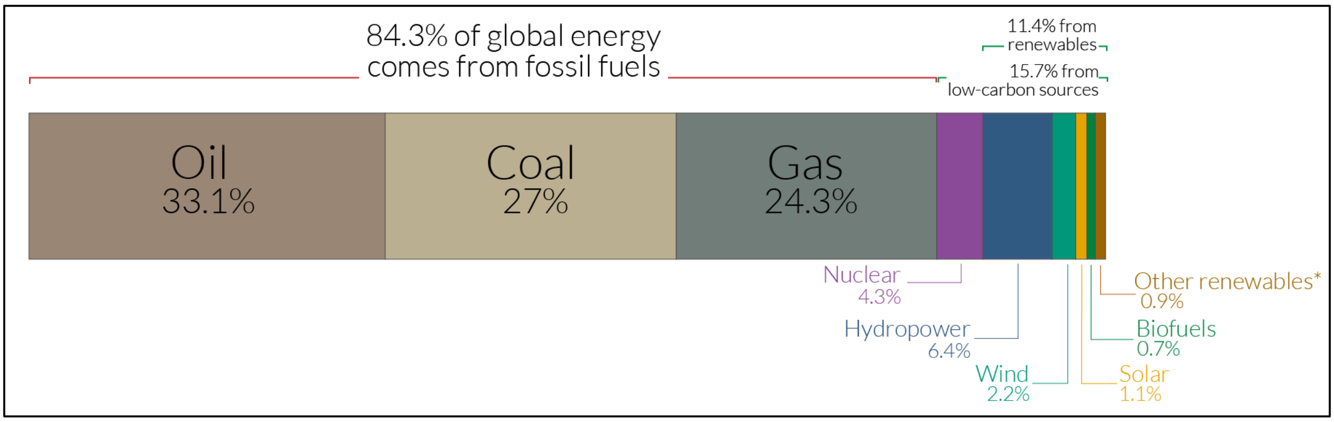

Fig. 5: Global energy share of different resources in 2020[15].

In this regard, supercritical CO_2 power cycles (SCDC) seem to have a promising future for reducing the carbon footprint. Pre and oxy-fuel combustion SCDCs have high thermal efficiency[16], capture CO_2 and other pollutants, and can use an air separation unit (ASU) as an energy storage system for peak shaving of the electricity grid[17].

Fig. 6: NET Power's supercritical carbon dioxide power cycle demonstration plant (Courtesy of NET Power and McDermott)[18]

Due to their performance, SCDCs are the candidates for the next generation of high-temperature zero-GWP heat sources such as high-temperature concentrated solar receivers, molten salt reactors, non-uranium reactors, and fusion power[19][20]. They have the potential to be combined with their pre and oxy-fuel combustion counterparts and form an integrated major power production and regulation sites[19].

SCDCs can be coupled with supercritical CO_2 energy storage units. This method can be used in solar thermal power plants and provide electricity to the grid after sunset[21][22].

SCDCs have undeniable weight and volume advantages over other cycles[23]. They can start faster than steam cycles and have more resistance to the thermal shocks. Because of this, they can replace the sub and supercritical steam cycles in combined and conventional power plants and improve thermal efficiency[24]. The small size of these cycles may help to introduce nuclear and CO_2 capture technologies to the marine vessels.

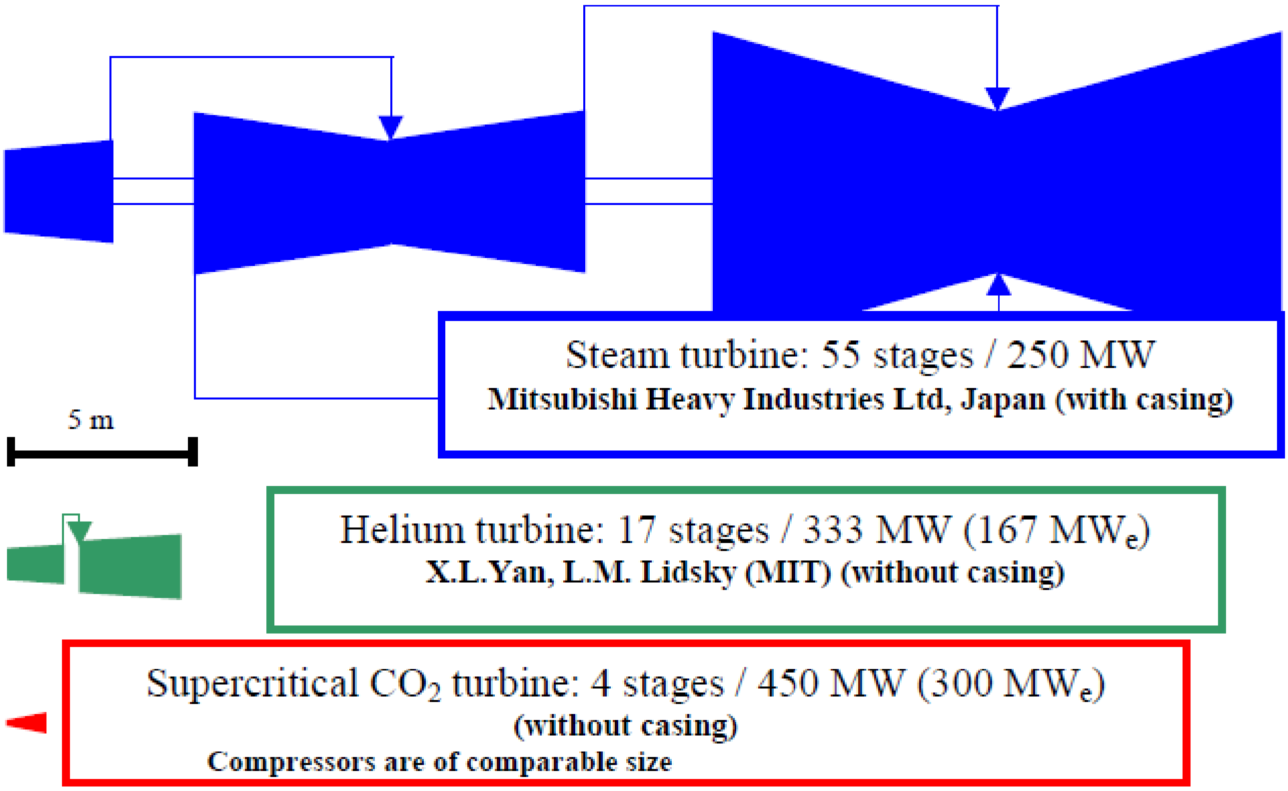

Fig. 7: Comparison of turbine sizes for water steam, helium, and SCDC[23].

The challenges that facing SCDC are mainly due to its youngness. The technology is in the research and demonstration stage and it needs time and funds to reach a certain level of practical operation. Metallurgical science in the area of superalloys must be developed.

5. Bridging the gaps

CO_2 is now the main reason for global warming and the major issue in the environmental sciences. However, it seems tricky and special that CO_2 can be used to effectively reduce the CO_2 emissions and additionally reach some co-benefits. Carbon dioxide (R744), as a safe and environmentally friendly refrigerant and working fluid, possesses several desirable properties such as nontoxicity, incombustibility, high volumetric capacity compatibility with most lubricants, abundance, and preferable heat transfer[25][12] properties.

Fig. 8: source iKegger NZ

Research on CO_2 cycles is a hot topic and numerous researches have been conducted that and many conclusions have been submitted. But, undiscovered methods to enhance the performance were still available. Thermodynamics is a powerful tool to analyze the performance of the cycles. 1st law of thermodynamics balances the energy, mass, and momentum equations in the cycle and finds the efficiency and performance of the unit. 2nd law of thermodynamics shows how far the performance is away from its ideal performance and finds and controls the main points of entropy generation in the cycle.

This dissertation illustrates the investigation of CO_2 heat pumps and power cycles. It is separated into two parts. Part one is about a novel R744 low-temperature refrigeration cycle. Part two is about a hybrid supercritical CO_2 power and lithium bromide absorption refrigeration cycle. Below are the main targets of this thesis.

1) Using environmentally friendly natural refrigerants (especially CO_2) to design cycles.
2) Suggesting new equations, solutions, and optimization methods for calculation.
3) Investigating the mathematical relation of parts that has most interactions with each other
4) Using comprehensive parametric analysis to cover as much as available situations

Part I: 1st and 2nd Law Modeling of an Improved Transcritical Carbon Dioxide Cycle with Ejector for Low-Temperature Refrigeration Applications

1. Background

Climate change mitigation regulations address restrictions over the rate of global warming. In this regard, the effect of heat pump cycles is noticeable since they have both direct and indirect global warming potential. The direct effect is the global warming potential of refrigerants, and the indirect effect is the large share of air-conditioning and refrigeration systems in the global energy demand.

In comparison to the refrigerants used in most heat pump cycles, transcritical CO_2 cycles have a higher lift. Consequently, their coefficient of performance (COP) is often lower than cycles that run with conventional refrigerants. Towards increasing COP, many researchers have focused on different methods, such as internal heat exchangers [26], cascade cycles [27][28], turboexpanders [29][30], multi-stage compression [31][32][33], vortex tube expansions [34], and subcooling boost [35][36].

In addition to the mentioned methods, the utilization of ejectors is also an examined and popular approach. Li and Groll [37] and Deng et al.[38] theoretically studied an ejector in a transcritical CO_2 cycle. Li and Groll [37] employed a two-phase ejector assumption for a transcritical air-conditioning system and reported a COP improvement of up to 16%. Deng et al. [38] unveiled that the highest COP in the ejector expansion cycle was up to 22% better than other vapor compression cycles. Elbel [39] reported COP and cooling capacity improvements up to 7% and 8%, respectively, by utilizing an ejector. Banasiak et al.[40] conducted an experimental and numerical study for a small capacity CO_2 ejector heat pump and reported an 8% increase in the COP compared to a conventional expansion valve system. Zhu et al. [41] experimentally investigated the performance of a transcritical CO_2 ejector water heater system and reported 10.3% COP improvement over the primary cycle. In a transcritical cycle, gas cooler pressure has a significant effect on the COP. There is an optimum pressure that maximizes the COP of the system [42][43][44]. Elbel[39] reported a brief analysis of some uncommon layouts for transcritical CO_2 cycles with unique features such as [45] and [46].

Propylene (R1270) is a new emerging substance for both low-temperature waste heat recovery units and refrigeration cycles[47][48]. Despite disadvantages which are flammability and low-performance for low-temperature systems, due to its environmental benignity and desirable thermodynamics properties for Organic Rankine Cycle (ORC)[49][50], it is considered as a replacement for R22 and R32 refrigerants.

Table 2: Some properties of R744 and R1270

Refrigerant	**CO_2 (R744)**	**Propylene (R1270)**
ODP	0	0
Net GWP 100-yr	1	1.8
Flashpoint at 1 atm	non	-108℃
Critical Point	30.98℃, 7.377 MPa	91.06℃, 4.555 MPa
Triple point	-56.56℃, 0.518 MPa	-185.2℃, 0.7 kPa
Toxicity OEL/OPL	5000 ppm	500 ppm

Low-temperature refrigeration, which includes industrial warehousing of frozen provisions and deep-freezing systems, operates at evaporation temperatures ranging from -30 to -65℃. Applications are food, pharmaceutical, chemical, and petrochemical industries, oil and gas plants, superconductors, cold warehousing, etc.

Table 3: Refrigeration classes

Refrigeration commercial category	The refrigeration range (°C)
Cooling	Over 10
Chilling	Between 0 and 10
Sub-zero cooling	Between -5 and 0
Freezing	Between -30 and -5
Low-temperature refrigeration	Between -30 and -65
Ultra-low-temperature and cryogenic refrigeration	Less than -65

Fig. 9: GEA Piston Compressor Packages at a Processing Facility. Source: GEA Industrial Refrigeration Solutions[51]

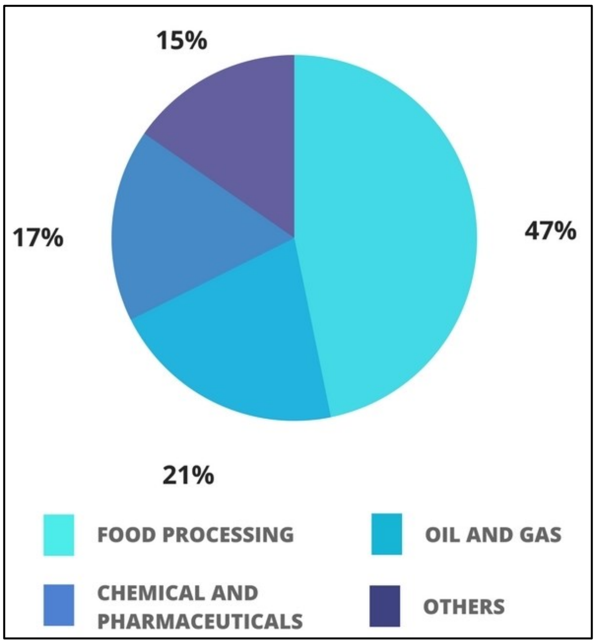

Fig. 10: Technavio 2016 report on the global industrial refrigeration market by application (Graphic: Business Wire)[52]

Deep-freezing has an important role in direct and indirect greenhouse gas production. It is widespread, energy-intensive, and mostly works 24 hours a day 7 days of the week at high capacities. The exact share of the market and energy consumption is unknown. However, different estimations show the values of between 15 to 25%.

Due to the high-temperature difference between evaporation and condensation (cooling), it is not economically viable to utilize a single-stage system. Significant pressure-ratios cause lubrication difficulties, reduce the volumetric efficiency of compression and increase the throttling loss. To date, several simulation and experimental investigations have been conducted by many researchers using various layouts of cascade systems with different refrigerants. The combination of the layouts, optimization of the inter-cascade pressure, multi-refrigerant cycles, and parametric and the 2nd law analysis are the area of research interest in this field. Recently, Sun et al.[53] provided a comprehensive literature review on cascade units. Some researchers even considered putting conventional ejector cycles into the cascade units for improved performance. Yari et al.[54] combined a simple bottoming cycle with a conventional ejector cycle. A power CO_2 cycle was also recommended to increase performance. Megdouli et al. [55] utilized a thermally-driven ejector refrigeration cycle to enhance the heat pumping of the cascade cycle by the regeneration from the condenser. Table 4 presents a review of theoretical and experimental studies that targeted the performance improvement aiming at low-temperature refrigeration. The mentioned positive temperatures are the gas cooler outlet or condenser temperature. The negative temperatures are the evaporator temperatures. If the temperatures are not mentioned, the gas cooler or condenser temperature is 40°C, and the evaporator temperature is -45°C. COPs between this temperature range are extracted from the references to compare the performance of deep-freezing technologies with the current study. According to the referenced studies, 2-stage refrigeration is a necessity, and coupling the different refrigerants in order to reach better performance and more efficient compression is a routine. On the other hand, using different refrigerants increases complexity and maintenance costs. Coupling the compression cycles with absorption ones, even if conduces to preferable economical operation, will decrease the system's volumetric advantages.

1.1 is the estimated average COP of the cycles in the cooling mode in Table 4 at -45°C evaporation and 40°C cooling. Many of the studies use high and medium GWP refrigerants. R744 cycles mostly have less COP, especially if they were coupled with absorption cycles. R744 was usually used inside the bottom cycle. The reason is that CO_2 compressors must have a high compression ratio for the top cycle. R744 and R717 are the best GWP-friendly couple. However, R717 is toxic and requires special handling and maintenance.

Heat exchangers have been used in the multi-stage compression cascade cycles. However, designing heat exchangers always involves a trade-off between effectiveness, size, and cost. For this reason, it appears that efficient multi-stage cycles without the inter-stage heat exchanger have an edge compared to other multi-compressor cycles.

In most ejector cycles, the pressure of the secondary fluid is the pressure of the evaporator, and the outlet pressure of the ejector is directly exerted to the cycle. Controlling these pressures can probably affect the COP and finding the optimal point for these pressures can define new COP boundaries for ejector-based cycles.

Table 4: A literature review of various low-temperature (-30 to -85 °C) refrigeration systems.

Reference	Cycle description (Top cycle/Bottom cycle refrigerants)	Method	Remarks (COP & relative conclusions)
[56]	Cascade R41/R404A & R23/R404A	Sim.	COP 1.37, R41/R404A has better 1st and 2nd law performance
[57]	Cascade R744/R404A, single-stage R404A & single-stage R22	Exp.	Cascade 744/R404A reduces the running costs and environmental impacts
[58]	Cascade compression-absorption R744/NH3H2O & R717/NH3H2O	Sim.	COP 0.25, both cycles have the same performance, feasibility of powering the cycle by cogeneration was discussed
[59]	Cascade R744/R134a	Exp.	COP 1.12 at -40°C, internal heat exchanger in 744 cycle increases the performance.
[60]	Five different cascade and 2-stage cycles with several different refrigerants	Sim.	COP 1.6 at 30°C, Cycles with R744 top cycle has better performance and less GWP impact at deep freezing application conditions.
[61]	Cascade R23 coupled with six different refrigerants	Sim.	COP 1.23, R1717/R23 cycle has the best 1st and 2nd law performance
[62]	Cascade R134a/R744 & R152a/R744	Exp.	COP 1.06 at -40°C, Both cycles have comparable performance. R152a was recommended as a candidate for R134a drop in replacement.
[63]	Cascades R744/R717 both flash tank intercooling for R744	Sim.	COP 1.38 at -40°C and 36°C, using flash intercooler with indirect sub-cooler increases the performance.
[64]	Cascade R744/R134a & R744/R404a	Exp.	R744/R134a couple has superior performance over the drop in replacement.
[65]	Cascade R744/R717	Exp.	COP 1.15 at 30°C, The results confirm the tendencies obtained from theoretical studies.
[66]	Cascade R744/R717	Exp.	COP 1.27, The results confirm the previous simulation. The cascade heat exchanger temperature has a direct impact on capacity.
[67]	Cascade R744/R717 & R744/R290	Sim.	COP 1.29, The cycles were optimized. R717 has the same performance as R290. However, it is riskier and costlier.
[68]	Combined absorption-compression R744/NH3H2O	Sim.	COP 0.33 at 35°C, The proposed cycle shows improved performance over a two-stage ammonia-water absorption system.

[69]	Cascade with a various couple of refrigerants	Sim.	COP 1.27 at -50°C, R134a/R170 pair has the best performance among numerous analyzed pairs.
[70]	SHC Cascade R1270/R744 with internal heat exchanger	Sim.	COP 3.34. Transcritical cycle with CO_2–propylene gives better system performance than subcritical cascade cycle.
[71]	Cascade R744/various refrigerants	Sim.	COP 1.51 at -50°C, R744/Ethanol has the best performance among the investigated refrigerants. The sub-cooling and heating effects were investigated.
[72]	Cascade R12/R13, R290/R23, and R404A/R23	Sim.	COP 1.01 at -80°C, R290/R23 showed the highest COP and exergy efficiency.
[73]	Cascade R744/R717	Sim.	COP 1.25, The optimum condensing temperature in the cascade heat exchanger for different approach temperatures was calculated.
[74]	Cascade R23/R507A	Sim.	COP 0.7 at -82°C, Superheating in the bottom cycle has a negative effect on COP. Superheating in the top cycle and subcooling in both cycles improves the performance.
[75]	Cascade R744/HFE7000	Sim.	COP 1.81 at -30°C, 1^{st} and 2^{nd} law performance of the cycle is similar to R744/R134a.
[76]	Cascade R744/R134a	Exp.	COP 1.1, In nominal conditions, the efficiency of R744 and R134a compressors are identical. Cooling capacity is highly sensitive to the bottom cycle evaporator temperature. The discharge temperature of the R744 compressor is hotter than the environment. It was recommended to cool the R744 before sending it to the cascade heat exchanger.
[77]	Cascade R23/R22	Exp.	COP 1.1 at -60°C and 30°C, The experiment proved that the dual-mode refrigeration is feasible at the mentioned temperatures.
[78]	Cascade (R744-R170 blend)/R290	Sim.	COP 0.82 at -48°C and 56°C, the multi-objective optimization was conducted, and the optimum mass fraction of R744 and condensing temperature of the bottom cycle were calculated.
[79]	Cascade, various refrigerants are considered for top and bottom cycle. The R23/R134a cycle was used as a base.	Sim.	The same COP can be achieved by replacing R23 with other low GWP refrigerants for low-temperature purposes.

[80]	SHC Cascade R744A/R744	Sim.	COP 2.4, The internal heat exchangers marginally affect the performance in top and bottom cycles. Swapping the fluids does not notably change the performance.
[81]	Cascade R744/R404a	Sim.	COP 1.16 at -40°C, Multiple standard conditions were investigated. Optimum energy and exergy performances were calculated.
[82]	R744 hybrid cycle with ejector	Sim.	COP 0.67, 1st and 2nd law analysis and optimization. The hybrid cycle could simultaneously perform dual cooling temperatures with high performance.
[83]	Cascade R744/R717 both ejector	Sim.	COP 1.6, This novel cascade system can increase the COP by an average of 7 percent and reduce the exergy loss during expansion.
[84]	Cascade integrated compression absorption R744/LiBr-H2O	Sim.	COP 0.87 at -40°C and 30°C, Cascade integrated compression absorption system has better energy, exergy, and economic performance than single-stage compression cycle in low-temperature refrigeration in hot climates.
[85]	2-stage absorption NH3-H2O with assisted compression dual-mod	Sim.	COP 0.65 at -35°C, The proposed cycle has better performance and economic feasibility than the conventional absorption water ammonia cycle in certain operating conditions
[86]	Various R744 cycles coupled to absorption cycles for after-cooling	Sim.	COPs as high as 0.9 were reported. Eleven configurations were analyzed. Absorption refrigeration cycles can be a possible option for improving the COP of transcritical R744 low-temperature cycles.
[87]	R744 2-stage with ejector	Sim.	COP 1.71 at -30°C, Under a typical condition, the COP and exergy efficiencies of the novel system are respectively 19.6% and 15.9% higher than those of the conventional system.

This thesis proposes an innovative layout for a low-temperature multi-stage trans-critical carbon dioxide ejector-based refrigeration cycle. It investigates the effects of three extra components, namely, a **compressor** and a **gas cooler** before the secondary entrance of the ejector and a **turboexpander** immediately after the ejector, in a conventional ejector refrigeration cycle. The new layout does not include an inter-stage heat exchanger, and the state points' pressures before and after the ejector are controllable. Additionally, the expansion valve which is located after the flash chamber (separator) was changed with a turboexpander. Conventionally, due to the insignificance pressure difference between the ejector's discharge and the evaporator, turboexpanders and ejectors are not utilized together. In this study, the mentioned pressure difference is noticeable, so the authors were convinced to change the expansion valves with turboexpanders. In the last two decades, new compressors became more and more efficient, and a new generation of compressors is on the way. The same condition is also valid for turboexpanders. Therefore, single-refrigerant systems are an option that worth to be considered.

The feasibility of the new layout was studied by finding the optimal operating condition's pressures by the first law parametric analysis. Second law analysis, which is a useful method to study the primary sources of irreversibility in the cycle, was performed comprehensively. From the thermodynamics point of view, the current cycle has reasonable energy and exergy performance without using an inter-stage heat exchanger and multi-refrigerants. Studying the parallel effects of both ejector and turboexpander is a unique investigation in the field of heat pumping systems.

This study also presents a combined layout with the inclusion of ORC for the recuperation of heat from the discharge of compressors and regenerated a fraction of lost work to improve the performance.

2. Cycle schematics and analysis method

2.1. The layout and introduction of cycle

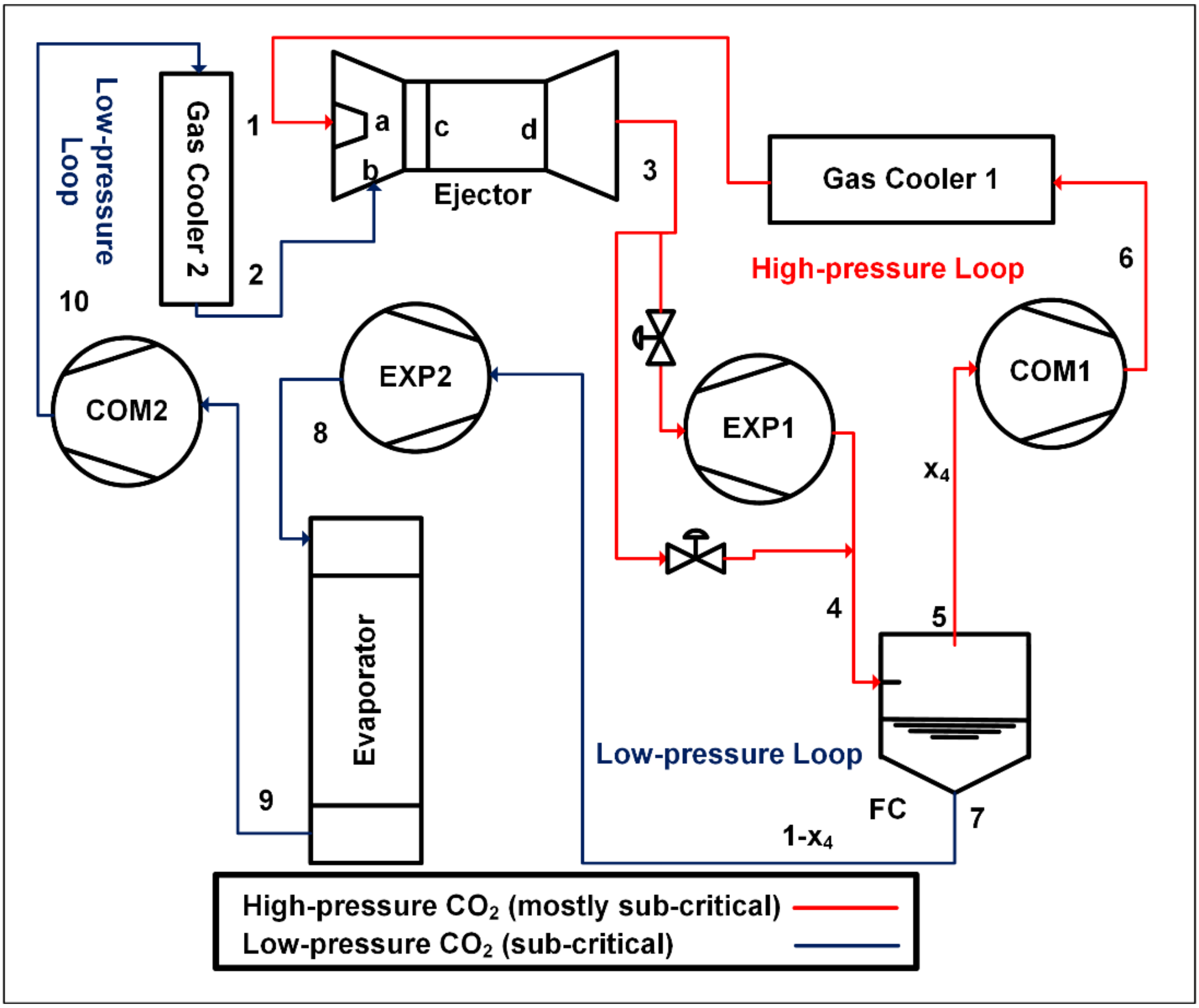

Fig. 11: The Schematic diagram of the proposed cycle

Fig.11 shows the layout of the proposed ejector cycle for low-temperature refrigeration. The compressor consumes work and increases the pressure of refrigerant in an adiabatic process. Expander decreases the pressure of the refrigerant and produces a small fraction of work in an adiabatic process. The Flash chamber separates the vapor from 2-phase (vapor-liquid) flow in an adiabatic isobaric process. Evaporator receives heat from the refrigerated space and vaporizes the refrigerant. The gas cooler dissipates the heat to the environment and cools the refrigerant. Both evaporator and gas cooler are isobaric. The ejector creates a vacuum with the help of the primary nozzle and sucks the secondary flow. Then it mixes both flows and discharges them with a lift in the pressure. In this paper, the pressure after the ejector is termed as the purged pressure. The components of the ejector are shown in Fig. 11. The primary and secondary nozzles, diffuser, and constant area chamber are adiabatic. The mixing section is isobaric and adiabatic. Two control valves are placed to isolate the EXP1 from the system. The application of these valves is explained in section 3.2.

Types of machinery were not discussed because the thermodynamic simulation is the priority of this study. Fig. 12 and Fig.13 show the T-s and P-h diagrams of the cycle, according to Table 8.

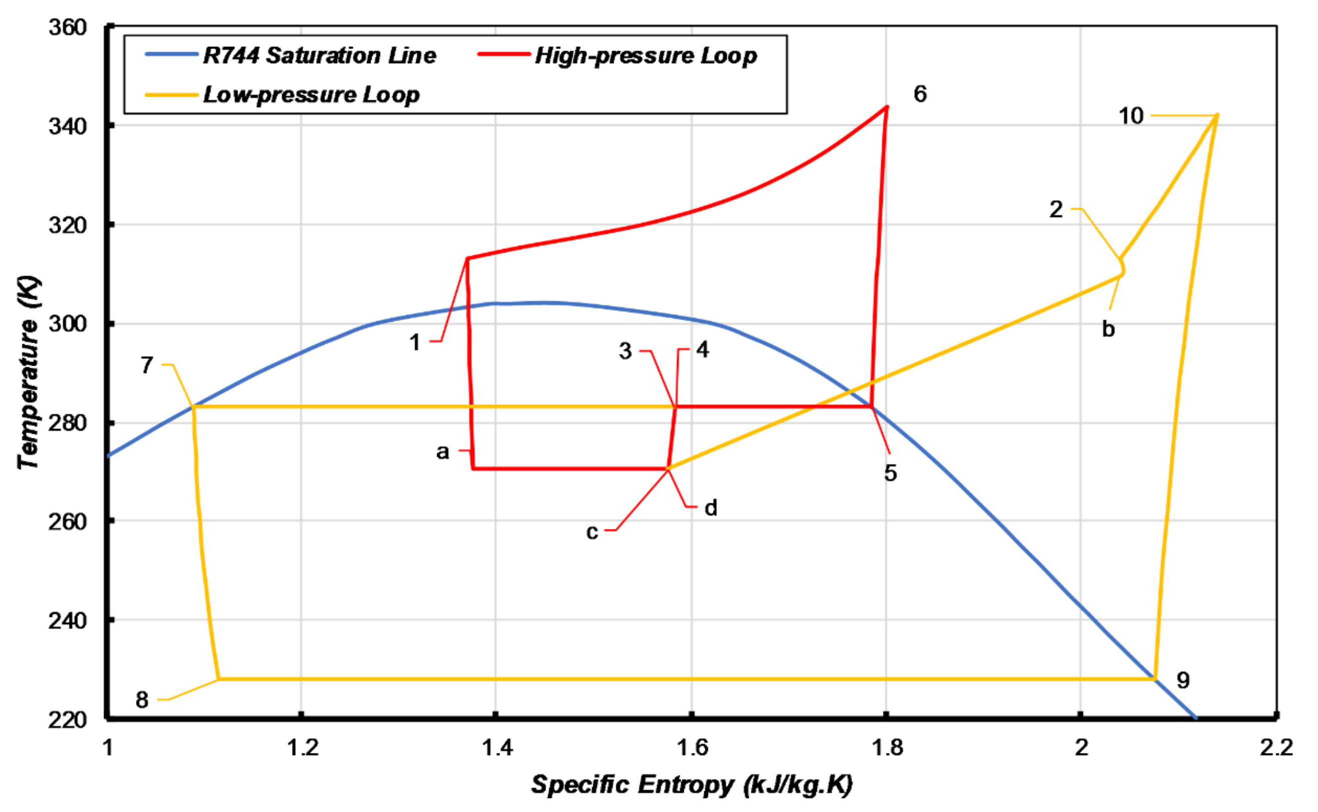

Fig. 12: The Temperature-Specific entropy diagram of the cycle according to optimal COP

The effects of pipes are not considered. Also, the friction loss in components is assumed to be zero. This cycle has two loops. It is reasonable to say that this cycle has connected two conventional cycles with an ejector. The low-pressure loop is pumping the heat from the evaporator to the second gas cooler and mainly to the high-pressure loop. The high-pressure loop mostly drives the low-pressure-loop and transfers the heat to the ambient.

In the CO_2 section, the impossibility of wet compression is another assumption, although the wet expansion is unconditionally accepted. However, in the propylene section, the pump can start from the saturation liquid point and humidity in the turbine is unacceptable.

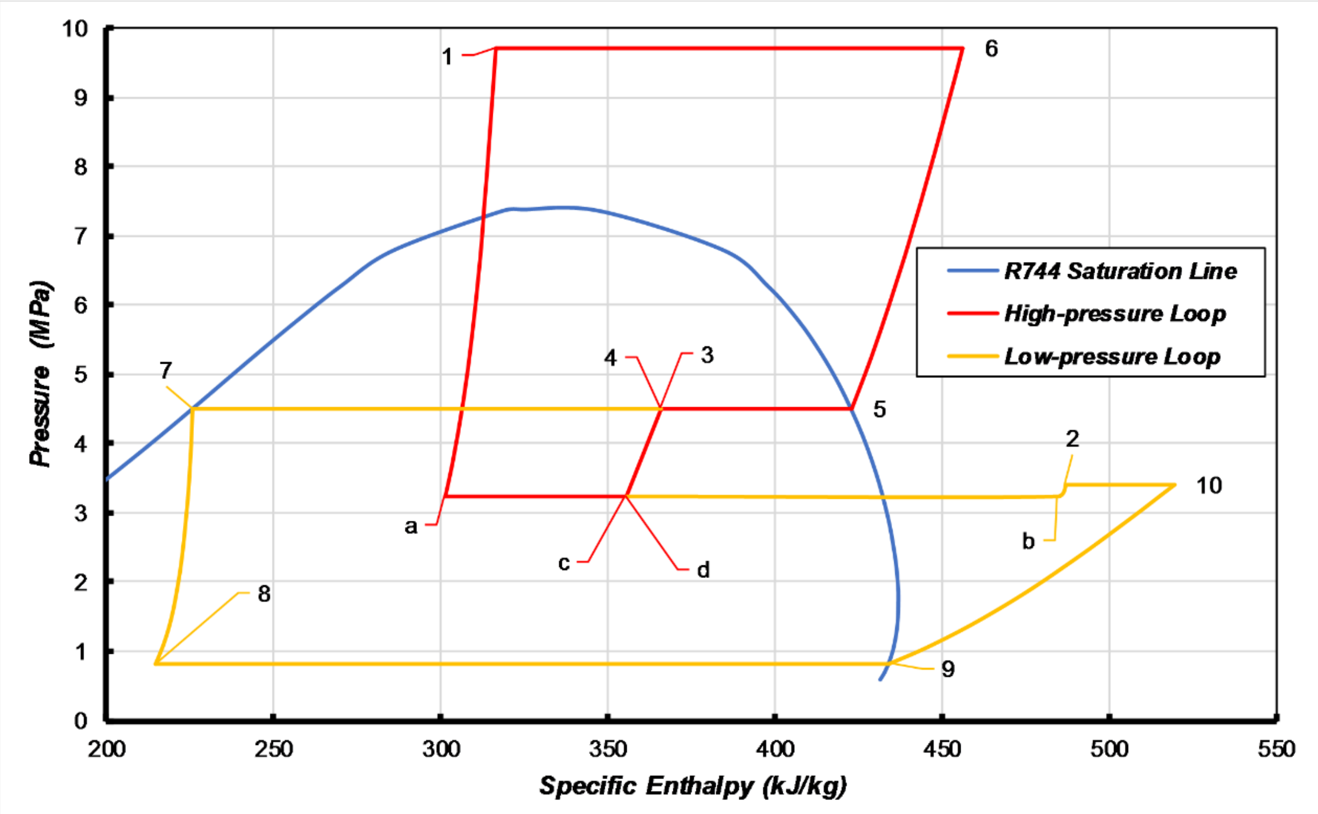

Fig. 13: The Pressure-Specific enthalpy diagram of the cycle according to optimal COP

2.2 Energy analysis

The First law of thermodynamics for steady-state steady-flow control volume with the negligible potential energy of the flow is:

$$q - w = \sum(h_{out} + \frac{V_{out}^2}{2}) - \sum(h_{in} + \frac{V_{in}^2}{2}) \tag{1}$$

The speed of flow was considered negligible in all cycle's state points except for the points inside the ejector. The thermophysical properties of carbon dioxide were calculated using Klein SA. Engineering Equation Solver (Version V10.644), F-Chart Software 2019 [88], based on real state (non-ideal) condition. Furthermore, the main structure of data was recalculated by calling REFPROP [89] libraries in Phyton. The mass, energy, and exergy balance equations are listed in Table 6. Table 7 contains the mass and energy balance equations of the hybrid cycle. The exergy analysis for the hybrid cycle is not shown here, because it does not contain any informatic findings. Optimization of all results for every calculation is the strategy of this study. Due to the numerosity of data points and the chaotic nature of the formulas, which in turn need more human intervention, the "Variable Metric" method was chosen. This method seemed to be smoother and more efficient. To examine the algorithm, other methods (Conjugate Directions, Nelder-Mead Simplex) optimized random points of the cycle, and the same output was observed.

2.2.1 Compression and expansion

The results of the simulation would only be in the range of the ideal cycle if both compressors had the isentropic efficiency of 100%. Suction pressure and lift are essential factors that affect the efficiency of the compressor. Equations (2) to (6) illustrate the relationship between efficiency and compression ratio. Even though these five models do not consider the suction pressure in the compression for CO_2, they were mostly obtained from the experimental results and are accurate enough. The 6th model is a constant quantity, which is the average mean integral value of the other five models with compression ratios between 1 to 5.

Model 1[90]) $$\eta_{COM} = 1 - 0.04CR \quad (2)$$

Model 2[91]) $$\eta_{COM} = 1.003 - 0.121CR \quad (3)$$

Model 3[56]) $$\eta_{COM} = 0.9343 - 0.04478RC \quad (4)$$

Model 4[29]) $$\eta_{COM} = 0.815 + 0.022CR - 0.0041CR^2 + 0.0001CR^3 \quad (5)$$

Model 5[73]) $$\eta_{COM} = 0.8981 - 0.9238CR + 0.00476CR^2 \quad (6)$$

Model 6) $$\eta_{COM} = 0.75 \quad (7)$$

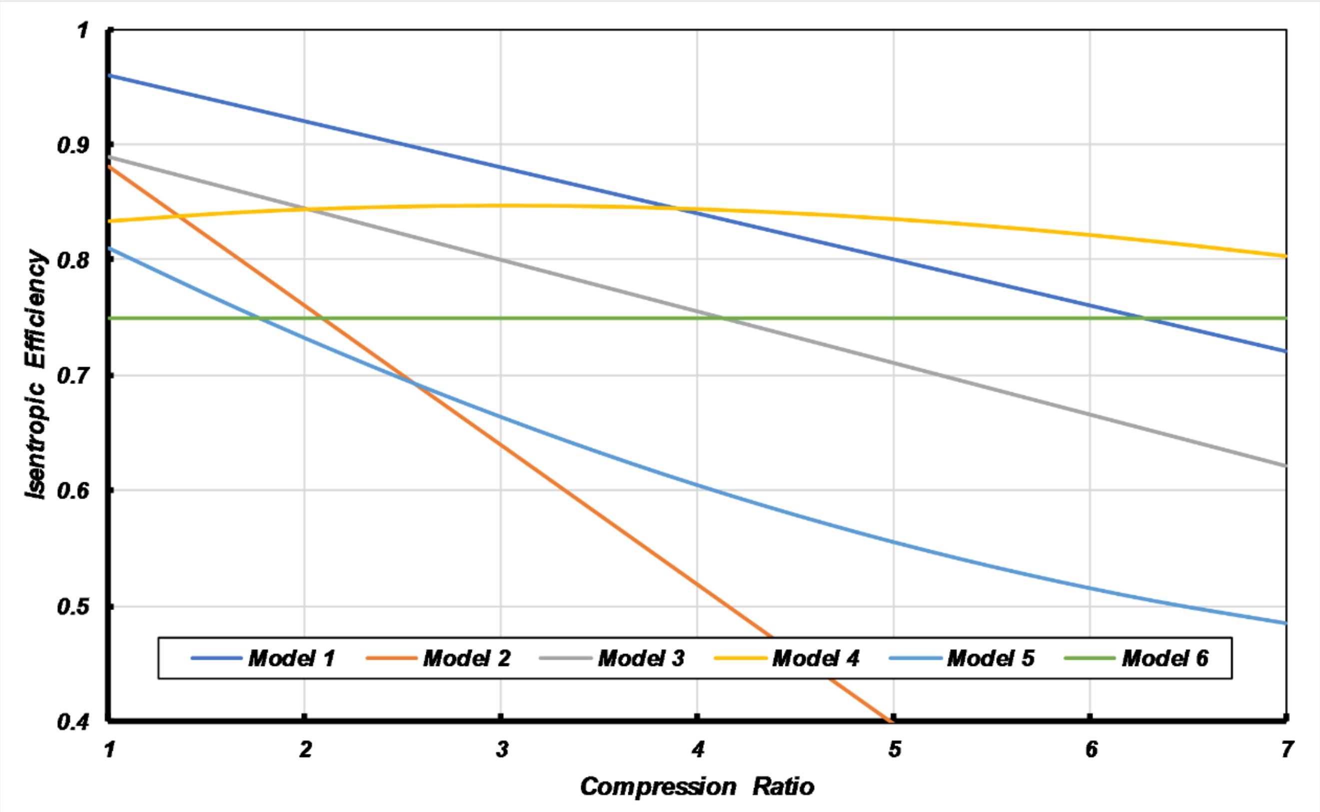

Fig. 14: Isentropic efficiency of the compressor versus compression ratio in different models of compressors.

For the main calculations, model 3 was used. However, for the parametric analysis, all models were considered.

$$h_{out} = h_{in} + \frac{h(P_{out}, s_{in}) - h_{in}}{\eta_{COM}} \quad (8)$$

The relation between the isentropic efficiency of the compressor and the compression ratio was presented in Fig. 14. The presented models almost have better performance at lower pressure ratios. Because of this, the least possible compression ratios were usually observed in the optimum results.

Pumps of the ORC use the same equation as (8). The isentropic efficiency of pumps is 0.8[48].

Neither turboexpanders are also 100 percent efficient. The isentropic efficiency of the turboexpanders is considered 65%. Isentropic efficiencies from [29][92][93] were used for parametric analysis.

$$h_{out} = h_{in} - \eta_{EXP}(h_{in} - h(P_{out}, s_{in})) \quad (9)$$

If the efficiency of the turboexpander approaches zero, it behaves like a normal throttling valve. It is also possible that in turboexpanders, the recovered work doesn't utilize. Both conditions were studied in parametric analysis.

Turbines of the ORC use the same equation as (9). The isentropic efficiency of turbines is 0.8[48].

Two parameters are used to compare the feasibility of using a turboexpander in the cycle. The first one is cooling capacity boost percentage which indicates who much the latent heat in the evaporator was increased if a turboexpander was used instead of a throttling valve.

$$CCB = \left(1 - \frac{h_{out,EVA} - h_{out,EXP}}{h_{out,EVA} - h_{in,EXP}}\right) \times 100 \quad (10)$$

The second one is the recovered work percentage which illustrates the fraction of the consumed worked that recovered by the expander or expanders.

$$RW = \frac{Sum\ of\ all\ work\ produced\ by\ the\ turboexpanders}{Sum\ of\ all\ work\ consumed\ by\ the\ compressors} \times 100 \quad (11)$$

2.2.2 Mass flow rate

The mass flow rate of the refrigerant in the evaporator (which is also the mass flow rate of secondary flow of ejector) is given as:

$$\dot{m}_{EVA} = \dot{m}_{sec} = \frac{3516.9}{h_9 - h_8} \quad (12)$$

$$\dot{m}_{total} = \frac{\dot{m}_{sec}}{1 - x_4} \quad (13)$$

$$\dot{m}_{pri} = x_4 \frac{\dot{m}_{sec}}{1 - x_4} \quad (14)$$

Note that the unit of the calculated mass flow rate is grams per second per refrigeration ton.

2.2.3 Ejector

2.2.3.1 Nozzles

The isentropic efficiency of nozzles can be defined as the same as compressors. The nozzles' simulation is only thermodynamic and independent from the cross-section area and area ratios. It was also supposed that in the case of the supersonic speed in the nozzle, the normal shock would not happen in the primary nozzle. So, there is no need for calculation of critical area ratio, and throat pressure, and a converging nozzle model can be used for the simulation of both subsonic and supersonic speeds. For the primary nozzle:

$$h_a = h_1 - \eta_n(h_1 - h(P_a, s_1)) \quad (15)$$

$$V_a = \sqrt{2(h_1 - h_a)} \quad (16)$$

The same method was used for the secondary nozzle. To produce a vacuum for the secondary flow, the discharge pressure of the primary nozzle is set to 95% suction pressure of the secondary nozzle.

$$h_b = h_1 - \eta_n(h_1 - h(P_b, s_1)) \quad (17)$$

$$V_b = \sqrt{2(h_1 - h_b)} \quad (18)$$

The final pressures of primary and secondary nozzles are the same.

2.2.3.2 Speed of sound in 2 phase liquid-vapor condition

Niguen et al.[94] proposed an accurate equation to determine the speed of sound in the 2-phase condition.

$$C = \frac{1}{(1-\alpha)\sqrt{\frac{1-\alpha}{C_l^2} + \frac{\alpha\rho_l}{\rho_v C_v^2}} + \alpha\sqrt{\frac{\alpha}{C_v^2} + \frac{(1-\alpha)\rho_v}{\rho_l C_l^2}}} \quad (19)$$

where α is the void fraction of fluid. It is supposed that the 2-phase medium is homogenous.

$$\alpha = \frac{x\rho_l}{x\rho_l + (1-x)\rho_v} \quad (20)$$

2.2.3.3 Mixing section

In this cycle, the entrainment ratio of the ejector depends on the quality of vapor after the first expander.

$$R = \frac{\dot{m}_{sec}}{\dot{m}_{pri}} = \frac{1 - x_4}{x_4} \quad (21)$$

Usually, the mixing factor is used as a form of mixing efficiency or mixing chamber effectiveness. However, in this paper new equation was derived for the mixing efficiency.

From the conservation of momentum in an isobaric medium:

$$V_a + R(V_b) = (1 + R)(V_{c.id}) \quad (22)$$

Conservation of energy:

$$h_a + \frac{V_a^2}{2} + R(h_b + \frac{V_b^2}{2}) = (1 + R)(h_{c,id} + \frac{V_{c,id}^2}{2}) = (1 + R)(h_c + \frac{V_c^2}{2}) \quad (23)$$

$$\eta_m = \frac{(1+R)h_{c,id} - h_a - Rh_b}{(1+R)h_c - h_a - Rh_b} = \frac{V_a^2 + RV_b^2 - (1+R)V_{c,id}^2}{V_a^2 + RV_b^2 - (1+R)V_c^2} \quad (24)$$

2.2.3.4 Shock

It is assumed that if the flow stream after the mixing process is supersonic, there will be a normal shock in the constant area chamber. Otherwise, all properties of refrigerants remain the same. The position of the shock is assumed to be after the mixing chamber. Otherwise, the assumption for the isobaric mixing chamber cannot be satisfied. For the normal shock, it starts with the conservation of mass:

$$\rho_c V_c = \rho_d V_d \quad (25)$$

Conservation of momentum:

$$P_c + \rho_c {V_c}^2 = P_d + \rho_d V_c V_d \quad (26)$$

Conservation of energy:

$$h_c + \frac{{V_c}^2}{2} = h_d + \frac{{V_d}^2}{2} \quad (27)$$

Thermodynamic state equation for density:

$$\rho_d = \rho(P_d, h_d) \quad (28)$$

For the initial guess for the density, the conventional formula for ideal gas was used.

$$\rho_d = \rho_c\left(\frac{(\gamma+1)M_c^2}{(\gamma-1)M_c^2 + 2}\right) \quad (29)$$

In which γ for single-phase:

$$\gamma = \frac{c_p(P_c, h_c)}{c_v(P_c, h_c)} \quad (30)$$

For 2-phase:

$$\gamma = x_c\left(\frac{c_p(P_c, x=1)}{c_v(P_c, x=1)}\right) + (1 - x_c)\left(\frac{c_p(P_c, x=0)}{c_v(P_c, x=0)}\right) \quad (31)$$

This mathematical modeling is not only unable to predict the oblique and pseudo-shocks, but also returns questionable results about normal shockwaves. According to [95][96][97], the hydraulic boundary layer and the geometry of the ejector have a significant impact on the shape, location, and strength of the shockwaves. Yazdani et al.[97] stated that the supersonic core can be extended from the neck of the primary nozzle to the beginning of the diffuser and the quality of the vapor mimics the pressure-velocity profile. Previous CFD and experimental studies [98][99][100] on the R744 ejector show that the normal shock tends to migrate to the discharge of the primary nozzle and all different kinds of shocks cause continuous massive turbulence before and after constant area chamber and affect the performance negatively. Equations 25-27 don't include any geometry or friction terms and only present the pure thermodynamic form of the jump conditions. However, due to the reasons below, it was decided to include these conditions in the algorithm.

1. There is not any comprehensive and geometry-free model to fulfill the design policy of this study and it is probable that will not be available in the future. The results from experiments and CFD studies are highly case-oriented.

2. Even though the current model cannot calculate the shockwave correctly, it creates a dent in the profile of performance and pushes the optimization algorithm away from creating the normal shockwaves and it is rare to counter the supersonic situation in final optimized results. In a nutshell, the jump conditions are considered in order to be identified and to the utmost be avoided.

3. After the initial calculations, it was disclosed that the Mach number after the mixing does not exceed 1.2 even in the far valued parametric analysis, which indicates that probably the shock is not intensive and the outcome would not be considered as an outliner.

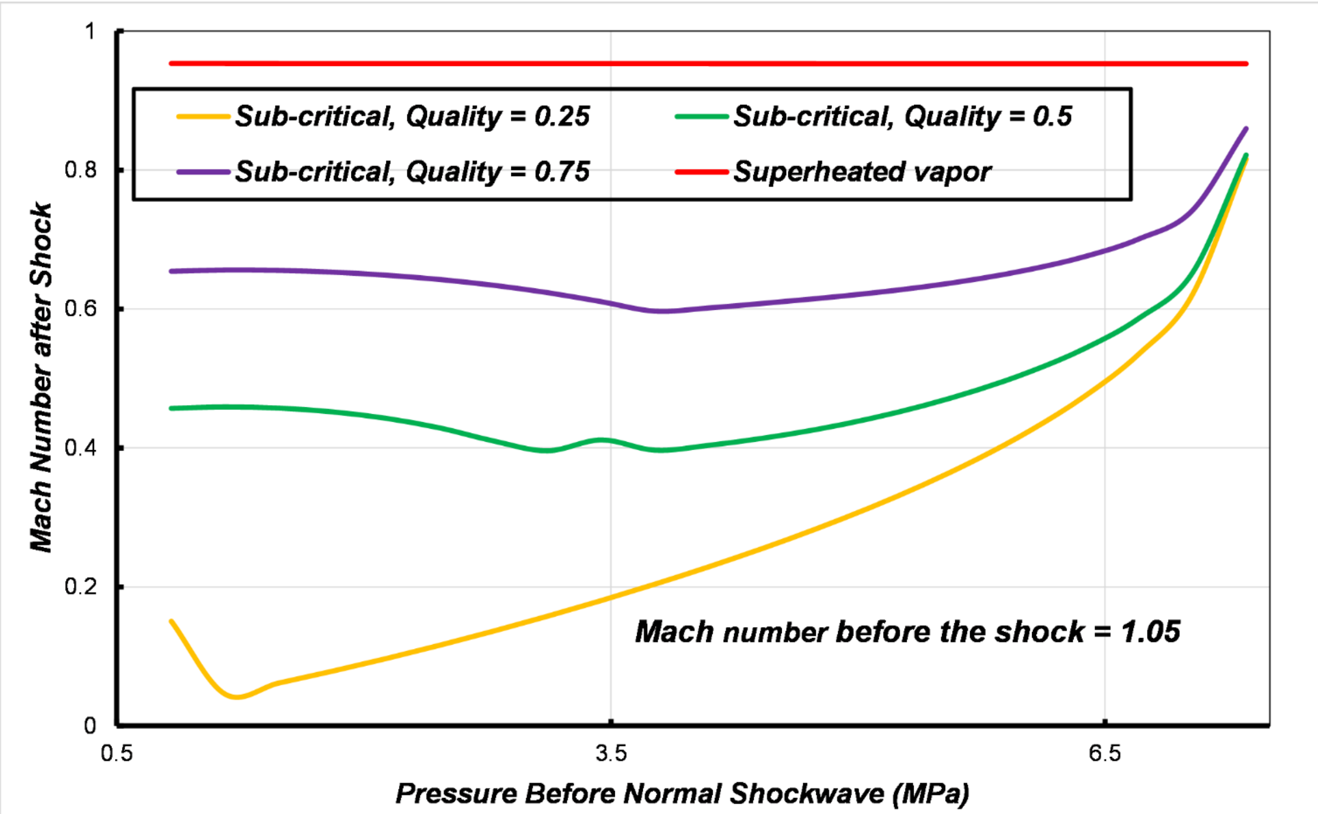

Fig. 15: Mack number after the normal shock wave of Mack 1.05 in 2-phase and superheat regions

Fig. 15 to Fig. 24 illustrate the results from the shock equations. As it was stated before, there is no set of data that can be used to validate these results. However, the trends are acceptable. In all the points the Mach number reduction takes place and the entropy generation has happened. In the 2-phase state, the changes are sharp at the low quality of vapor and when it approaches the saturated vapor the shock becomes milder.

The sub-critical and superheat region temperature is 7 degrees away from the saturation line. The results from non-2-phase conditions are shown only for Mack 1.05 because the shock wave in these regions are not as intense as the 2-phase section and bringing them here may unnecessarily lengthen the report. Mack 1.05 was chosen because it has the mildest shockwave. By increasing the Mack number, the intensity is increased.

The results from the shockwave model are not reliable but they can be used to make a dent in the optimization algorithm to prevent the refrigeration cycle to enter the supersonic state.

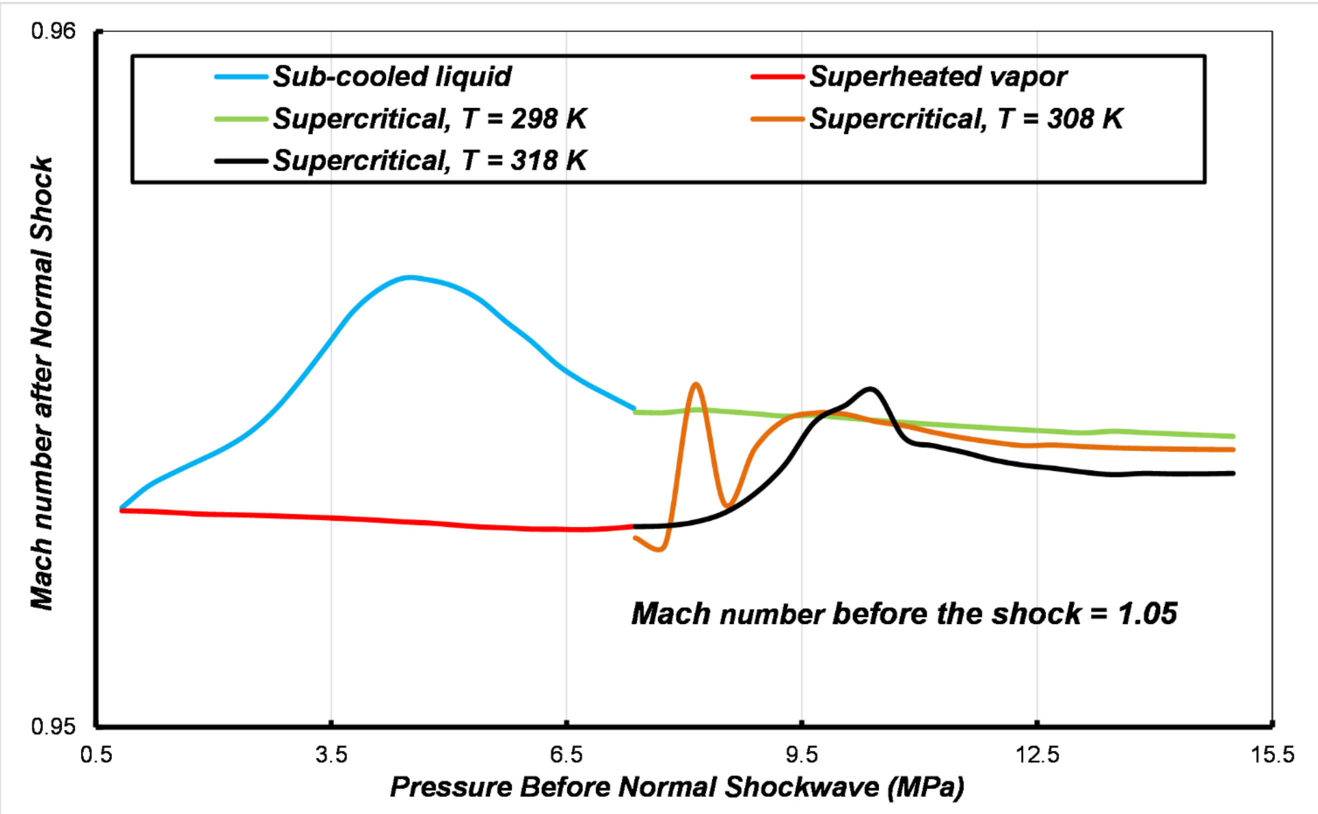

Fig. 16: Mack number after the normal shock wave of Mack 1.05 in non-2-phase regions

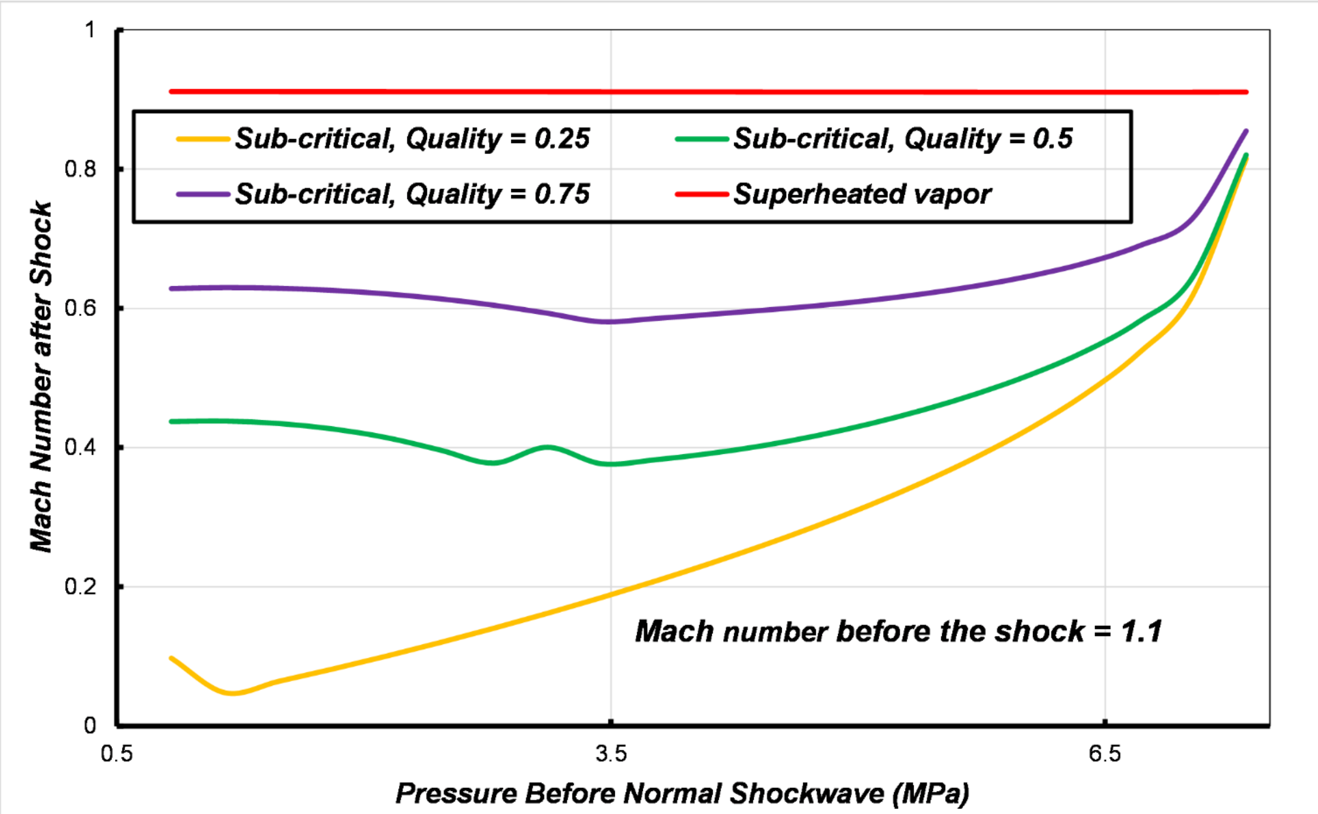

Fig. 17: Mack number after the normal shock wave of Mack 1.1 in 2-phase and superheat regions

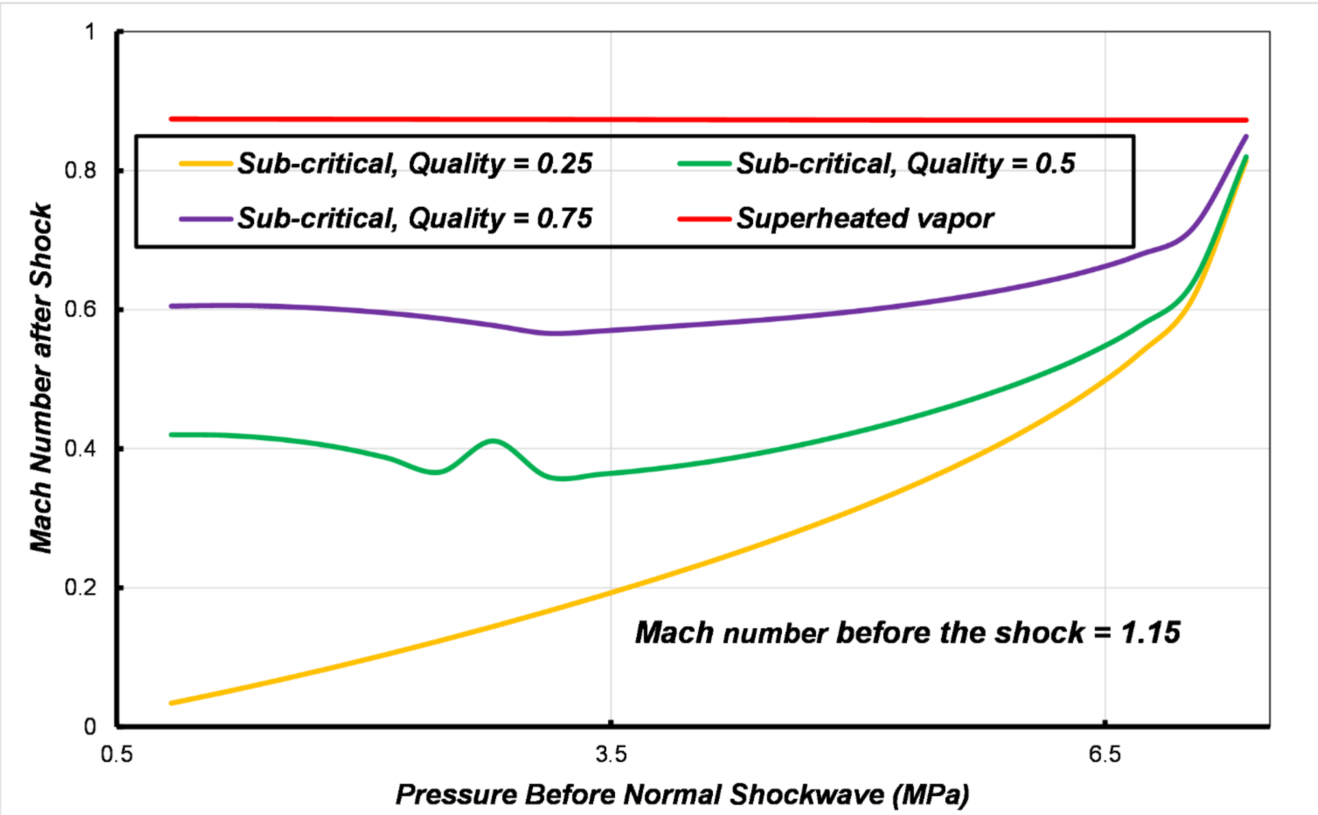

Fig. 18: Mack number after the normal shock wave of Mack 1.15 in 2-phase and superheat regions

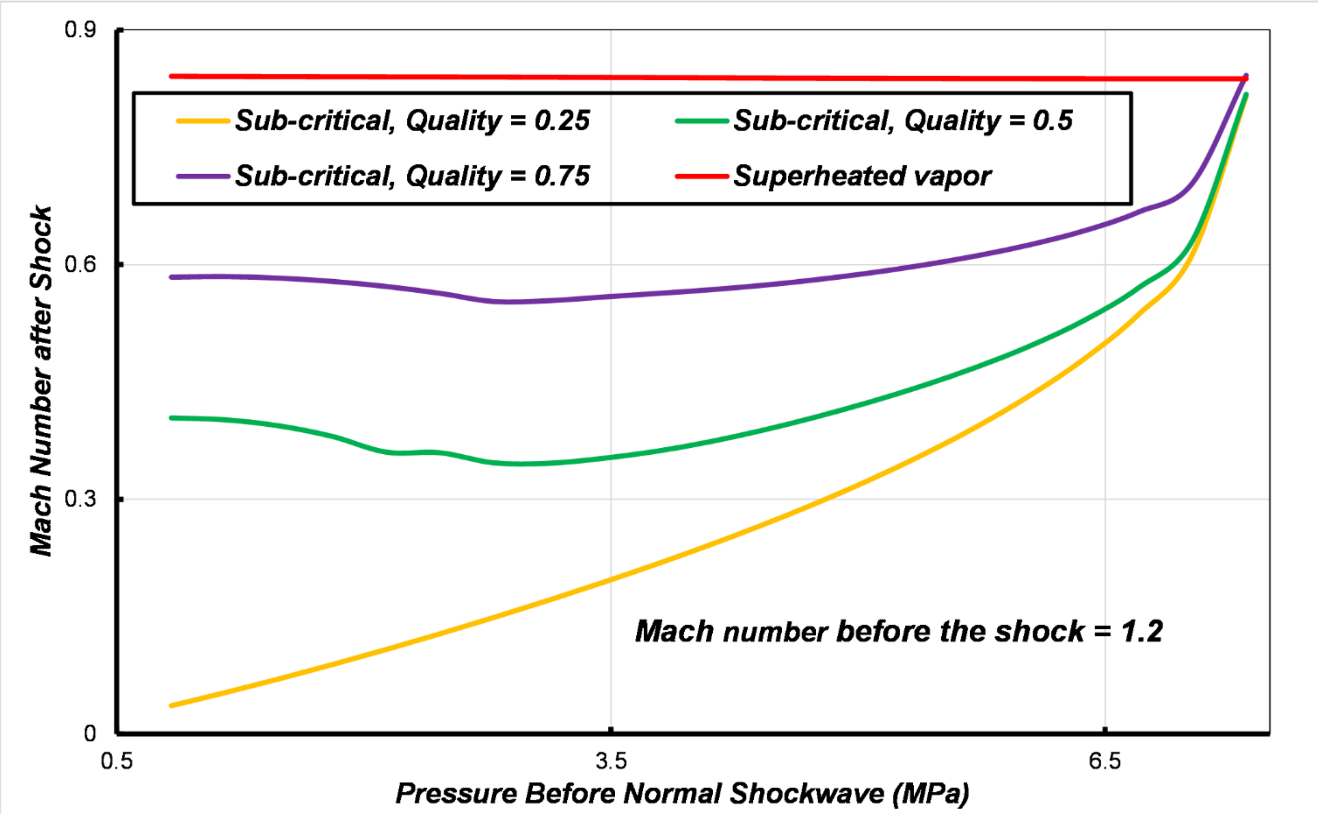

Fig. 19: Mack number after the normal shock wave of Mack 1.2 in 2-phase and superheat regions

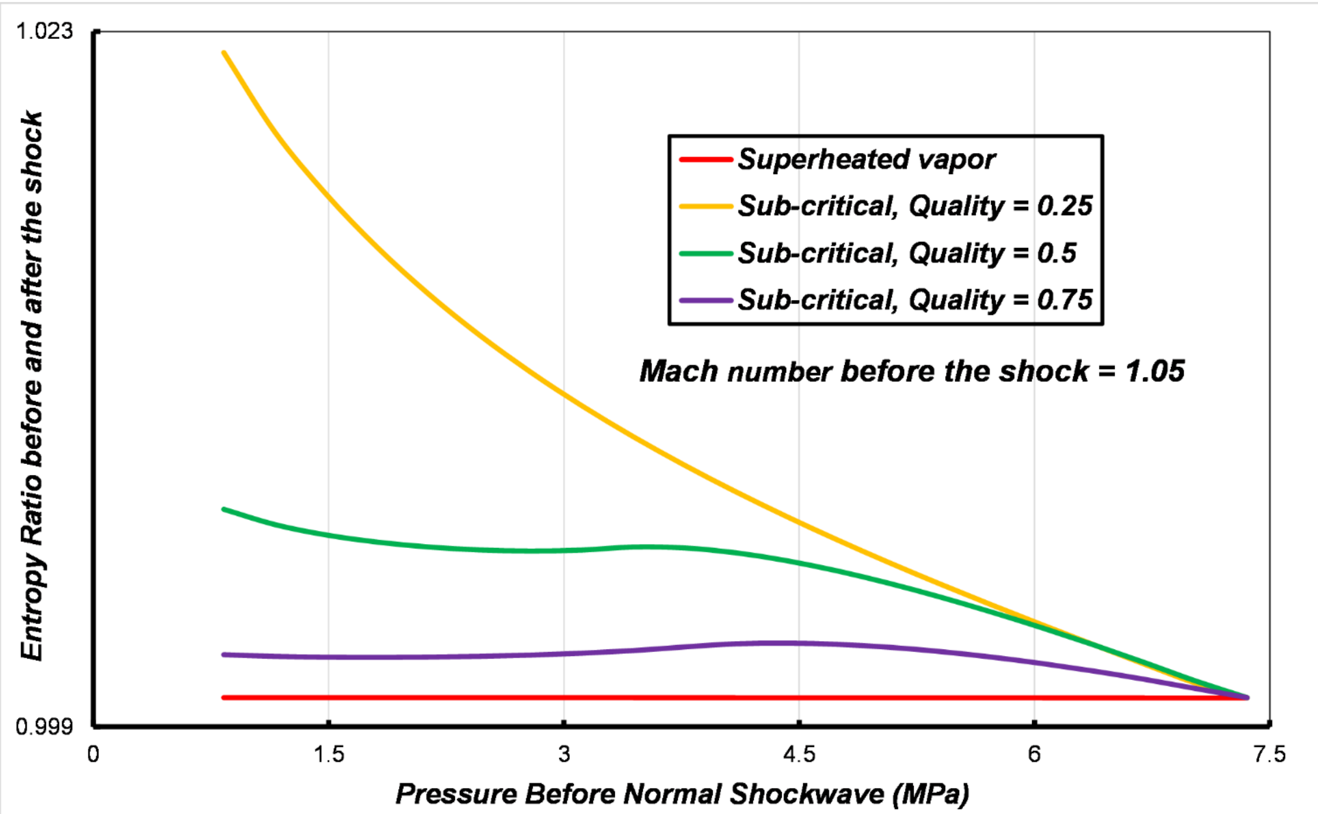

Fig. 20: Entropy ratio after the normal shock wave of Mack 1.05 in 2-phase and superheat regions

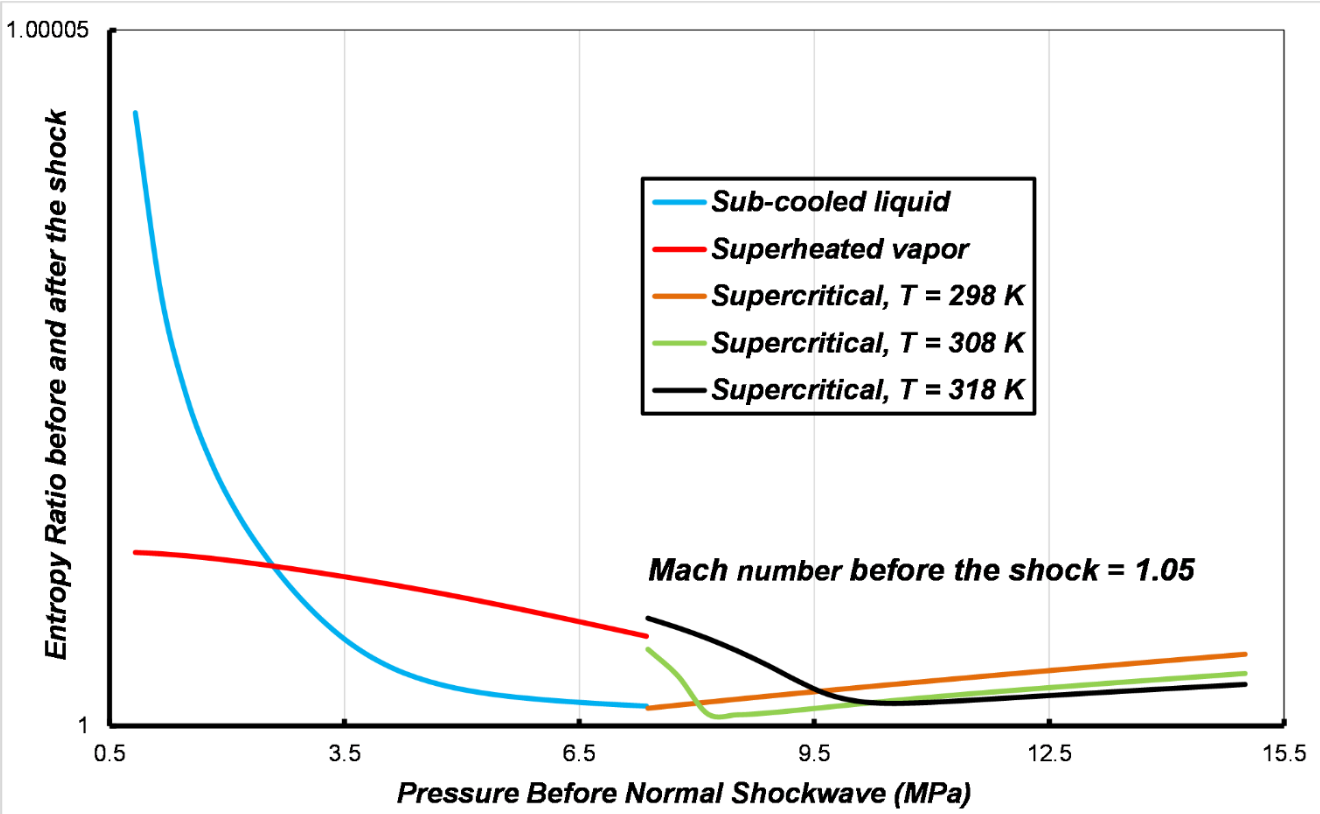

Fig. 21: Entropy ratio after the normal shock wave of Mack 1.05 in non-2-phase regions

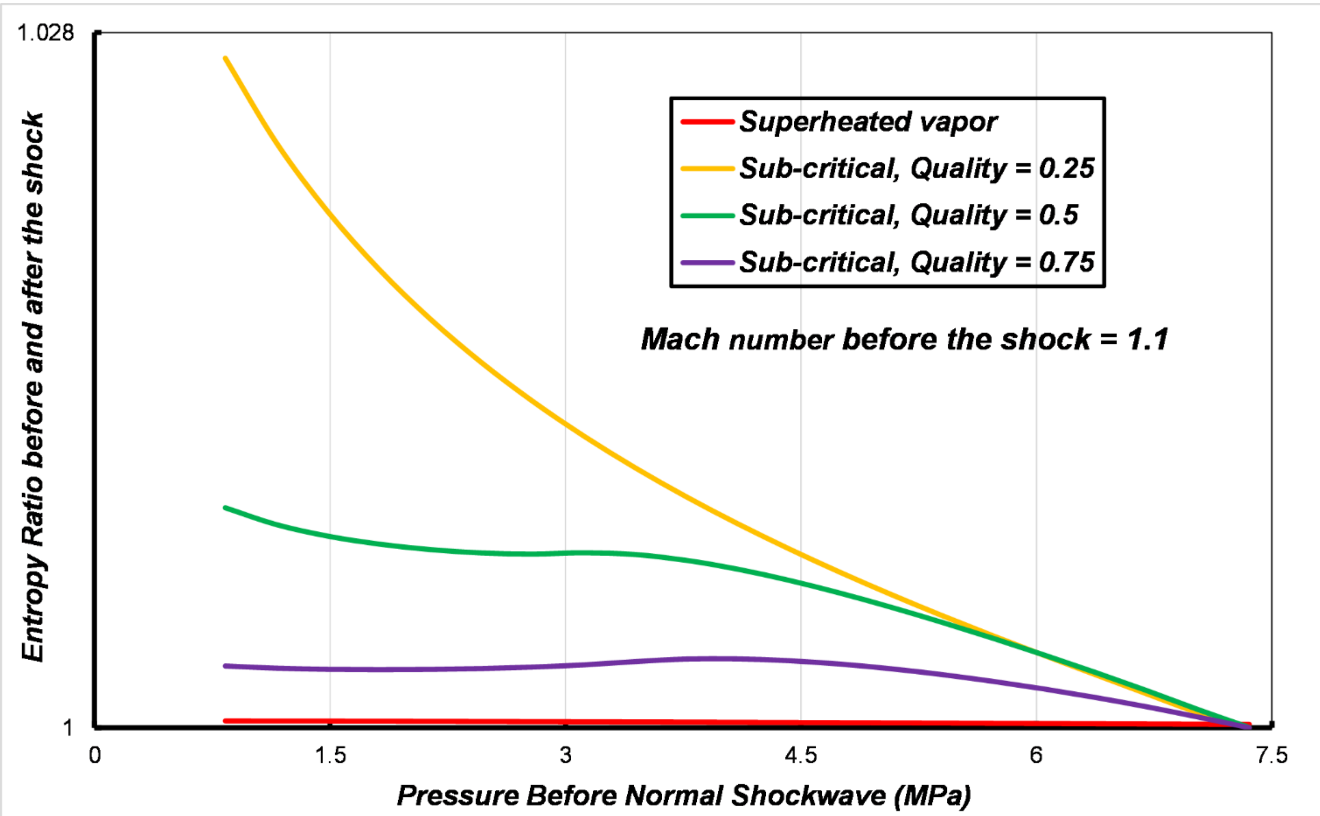

Fig. 22: Entropy ratio after the normal shock wave of Mack 1.1 in 2-phase and superheat regions

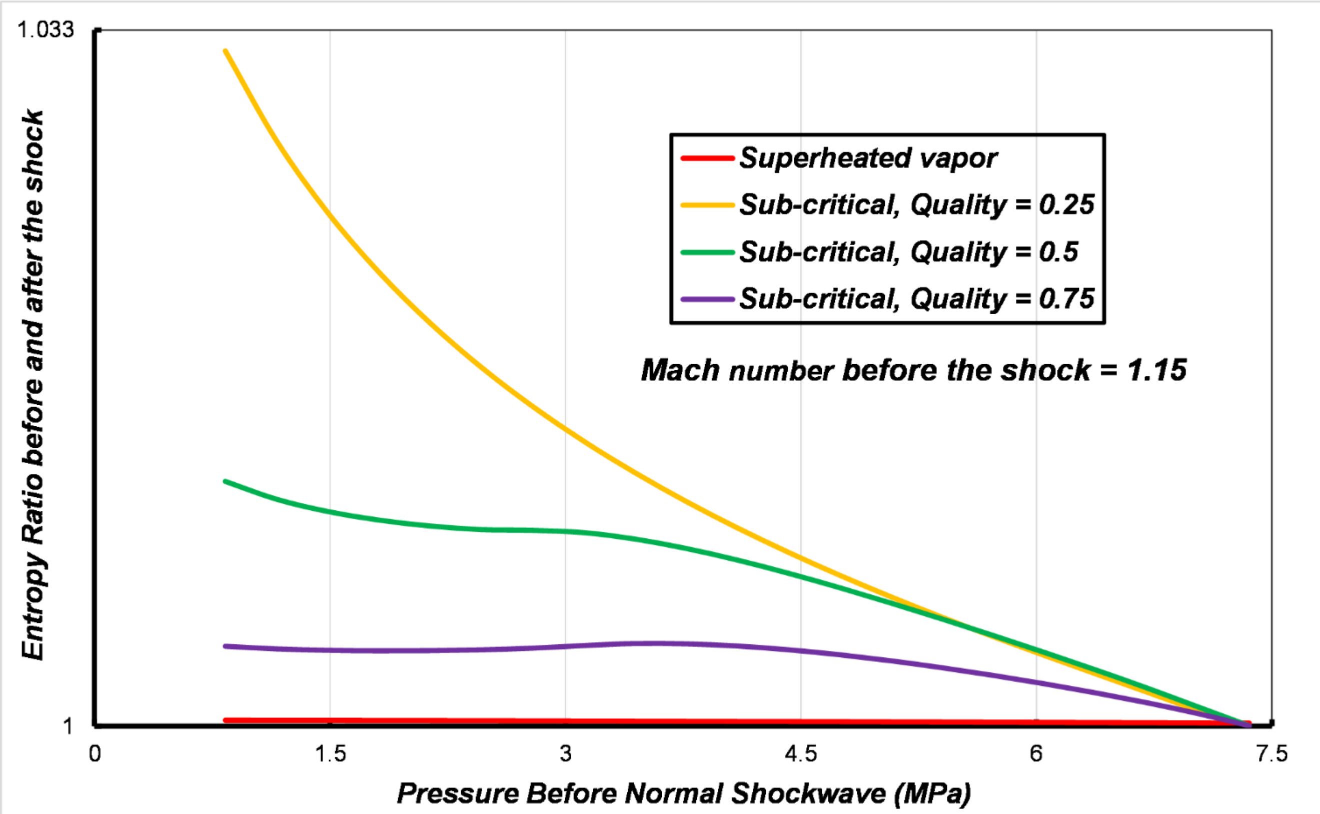

Fig. 23: Entropy ratio after the normal shock wave of Mack 1.15 in 2-phase and superheat regions

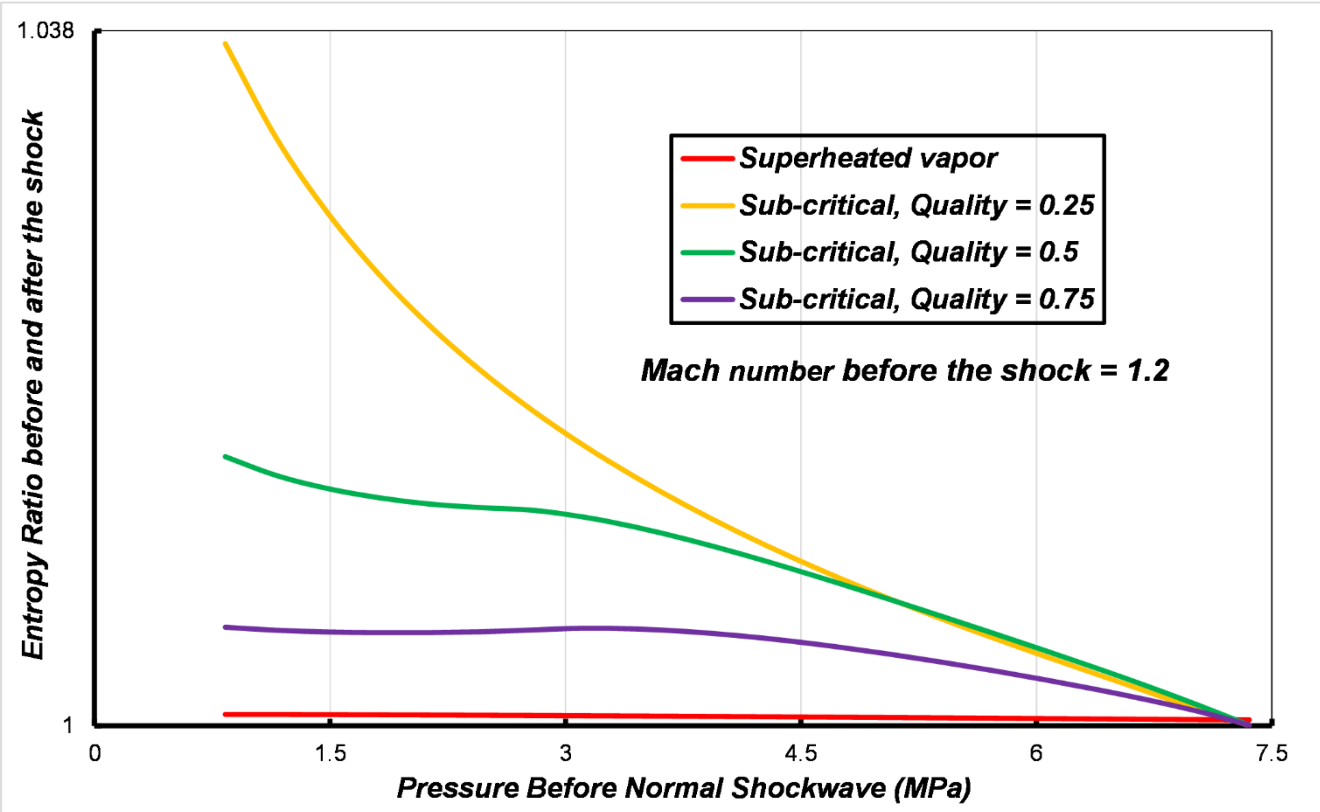

Fig. 24: Entropy ratio after the normal shock wave of Mack 1.1 in 2-phase and superheat regions

2.2.3.5 Diffuser:

$$h_3 = h_d + \frac{V_d^2}{2} \tag{32}$$

$$h_{3,is} = h_d + \eta_d (h_3 - h_d) \tag{33}$$

$$P_3 = P(h_{3,is}, s_d) \tag{34}$$

$$T_3 = T(P_3, h_3) \tag{35}$$

The efficiencies of ejector components are derived from [101], which performed a comprehensive review of different articles to find various assumptions for ejector components efficiencies. Table 5 shows a condensate of previous studies that were used for parametric analysis.

Table 5: Ejector component efficiencies in other studies

Ejector Model	Reference	Primary Nozzle	Secondary Nozzle	Mixing Area	Diffuser
I	[102]	0.9	0.9	1	0.9
II	[103]	0.85	0.85	1	0.75
III	[38]	0.7	0.7	1	0.8
IV	[42]	0.8	0.8	1	0.75
V	[104]	0.8	0.8	1	0.8
VI	[105]	0.9	0.9	1	0.8
VII	[106]	0.7	0.7	0.95	0.8

In this study, the VI model is used for the main calculation. Other models were considered in the parametric analysis.

2.2.4 Heat exchangers in ORC

The effectiveness of heat exchangers used as the main equation to identify their temperature profile. In this regard, the heat capacitance rate (not the specific heat) plays an important role. It is the multiplication of specific heat capacity and mass flow rate. The heat exchangers are counter-current with the effectiveness of 0.85[48]. If the heat capacitance rate at the R1270 side is higher.

$$Q_{max} = \dot{m}_{R744}\left(h_{in,R744} - h(R744@T_{in,R1270}\&P_{in,R744})\right) \tag{36}$$

If the heat capacitance rate at the R744 side is higher.

$$Q_{max} = \dot{m}_{R1270}\left(h\left(R1270@T_{in,R744}\&P_{in,R1270}\right) - h_{in,R1270}\right) \tag{37}$$

$$\lambda = \frac{\dot{m}_{R1270}(h_{out} - h_{in})_{R1270}}{Q_{max}} = \frac{\dot{m}_{R744}(h_{in} - h_{out})_{R744}}{Q_{max}} \tag{38}$$

When the temperature profiles are identified, the LMTD method is used to calculate the UA factor of heat exchangers. 5 degrees is the limitation of approach temperature in the heat exchangers.

2.2.5 Coefficient of performance

$$COP = \frac{\dot{m}_{sec} \times q_{EVA}}{\dot{m}_{pri} \times w_{COM1} + \dot{m}_{sec} \times w_{COM2} - \dot{m}_{total} \times w_{EXP1} - \dot{m}_{sec} \times w_{EXP2}} \quad (39)$$

Other COPs are also calculated and shown in Table 9. Internal ideal COP shows the performance if the efficiency of COMs, EXPs, and ejector components are 1. External ideal COP states the hypothetical performance if the approach temperatures in GCs and EVA become zero. The ideal COP is the union of the ideal external and internal performances. Note that these COPs are optimized.

For the hybrid cycle, this equation must be used.

$$\begin{aligned} COP = {} & \dot{m}_{sec} \times q_{EVA} \\ & /\big(\dot{m}_{pri} \times w_{COM1} + \dot{m}_{sec} \times w_{COM2} + \dot{m}_y \times w_{PU1} + \dot{m}_z \times w_{PU2} \\ & - \dot{m}_{total} \times w_{EXP1} - \dot{m}_{sec} \times w_{EXP2}(40) - \dot{m}_y \times w_{TUR1} - \dot{m}_z \times w_{TUR2}\big) \end{aligned} \quad (40)$$

Fig. 25 was drawn for a better understanding of the simulation. This is the flow chart of a successful program that ran in EES and Python. In addition to this algorithm, an extra layer was used to check the dependence of the final result on the additional number of iterations and initial guessed values.

Fig. 26 presents the flow chart for the solution and optimization of the ORC section. The integrated compilation of the code was problematic and expensive. Because of this, it was decided to break the code into smaller libraries and linearize the optimization. In this regard, at the first step, the R744 cycle is calculated and optimized. Then the results of the R744 cycle include the terminal temperature and mass flow rates of CO_2 in the heat exchangers and the net work and inlet thermal energy of the R744 cycle. After that, the program starts to calculate the ORC. The limitation of this code is the negative temperature profiles in the heat exchangers. Two different single objective optimizations run. One aims the maximum possible thermal efficiency (ALPHA algorithm) of the ORC and the other one (BETA algorithm) targets the least possible humidity in turbines. Finally, the two results are compared by the decider code and the best COP which satisfies the dry expansion in the turbine is accepted.

It was observed that the results from the ALPHA did never satisfied the dry expansion, despite it has better COP. However, BETA can identify the point in which the outlets of both turbines are saturated vapor.

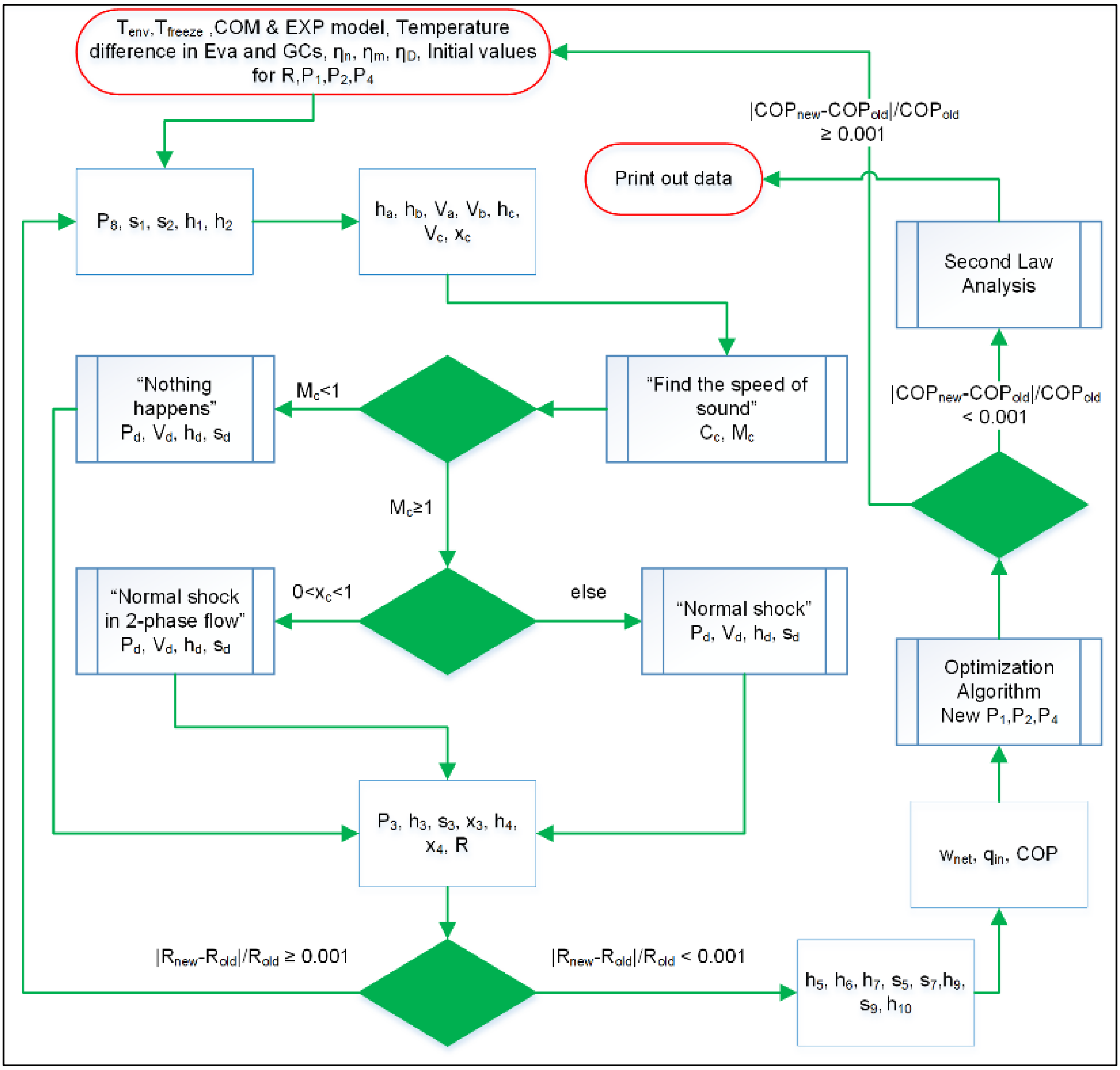

Fig. 25: The flow chart of the code to solve the R744 section of the cycle

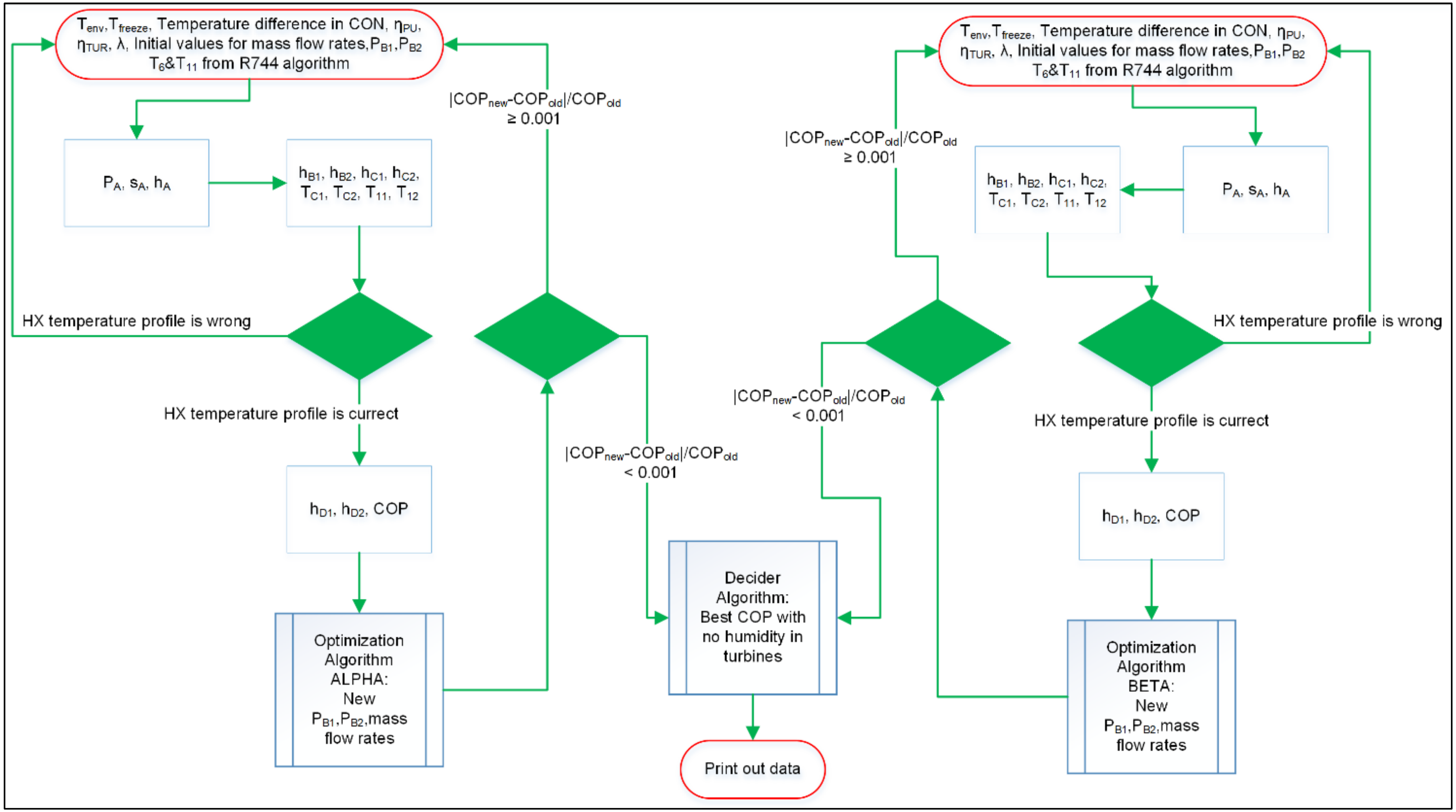

Fig. 26: The flow chart of the code to solve the R1270 section of the cycle

2.2.6 Sensitivity of performance to the efficiency of components

For every assumption for component efficiencies and models, optimized pressure matrixes were produced for two temperature ranges of evaporation and cooling. When a new model was studied, the returned results were also in matrix form. Equation (41) is used to calculate the difference between new and base assumption and also the reduction of the amount of data for presentation. Ω is a variable that resulted from the optimization of the cycle, and i, j are the temperature indexes. The median value was preferred to the average value to present the difference. It was observed that often the new results are heterogeneously far from the base model and have noticeably different peaks and valleys in their contours. Median showed a more logical conclusion, and if the new results are homogeneous, the difference between the median and average value is negligible.

$$\Delta\Omega\% = median\left(\frac{\Omega_{new}@(T_{1,i}, T_{2,j}) - \Omega_{base}@(T_{1,i}, T_{2,j})}{\Omega_{base}@(T_{1,i}, T_{2,j})}\right) \times 100 \tag{41}$$

2.3 Exergy Analysis

The general exergy balance equation for steady-state steady-flow control volume negligible kinetic and potential energy of the flow is:

$$Input\ Exergy = Output\ Exergy + Destroyed\ Exergy \tag{42}$$

Mass independent mathematical form:

$$\left(1 - \frac{T_0}{T}\right)\dot{Q}_{in} + \dot{W}_{in} + \sum \dot{m}_{in}a_{in} = \left(1 - \frac{T_0}{T}\right)\dot{Q}_{out} + \dot{W}_{out} + \sum \dot{m}_{out}a_{out} + \dot{E}_D \tag{43}$$

Specific exergy of flow with negligible potential energy:

$$a = (h - h_0) - T_0(s - s_0) + \frac{V^2}{2} \tag{44}$$

In the calculations, the ejector was assumed as a single unit, and exergy analysis didn't apply to its internal parts. Unlike the evaporator, the temperature of gas coolers is not constant. The mean temperature of the heat rejection in gas coolers:

$$T_{mean} = \frac{T_{in} - T_{out}}{\ln \frac{T_{in}}{T_{out}}} \tag{45}$$

The share of destroyed exergy for every component:

$$\psi_D = \frac{Destroyed\ Exergy\ in\ the\ component}{Sum\ of\ all\ destroyed\ exergy\ in\ all\ components} \times 100 \tag{46}$$

The exergy efficiency for every component:

$$\varepsilon = 1 - \frac{Destroyed\ Exergy}{Input\ Exergy} \tag{47}$$

The environment temperature, cold space temperature, and temperature difference in evaporator and outlet of gas coolers are 303 K, 233 K, 5 K, and 10 K, respectively.

The Reversible COP of the cycle:

$$External\ Reversible\ COP = \frac{T_{RS}}{T_0 - T_{RS}} \tag{48}$$

The reversible COP is calculated externally to make the results closer to the real condition. Internal reversible COP can be calculated from the EVA and GC outlet temperatures.

The second law efficiency of the cycle:

$$\eta_{II} = \frac{COP}{External\ Reversible\ COP} \tag{49}$$

Table 6: Mass, energy, and exergy balance equations used in the single cycle

Component	**Mass balance**	**Energy balance**	**Exergy balance**
COM1	$\dot{m}_5 = \dot{m}_6 = \dot{m}_{pri}$	$w_{COM1} = x_4 \frac{h(P_6, s_5) - h_5}{\eta_{COM}}$	$e_{D,COM1} = x_4(a_5 - a_6) + w_{COM1}$
COM2	$\dot{m}_{10} = \dot{m}_2 = \dot{m}_{sec}$	$w_{COM2} = (1 - x_4)\frac{h(P_{10}, s_9) - h_9}{\eta_{COM}}$	$e_{D,COM1} = (1 - x_4)(a_9 - a_{10}) + w_{COM2}$
EXP1	$\dot{m}_3 = \dot{m}_4 = \dot{m}_{total}$	$w_{EXP1} = \eta_{EXP}(h_3 - h(P_4, s_3))$	$e_{D,EXP1} = a_3 - a_4 - \dot{w}_{EXP1}$
EXP2	$\dot{m}_7 = \dot{m}_8 = \dot{m}_{sec}$	$w_{EXP2} = (1 - x_4)\eta_{EXP}(h_7 - h(P_8, s_7))$	$e_{D,EXP2} = (1 - x_4)(a_7 - a_8) - \dot{w}_{EXP2}$
Ejector	$\dot{m}_1 + \dot{m}_2 = \dot{m}_3$	$(1 - x_4)h_2 + x_4 h_1 = h_2$	$e_{D,EJE} = x_4 a_1 + (1 - x_4)a_2 + a_3$
FC	$\dot{m}_4 = \dot{m}_5 + \dot{m}_7$	$h_4 = (1 - x_4)h_7 + x_4 h_5$	$e_{D,FC} = a_4 - x_4 a_5 - (1 - x_4)a_7$
GC1	$\dot{m}_6 = \dot{m}_1 = \dot{m}_{pri}$	$q_{GC1} = x_4(h_6 - h_1)$	$e_{D,GC1} = \left(\frac{T_0}{T_{mean,GC1}} - 1\right) q_{GC1} + x_4(a_6 - a_1)$
GC2	$\dot{m}_{10} = \dot{m}_2 = \dot{m}_{sec}$	$q_{GC2} = (1 - x_4)(h_{10} - h_2)$	$e_{D,GC2} = \left(\frac{T_0}{T_{mean,GC2}} - 1\right) q_{GC2} + (1 - x_4)(a_{10} - a_2)$
EVA	$\dot{m}_8 = \dot{m}_9 = \dot{m}_{sec}$	$q_{EVA} = (1 - x_4)(h_9 - h_8)$	$e_{D,EVA} = \left(1 - \frac{T_0}{T_{Eva}}\right) q_{EVA} + (1 - x_4)(a_8 - a_9)$

Table 7: Mass and energy balance equations used in the hybrid cycle

Component	Mass balance	Energy balance
COM1	$\dot{m}_5 = \dot{m}_6 = \dot{m}_{pri}$	$w_{COM1} = x_4 \dfrac{h(P_6, s_5) - h_5}{\eta_{COM}}$
COM2	$\dot{m}_{10} = \dot{m}_{11} = \dot{m}_{sec}$	$w_{COM2} = (1 - x_4)\dfrac{h(P_{11}, s_{10}) - h_{10}}{\eta_{COM}}$
EXP1	$\dot{m}_3 = \dot{m}_4 = \dot{m}_{total}$	$w_{EXP1} = \eta_{EXP}(h_3 - h(P_4, s_3)$
EXP2	$\dot{m}_8 = \dot{m}_9 = \dot{m}_{sec}$	$w_{EXP2} = (1 - x_4)\eta_{EXP}(h_8 - h(P_9, s_8)$
Ejector	$\dot{m}_1 + \dot{m}_2 = \dot{m}_3$	$(1 - x_4)h_2 + x_4 h_1 = h_2$
FC	$\dot{m}_4 = \dot{m}_5 + \dot{m}_8$	$h_4 = (1 - x_4)h_8 + x_4 h_5$
GC1	$\dot{m}_7 = \dot{m}_1 = \dot{m}_{pri}$	$q_{GC1} = x_4(h_7 - h_1)$
GC2	$\dot{m}_{12} = \dot{m}_2 = \dot{m}_{sec}$	$q_{GC2} = (1 - x_4)(h_{12} - h_2)$
EVA	$\dot{m}_9 = \dot{m}_{10} = \dot{m}_{sec}$	$q_{EVA} = (1 - x_4)(h_{10} - h_9)$
HX 1	$\dot{m}_{B1} = \dot{m}_{C1} = y\dot{m}_{ORC}$ $\dot{m}_7 = \dot{m}_6 = \dot{m}_{pri}$	$\lambda Q_{max} = \dot{m}_{B1}(h_{C1} - h_{B1}) = \dot{m}_{pri}(h_6 - h_7)$
HX2	$\dot{m}_{B2} = \dot{m}_{C2} = z\dot{m}_{ORC}$ $\dot{m}_{12} = \dot{m}_{11} = \dot{m}_{sec}$	$\lambda Q_{max} = \dot{m}_{B2}(h_{C2} - h_{B2}) = \dot{m}_{sec}(h_{11} - h_{12})$
PU1	$\dot{m}_{A1} = \dot{m}_{B1} = y\dot{m}_{ORC}$	$w_{PU1} = \dfrac{h(P_{B1}, s_A) - h_A}{\eta_{PU}}$
PU2	$\dot{m}_{A2} = \dot{m}_{B2} = z\dot{m}_{ORC}$	$w_{PU1} = \dfrac{h(P_{B2}, s_A) - h_A}{\eta_{PU}}$
TUR1	$\dot{m}_{C1} = \dot{m}_{D1} = y\dot{m}_{ORC}$	$w_{TUR1} = \eta_{TUR}(h_{C1} - h(P_D, s_{C1})$
TUR2	$\dot{m}_{C2} = \dot{m}_{D2} = z\dot{m}_{ORC}$	$w_{TUR2} = \eta_{TUR}(h_{C2} - h(P_D, s_{C2})$
CON	$\dot{m}_A = \dot{m}_D = \dot{m}_{ORC}$	$q_{CON} = (h_D - h_A)$

3. Results and discussions

3.1. 1st law analysis

Table 8 shows the thermodynamic properties of every point in the cycle, plus COPs and mass flow rate information. In order to avoid the negative values, the IIR standard was selected as the reference point for enthalpy and entropy. This is the optimal operation point of this cycle for the fixed source and sinks temperatures (Namely -45°C & 40°C, respectively). The velocity of flow out of the ejector was assumed to be negligible. Because of this, the Mach number for those points is shown by 0^+. Mass flow of the cycle in the evaporator, entrainment ratio, and different COPs of the cycle were shown in Table 9.

The calculated COP shows that this cycle has a noticeable performance in this evaporation temperature. The assumptions are realistic, and the results are reasonable compared to other cycles' performance.

For the parametric analysis, there are other assumptions and limitations. There are three inputs for this purpose. P_1 is the maximum pressure of the cycle, the discharge pressure of the first compressor, the first gas cooler, and the primary flow of the ejector. P_2 is equal to the discharge pressure of the second compressor, the second gas cooler, and the secondary flow of the ejector. P_4 is the expansion pressure after the first expander and the pressure of the flash chamber. All of these pressures impact purge pressure and, the purge flow can be 2-phase, superheated vapor, or supercritical fluid depending on purge pressure.

Table 8: The thermodynamic properties of all points in the cycle

State#	T (K)	P (MPa)	h (kJ/kg)	s (kJ/kg.K)	x (kg/kg)	Mach Number	a (kJ/kg)
1	313	9.711	316.8	1.37	Supercritical	0^+	225.2
a	270.4	3.24	301.4	1.376	0.452	0.96	223.3
2	313	3.411	486.8	2.04	Superheat	0^+	192
b	309.4	3.24	484.5	2.04	Superheat	0.27	191.7
c	270.4	3.24	355.5	1.576	0.678	0.72	211.8
d	270.4	3.24	355.5	1.576	0.678	0.72	211.8
3	283.1	4.502	365.9	1.583	0.711	0^+	209.6
4	283.1	4.502	365.9	1.584	0.711	0^+	209.6
5	283.1	4.502	422.9	1.785	1	0^+	205.6
6	344	9.711	456.4	1.801	Supercritical	0^+	234.3
7	283.1	4.502	225.7	1.088	0	0^+	219.4
8	228	0.827	214.9	1.114	1	0^+	200.8
9	228	0.827	434.1	2.076	Superheat	0^+	128.7
10	342.2	3.411	519.3	2.14	Superheat	0^+	194.4

Table 9: The performance and other characteristics of the cycle

Evaporator Mass Flow Rate per Ton of Refrigeration	16 gr/sec
Entrainment Ratio in Ejector	0.4056
COP of cycle	1.399
External Ideal COP	2.039
Internal Ideal COP	2.337
Ideal COP	3.032
External Reversible COP	3.329
Internal Reversible COP	2.689

In this cycle, the flash chamber is used as a separator of flow between the two loops. If, during the parametric analysis, the inlet flow to the flash chamber becomes a single phase, the calculations are terminated, and the control valves by-pass the EXP1.

Another limitation is related to the discharge pressure of the ejector. In the parametric analysis, the P_4 cannot be higher than P_3. If this happens, it means that the first expander works as a compressor, which has wet compression.

3.2 Parametric analysis and optimization

Fig. 28 to Fig. 34 shows the COP, purge pressure, and entrainment ratio of the cycle according to 3 different pressure inputs. T_1 and T_2 are 313 and 228 K, respectively. The same color was chosen for the same pressure lines. For the sake of simplicity and size, the legend entries for Fig. 28 to Fig. 34 are shown in Fig. 7. The similarity of color for each line identifies which data series belongs to the right COP, pressure, or entrainment ratio. The COP, purge pressure, and entrainment ratio are shown by marked, solid, and dashed lines, respectively. The horizontal black lines in Figs. 29 to 34 are the supercritical pressure of CO_2 and illustrate the phase condition of the stream at point 3.

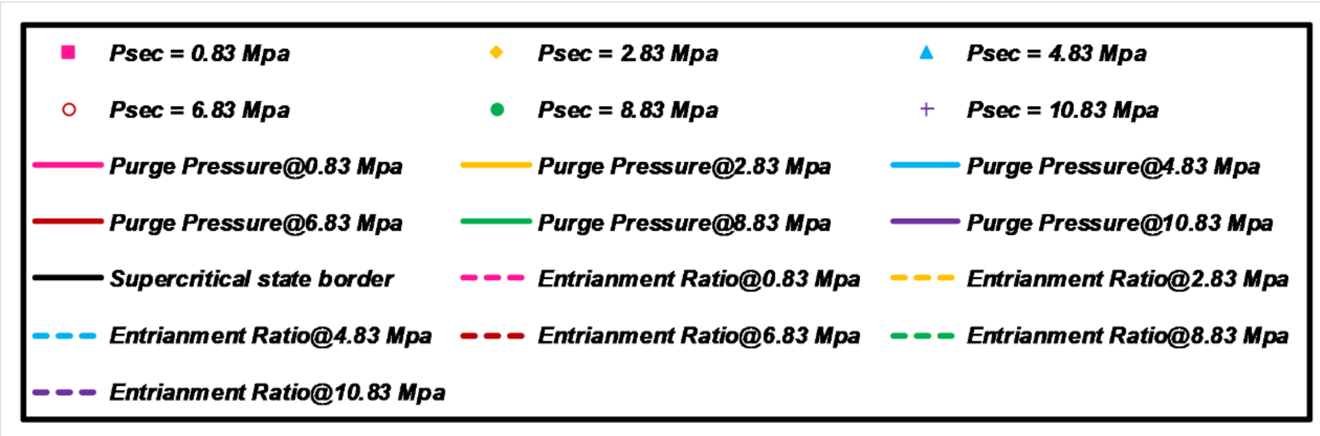

Fig. 27: The complete legend guide for **Fig. 7** to **Fig. 13**.

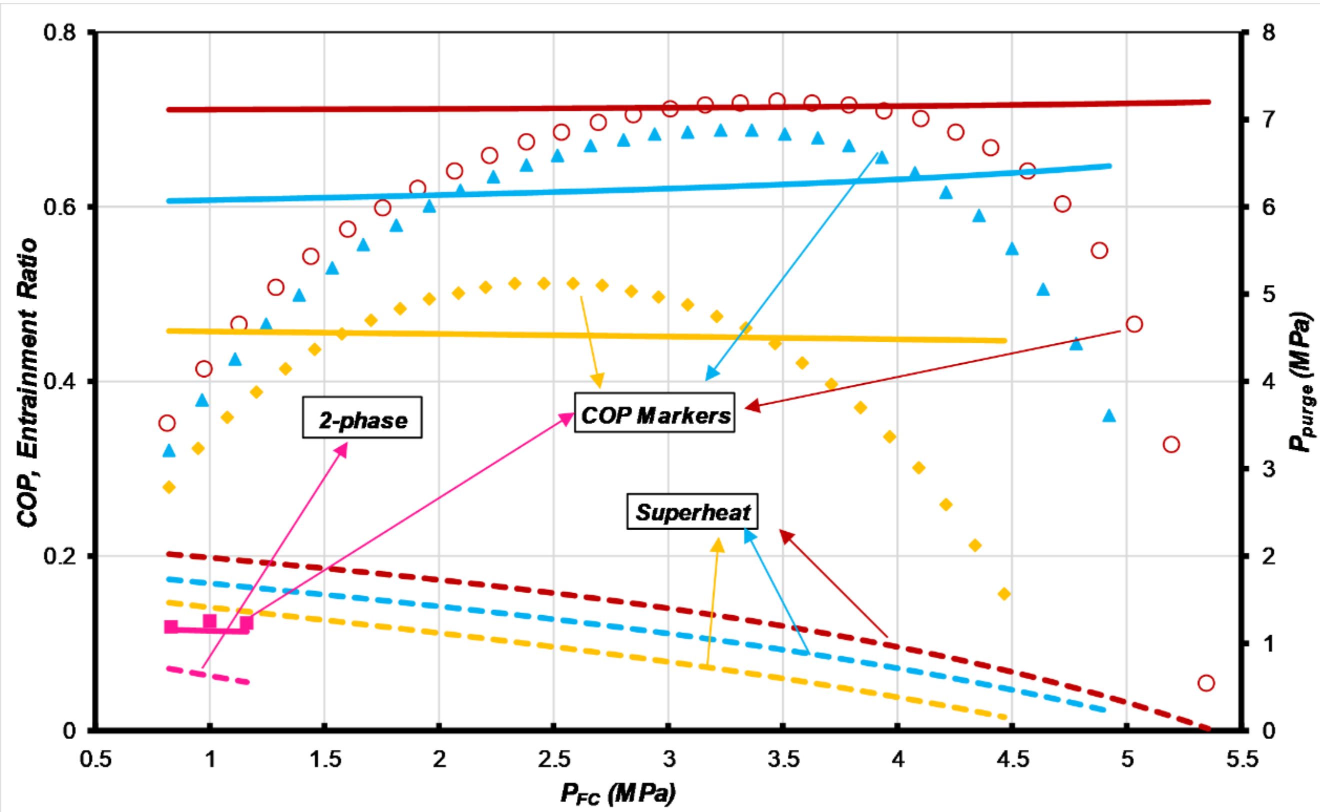

Fig. 28: Parametric analysis for $P_{pri} = 7.5$ MPa

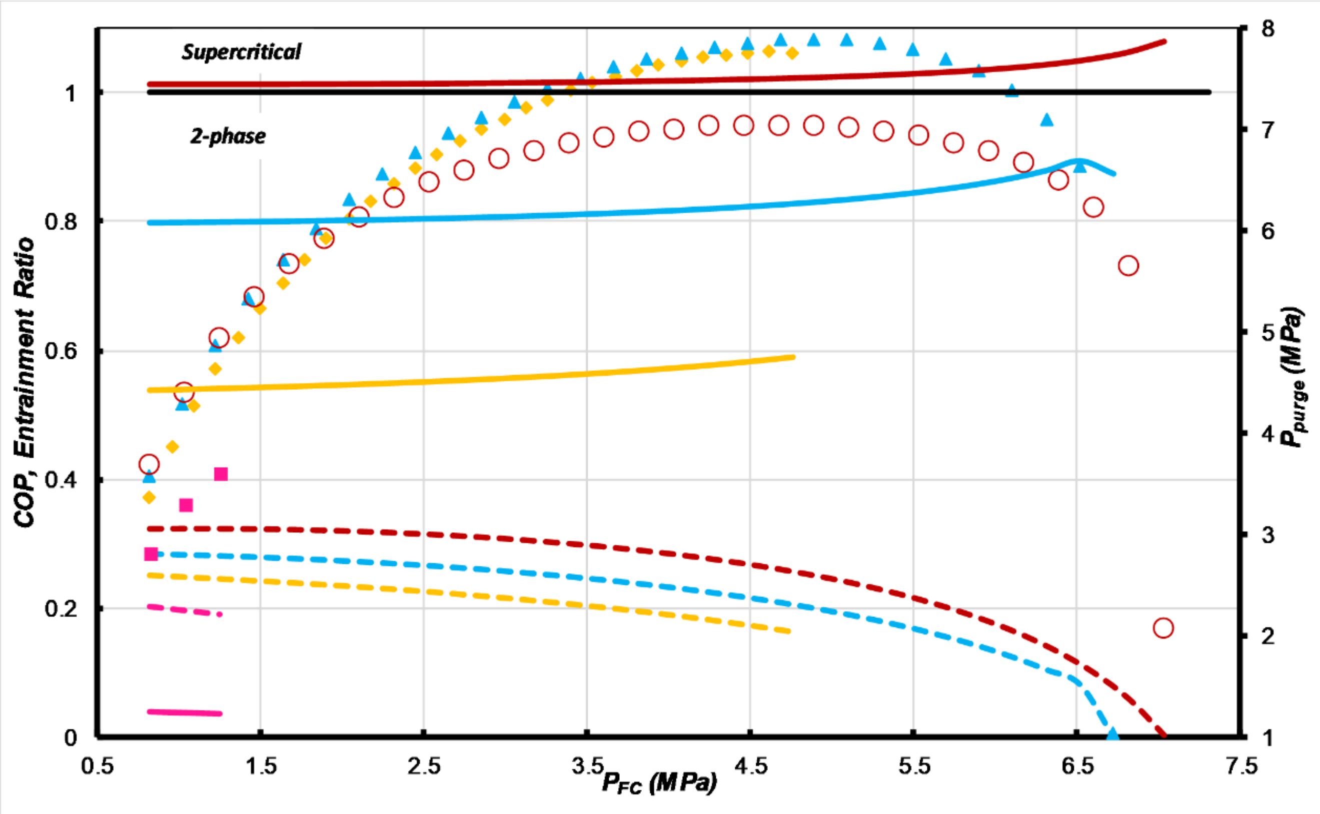

Fig. 29: Parametric analysis for P_{pri} = 8.5 MPa

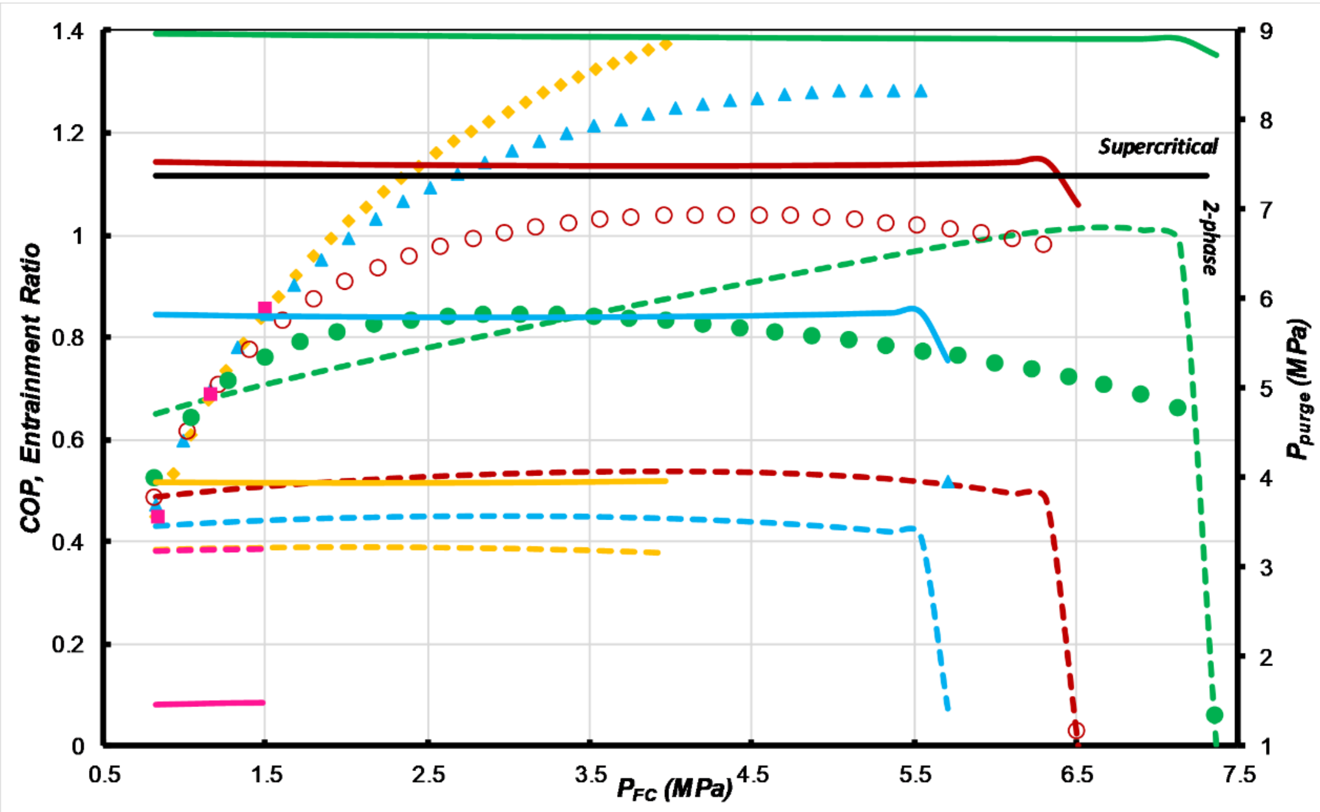

Fig. 30: Parametric analysis for P_{pri} = 9.5 MPa

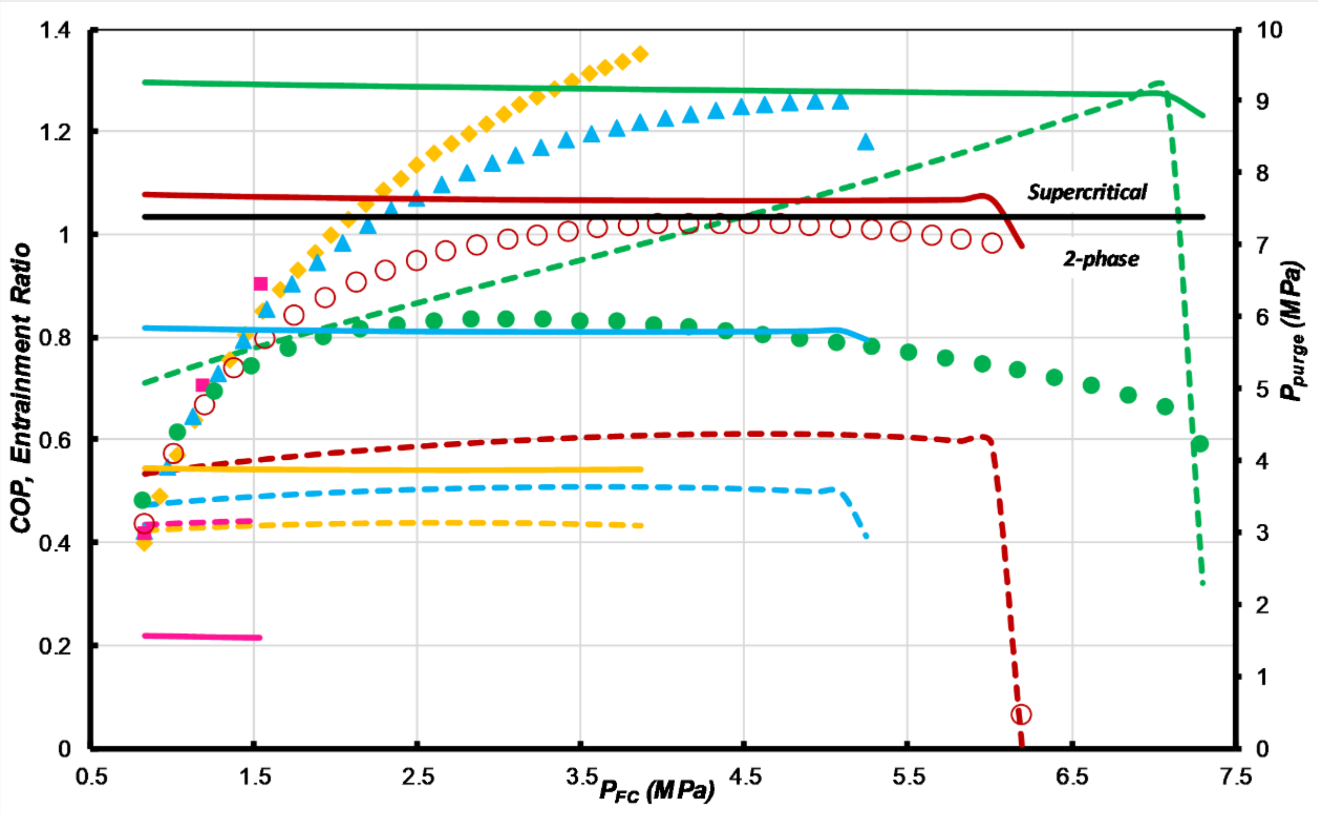

Fig. 31: Parametric analysis for P_{pri} = 10.5 MPa

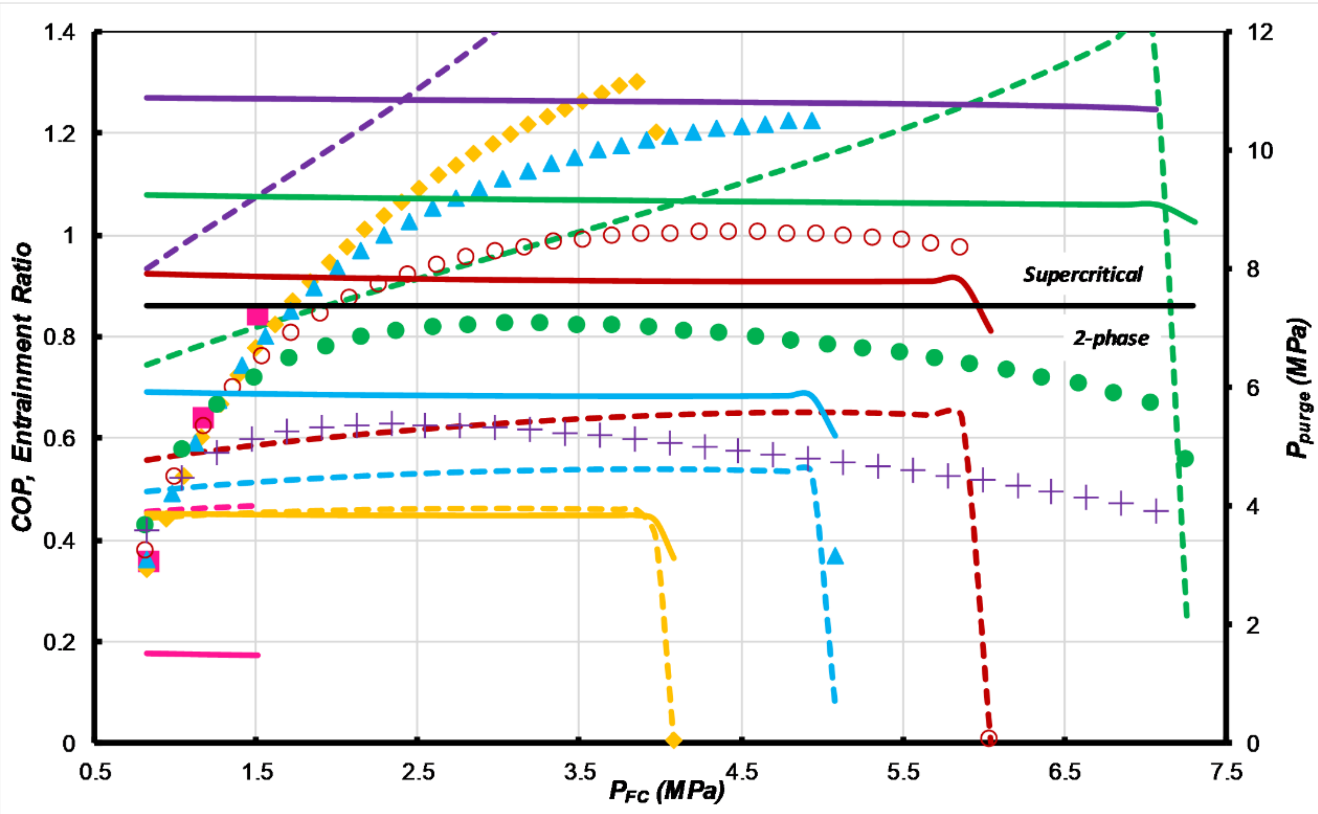

Fig. 32: Parametric analysis for P_{pri} = 11.5 MPa

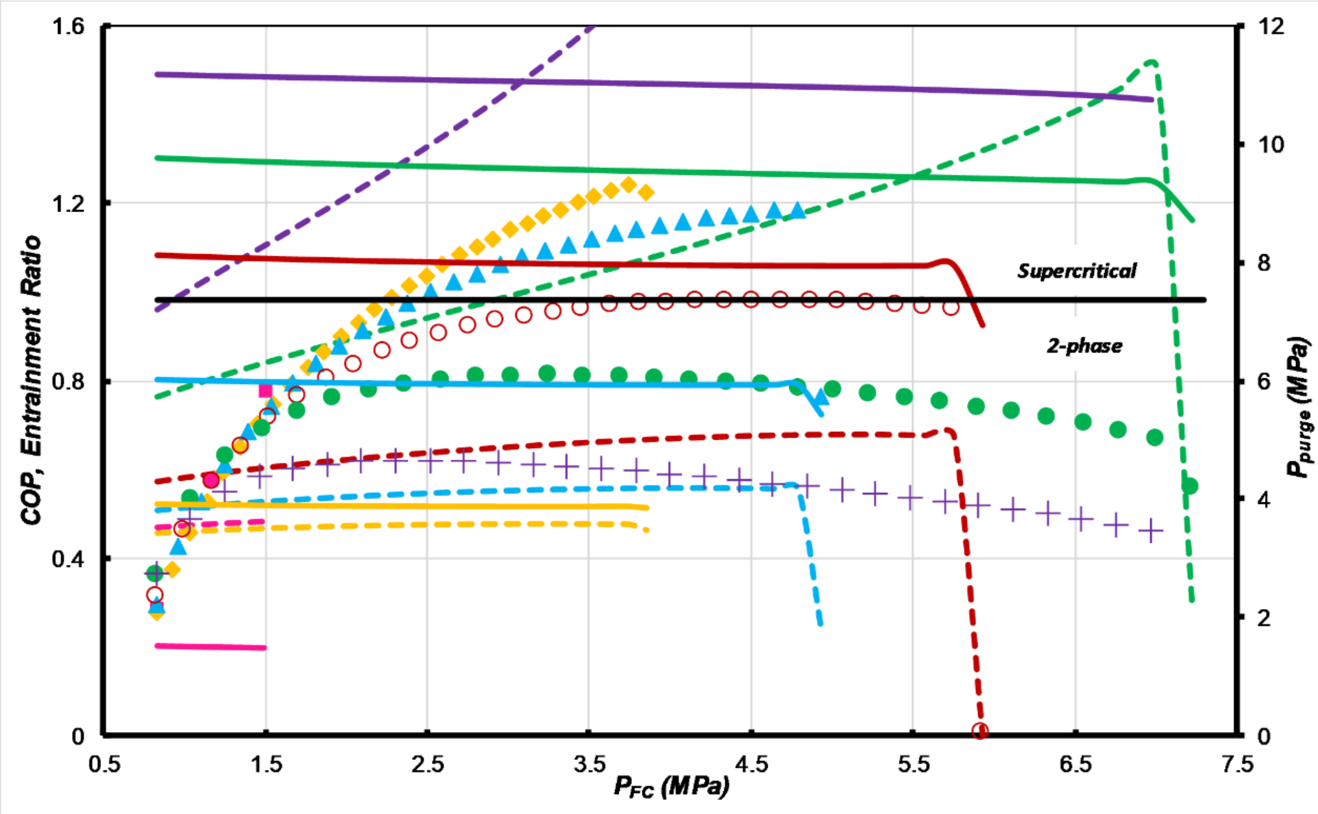

Fig. 33: Parametric analysis for P_{pri} = 12.5 MPa

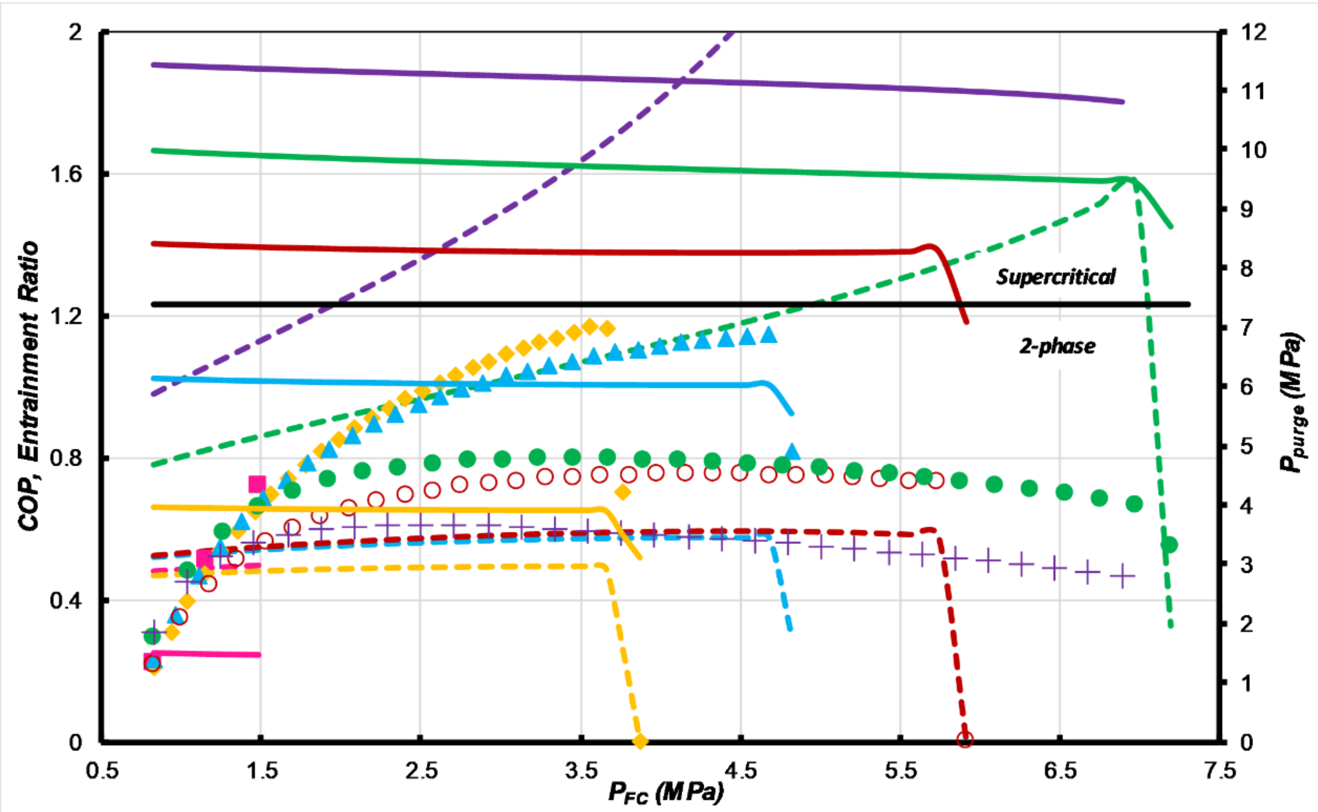

Fig. 34: Parametric analysis for P_{pri} = 13.5 MPa

The entrainment ratio of the ejector is a crucial parameter in COP, which directly depends on the quality of vapor after the 1st expander. Because of this, the graphs usually illustrate a change of behavior after passing the critical point.

In Fig. 28 to Fig. 34, there is the shortest curve. It shows a situation without the second compressor and condenser. The endpoint of this curve is the situation that there is no first expander in the system. This point shows a conventional ejector cycle with an expander. COP, at this point, is the same as the COP of previous studies in the same entrainment ratio, which validates the calculation of this study.

In all mentioned charts, the COP increases with the increase of the secondary pressure to an optimal point. Installing the compressor after the evaporator in the cycle significantly increased the COP. It seems that without the 2nd compressor, a vast range of data was ignored during previous simulations for conventional ejector cycles.

The presence of GC2 is also essential. If the discharge temperature of COM2 is higher than 313K, the efficiency decreases. At higher temperatures, it even leads to a shift from 2-phase into the single-phase in the outlet of the ejector. This matter was considered in the program. GC2 only works when the discharge temperature of COM2 exceeds 313K.

The sensitivity of the cycle's performance to P_{FC} is high. The cycle has the lowest COP at the lowest possible P_{FC}, which is equal to the evaporation pressure. The COP rises with the accretion in P_{FC} and reaches its peak. After that, different situations happen. Figs. 28 to 34 illustrate these situations. If the purge pressure is low enough, the peak occurred at the exact thermodynamic point after the ejector. If the outlet state of the ejector is supercritical or in superheat condition, the P_{FC} can increase to its high limit, which is the saturation line, and till that point, the COP decreases. If the purge pressure is higher than the first situation but still in subcritical condition, P_{FC} can advance by a dozen kPa. Then COP faces a sharp drop, which is the result of the sudden approach of entrainment ratio to zero. Purge pressure usually remains constant.

The entrainment ratio leads to zero when the x_4 approaches 1, and when the x_4 approaches zero, the entrainment ratio jumps up to infinity. The results show that in sub-critical purge pressure, R mostly levels off before drops to zero. In supercritical pressure, R initially rises and then suddenly free-falls to zero. In higher pressures (more than 11), R approaches infinity or experienced an acute rise and fall. It happens because the discharge of EXP1 is near the summit of the saturation dome, and the distance between saturated liquid and saturated vapor becomes smaller and smaller.

At the initial phase of this study, EXP1 seemed to be necessary for controlling the entrainment ratio in the sub-critical purge stream and performing the critical role of throttling for supercritical purge flow. In the final code, which contains the optimization algorithm, the simulation results did not run smoothly, and the results are discreet. The algorithm was slow and mostly encountered divergence or illogical results. It was decided to run the code in two scenarios, with different initial guesses for each one. In the first scenario, the EXP1 is a part of the cycle, and in the second scenario, the EXP1 is isolated by two valves. The result of the two scenarios was compared at the last stage. In all of the temperature ranges and for every parametric analysis, it is observed that the cycle has a higher COP and lower exergy destruction rate in the second scenario than the first scenario. Figures the same as figures 28 to 34 were produced for other temperatures and component efficiencies, and the same trend was observed in all of them. The research team reached the conclusion that in the optimum operation condition, the expansion device right after the ejector is unnecessary. This model proves that the ejector performs its duty completely without relying on other means for expansion. However, it does not mean that the EXP1 is totally useless. It may be useful for transient conditions. A transient numerical model is needed to prove this.

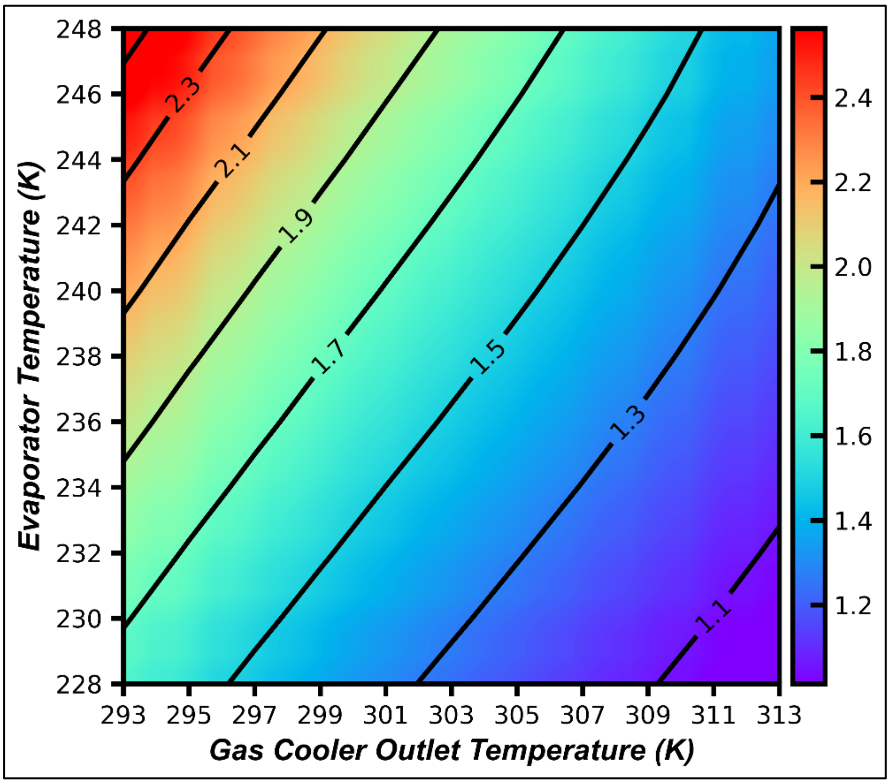

Fig. 35: Maximum COP versus evaporator temperature under different gas cooler outlet temperatures

Fig. 35 illustrates the maximum COP-temperature contour. It is expected that performance has a direct relation with the temperature lift of the cycle. The cycle has a noticeable performance even in the highest temperature differences. Fig. 36 shows the optimum primary pressure-temperature contour. Primary pressure depends on GC outlet temperature and only mildly change by evaporator temperature. At 308 K, the slope of isolines changed.

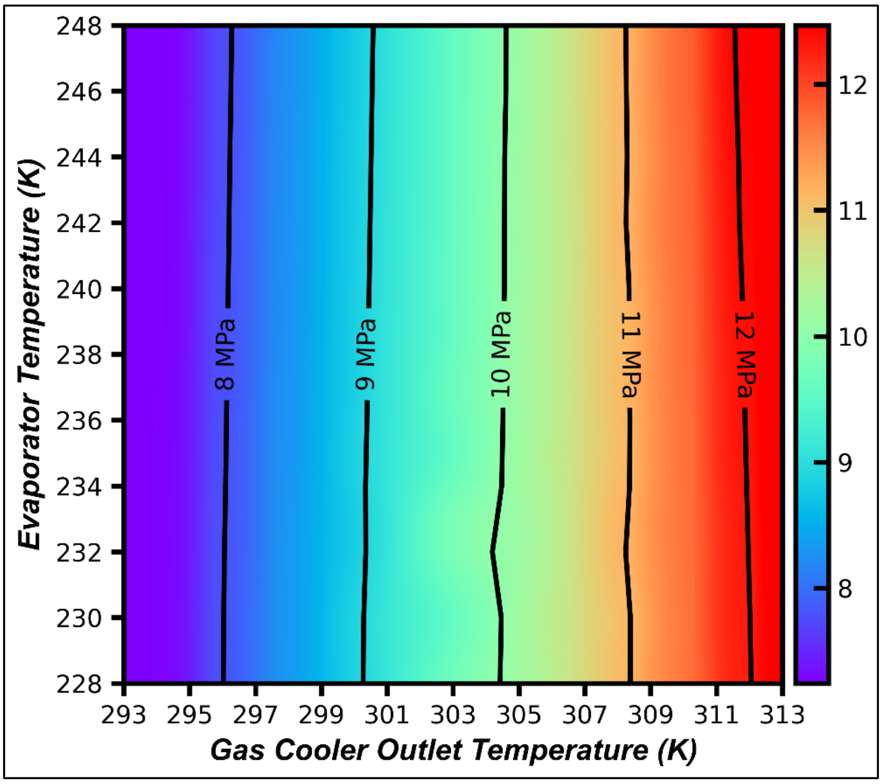

Fig. 36: Optimum primary pressure versus evaporator temperature under different gas cooler outlet temperatures

Fig. 37 presents the optimum secondary pressure-temperature contour. The secondary pressure is affected by both temperatures. However, it mostly depends on the evaporation temperature. Fig. 38 shows the purge pressure-temperature contour at optimum condition. Purge pressure acts as the resultant of primary and secondary pressures.

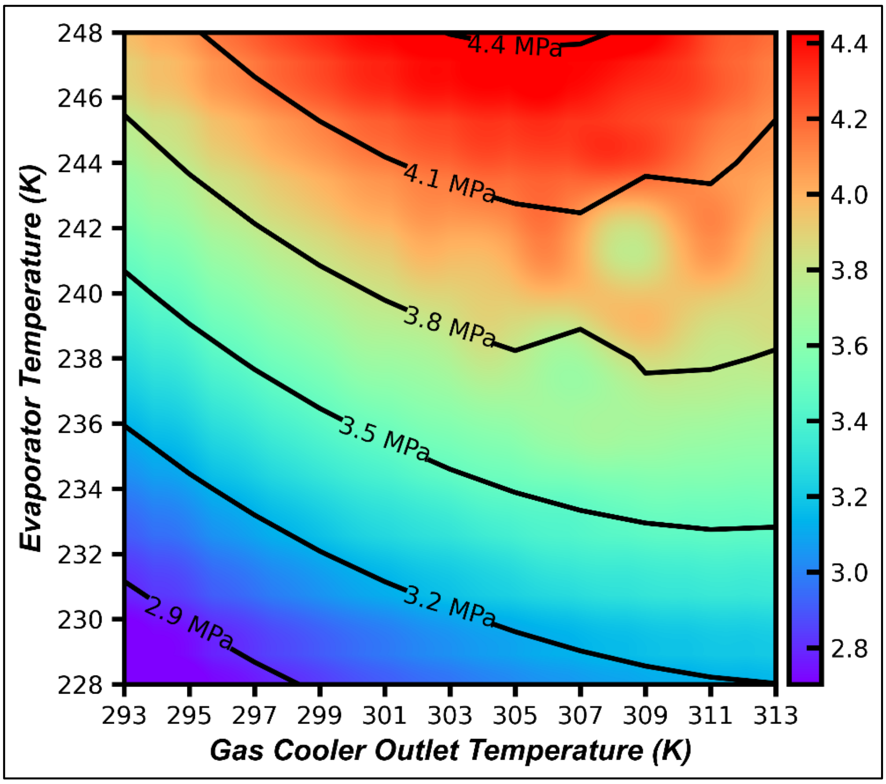

Fig. 37: Optimum secondary pressure versus evaporator temperature under different gas cooler outlet temperatures

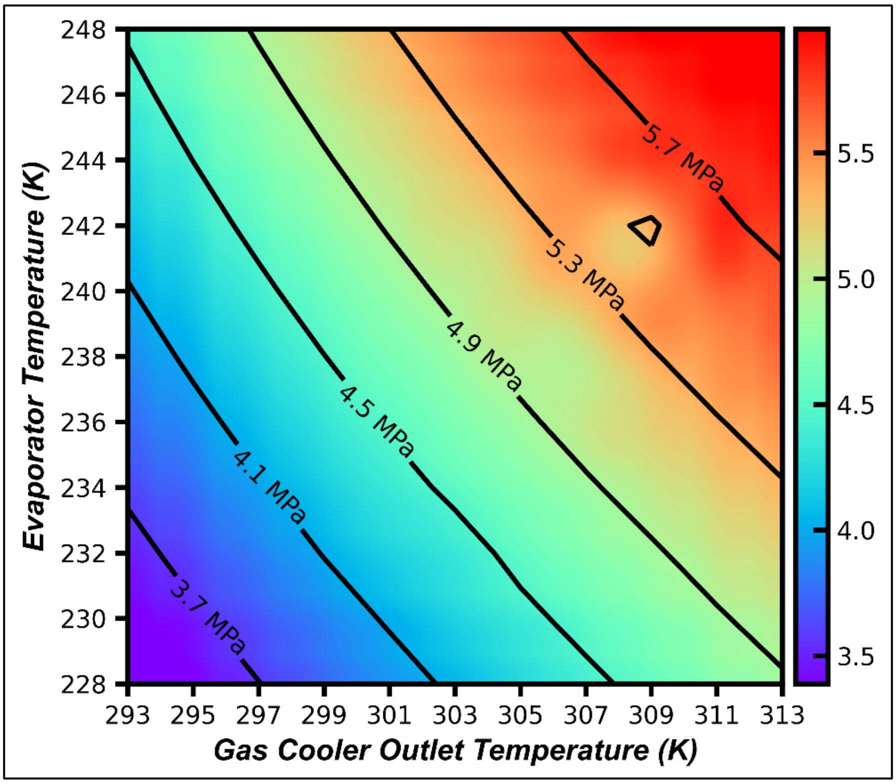

Fig. 38: Purge pressure versus evaporator temperature under different gas cooler outlet temperatures in optimum performance

Fig. 39 reveals the entrainment ratio-temperature contour. Comparing it to Fig. 36, it can be deduced that the entrainment ratio and primary pressure have the reverse trend towards temperature. The COP and R have the same profile. The primary pressure locates the whereabouts of R, and the secondary pressure to identify the exact value for R. R is an essential factor in the cycle. It changes not only the COP but also the final velocity of flow in the constant area chamber and the total mass flow rate of the cycle. In this study, R and purge pressure are the products of the simulation. The entrainment ratio is less than 0.52. Due to this, the high-pressure loop must circulate a large amount of energy.

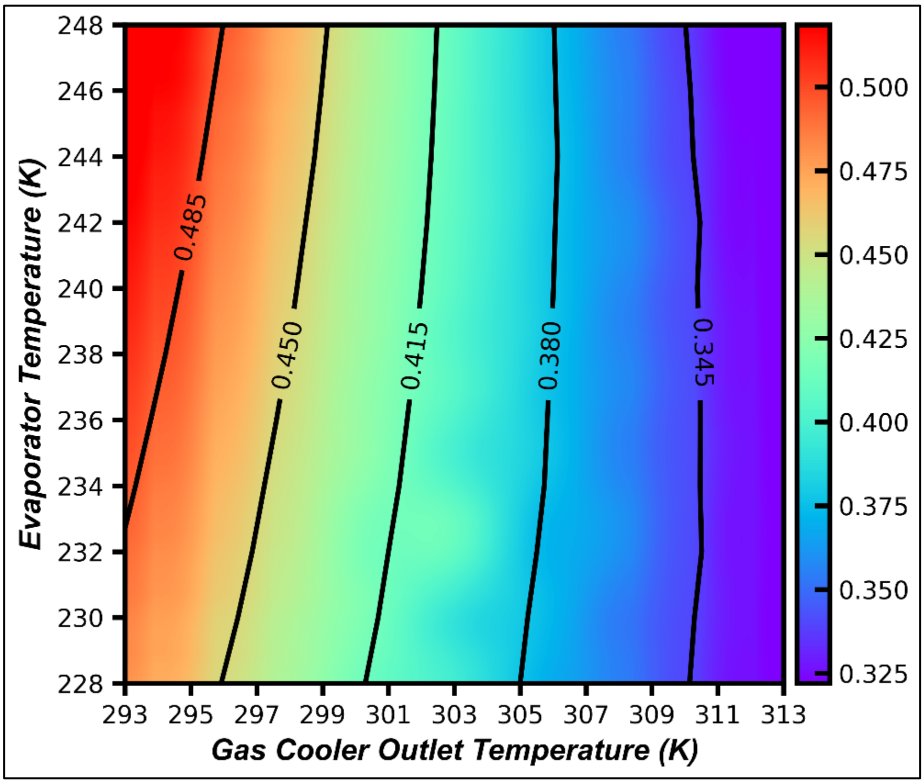

Fig. 39: Entrainment ratio versus evaporator temperature under different gas cooler outlet temperatures in optimum performance

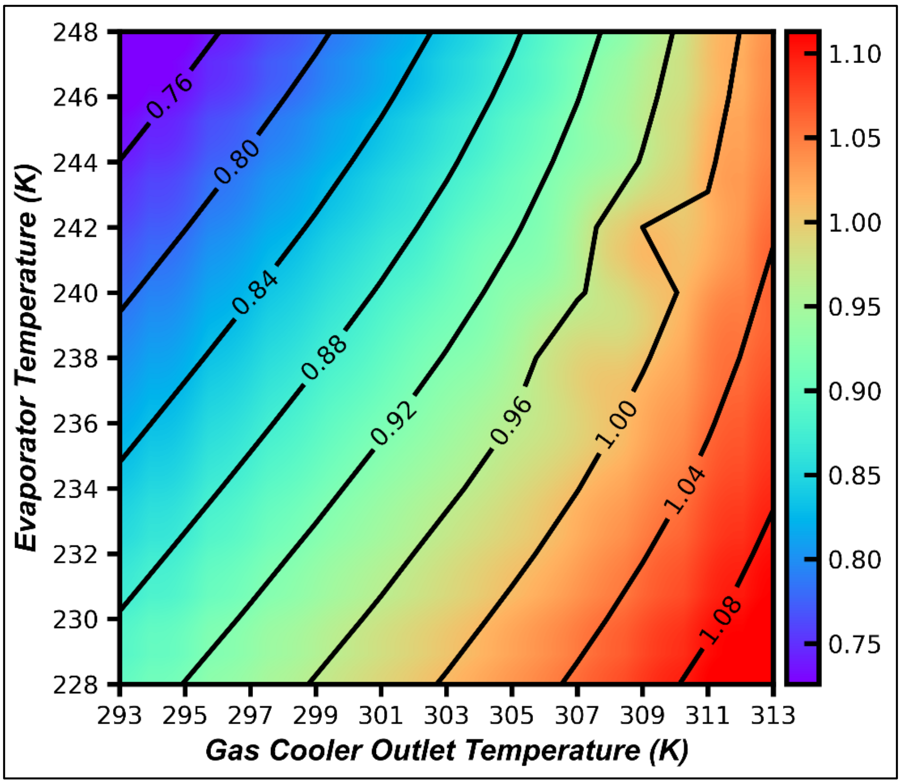

Fig. 40: Mach number after primary nozzle versus evaporator temperature under different gas cooler outlet temperatures in optimum performance

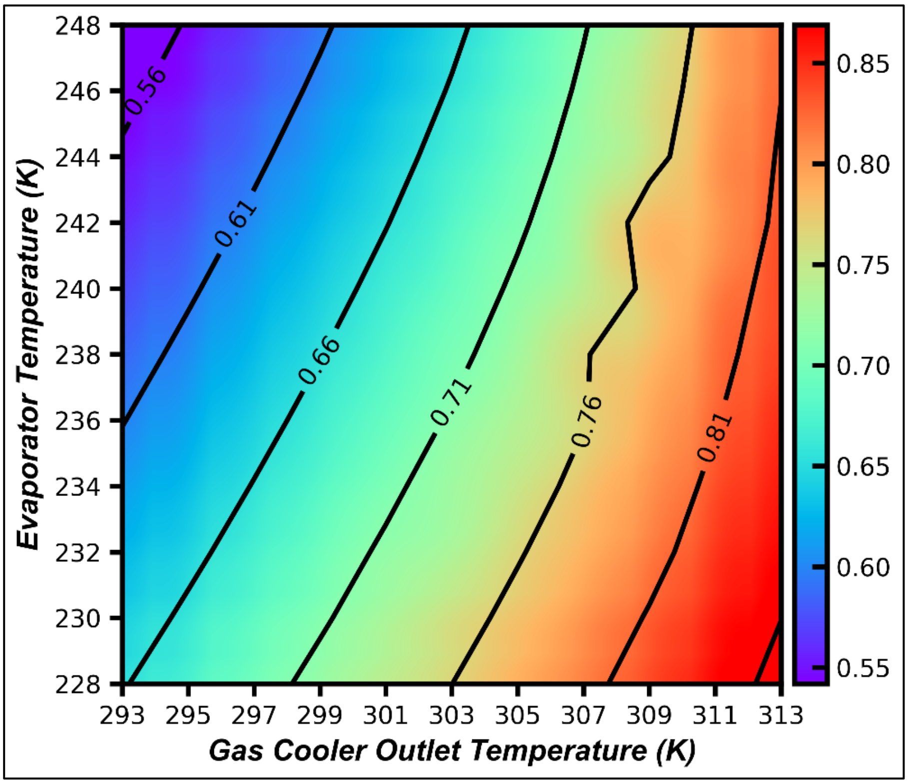

Fig. 41: Mach number after mixing chamber versus evaporator temperature under different gas cooler outlet temperatures in optimum performance

Fig. 40 and 41 illustrate the Mach number-temperature contours. In this cycle, there is no normal shock in the ejector at the optimum condition. Because of this, future simulations and experimental data are appaired to have marginally identical results. In the conventional ejector cycles, the normal shock wave in the ejector is the main reason that the thermodynamic results are hard to achieve in experimental trials. However, the velocity is still high, and oblique, and pseudo-shocks are imminent to happen. The turbulence will be high in the ejector, and there will be a chance that choking occurs. However, comparing the conventional cycle, this cycle is not in the critical zone. Mach number at point c has a fast slope against the temperature. The decrease in R in higher pressures accelerates this increase.

Fig. 42 shows the mass flow rate-temperature contour. By an increase in the temperature difference of this cycle, the mass flow rate increase to satisfy the same cooling load. If the mass flow rate increase, the size, and weight of the system also rise.

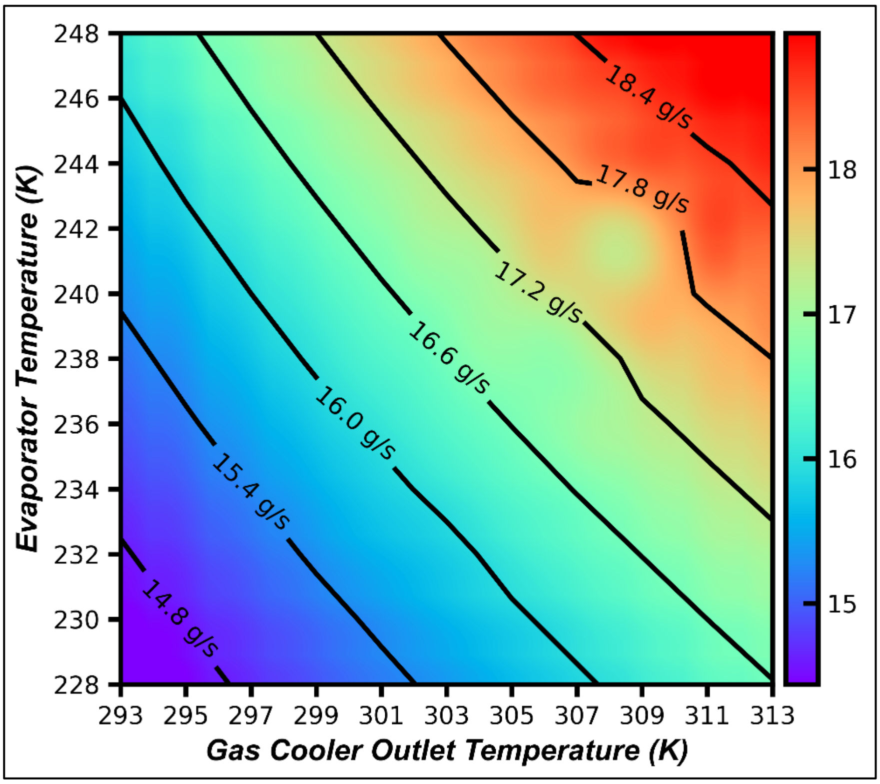

Fig. 42: Mass flow rate in evaporator per one refrigeration ton versus evaporator temperature under different gas cooler outlet temperatures in optimum performance

Figs. 43 and Fig. 44 present the discharge temperature of COM1 and COM2, respectively. The discharge temperature of COM1 is usually higher than its counterpart in COM2. However, when the temperature lift of the cycle reduces, temperatures approach each other and even in the top-left corner T_{10} exceeds T_6.

Figs. 45 and 46 are the isentropic efficiencies of the compressors, which follow the same trend as Figs. 43 and 44.

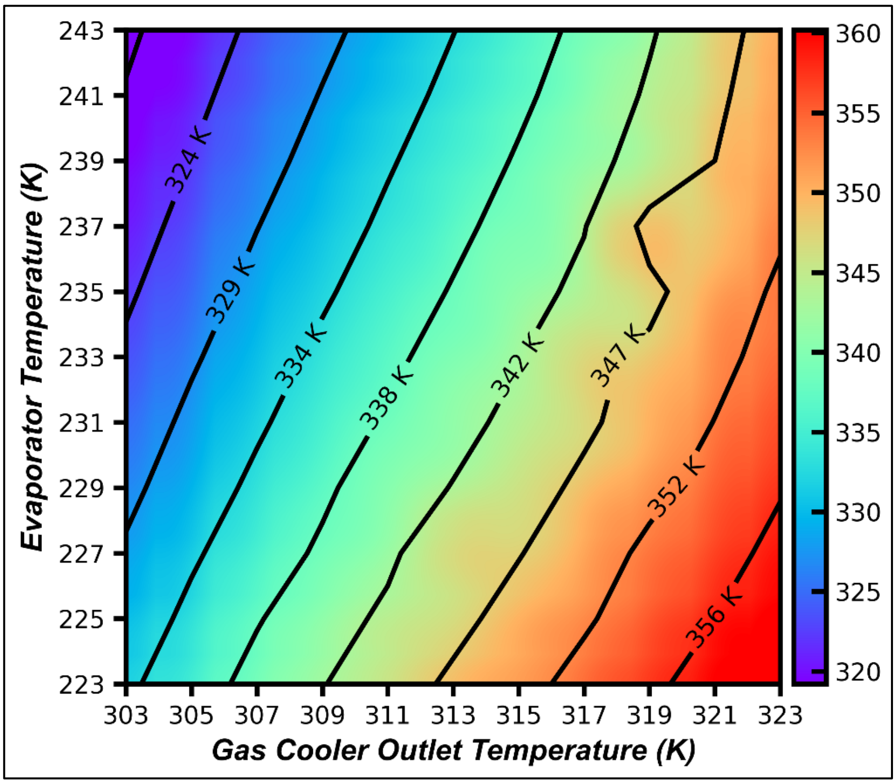

Fig. 43: Discharge temperature of COM1 versus evaporator temperature under different gas cooler outlet temperatures in optimum performance

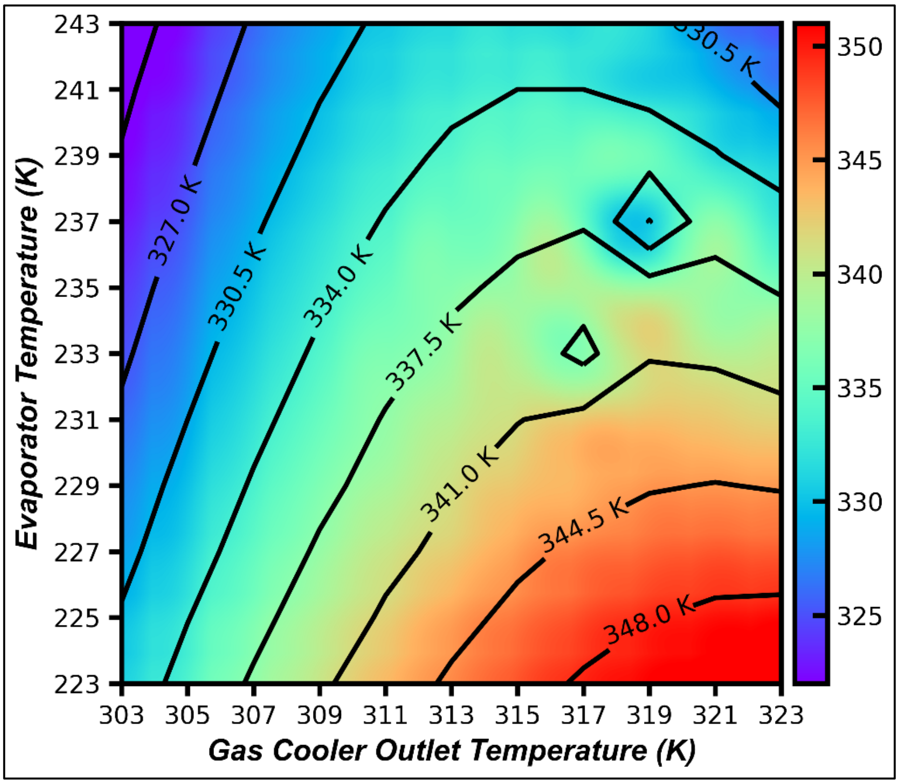

Fig. 44: Discharge temperature of COM2 versus evaporator temperature under different gas cooler outlet temperatures in optimum performance

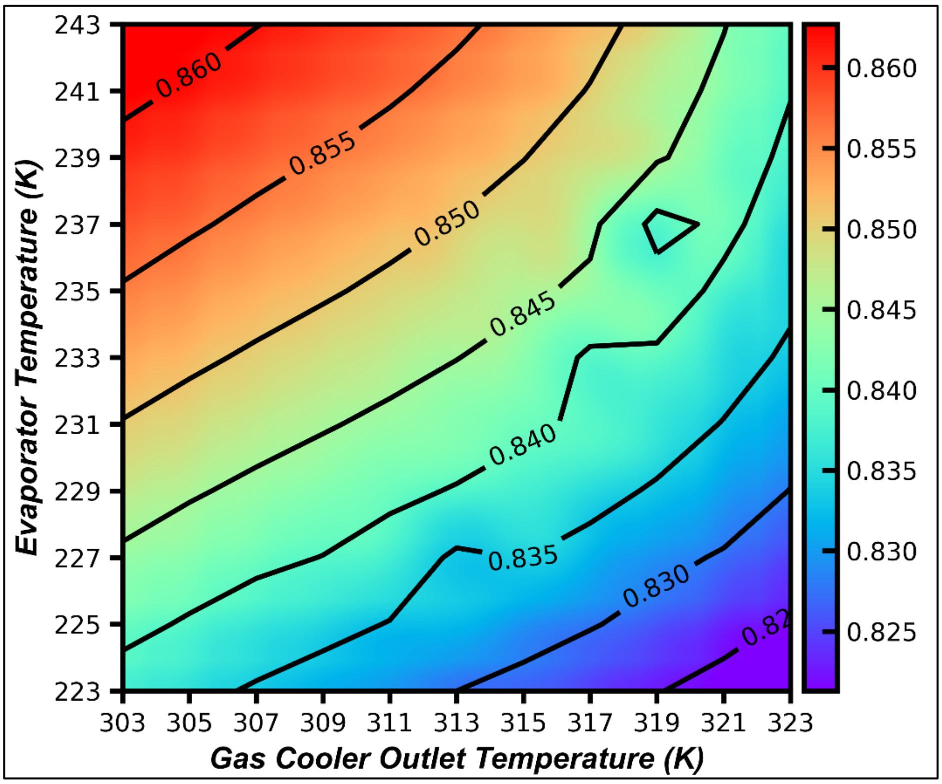

Fig. 45: Isentropic efficiency of COM1 versus evaporator temperature under different gas cooler outlet temperatures in optimum performance

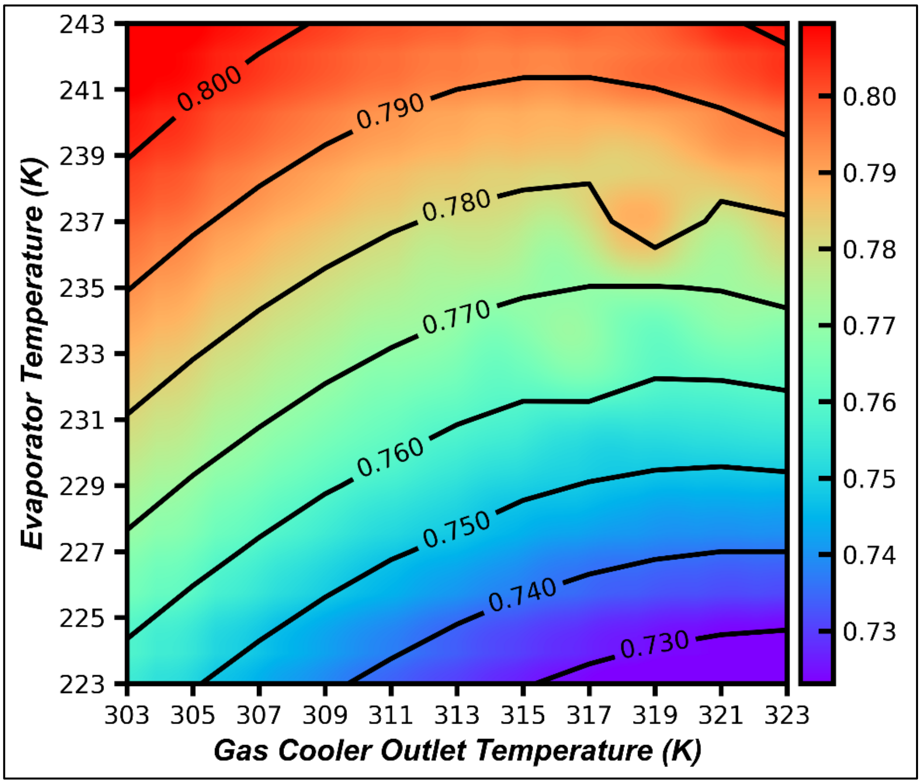

Fig. 46: Isentropic efficiency of COM2 versus evaporator temperature under different gas cooler outlet temperatures in optimum performance

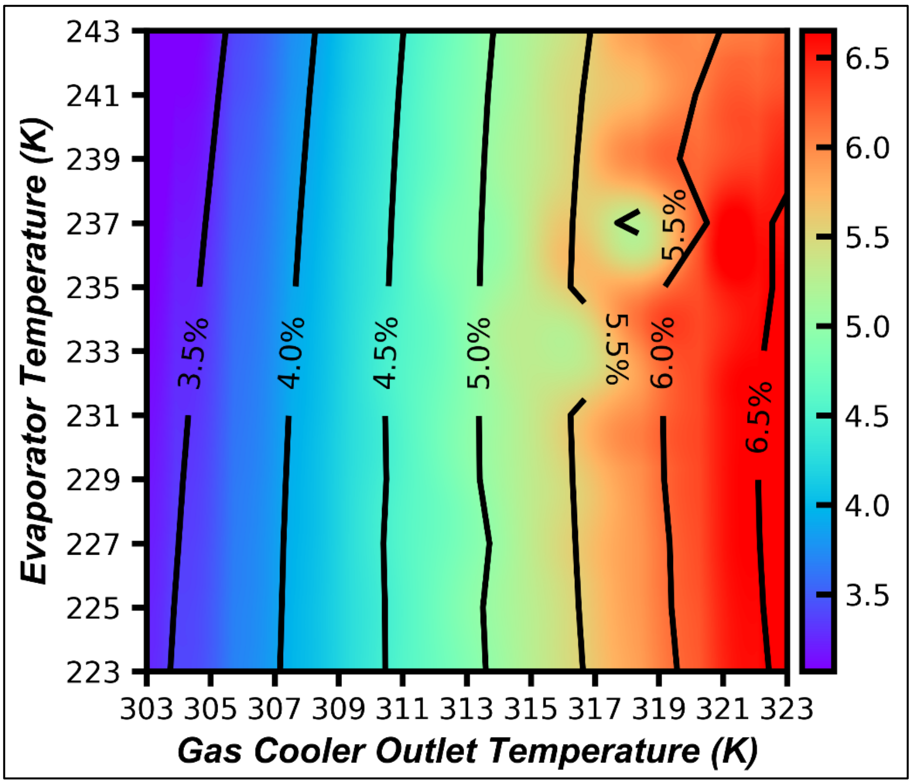

Fig. 47: Cooling capacity boost (CCB) versus evaporator temperature under different gas cooler outlet temperatures in optimum performance

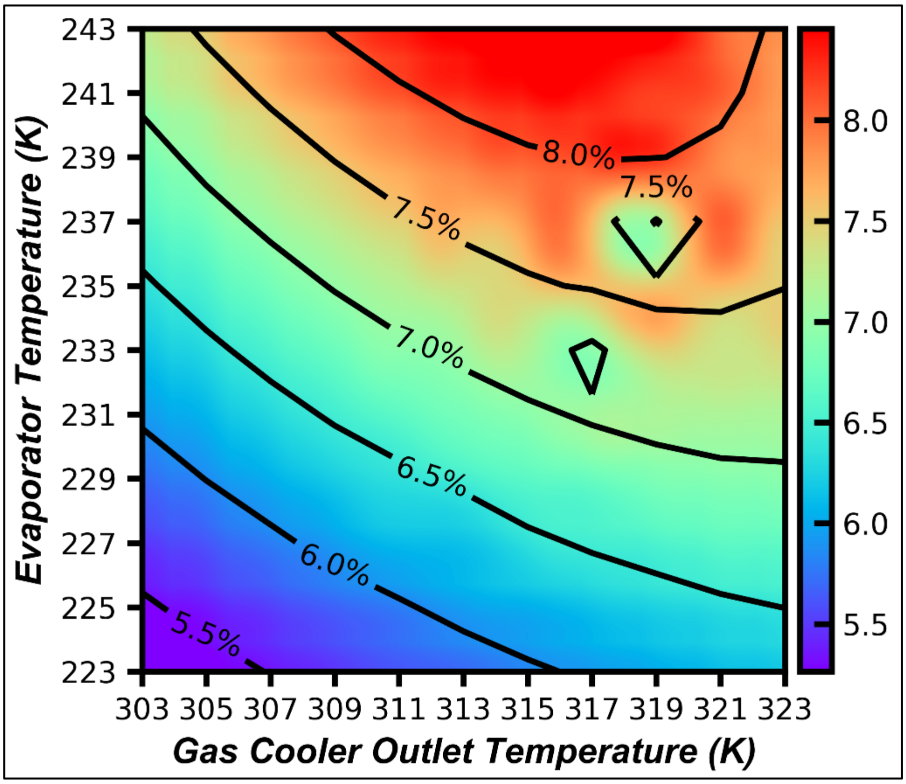

Fig. 48: Recovered work (RW) versus evaporator temperature under different gas cooler outlet temperatures in optimum performance

Fig. 47 is the CCB-temperature contour. The evaporation temperature does not have a strong impact on CCB. CCB seems to follow the primary pressure and entrainment ratio of the ejector. By increasing the GC outlet temperature, CCB is also increased. At higher temperatures, CCB reaches 6.5%.

Fig. 48 presents the RW-temperature contour. The secondary pressure is the main influencer of RW. At higher temperatures, RW reaches 8.25%. CCD and RW contours prove that using a turboexpander is feasible, especially at higher GC temperatures.

In Fig. 49, the results from the comparison of the performance of different compression models were graphed. If a higher quality compression model is used, the cycle intends to increase its pressures and the entrainment ratio, and the reverse of this statement is also true. Contrarily, in Model 6, the secondary pressure rises significantly when the overall performance is reduced. For all the models, the change in the primary pressure is not noticeable. The primary pressure is also independent of the efficiency of the compressor.

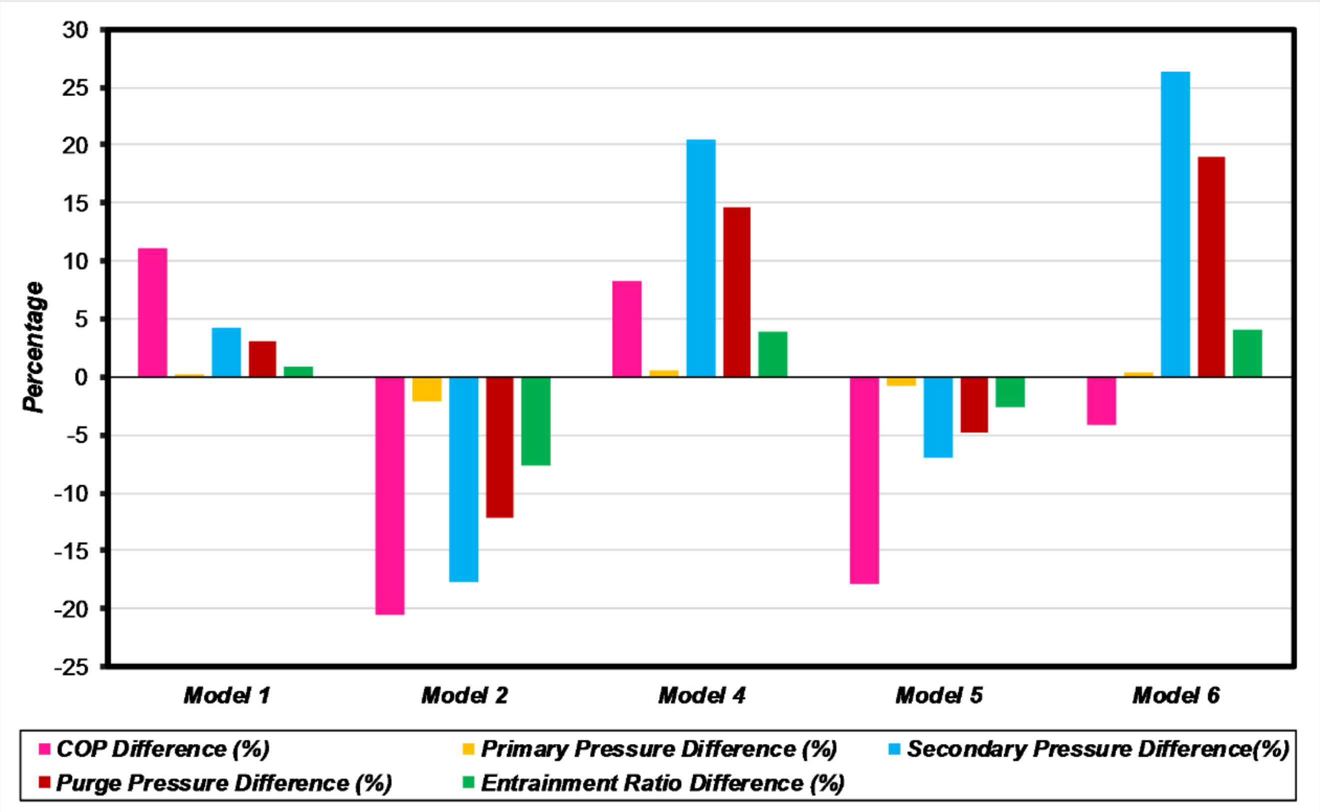

Fig. 49: Comparison of the cycle with different models of compressors. (Notice that Model 3 is absent because it is used in the base assumption!)

Fig. 50 reveals the relation of performance and the optimum pressures with the efficiency of the ejector. The primary and secondary pressures are increased by a reduction in performance. The reverse is also true. The cycle must compensate for the lower quality of the ejector by increasing the pressures and the entrainment ratio. This figure also shows that the primary pressure mildly and the secondary pressure heavily related to the performance of the ejector the same as the R.

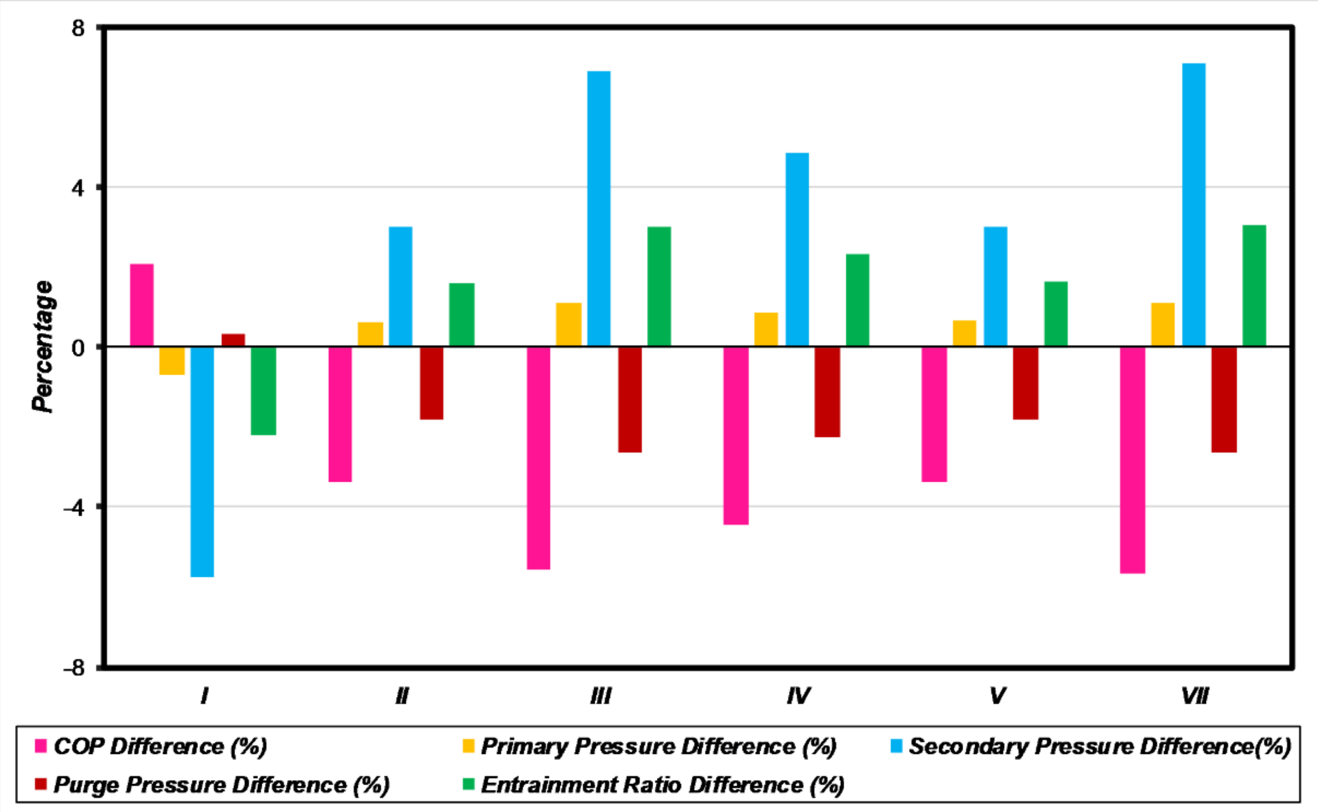

Fig. 50: Comparison of the cycle with different models of ejectors. (Notice that Model VI is absent because it is used in the base assumption!)

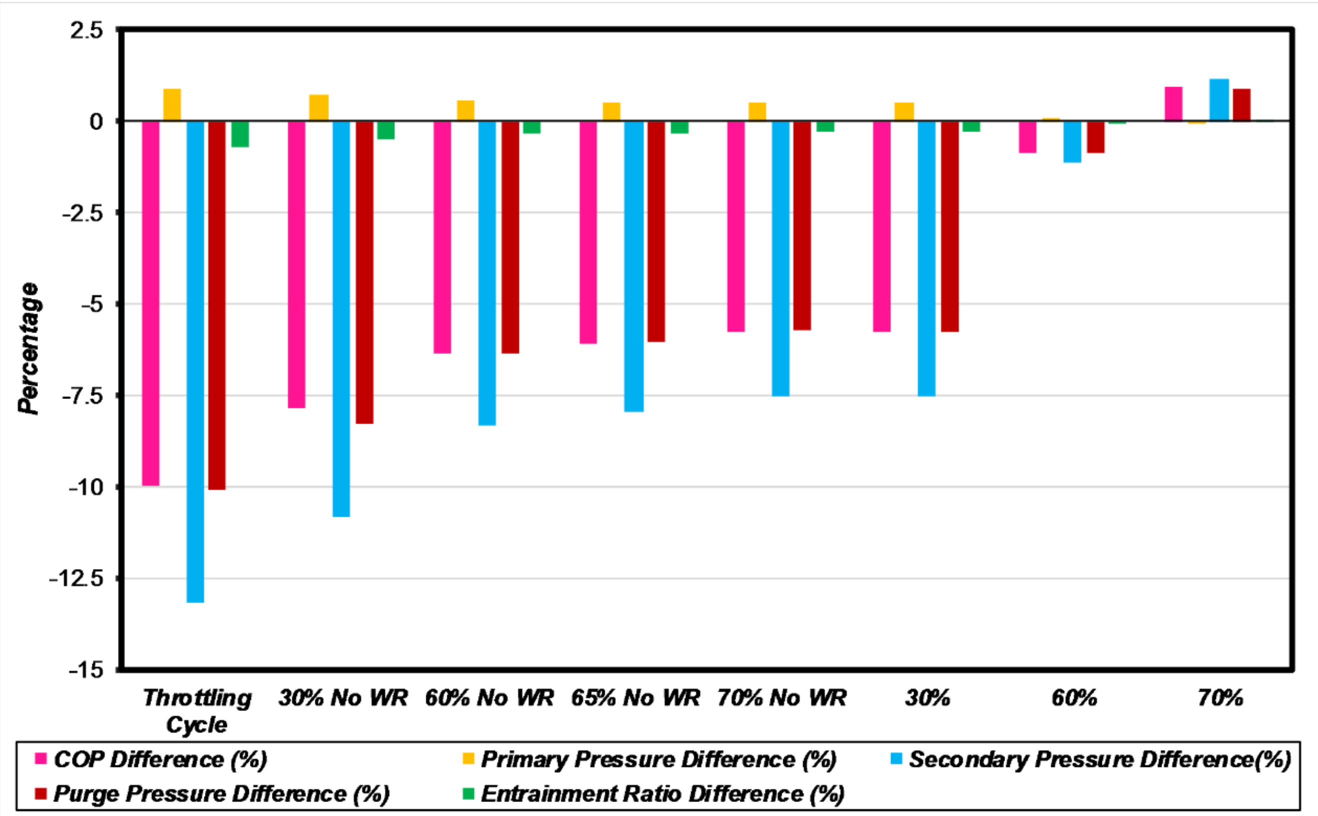

Fig. 51: Comparison of the cycle with different models of expansion devices. (Notice that the 65% is absent because it is used in the base assumption!)

Fig. 51 illustrates the effect of the expansion device performance on the COP. Work recovery has a positive impact on the COP. The 30% isentropic efficiency with WR is equal to 70% efficiency without WR. If a normal throttling valve is used instead of the turboexpander, the COP will drop by 10%. It also seems that by fall in the efficiency of the EXP2, the primary pressure and secondary pressure will increase and sharply decrease, respectively. The reason for the reduction of secondary pressure may be the change in the quality of the vapor after the EXP2 due to the approach to the isenthalpic expansion process.

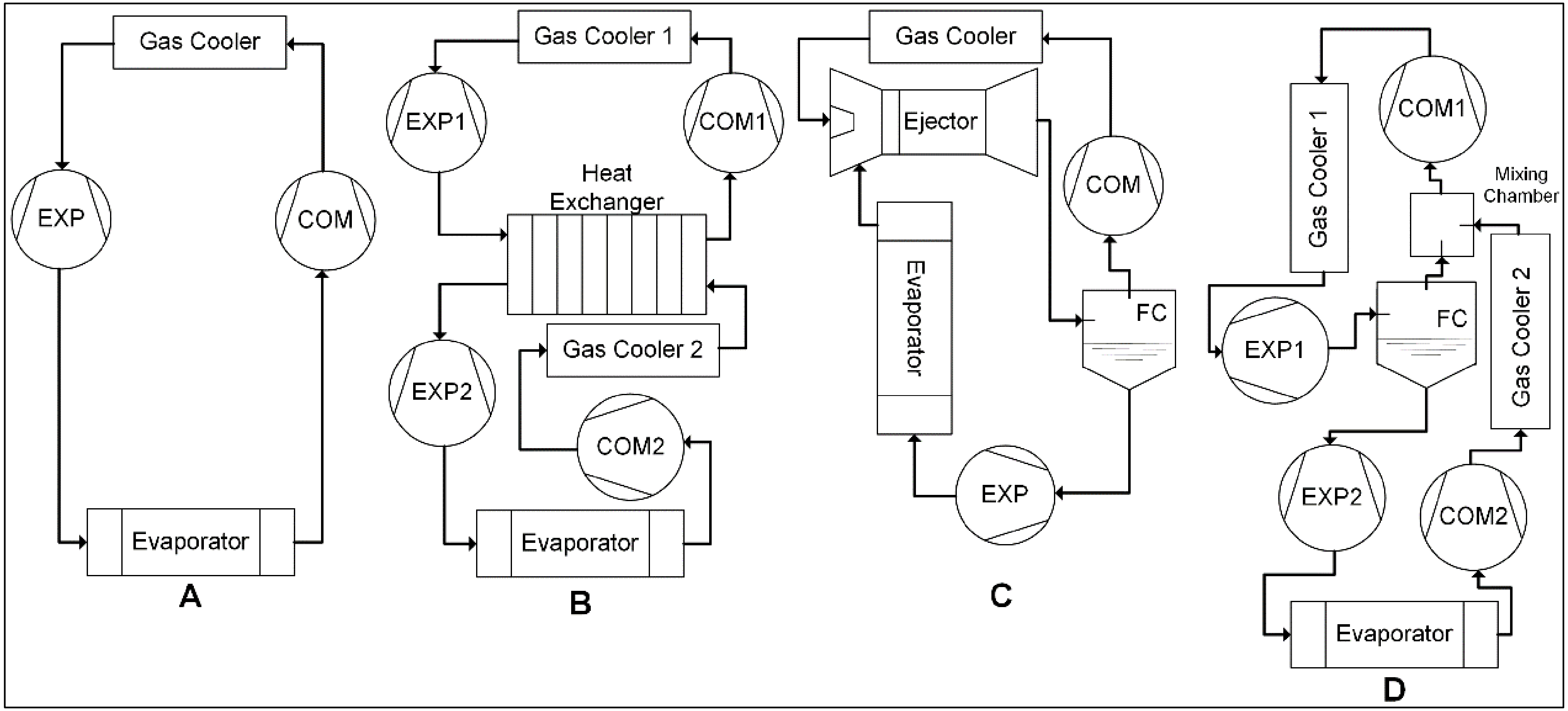

Fig. 52: The 4 layouts of R744 trans-critical refrigeration cycle with turboexpander. From left to right: (A) Single-stage with turboexpander, (B) Cascade 2-stage with Turboexpander and Extra Gas Cooler, (C) Simple Ejector with Turboexpander & (D) 2-stage Flash Tank External intercooling with a turboexpander

In order to compare the present study with other cycles and finding the positive points and disadvantages, the cycles in Fig. 52 were simulated. The layouts use the turboexpander to reduce the performance gap between them. The assumptions are the same as the current study (Table 8) and the pressures were optimized. The same compression, expansion, and ejector models were utilized, and the approach temperatures and capacity are universal. The same equations were used to balance the energy and exergy. The only new thing is the heat exchanger of layout B. It is a counter-flow heat exchanger with a temperature difference of 5 K on the left side. LMTD or NTU method is not necessary at this point.

Cycles A and C are presented as the baseline performance and Cycles B and D are high-performance known methods for low-temperature refrigeration. Subcooling technology is not considered because it can increase the COP for all of the layouts in the same way.

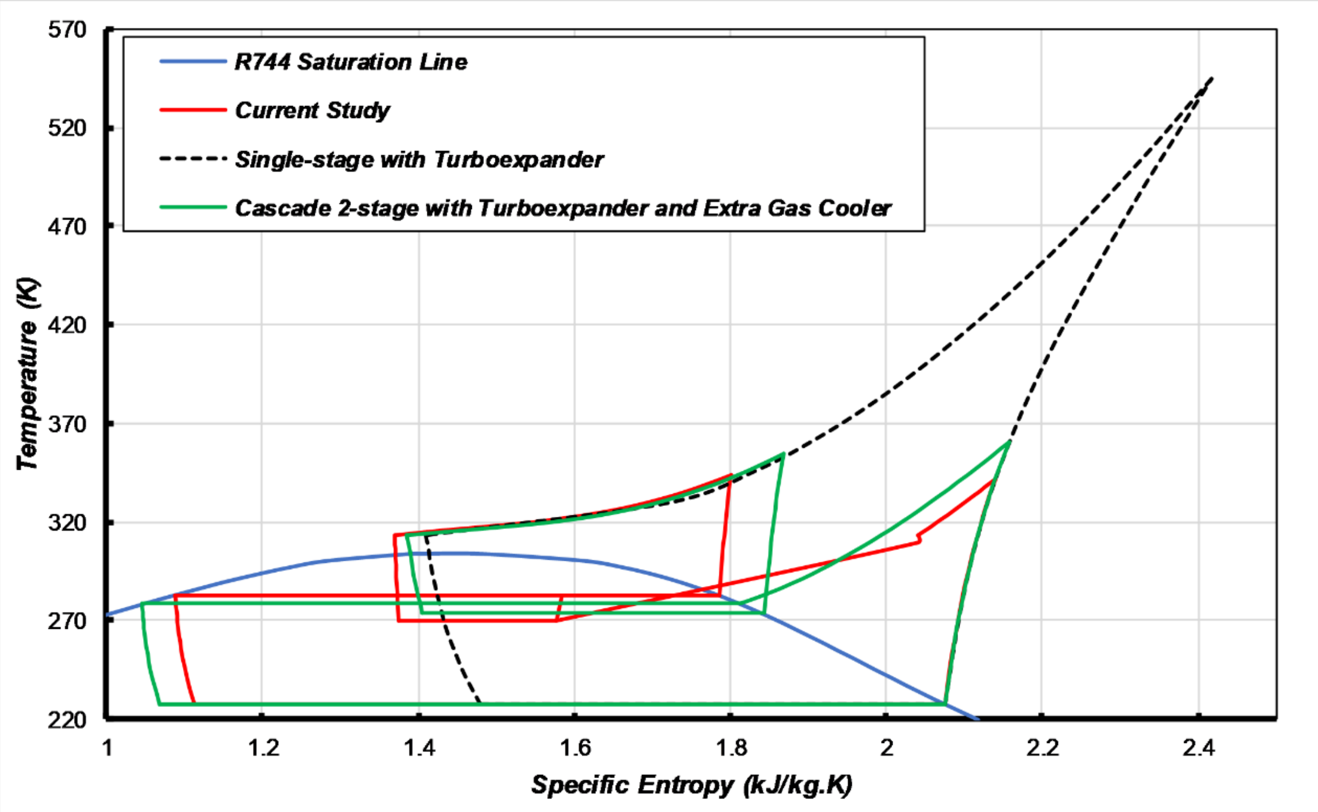

Fig. 53: The Temperature-Specific entropy diagram of the current study and layouts A and B

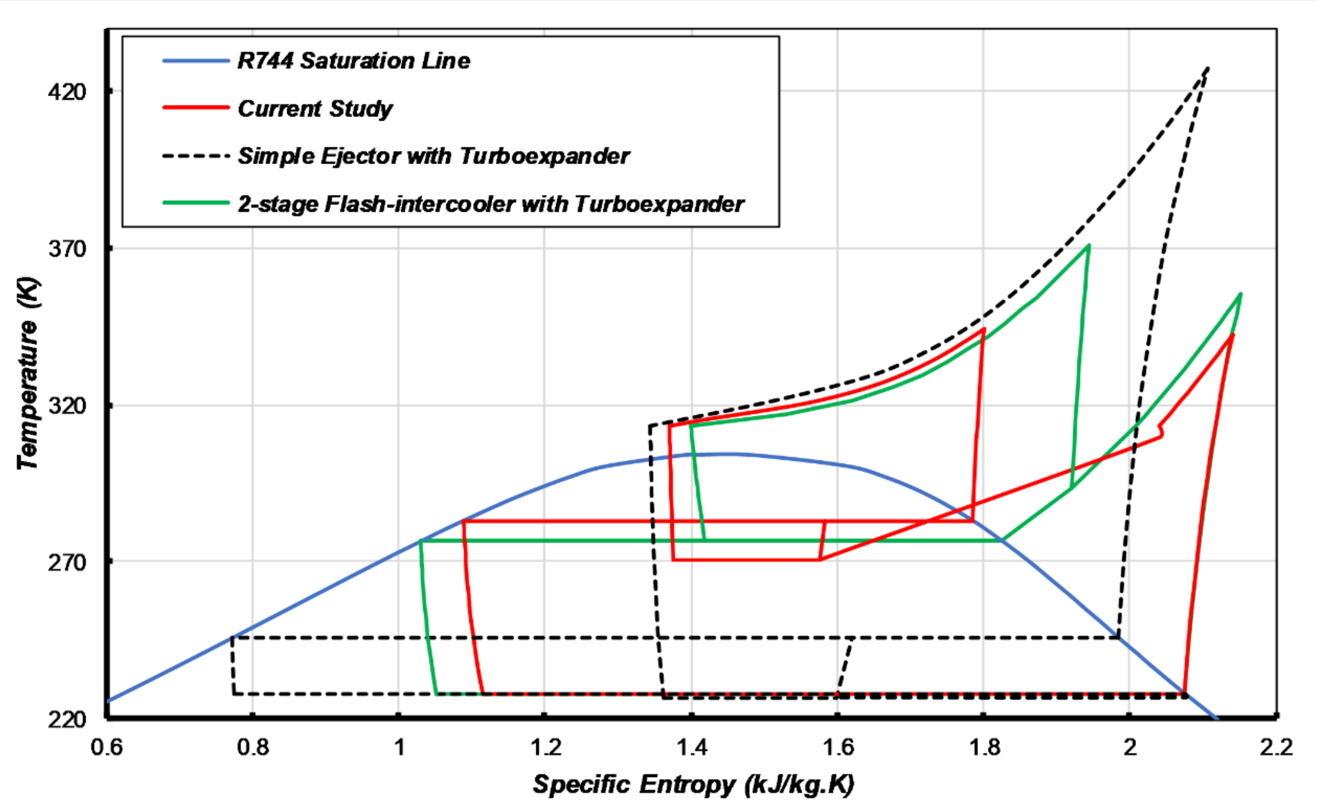

Fig. 54: The Temperature-Specific entropy diagram of the current study and layouts C and D

Table 10: The comparison of important characteristics of all layouts and the present study at optimal operation conditions with EVA and GC temperatures of 228 and 303 K.

Name of the cycle	**Single-stage with Turbo expander**	**Cascade 2-stage with Turbo expander and Extra Gas Cooler**	**Simple Ejector with Turbo expander**	**2-stage Flash Tank External intercooling with Turbo expander**	**Present Study**
COP	0.536	1.295	0.926	1.397	1.399
Evaporation Mass flow rate (g/s.RT)	25.9	15.3	11.9	15.1	16
Mass flow rate in GC1 (g/s.RT)	25.9	34.1	27.4	29.4	39.5
2nd Law efficiency	0.161	0.389	0.278	0.42	0.42
Compression Ratio in COM1	11.22	2.7	6.55	2.45	2.16
Compression Ratio in COM2	-	4.85	-	4.63	4.12
Isentropic efficiency of COM1	0.43	0.81	0.64	0.82	0.84
Isentropic efficiency of COM2	-	0.72	-	0.73	0.75
Maximum pressure (MPa)	9.3	9.5	10.2	9.4	9.7
Inter-stage pressure (MPa)	-	3.5	-	3.8	3.4
GC1 Temperature (K)	545	355	427	371	344
GC2 Temperature (K)	-	361	-	355.5	342
Exergy Destruction Rate (kW/RT)	3.84	1.06	1.99	0.99	1.03
CCB (%)	28.43	4.11	0.44	3.75	4.95
RW (%)	10.61	15.32	0.4	13.92	6.48

From Table 10 and Figs. 53 and 54, it can be concluded that the designed cycle has the best performance among others. It also possesses the most benign compression, which leads to the lowest discharge temperature and best compression efficiency. The exergy destruction rate is 2nd among the others. The main rival of this study is the 2-stage flash-intercooler cycle, which has almost the same COP, better second law characteristics, and less mass flow rate for the same capacity. Speaking of the mass flow rate, which is the main factor for size and the total weight of the setup, the current study has an acceptable mass flow rate for evaporation. However, the size of the gas cooler would be a challenge for the operation. Fortunately, compared to cycle D, it has 34% more mass flow rate in GC, but the discharge temperature from COM1 is 27 degrees less.

In comparison to a simple ejector cycle with a turboexpander, the performance improved by 51%, and the compression ratio reduced to 1/3 and destroyed exergy to a half. From CCB and RW points and comparing to C layout, the present study has a good potential in the utilization of the turboexpander.

3.3. 2nd law analysis

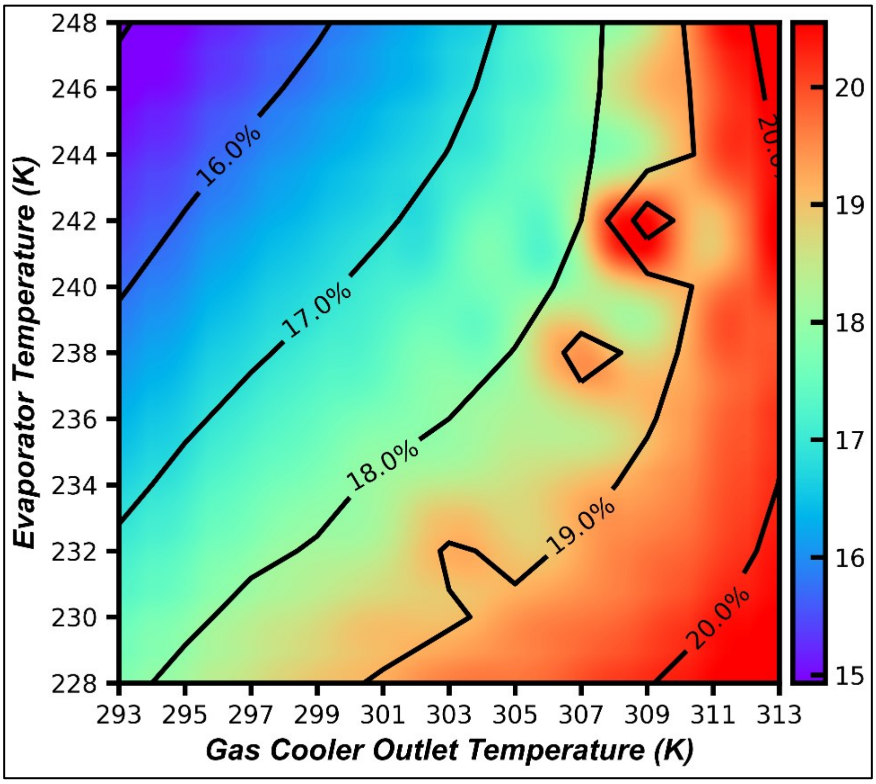

Fig. 55: Share of exergy destruction in COM1 versus evaporator temperature under different gas cooler outlet temperatures in optimum performance

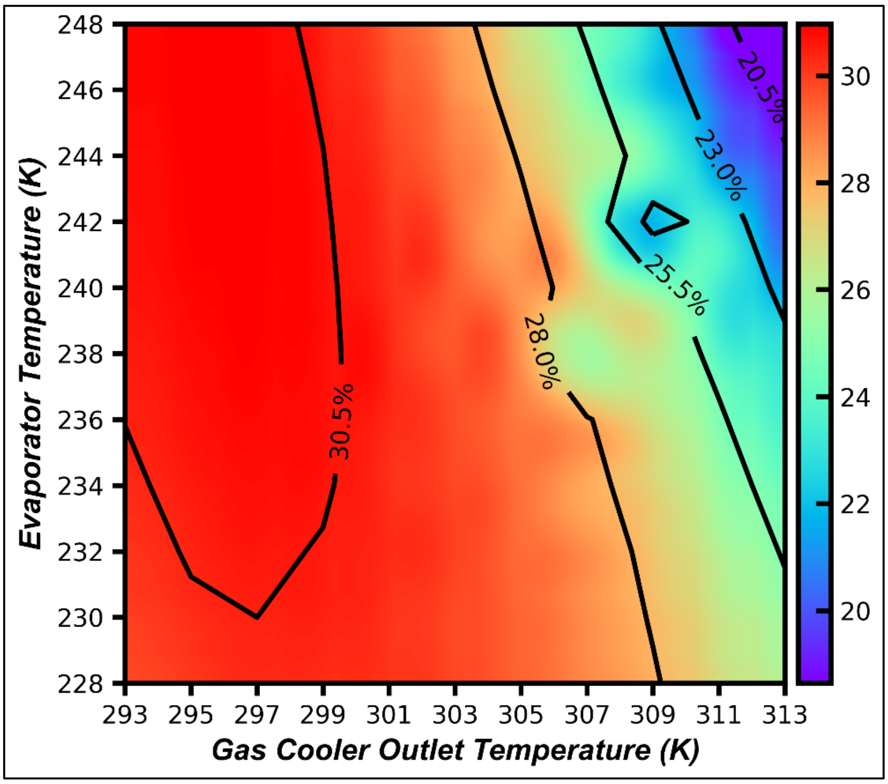

Fig. 56: Share of exergy destruction in COM2 versus evaporator temperature under different gas cooler outlet temperatures in optimum performance

Fig. 55 and Fig. 56 show the share of exergy destruction-temperature contour for COM1 and COM2 respectively. COM1 share of exergy destruction is increased by the temperature difference of the cycle. The first reason is the increase in the pressure ratio of COM1 and the decline in the isentropic and consequently the exergy efficiency of COM1 (see Fig. 61). The second reason is the reduction of R and increases the exergy rate of the COM1. COM2's share also has a predictable behavior. Exergy destruction in COM2 tends to increase by the temperature difference of the cycle. Because the exergy efficiency of COM2 is like COM1 (see Fig. 62). However, the decrease in the R nullifies the increase in exergy destruction. In Fig. 55 left side, COM2 share is huge. In this area, the share is increased because of the increase in R and decrease of the share of other components of the cycle in exergy destruction.

In Fig. 57, GC1's share of exergy destruction-temperature contour presented a form that contradicts the resultant of entrainment ratio and the pressure ratio. It is caused by the decrease of exergy destruction in other components and an increase in logarithmic mean temperature of the GC1 which in return increases the exergy destruction.

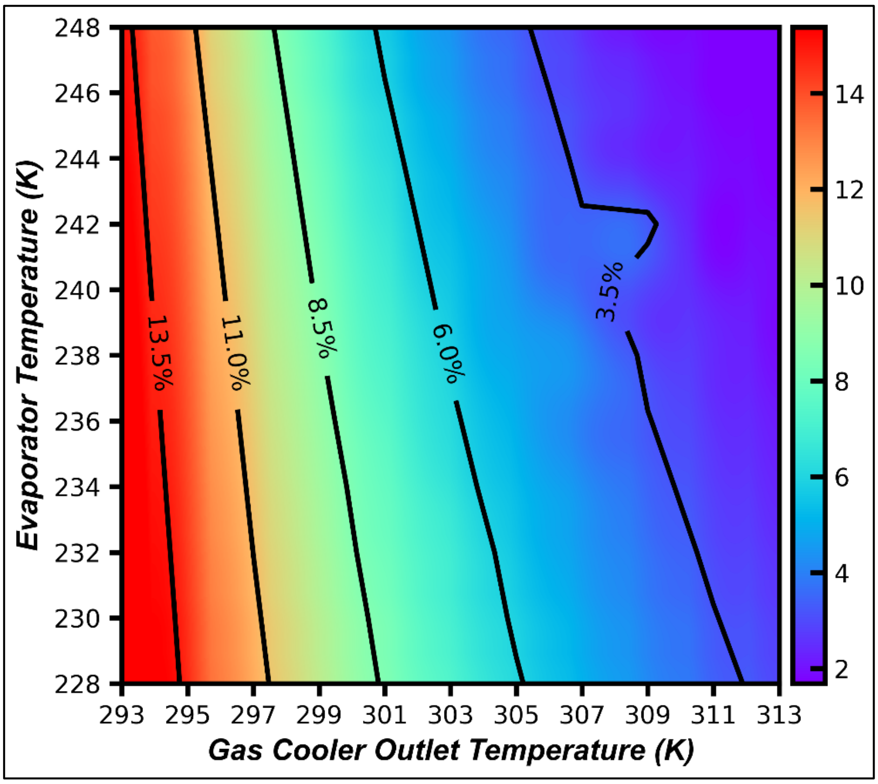

Fig. 57: Share of exergy destruction in GC1 versus evaporator temperature under different gas cooler outlet temperatures in optimum performance

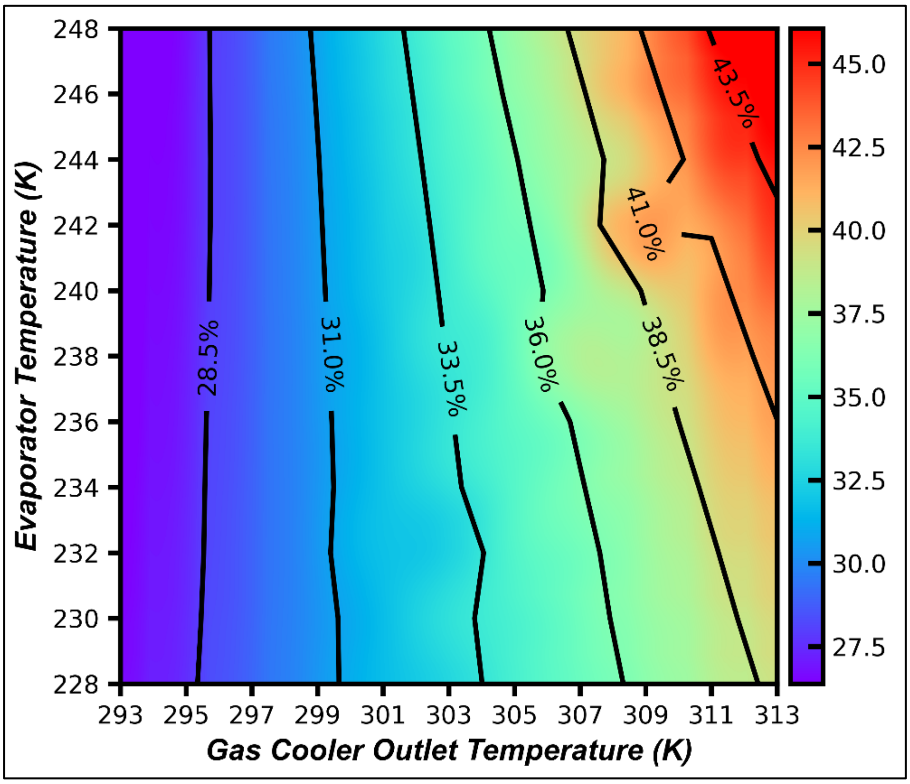

Fig. 58: Share of exergy destruction in EJE versus evaporator temperature under different gas cooler outlet temperatures in optimum performance

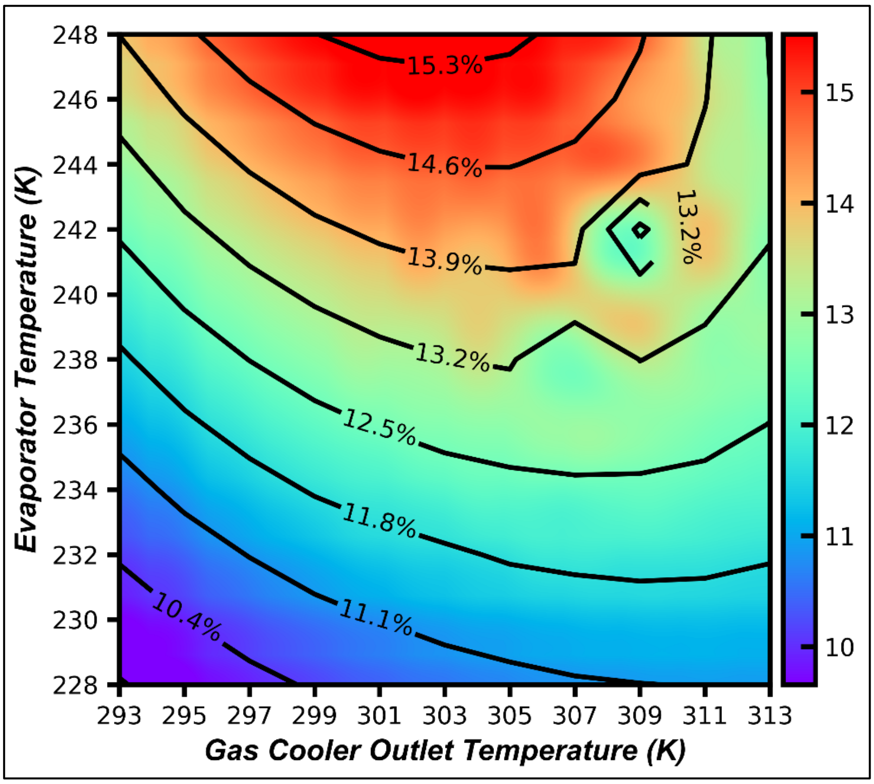

Fig. 59: Share of exergy destruction in EXP2 versus evaporator temperature under different gas cooler outlet temperatures in optimum performance

The top right corner of Fig. 58 shows the largest share in the ejector. There are many grounds for this behavior. They include the decline in R, increase in mass flow rate (see Fig. 42), increase in the pressure fall in the primary nozzle, and increase the pressure lift by the diffuser. Share of EXP2 (Fig. 59) is like a set of parallel layers. Purge pressure has a direct impact on the elimination of exergy in EXPs. Fig. 59's contour is the result of pressure drop in EXP2 (see Fig. 38), entrainment ratio, and the mass flow rate.

Most of the contours share a few dents in the upper right corner. At that point, the pressure ratio of compressors passes a relative extremum point. This extremum point impacts the mass flow rate, the pressure drop in the nozzle, pressure lift in the diffuser, and the efficiency of the compressors. This has reciprocating effects on overall components. Surprisingly, these points are not visible in the R, total destroyed exergy, and COP contours. It is possible that the wild interaction between the components finally finds a surface to equalize itself. These points made the largest over-shoot in the optimization algorithm and finding them required a good initial guess.

This analysis does not include the evaporator, the flash chamber, and GC2. Because their destroyed exergy is zero and their exergy efficiency is 100%. In real situations, the destroyed exergy in the evaporator is magnificent due to the temperature difference in heat transfer and pressure drop inside and outside the evaporator. Also, the shocks, turbulence, and friction inside the ejector are huge sources for irreversibly and entropy generation. However, in this study, those factors were not considered. In a real situation, the magnitude of destroyed exergy must be higher than this simulation.

From the nature of this study, it can be understood that the exergy destruction in the gas coolers and the evaporator is due to external irreversibility and exergy destruction in other components are the result of internal irreversibility.

The total rate of destroyed exergy contour is shown in Fig. 60. The profile is like COP since it mostly depends on the external factors, which is the temperature in this simulation.

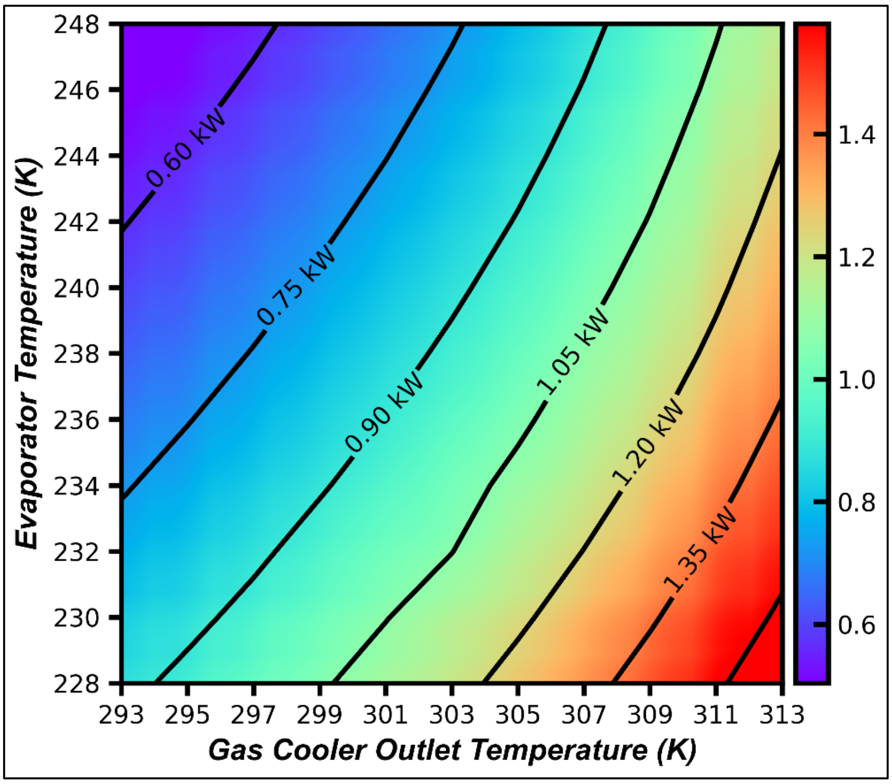

Fig. 60: Total rate of exergy destruction per refrigeration ton versus evaporator temperature under different gas cooler outlet temperatures in optimum performance

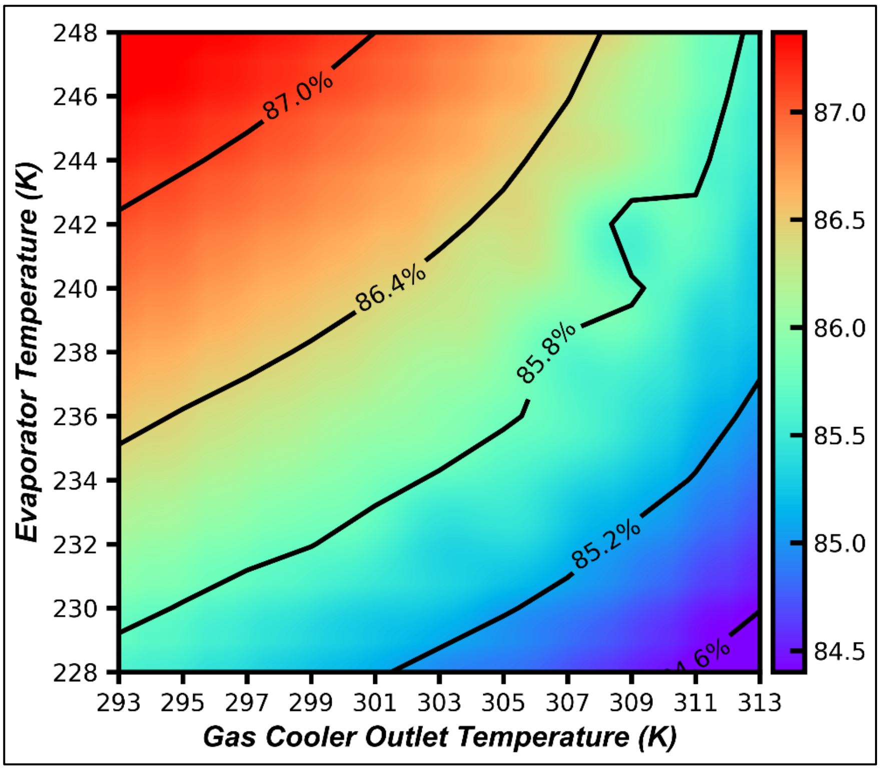

Fig 61: Exergy efficiency of COM1 versus evaporator temperature under different gas cooler outlet temperatures in optimum performance

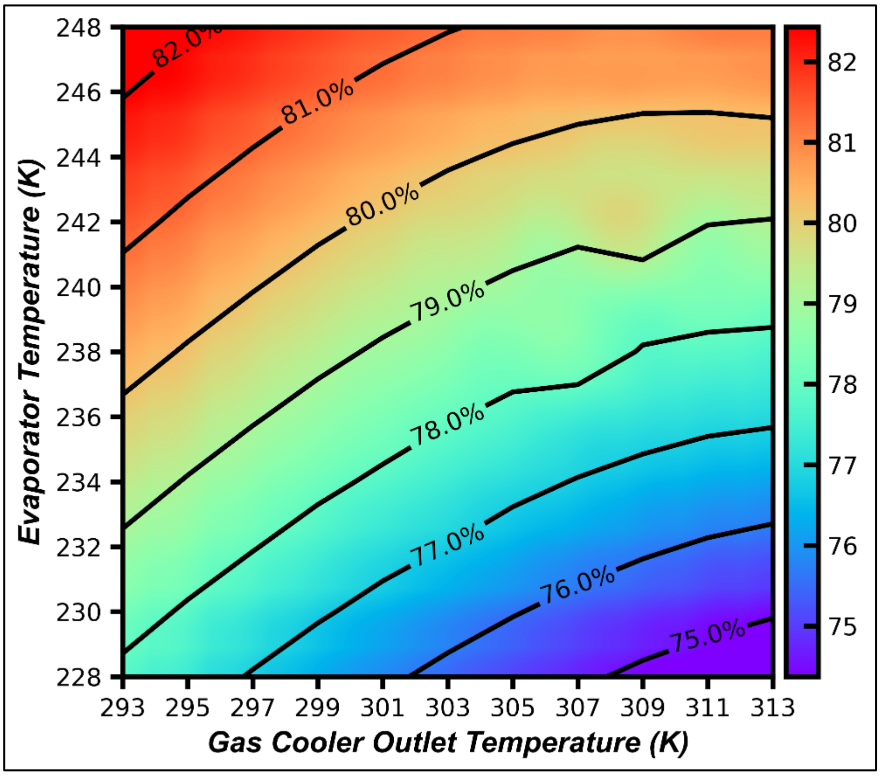

Fig 62: Exergy efficiency of COM2 versus evaporator temperature under different gas cooler outlet temperatures in optimum performance

Fig. 61 and Fig. 62 show exergy efficiency-temperature contour for COM1 and COM2 respectively. Comparing them with figures 36, 37, and 14, it can be concluded that their exergy efficiency is imitating their isentropic efficiency. In Fig. 63, the same trend is surfing. Even though the isolines don't follow Fig. 38, this profile can be explained in this way. Purge pressure is following the primary and secondary profile and EXP2 exergy efficiency has followed the purge pressure. Logically, the direction of the EXP2 contour is like Fig. 36 and Fig. 37.

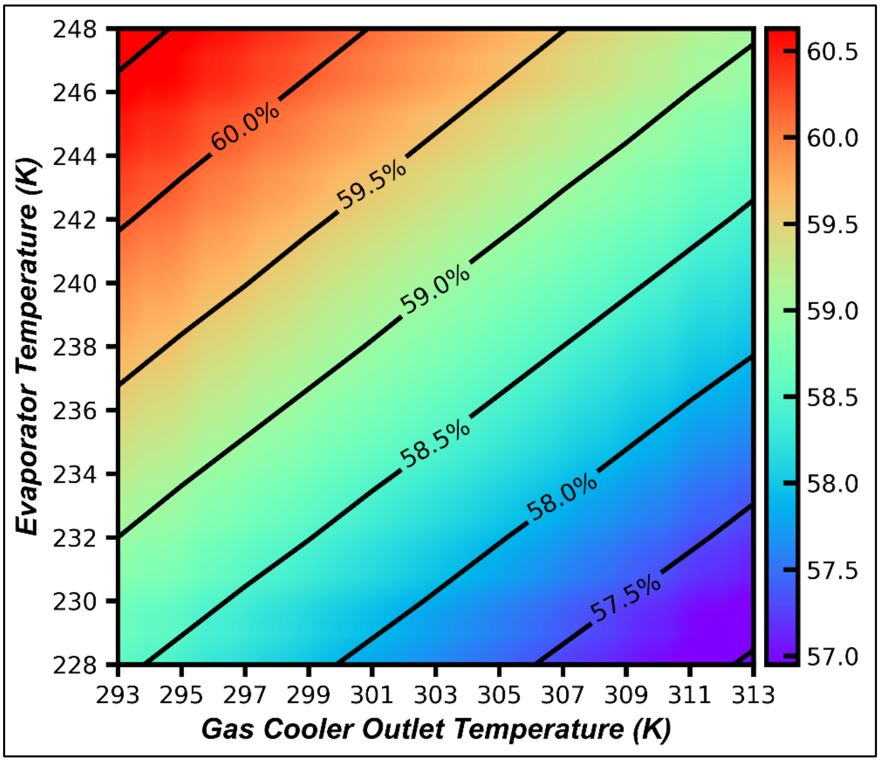

Fig. 63: Exergy efficiency of EXP2 versus evaporator temperature under different gas cooler outlet temperatures in optimum performance

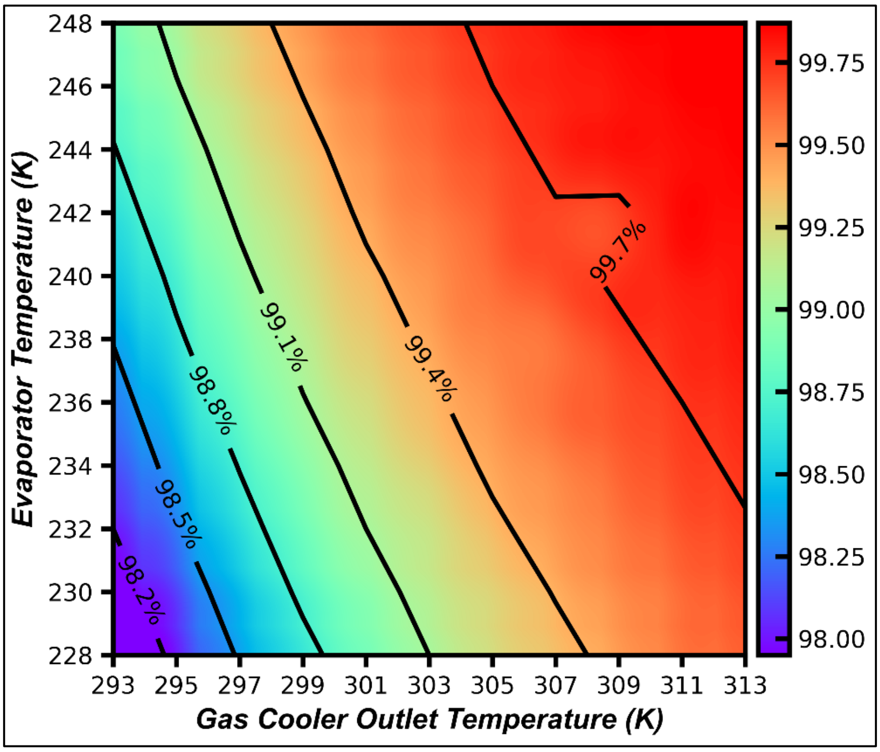

Fig. 64: Exergy efficiency of GC1 versus evaporator temperature under different gas cooler outlet temperatures in optimum performance

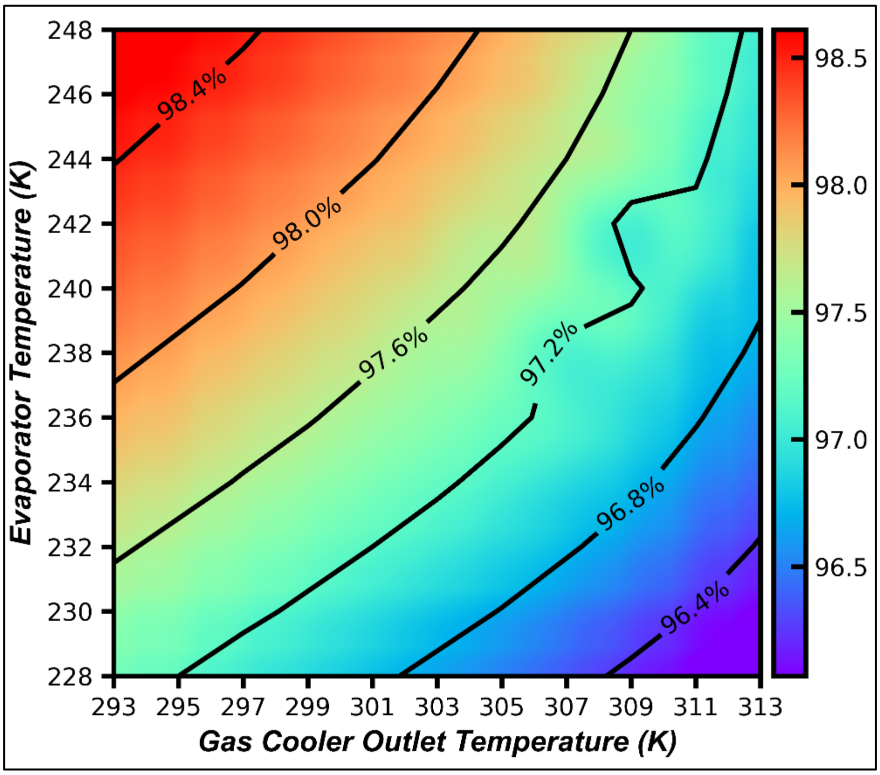

Fig. 65: Exergy efficiency of EJE versus evaporator temperature under different gas cooler outlet temperatures in optimum performance

Fig. 64 and Fig. 65 show exergy efficiency-temperature contour for GC1 and EJE respectively. Their exergy efficiency is high but still changes by temperature and their contours are not single-surfaced. As it was mentioned before, the simple thermodynamic model for this paper is unable to calculate the real efficiency. The amount of the efficiencies must be less than these values. However, the profile is correct.

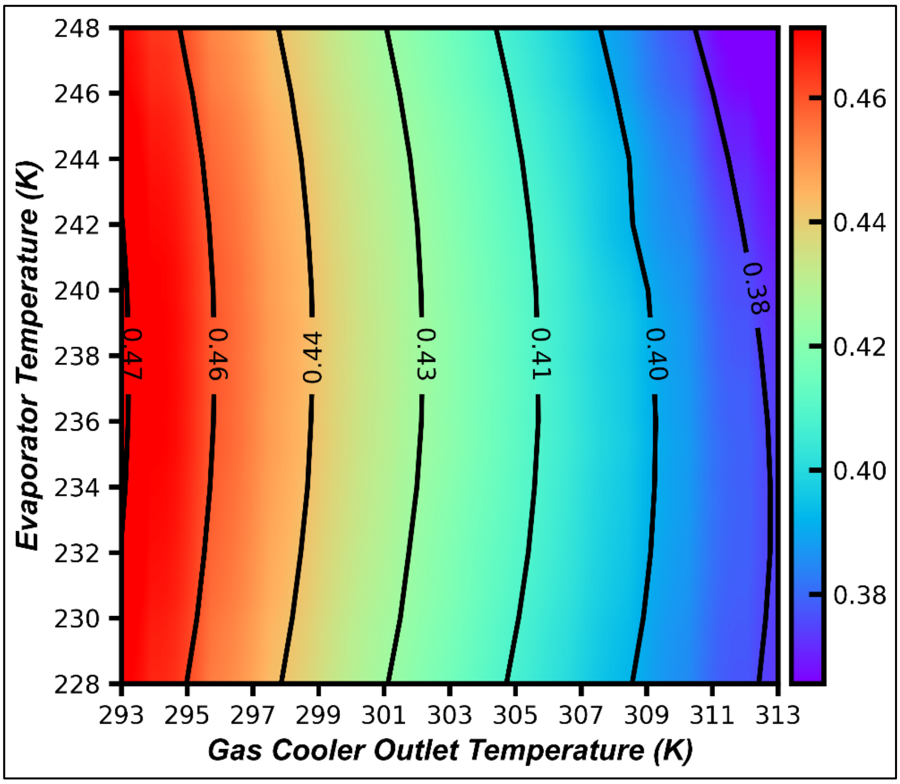

Fig. 66: The second law efficiency versus evaporator temperature under different gas cooler outlet temperatures in optimum performance

3.4. Energy and Exergy Flow

Fig. 67 and Fig. 68 presented the Sankey diagrams of energy and exergy flow of the cycle, according to Table 4. The width of the arrows is proportional to the amount of energy and exergy for one ton of refrigeration cooling load. The amount of specific enthalpy is from the IIR reference of CO_2. These diagrams are presented to facilitate the understanding of the cycle's operation. It can be deduced that a low-pressure loop does the compression and expansion for the refrigeration, and the high-pressure loop does the pumping (moving the fluid) and the cooling. In Fig. 24, the other losses include the exergy loss in both gas coolers and the evaporator. However, the exergy loss in the GC2 and the evaporator is 0.15%.

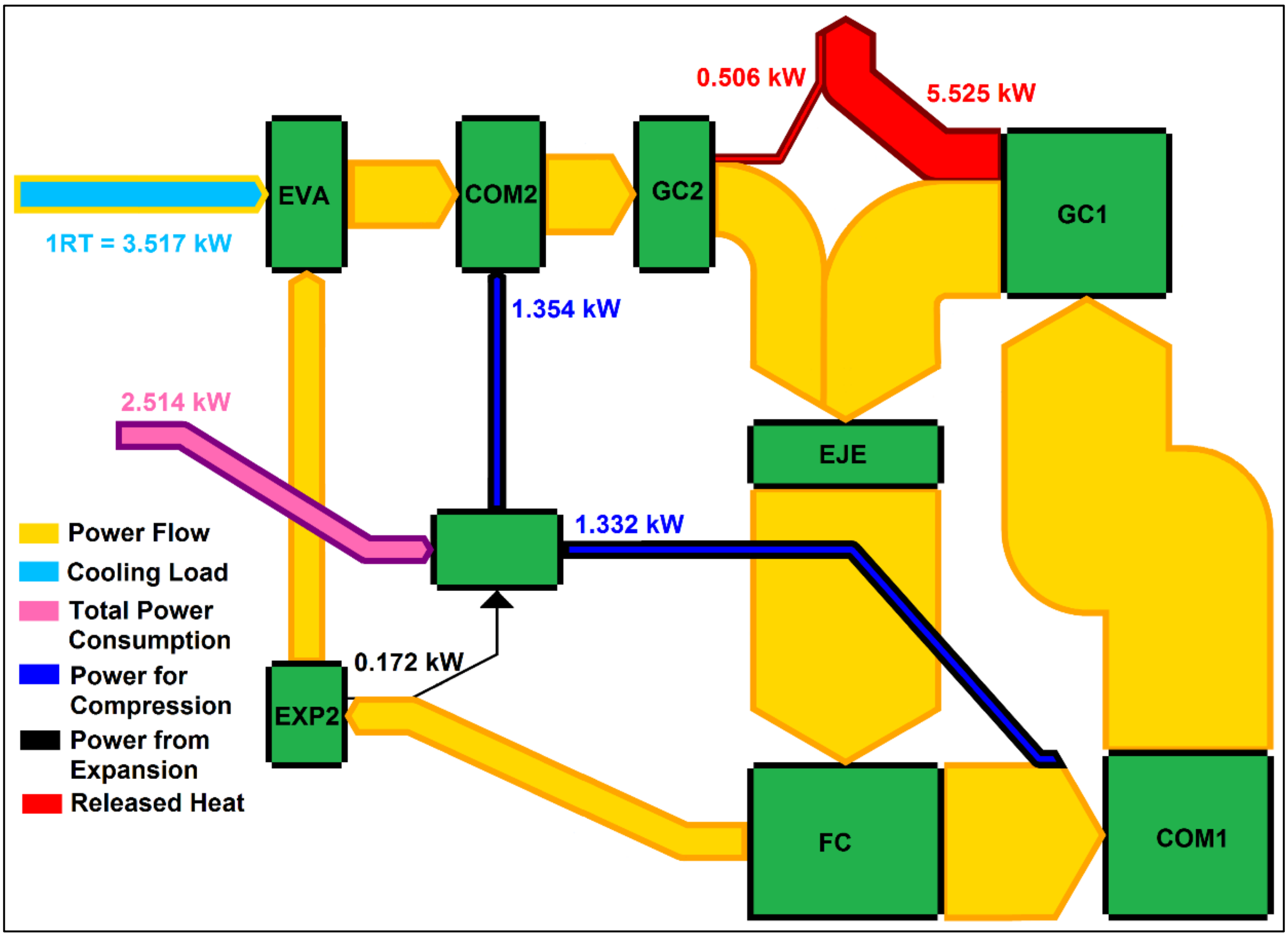

Fig. 67: Sankey diagram of energy flow in the cycle according to Table 8

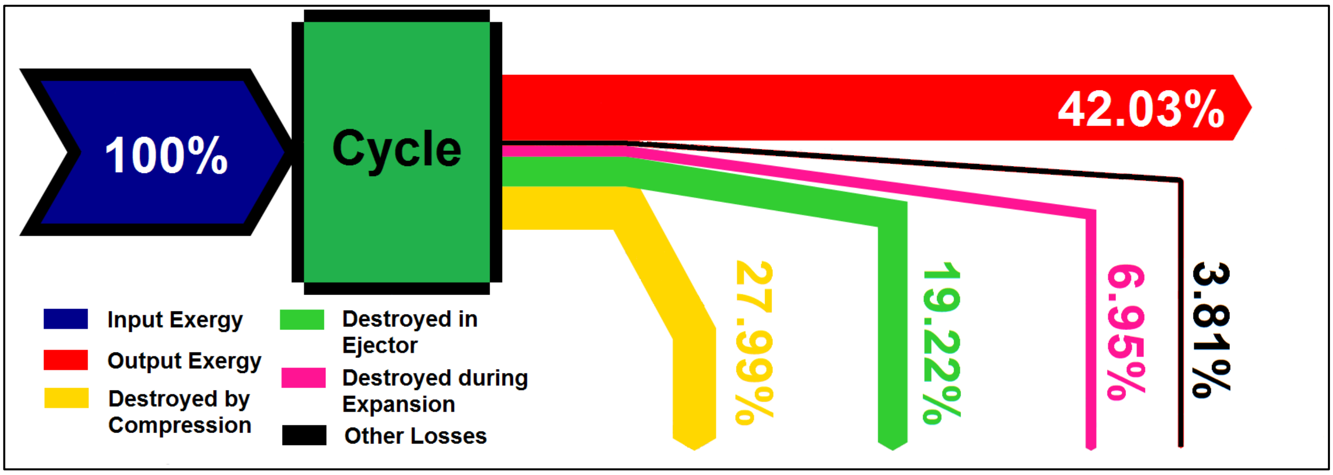

Fig. 68: Sankey diagram of exergy flow in the cycle based on Table 8

3.5. Improving the performance

As it was mentioned in the introduction, R744 cycles have large pressure lifts. Hence, the compressor discharge temperature is high. The ejector cycle, which was designed by the research team, despite having the most benign compression ratios still has noticeable high discharge temperatures. It was suggested that an ORC was implemented, and a small fraction of work was recovered from the GCs. Several layouts of the propylene cycle were tried and final the layout of Fig. 69 was chosen. It has the best possible performance and can completely satisfy the dry expansion in turbines and temperature profiles of HXs.

Table 11 and Table 12 show the characteristics of the hybrid cycle. They are the continuation of Table 8 and 9 cycles. Because the optimization code was linear.

Table 11: The thermodynamic properties of extra points of hybrid cycle

State #	T (K)	P (MPa)	h (kJ/kg)	S (kJ/kg.K)	x (kg/kg)
7	319.2	9.711	368.2	1.532	Supercritical
12	319.1	3.411	493.8	2.063	Superheat
A	313	1.646	304.6	1.35	0
B1	314	2.653	307.2	1.351	Sub-cool
B2	314.1	2.572	307	1.351	Sub-cool
C1	339	2.653	625.3	2.306	Superheat
C2	337.2	2.572	624.2	2.307	Superheat
D	313	1.646	608.1	2.32	1

Table 12: The performance and other characteristics of the cycle

COP of combined cycle	1.505
ORC to R744 mass flow ratio in Loop 1	0.2772
ORC to R744 mass flow ratio in Loop 2	0.0803
ORC mass flow rate Loop 1 per RT	10.91 gr/s
ORC mass flow rate Loop 2 per RT	1.28 gr/s
Total ORC mass flow rate per RT	12.2 gr/s
HX1 UA constant per RT	0.7 kW/K
HX2 UA constant per RT	0.08 kW/K

Fig. 70 and Fig. 71 are the T-s and P-h diagrams of Fig. 69 based on information from Table 8 and Table 10.

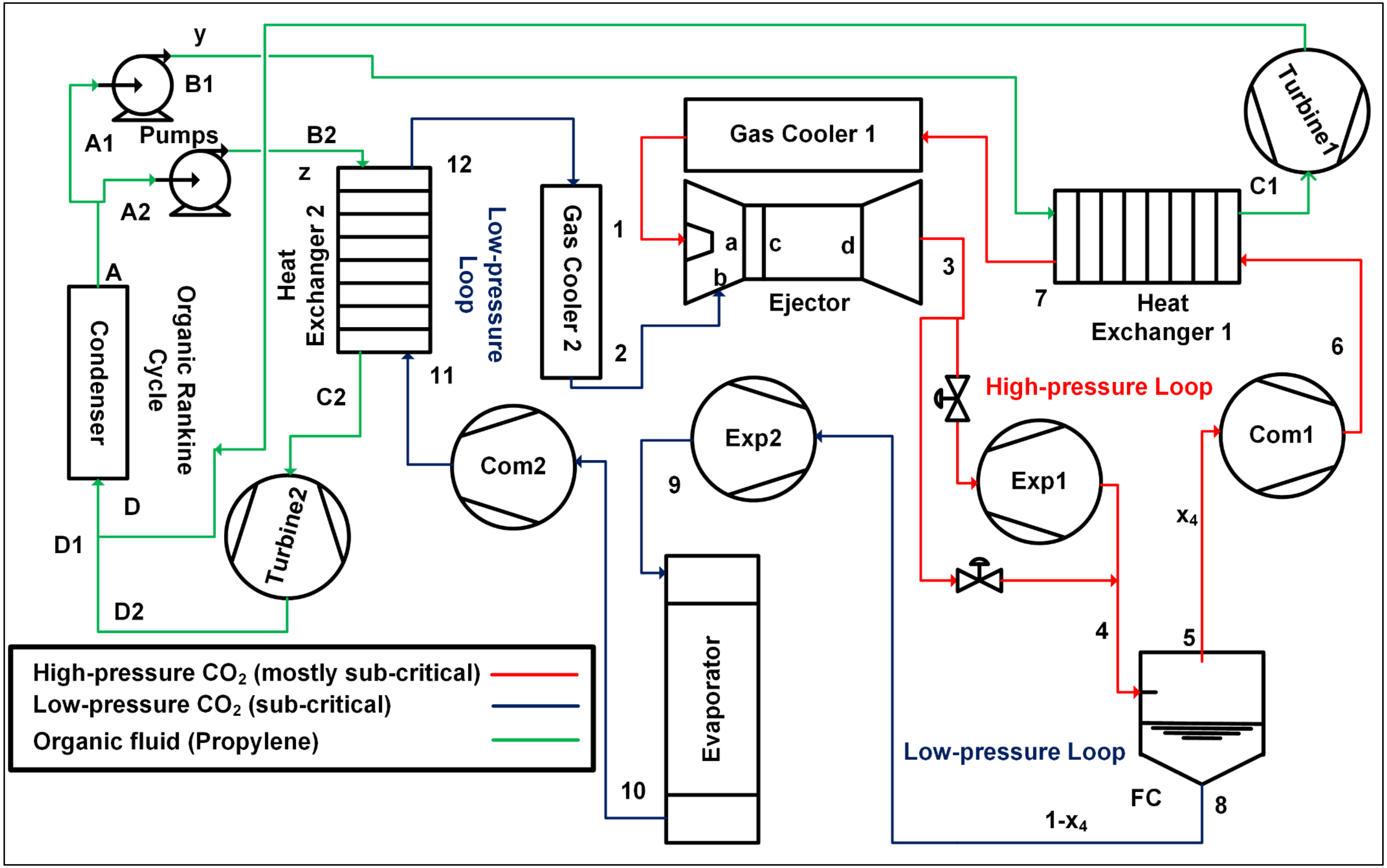

Fig. 69: Schematics of hybrid R744/R1270 cycle

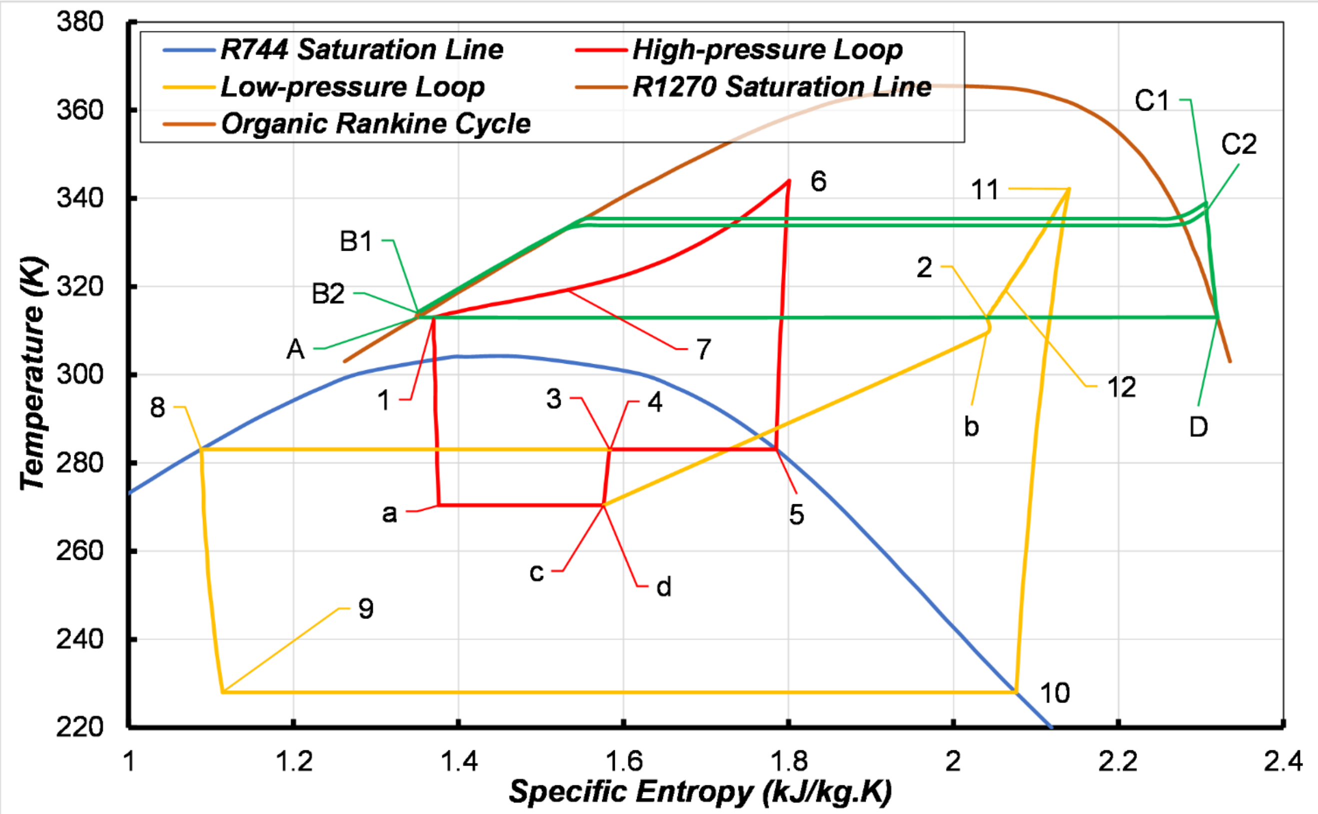

Fig. 70: The Temperature-Specific entropy diagram of the cycle according to Table 8 & Table 10

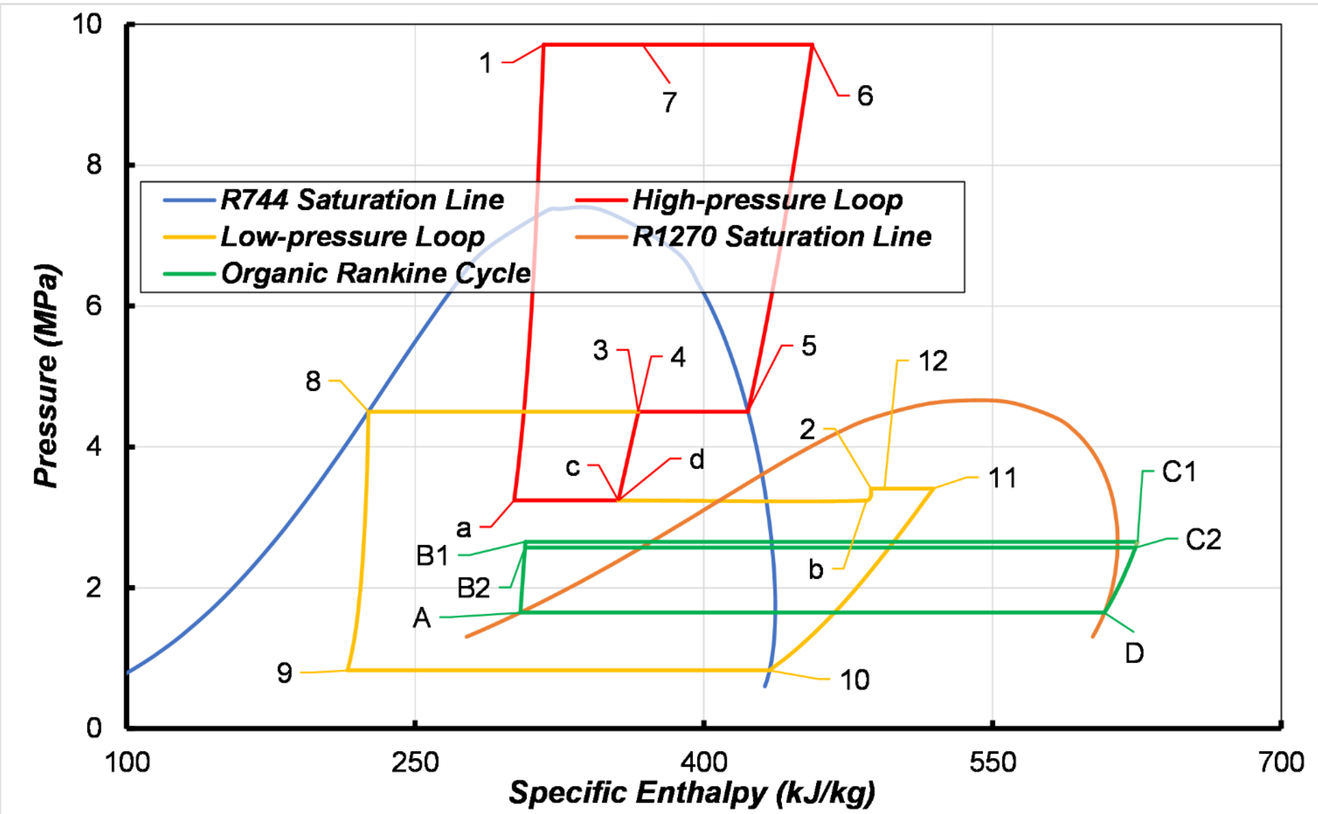

Fig. 71: The Pressure-Specific enthalpy diagram of the cycle according to Table 8 & Table 10

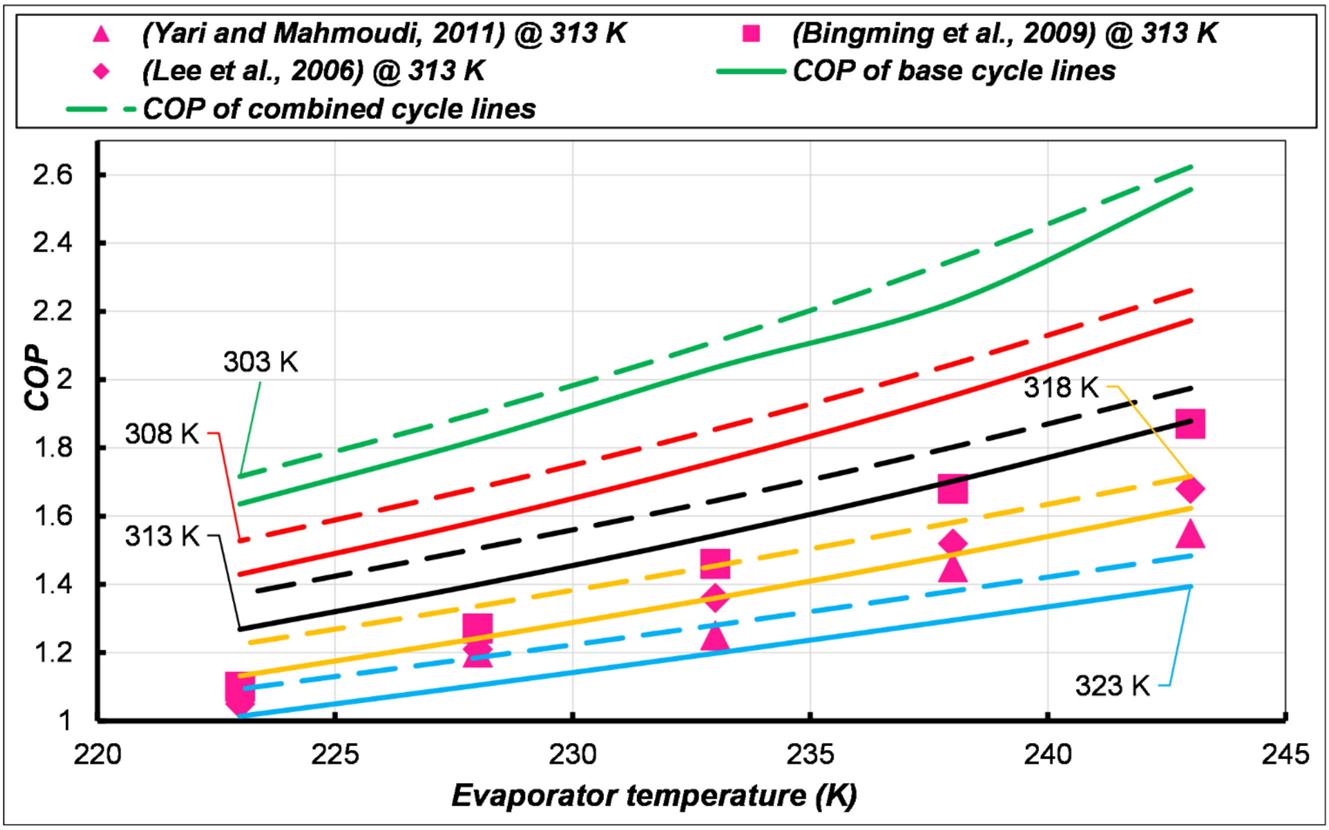

Fig. 72: The optimum performance of the base and combined cycle and some previous studies[54][66][73]

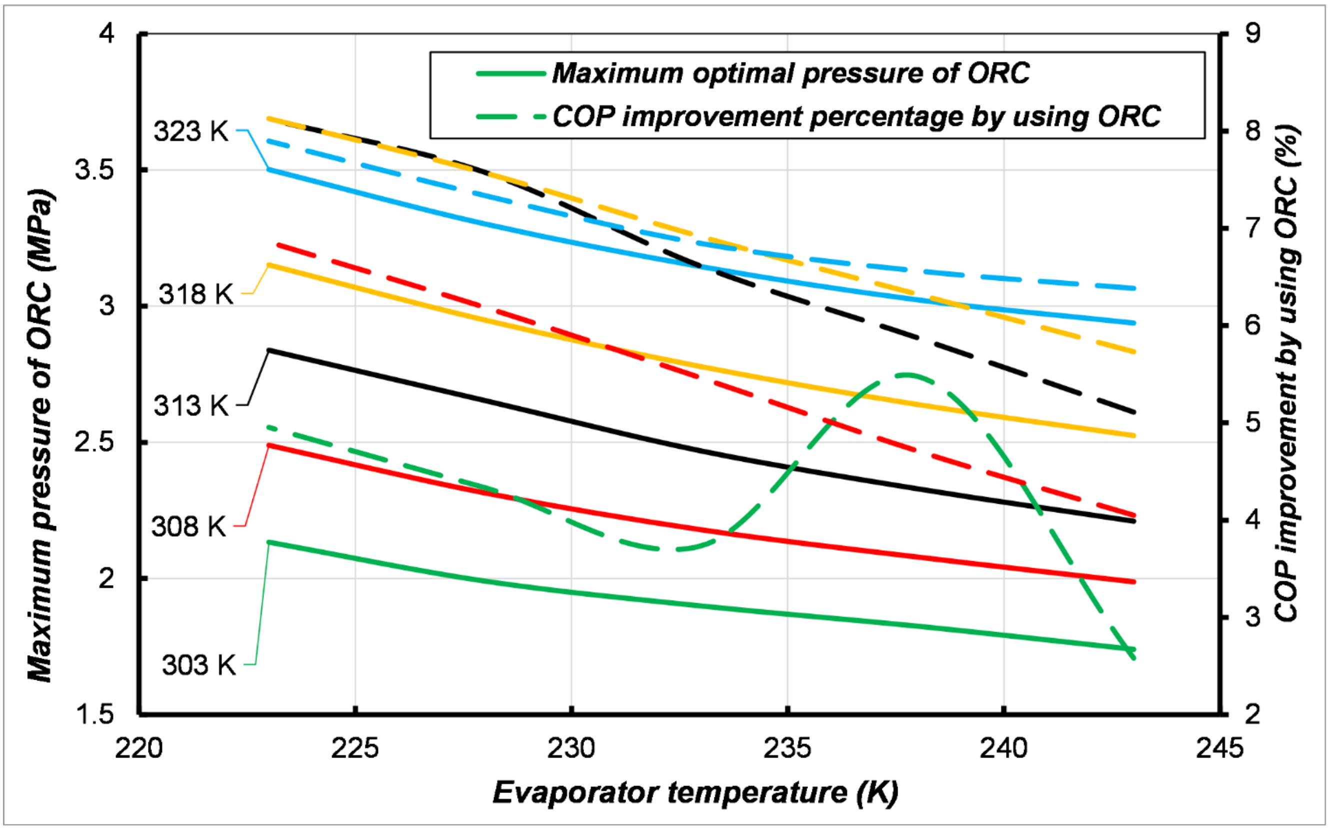

Fig. 73: The maximum pressures of R1270 and performance improvement by using ORC.

Fig. 72 presented the COP of single and combined cycles. A literature review was also added to comparing the results with other low-temperature refrigeration studies. The ORC always improves the performance and the combined cycle has a better performance than other studies which was reviewed in this thesis. The performance of the single cycle was approaching the other studies at higher evaporator temperatures. But at lower temperatures it is unchallengeable.

In Fig. 73, it is observed that the effectiveness of ORC was reduced by the reduction in temperature lift of the refrigeration cycle. The final discharge temperature of the compressors has a direct relation with their pressure lift. If the temperature lift of the system is reduced, the available heat for recovery is reduced. There is a sudden rise in the effectiveness of ORC at the 303K line. At that point the mass flow ratios of ORC loops become equal. Fig. 74 illustrates that by the decline in recoverable energy, the UA factor decreases. The UA factor for heat exchanger 1 is noticeably larger than its counterpart in heat exchanger 2 because the entrainment ratio is rarely past 0.5. The cost of HX1 can be high and its share of performance improvement is not noticeable. Adding that part to the cycle needs further economical assessments.

Finally, it was observed that the effusiveness of HX can not be higher than 0.8 if the approach temperature is limited to 5 degrees.

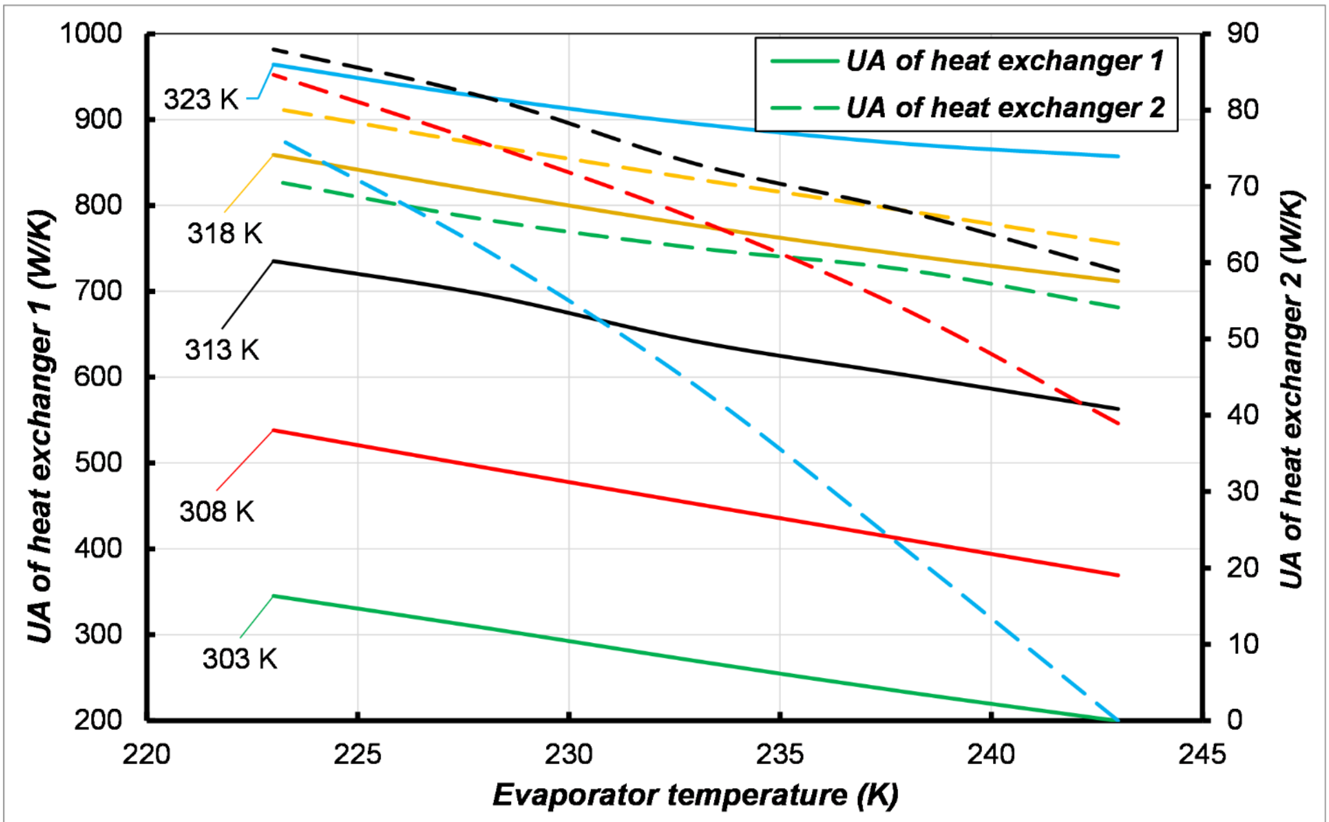

Fig. 74: The required UA factor for heat exchangers to reach this performance

4. Conclusion

A new layout for the ejector refrigeration cycle for the low-temperature application was proposed. It is a conventional ejector expansion trans-critical CO_2 cycle with three new components: A compressor and a gas cooler for secondary flow before the ejector and one turboexpander after the ejector. COP of the cycle is noticeable (around 1.4) for 228 K of evaporation and 313 K of gas cooler output. The main expansion valve of the cycle was also converted to a turboexpander. Literally, this is a multi-stage cycle without a heat exchanger.

The quality of the outlet flow of the ejector, in a fixed temperature condition, depends mainly on the final pressure of the cycle and discharge pressure of the new compressor, and slightly the pressure of the flash chamber. After optimizing the pressures, it was revealed that the compressor and gas cooler is vital to increase the performance. The expander right after the discharge of the ejector is also useful but optimally unnecessary. The limitations during the pressure optimization were the discharged pressure and vapor quality of the ejector. The sensitivity of COP was calculated against the different performances of the compressors, expansion devices, and ejector. The exergy analysis was performed and discussed for all components and the whole cycle. The ejector and the compression process destroy the most exergy during the operation. It can be concluded that the ejector becomes the main source of entropy production. But it reduces the overall exergy destruction rate of the cycle.

It was concluded that the present study has reasonable exergy performance and less compression ratio. The novel ejector system can utilize the turboexpander (which is unnecessary for conventional refrigeration cycles) as a meaningful reason to increase the COP. A brief comparison to other cycles was also conducted, and the advantages and disadvantages were discussed. Among known layouts without inter-stage heat exchangers, the proposed study has the lowest compression ratio. As it was mentioned in the introduction, avoiding the inter-stage heat exchanger is one of the policies of this simulation. However, if this cycle is used in a cascade system, it will defiantly increase the performance of that system, and even less compression ratio will be observed.

Finally, an ORC was added to the cycle to further improve the performance. The first law analysis of the hybrid cycle proved the feasibility of this idea. The hybrid cycle has an average of 4% higher COP than the single cycle.

The target of this study was a steady-state capacity-independent condition. In order to prove the claims of this study, further transient and capacity-dependent studies are recommended. The pressure drop in the gas coolers and evaporator, the heat transfer mechanism, and the behavior of the compressors at different speeds and loads could affect the results. However, due to the pessimistic assumption of the current model, the same finding will be expected to be observed.

Part II: Thermodynamic Modeling of Supercritical CO_2 Power Cycle Integrated with Lithium Bromide Absorption Refrigeration Cycle, Aiming Performance Improvement

1. Background

Supercritical Carbon Dioxide Power Cycle (SCDC) has achieved huge considerations due to its unique characteristics of small-sized components, uncomplicated cycle schematics, high thermal efficiency at medium turbine inlet temperature, and meager performance loss using dry cooling. SCDC is not a new phenomenon. In 1948, a partial condensation CO_2 Brayton cycle was proposed and patented by Sulzer Bros[23]. Around the 1960s, the potential of SCDC was discovered by ever-growing researchers, like Angelino[107] from Italy and Feher[108] from the United States, who concentrated on cycle performance optimization of different layouts. Circa 1975, the research activities shifted from thermodynamic modeling to accurate design parameters, especially for its applications in nuclear engineering and shipboard applications[23]. Dievot[109] suggested integrating SCDC with sodium fast reactor (SFR) in 1968. Strub and Frieder[110] used the recompression SCDC for the indirect conversion of helium-cooled fast reactor's thermal energy into electricity in 1970. At that time, even though the exceptional thermophysical properties of CO_2 and the positive points of SCDC had been realized by researchers, the technological limitations of the development of CO_2 turbomachinery and compact heat exchanger hinters the prevail of SCDC. In the 2000s, new progress in Heatric's printed circuit heat exchanger and CO_2 gas turbine technologies, as well as the publishing of numerous research works aiming the application of SCDC in nuclear engineering which were conducted by MIT[23][111][112][113] and ANL[114][115][116], SNL [117][118] in united states and Tokyo Institute of Technology in Japan [119], fueled the study affords in SCDC. The SCDC was then considered an auspicious power conversion system for more energy resources such as solar energy, fuel cell, coal power, geothermal energy, and so on [120][121]. Olumayegun and Wang[122] studied the dynamic performance of SCDC integrated as waste heat recovery system to evaluate its feasibility and benefits. Li et al., 2019a[123][124][125] carried out design determination for SCDC for commercial-scale coal-fired power plants, and the crucial matters and solution methods for coal-fired SCDC power plants were unraveled in the work of Xu et al.[126]. Neises and Turchi[127] evaluated the possibility of SCDC for concentrating solar power applications. Researchers from various fields spend funds and man-hours in the development of compact heat exchangers, high power density, and high-temperature components, gaining operation skills of supercritical CO_2 closed loop, which prompted technical maturity of SCDC in the laboratory.

The characteristics of SCDC make it well coupled with nuclear applications. SCDC offers high efficiency at mediate turbine inlet temperature (around 450–600 °C), which is close to the nominal core outlet temperature of fourth-generation reactors [128]. The simplicity and compactness of SCDC aid the nuclear reactor system reduce capital investments and make the nuclear power plant more preferable in the economy compared to other energy types[123][124][125][129]. SCDC has relatively small performance loss in dry cooling conditions compared to that of water-cooling conditions, which enables SMR's application in the water-deficient area[130][131]. The feature of small footprint gives nuclear power plant high power-to-weight ratio, makes it transportable by truck or train[132], which allows in-factory manufacture and on-site assembling of the nuclear power system. SCDC based nuclear reactors can also be applied in scenarios in which there is a huge need for space and power density, such as space reactor[133].

The primary logic in fourth-generation reactors' high operating temperatures is to boost the nuclear power plant efficiency which is currently less than fossil fuel power plants. The upsurge of the reactor outlet temperature generally causes higher turbine inlet temperature in the power cycles and potentially improves thermal efficiency according to the second law of thermodynamics.
Therefore, the Gen IV reactor thermal efficiency can be enhanced with an increase in reactor outlet temperature. Furthermore, related issues due to the low performance of current nuclear sites can be solved as well. As an example, the cooling water outlet condition of atomic power plants is exclusively higher compared with conventional power plants, and it is usually castigated from the economic and environmental protection point of view. Therefore, generation IV reactors should not only improve thermal efficiency but also lessen the influence on the environment.

The utilization of **Carbon Capture and Storage** (CSS) technology in electricity generation for the reduction of CO_2 emission into the atmosphere is considered as one of the technologies to issue climate change. The largest obstacle for CO_2 capture in traditional power plants is the huge cost of complicated technical processes with gargantuan power consumption and it also requires a huge amount of synthesized chemical substances[134][135]. In conventional coal power plants with carbon capture, the CO_2 composition of flue gas is only reduced by 65% while the thermal efficiency will at least drop 18%. It is crystal clear that oxy-fuel combustion has more advantages than regular combustion since the CO_2 content is concentrated with oxy-fuel combustion and can be easily separated from the mixture by available cooling methods[136], therefore it provides a simple measure for carbon capture. Scientists performed a technical and economic assessment on the operation of oxy-fuel combustion electricity production[137][138][139][140][141][142] in the current decade and reaseched the conclusion that oxy-fuel combustion is feasible with environment-friendly measures.

Besides the release of radiatively active gases, the shrinking resources and ever-growing global energy demand enforce the human society to reform the energy framework through improving energy efficiency and developing renewable energies. Some novel thermal cycles used in solar energy, biomass energy, and waste heat have been proposed and studied[143][144][145][146][147][148]. SCDC has been suggested in waste heat recovery [149] and thermal solar energy [150]. Zhang and Lior[151] proposed a CO_2 and H_2O mixture SCDC Rankine combined cycle using LNG and O_2 as fuel and oxidant, respectively. Although the thermal efficiency of this power cycle reaches as high as 50%, the cycle system with both gas turbine and steam turbine circuits is complex.

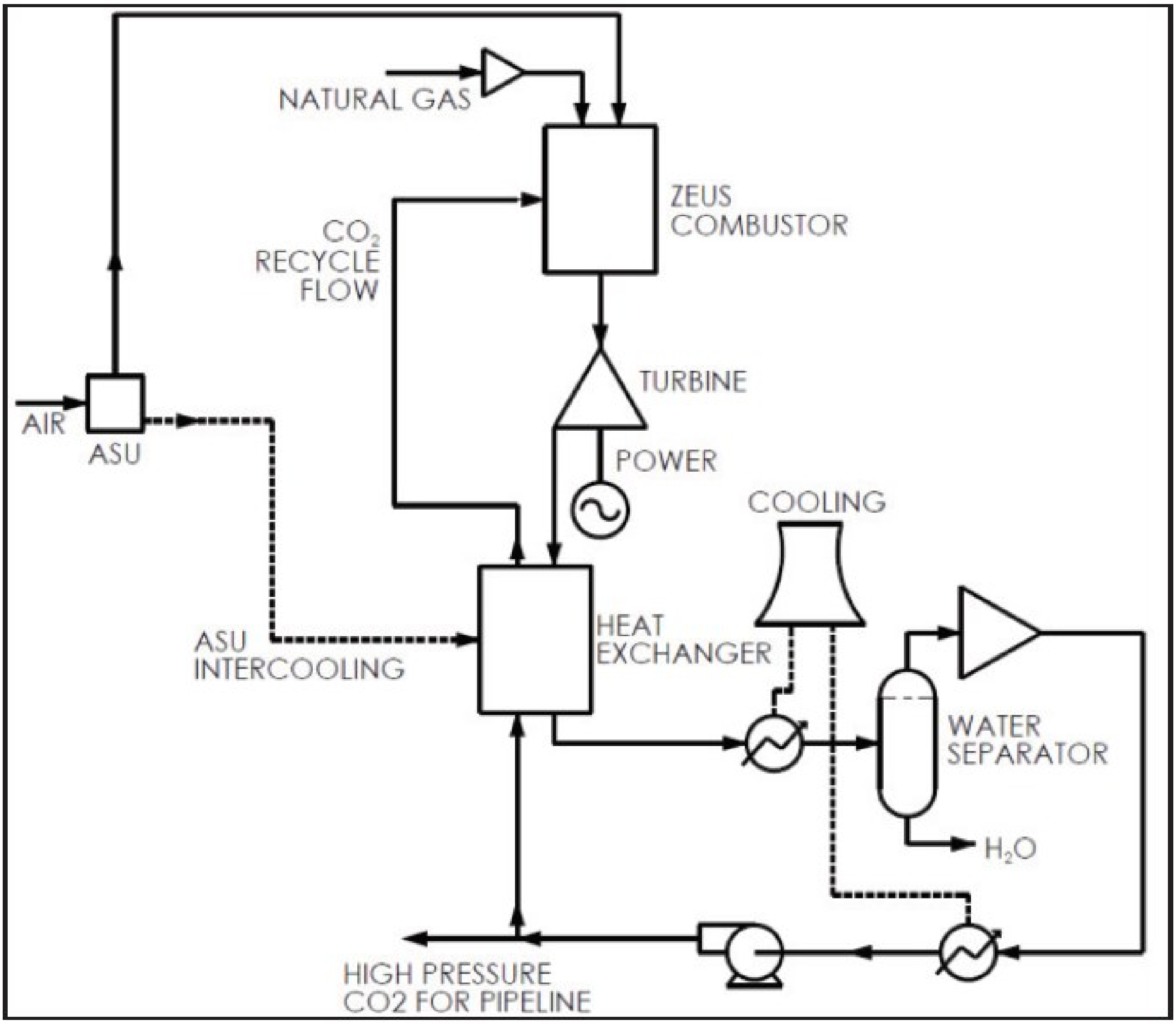

Fig. 75: Schematics of Allam cycle[152]

In their publications, Allam et al.[152][153] suggested a novel trans-critical carbon dioxide power cycle (Allam cycle) that utilizes combustion products and already circulating CO_2 mixture as working fluid. This cycle applied oxy-fuel combustion with negligible nitrogen in combustion to reach nearly zero NOX emission, to solve the issue of NOX emission of the traditional LNG power plants. Allam cycles can dramatically approach higher thermal efficiency than Rankine and Brayton cycles.

Using heat energy from the tail-end of gas turbine exhaust, an absorption refrigeration system can pre-cool the inlet air can be conditioned to lower temperatures than ambient. Zhang et al.[154]. Kakaras et al.[155]. It is found that for every degree rise in ambient temperature there will be a fall in gas turbine efficiency and power output to the equivalent of 0.07% and 1.47 MW respectively. Ashley et al.[156]. This method can also theatrically be used in closed cycles. Several methods are in use such as evaporative cooling, mechanical, absorption chillers, and or ice thermal storage Dincer et al.[157]. Gas turbine discharge temperature is an influential function of the ambient air temperature with its power output dropping by 0.5–0.9% for every 1 °C rise in ambient temperature Shukla et al.[158]. The economic study of gas turbine inlet air pre-cooling has shown a 23.4% financial return rate. Hence, the payback period is 4.2 years Ameri et al.[159]. The coupling of gas turbine inlet air pre-cooling system for a 100 MW Bryton cycle has been investigated and an 11% increase in power output was reported Mohanty et al.[160]. Different integrations with absorption cooling systems have been studied[161] [162][163][164][165]. Sherif et al.[166] presented the high-pressure regenerative turbine engine system combined with the absorption refrigeration which is capable of water extraction, work output improvement, and excess refrigeration. It was concluded that the maximum obtained efficiency will be 46% and estimated that 1.5 kg of water for one kg of fuel consumption will be extracted.

Integration of refrigeration cycles with SCDC has also been studied. Fan et al.[167] designed combined cooling, heating, and power system by combining a recompression SCDC with an ejector-based R134a simultaneous heating and cooling system. An increase in both the first and second law efficiency of the cycle was reported. Liang et al.[168] proposed a miniature CO_2 refrigeration cycle which is coupled with a simple SCDC to recovers the waste heat from the truck engine and convert it to a cooling effect. Li et al.[169] and Yang et al.[170] coupled Lithium Bromide and Ammonia absorption refrigeration cycle with recompression SCDC for combined cooling, heating, and power generation. Hafiz Ali Muhammad et al.[171] proposed an integrated system of power production and refrigeration cycles to reduce the power consumption for carbon capture and storage. The investigation on the utilization of the refrigeration cycle for improving the performance of the cycle is rare. Purjam et al.[172] designed a reheating, intercooler modified SCDC which used an R134a refrigeration cycle to increase the performance of the power cycle. The suction of the low-pressure compressor is cooled down by the power from the SCDC. However, the density of CO_2 before the compressor increased enough that overall performance was increased. They named their cycle forced cooling.

The motivation behind this study was based on filling this technology gap by using environmentally friendly refrigerants without using any external power. Lithium Bromide - Water absorption refrigeration was chosen. The high-temperature waste heat is not available and the target for forced cooling is not sub-zero.

2. Method and materials

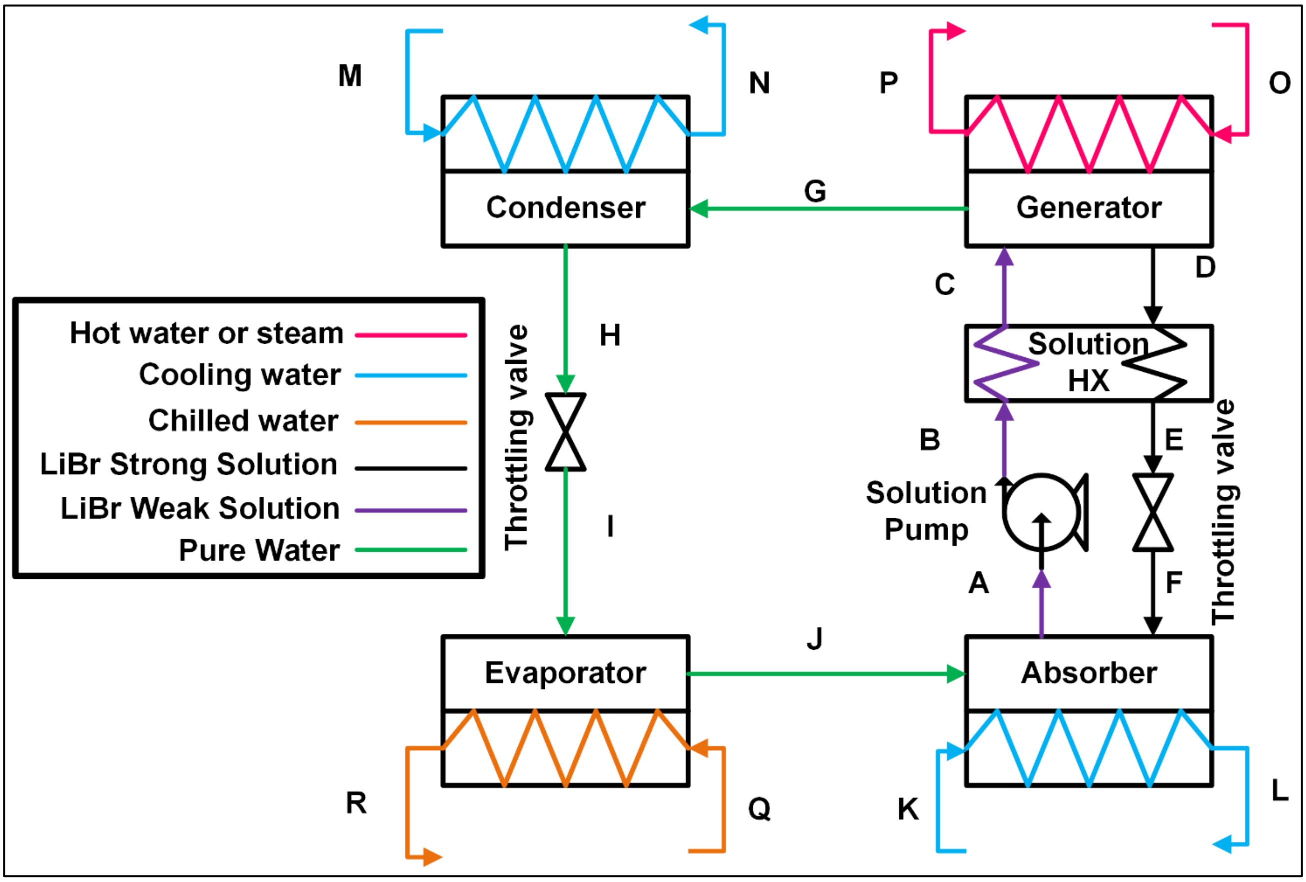

Fig. 76: Schematics of LiBr cycle

Fig. 76 shows the schematics of the LiBr cycle. The absorber is an isobaric vessel in which the warm strong solution interacts with the water vapor and absorbs water to itself and becomes the weak solution. This process requires cooling water because the absorption of lithium bromide in water is exothermic. The solution pump increases the pressure of the weak solution to the top pressure of the cycle in an adiabatic process. The solution heat exchanger is isobaric on both sides. The hot strong solution pre-heats cold weak solution. The generator is an isobaric vessel in which the weak solution is heated up by the hot source and water vapor is generated from the solution. Hot strong solution and steam leave the generator. Water vapor in the condenser, lose its heat and condense back to saturated liquid. In the evaporator, cold 2-phase water absorbs heat from the cold space and completely evaporates. There are two throttling valves. They reduce the pressure from top to bottom in an isenthalpic process. The thermophysical properties of the LiBr solution were extracted from [173]. This reference includes the equilibrium saturated solution pressure, temperature, specific isobaric heat capacity, specific enthalpy, specific entropy, and density. The crystallization temperature of the solution was extracted from [174].

The quality of vapor in a 2-phase vapor solution is determined by these 3 equations. These equations sometimes are called the flushing equation.

$$m_{total}h_{total}(T_{total}, z, P) - m_{sol}h_{sol}(T_{sol}, x, P) - m_{vapor}\left[h_{g,water}(P) - \frac{\delta H}{\delta m_{water}}(T_{sol}, x, P)\right] = 0 \tag{50}$$

$$\frac{\delta H}{\delta m_{water}}(T_{sol}, x, P) = h_{g,water}(P) - T_{sol}\left(v_{g,water}(P) - \frac{\delta V(T_{sol}, x)}{\delta m_{water}}\right)\frac{\delta P(T_{sol}, x)}{\delta T} \tag{51}$$

$$\frac{\delta V(T_{sol}, x)}{\delta m_{water}} = \frac{1}{\rho_{LiBr}(T_{sol}, x)}\left[1 + \frac{x}{\rho_{LiBr}(T_{sol}, x)}\frac{\delta \rho_{LiBr}(T_{sol}, x)}{\delta X}\right] \tag{52}$$

The solution is considered to be incompressible. In all cycles, the heat loss, friction loss and bubbling, condensation, and gravitational effects were negligible.

Table 13: LiBr governing equations

Component	Equations
Condenser	$T_H = \Delta T_{app} + T_M$ $P_H = P_{sat}(Water, T_H)$ $h_H = h@(Water, T_H, qu = 0)$
Evaporator	$T_J = T_M - \Delta T_{app}$ $P_J = P_{sat}(Water, T_J)$ $h_J = h@(Water, T_J, qu = 1)$ $mass\,flow\,ratio = \frac{h_J - h_I}{h_R - h_Q}$ $Q_{eva} = \dot{m}_J(h_J - h_I)$
Pressure equilibrium	$P_A = P_F = P_I = P_H$ $P_B = P_C = P_D = P_E = P_G = P_H$
Concentration equilibrium	$x_A = x_B = x_C = z_C$ $x_D = x_E = z_F$
Absorber	$T_A = \Delta T_{app} + T_K \quad x_A = x@(T_A \& P_A)$ $h_A = h@(T_A \& x_A) \quad \rho_A = \rho@(T_A \& x_A)$ $\dot{m}_A = \dot{m}_F + \dot{m}_J \quad \dot{m}_A x_A = \dot{m}_F z_F$ $Q_{abs} = \dot{m}_F h_F + \dot{m}_J h_J - \dot{m}_A h_A$
Pump	$w_{pump} = \frac{(P_B - P_A)}{\rho_A \eta_{pump}} \quad h_B = h_A + w_{pump}$ $T_B = T@(x_B, h_B) \quad c_{p,B} = c_p@(T_B \& x_B)$

Generator	$T_D = T_O - \Delta T_{app} \quad x_D = x@(T_D \& P_D)$ $h_D = h@(T_D \& x_D) \quad T_G = T_D (Small\ Generator\ Model)$ $T_G = \frac{T_C + T_D}{2}\ (Large\ Generator\ Model)$ $\dot{m}_C = \dot{m}_D + \dot{m}_G \quad \dot{m}_C z_C = \dot{m}_D x_D \quad h_G = h_{water}@(P_G \& T_G)$ $Q_{gen} = \dot{m}_G h_G + \dot{m}_G h_G - \dot{m}_C h_C$ $c_{p,D} = c_p@(T_D \& x_D)$
Solution HX	$C_D = \dot{m}_D c_{p,D}\ C_B = \dot{m}_B c_{p,B}$ $If\ C_B > C_D: Q_{max} = \dot{m}_D (h_D - h@(x_E, T_B))$ $If\ C_B < C_D: Q_{max} = \dot{m}_B (h@(x_C, T_D) - h_B)$ $\lambda_{LiBr} = \frac{\dot{m}_B (h_C - h_B)}{Q_{max}} = \frac{\dot{m}_D (h_D - h_E)}{Q_{max}}$
Throttling	$h_J = h_I$ $h_E = h_F$
COP	$COP = \frac{Q_{eva}}{Q_{gen} + \dot{m}_A w_{pump}}$

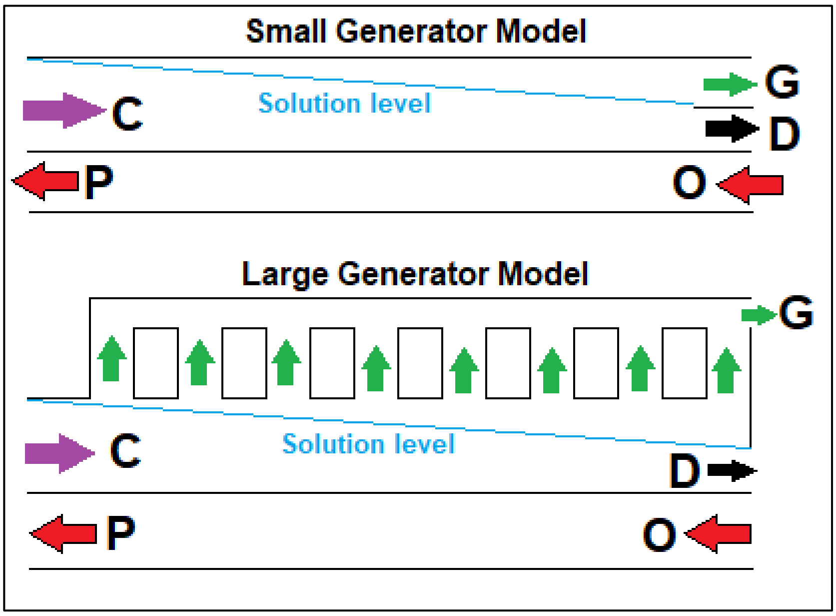

Fig. 77: Vapor generator models in LiBr

Fig. 77 visualizes the Generator model. A small model is used for validation of results and comparing them with conventional LiBr. However, the large model is coupled with the SCDC. For ordinary use, the generator size is chosen as small. It means that the generated water vapor still moves inside the tubes and receives the heat. This means that the vapor steals heat from the generator. But for large capacities, a large generator will be used. It allows the vapor to escape at every stage and does not carry extra heat with itself.

At this stage, the mass flow rate of the LiBr is not important because it has independence from mass and geometry. The mass flow rate inside the evaporator is chosen as 1 and the rest of the cycle will be solved instantly.

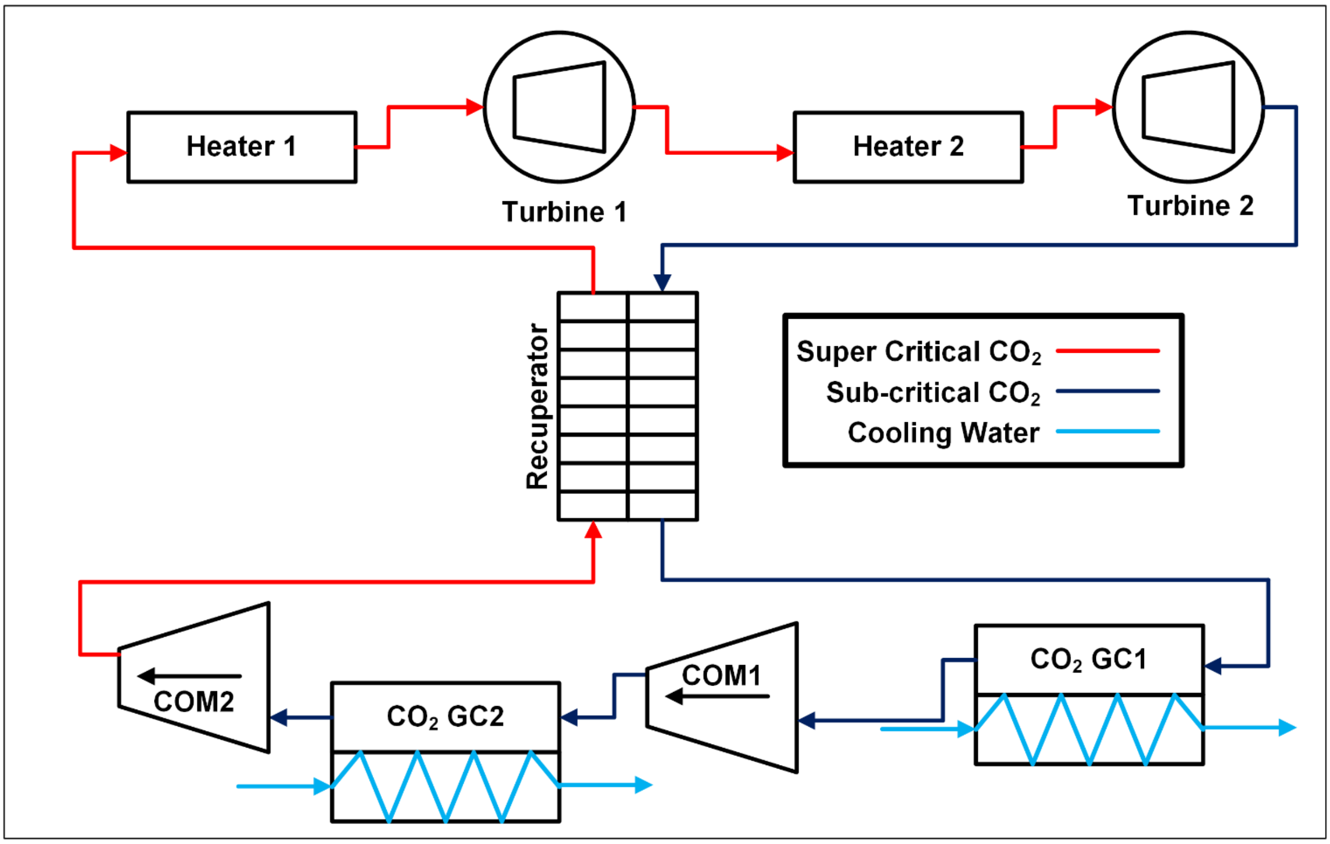

Fig. 78: Schematics of Layout A without LiBr

Two different layouts of SCDC were selected. Layout A is from [172]. This layout does not possess the highest efficiency, but it has a high-temperature gas cooler which gives it a great potential for waste heat recovery, and also it has a very high power-to-mass-ratio which makes it a good candidate for land, marine, and space vessels. Layout B is a conventional recompression cycle with single reheating. This is an already accepted design with high thermal efficiency.

Compressors and pumps increase the pressure of the fluid by consuming the work in an adiabatic process. The difference between them is the dryness of their suction. Pumps work in saturated liquid and sub-cooled states. Every other state belongs to the compressors. In a 2-phase region, a flash chamber must be used to separate the vapor and liquid. The isentropic efficiency of both is the same. Turbines convert the energy of the fluid to work by reducing its pressure and temperature. The process is adiabatic. Heaters increase the temperature of the fluid in an isobaric process. They can be nuclear reactors, solar receivers, external burners, or oxy-fuel torches.

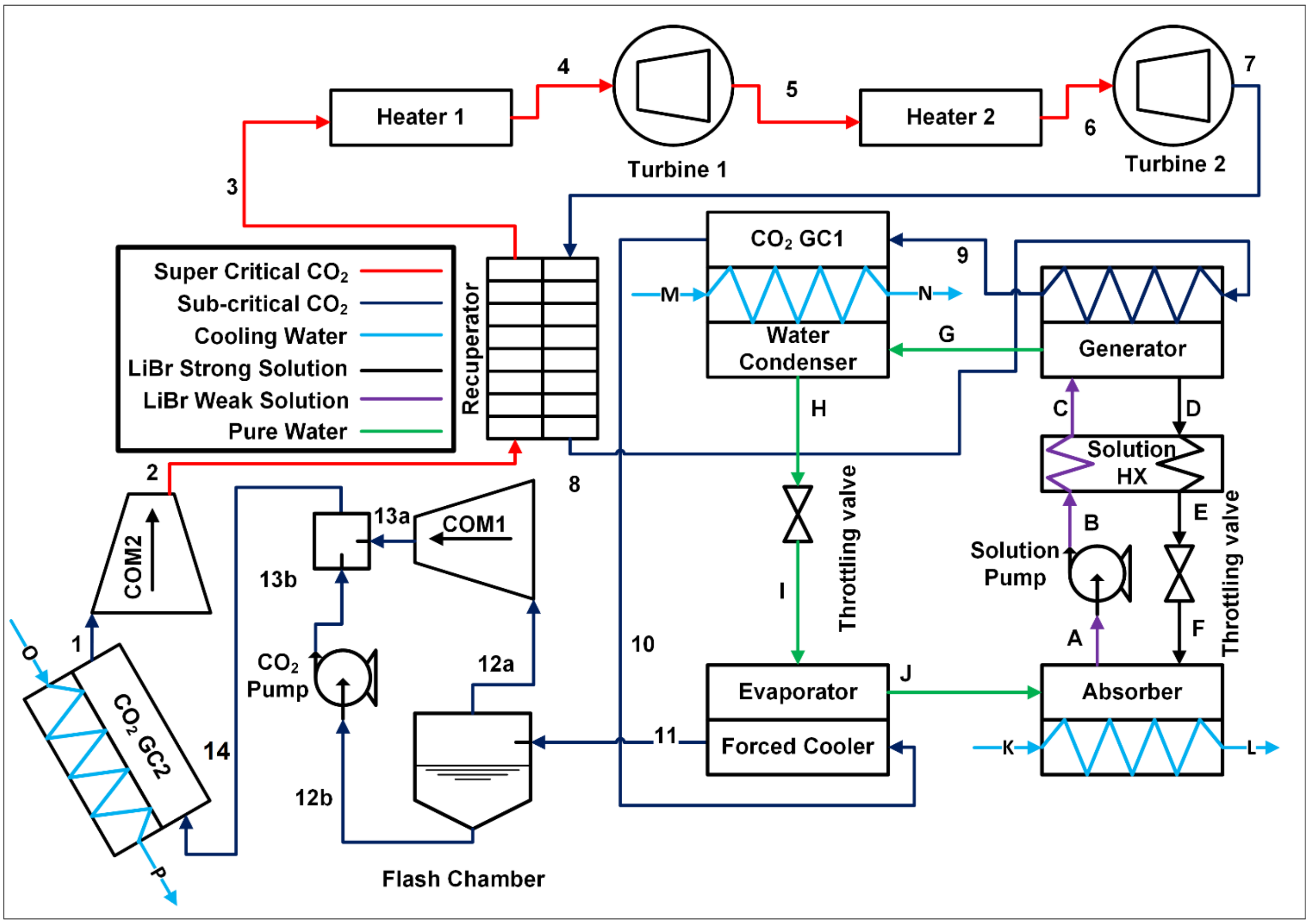

Fig. 79: Schematics of layout A with LiBr

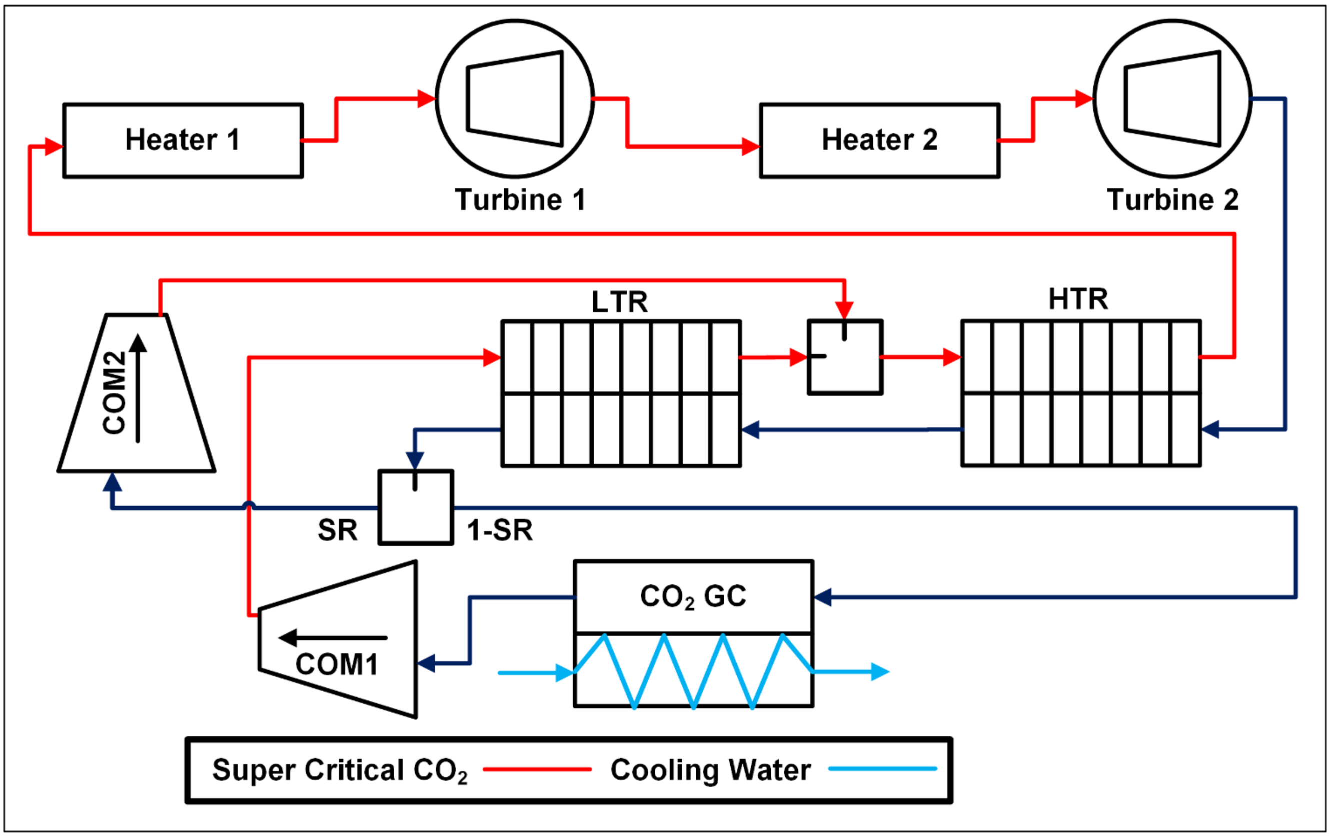

Fig. 80: Schematics of layout B without LiBr

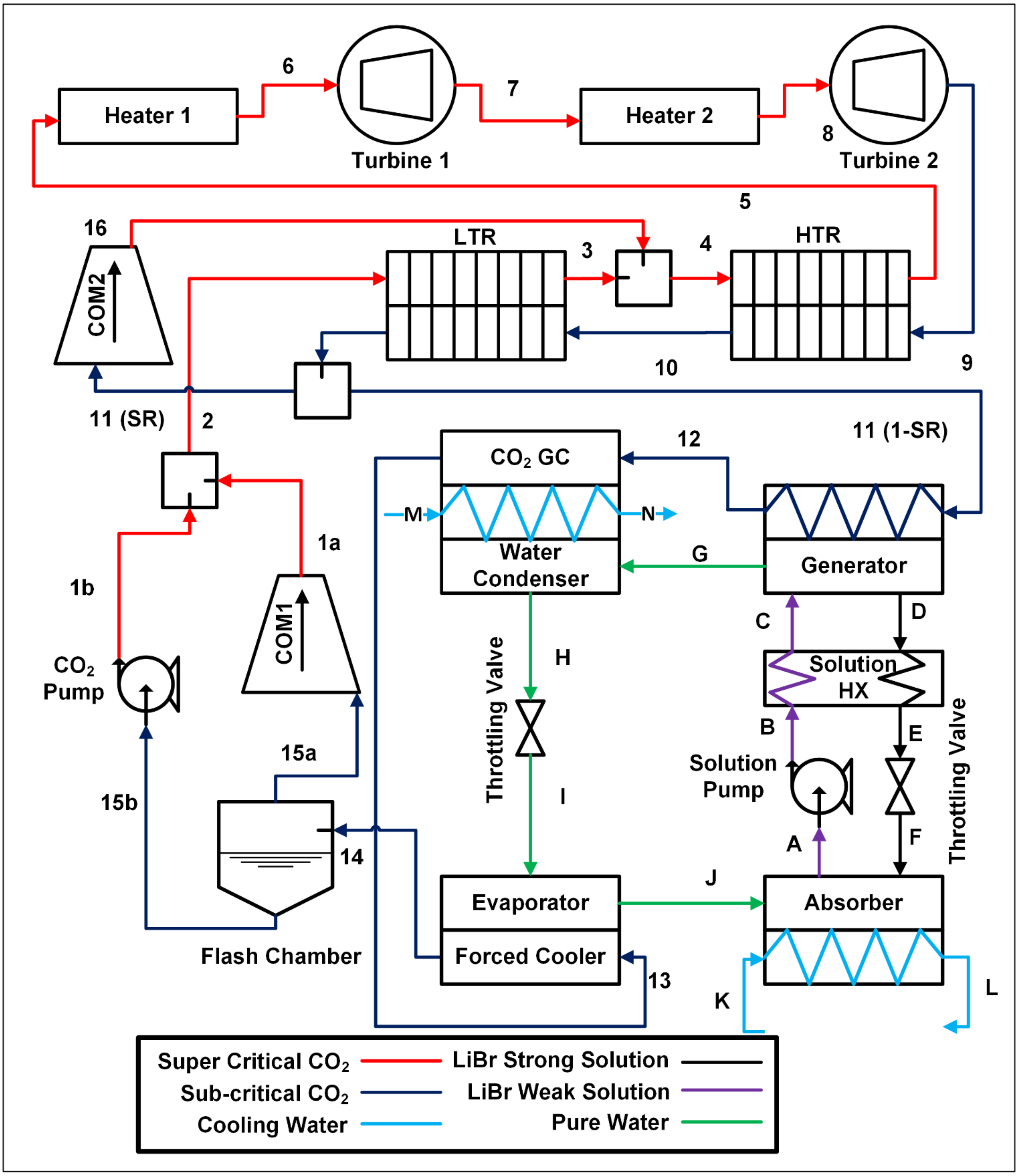

Fig. 81: Schematics of layout B with LiBr

Recuperators are heat exchangers that transfer the heat from the hot side to the cold side. Gas coolers are isobaric devices that reduce the temperature of the fluid. They do not condense the gas. The hot gas enters the generator and provides energy for the LiBr cycle. The forced cooler is a heat exchanger which reduces the temperature of the working fluid under the ambient temperature. The Flash chamber and separator divide the fluid into two parts. The difference is flash chamber separates the vapor from liquid, but the separator separates fluid into specific ratios. The mixer also mixes the fluid. All the mentioned components are isobaric.

The effectiveness of the generator and forced cooler is 1 but the recuperator is different. The equations the same as (36) and (37) are expected.

If the cold side heat capacity rate is higher.

$$Q_{max} = \dot{m}_{hot\ side}\left(h_{in,hot\ side} - h(T_{in,cold\ size}\&P_{in,hot\ side})\right) \tag{53}$$

If the heat capacitance rate on the hot side is higher.

$$Q_{max} = \dot{m}_{cold\ side}\left(h\left(T_{in,hot\ side}\&P_{in,cold}\right) - h_{in,cold\ side}\right) \tag{54}$$

Another important factor that must be extracted from the LiBr is the bypass heat transfer rate.

$$\Gamma = \frac{Q_{eva}}{Q_{gen}} \tag{55}$$

It indicates that if 1 unit of heat from the fluid is released to the LiBr how much heat will be extracted from it in the forced cooler.

Another important factor that must be extracted from the LiBr is the bypass heat transfer rate.

$$\Gamma = \frac{Q_{eva}}{Q_{gen}} \tag{56}$$

Table 14: Layout A with LiBr governing equations (Equations from Table 13 excluded)

Component	Mass balance	Energy Balance
Turbine 1	$\dot{m}_4 = \dot{m}_5$	$w_{tur1} = (h_4 - h@(P_5, s_4))\eta_{tur}\eta_{el}$
Turbine 2	$\dot{m}_6 = \dot{m}_7$	$w_{tur2} = (h_6 - h@(P_7, s_6))\eta_{tur}\eta_{el}$
Compressor 1	$\dot{m}_{12a} = \dot{m}_{13a}$	$w_{COM1} = \frac{h(P_{13a}, s_{12a}) - h_{12a}}{\eta_{COM}}$
Compressor 2	$\dot{m}_1 = \dot{m}_2$	$w_{COM2} = \frac{h(P_2, s_1) - h_1}{\eta_{COM}}$
Pump	$\dot{m}_{12b} = \dot{m}_{13b}$	$w_{PU} = \frac{h(P_{13b}, s_{12b}) - h_{12b}}{\eta_{PU}}$
Heater 1	$\dot{m}_3 = \dot{m}_4$	$q_{ht1} = (h_4 - h_3)$
Heater 2	$\dot{m}_5 = \dot{m}_6$	$q_{ht2} = (h_7 - h_6)$
Generator Forced Cooler	$\dot{m}_8 = \dot{m}_9$ $\dot{m}_{10} = \dot{m}_{11}$	$h_{10} - h_{11} = \Gamma(h_8 - h_9)$
Water CON CO_2 GC1	$\dot{m}_M = \dot{m}_N$ $\dot{m}_G = \dot{m}_H$ $\dot{m}_9 = \dot{m}_{10}$	$\dot{m}_N h_N + \dot{m}_9 h_9 + \dot{m}_G h_G = \dot{m}_M h_M + \dot{m}_H h_H + \dot{m}_{10} h_{10}$
CO_2 GC1	$\dot{m}_{14} = \dot{m}_1$	$q_{GC2} = h_{14} - h_1$
Flash chamber	$\dot{m}_{11} = \dot{m}_{12a} + \dot{m}_{12b}$	$h_{11} = qu_{11}h_{12a} + (1 - qu_{11})h_{12b}$
Recuperator	$\dot{m}_2 = \dot{m}_3$ $\dot{m}_7 = \dot{m}_8$	$\lambda Q_{max} = h_3 - h_2 = h_7 - h_8$
Mixer	$\dot{m}_{14} = \dot{m}_{13a} + \dot{m}_{13b}$	$h_{14} = qu_{11}h_{13a} + (1 - qu_{11})h_{13b}$

Table 15: Layout B with LiBr governing equations (Equations from Table 13 excluded)

Component	Mass balance	Energy Balance
Turbine 1	$\dot{m}_6 = \dot{m}_7$	$w_{tur1} = (h_6 - h@(P_7, s_6))\eta_{tur}\eta_{el}$

Turbine 2	$\dot{m}_8 = \dot{m}_9$	$w_{tur2} = (h_8 - h@(P_9, s_8))\eta_{tur}\eta_{el}$
Compressor 1	$\dot{m}_{15a} = \dot{m}_{1a}$	$w_{COM1} = (1 - SR) * q_{14}\dfrac{h(P_{1a}, s_{15a}) - h_{15a}}{\eta_{COM}}$
Compressor 2	$\dot{m}_{11} * SR = \dot{m}_{16}$	$w_{COM2} = SR\dfrac{h(P_{16}, s_{11}) - h_{11}}{\eta_{COM}}$
Pump	$\dot{m}_{15b} = \dot{m}_{1b}$	$w_{PU} = (1 - SR)(1 - q_{14})\dfrac{h(P_{1b}, s_{15b}) - h_{15b}}{\eta_{PU}}$
Heater 1	$\dot{m}_5 = \dot{m}_6$	$q_{ht1} = (h_6 - h_5)$
Heater 2	$\dot{m}_7 = \dot{m}_8$	$q_{ht2} = (h_7 - h_6)$
Generator Forced Cooler	$\dot{m}_{11} * SR = \dot{m}_{12}$ $\dot{m}_{13} = \dot{m}_{14}$	$h_{13} - h_{14} = \Gamma(h_{11} - h_{12})$
Water CON CO_2 GC1	$\dot{m}_M = \dot{m}_N \;\; \dot{m}_G = \dot{m}_H$ $\dot{m}_{12} = \dot{m}_{13}$	$\dot{m}_N h_N + \dot{m}_{12}h_{12} + \dot{m}_G h_G = \dot{m}_M h_M + \dot{m}_H h_H + \dot{m}_{13}h_{13}$
Flash chamber	$\dot{m}_{14} = \dot{m}_{15a} + \dot{m}_{15b}$	$h_{14} = qu_{14}h_{15a} + (1 - qu_{14})h_{15b}$
LTR	$\dot{m}_2 = \dot{m}_3 \quad \dot{m}_{10} = \dot{m}_{13}$	$\lambda Q_{max,LTR} = \dot{m}_2(h_3 - h_2) = \dot{m}_{10}(h_{10} - h_{11})$
HTR	$\dot{m}_4 = \dot{m}_5 \quad \dot{m}_9 = \dot{m}_{10}$	$\lambda Q_{max,HTR} = h_5 - h_4 = h_9 - h_{10}$
Separator	$\dot{m}_{11} = (1 - SR)\dot{m}_{11} + SR * \dot{m}_{11}$	$h_{11} = SR * h_{11} + (1 - SR)h_{11}$
Mixer 1	$\dot{m}_4 = \dot{m}_{16} + \dot{m}_3$	$h_3 = SR * h_{16} + (1 - SR)h_3$
Mixer 2	$\dot{m}_{14} = \dot{m}_{13a} + \dot{m}_{13b}$	$h_2 = qu_{11}h_{13a} + (1 - qu_{11})h_{13b}$

The mass ratio between the LiBr and SCDC can be calculated by:

$$\theta = \frac{\dot{m}_{LiBr}}{\dot{m}_{SCDC}} = \frac{\Delta h_{Forced\ Cooler}}{\Delta h_{Eva}} \tag{57}$$

The thermal efficiency of the layout A:

$$\eta_{thermal} = \frac{w_{tur1} + w_{tur2} - qu_{11}w_{COM1} - (1 - qu_{11})w_{COM2} - w_{COM2} - \theta\dot{m}_A w_{PU,LiBr}}{q_{ht1} + q_{ht2}} \tag{58}$$

The thermal efficiency of the layout B:

$$\begin{aligned}\eta_{thermal} = [&w_{tur1} + w_{tur2} - qu_{11}(1 - SR) * w_{COM1} - (1 - qu_{11})(1 - SR) * w_{PU} \\ &- SRw_{COM2} - (1 - SR)\theta\dot{m}_A w_{PU,LiBr}]/(q_{ht1} + q_{ht2})\end{aligned} \tag{59}$$

In the calculations, it was found that the solution pump work can be neglected. LMTD method UA factor gives some estimations about the possible size of the cycle. In this regard, the mass flow rate of the cycle is required. One of the strategies is to find the mass flow rate per some capacity. For this study capacity of 1 MWatt was chosen.

$$\dot{m} = \frac{1000}{w_{net}} \tag{60}$$

3. Results and discussions

3.1. Validation of LiBr simulation

Aphornratana S. and Sriveerakul T. (2007) [175] were used to validate the simulation of LiBr. According to [175] the isentropic efficiency of the solution pump is 0.8 and the effectiveness of the solution heat exchanger is 0.8.

Solution Circulation ratio (SCR) is the mass flow ratio of the weak solution to the steam. In Fig. 82 to Fig. 85 the SCR of the experimental result is much higher than the simulation because at real condition mass transfer rate of steam to the solution is much slower than the thermodynamic models. In fig. 84 the simulation results are similar but in the other three graphs, the differences are notable even if the exact temperature profiles are followed. Instead, the Lithium Bromide concentration of reference was put in the simulation, and results were analyzed. This COP is called COP_x. COPx shows the exact results except for lower generation temperatures and higher absorption and condensation temperatures.

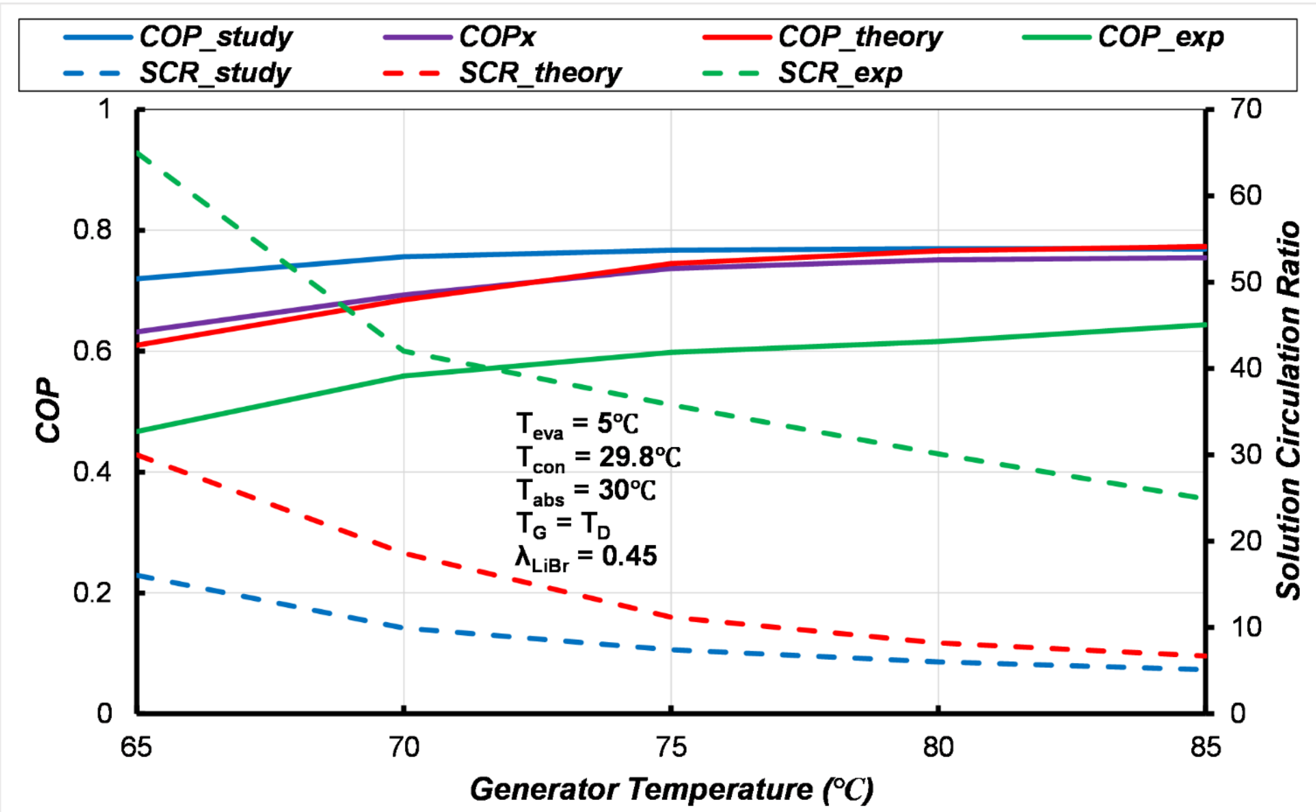

Fig. 82: Comparison of [175] with the LiBr simulation at different generator temperatures.

In the reference model, the effectiveness of the heat exchanger model depends on the SCR. But in this study the effectiveness is constant. So those differences are explained by this. Fig. 86 to Fig. 89 present the difference between the input temperature of the reference cycle to its real temperatures. This graph was used to find the temperature differences and approach temperatures in the reference.

Understanding all those temperature differences the code was revised and Fig. 90 was drawn which shows the parametric analysis of the LiBr versus generator and evaporator temperature which has the same COP as [175].

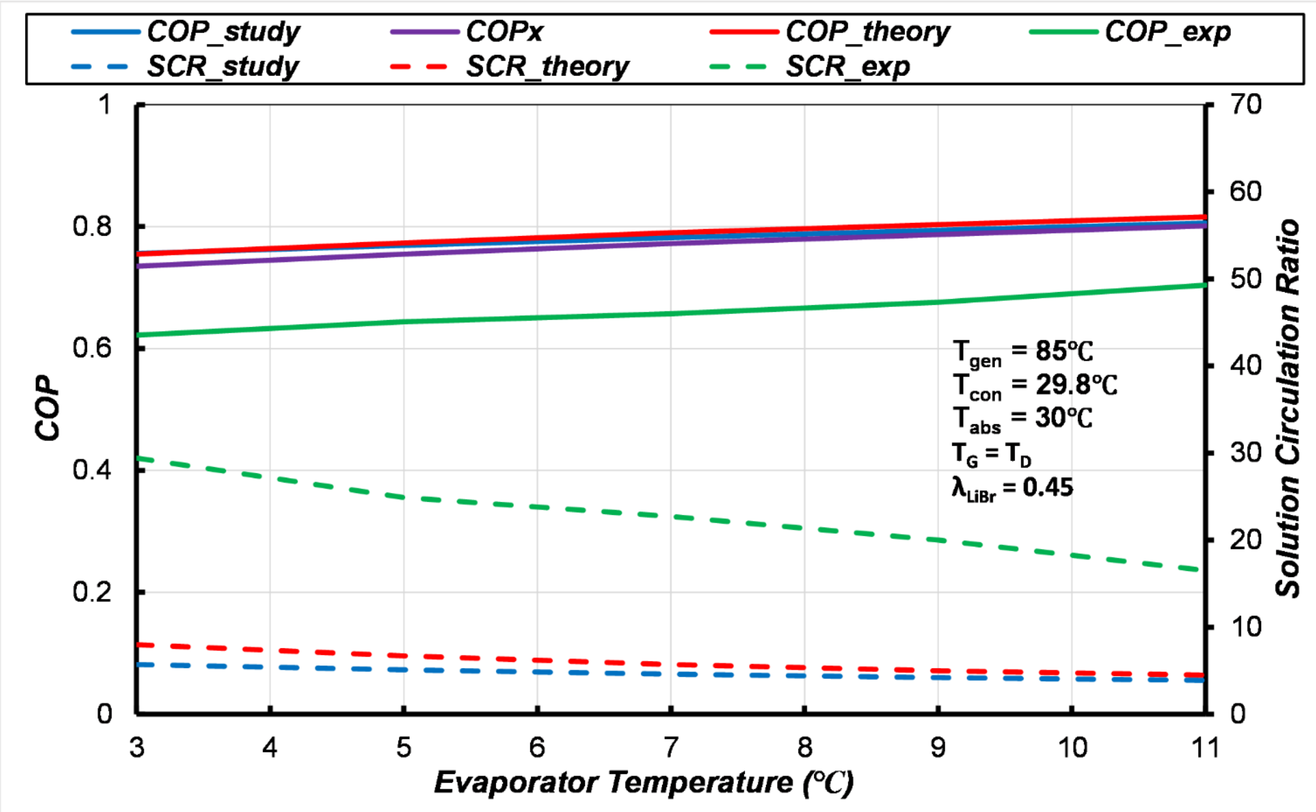

Fig. 83: Comparison of [175] with the LiBr simulation at different evaporator temperatures.

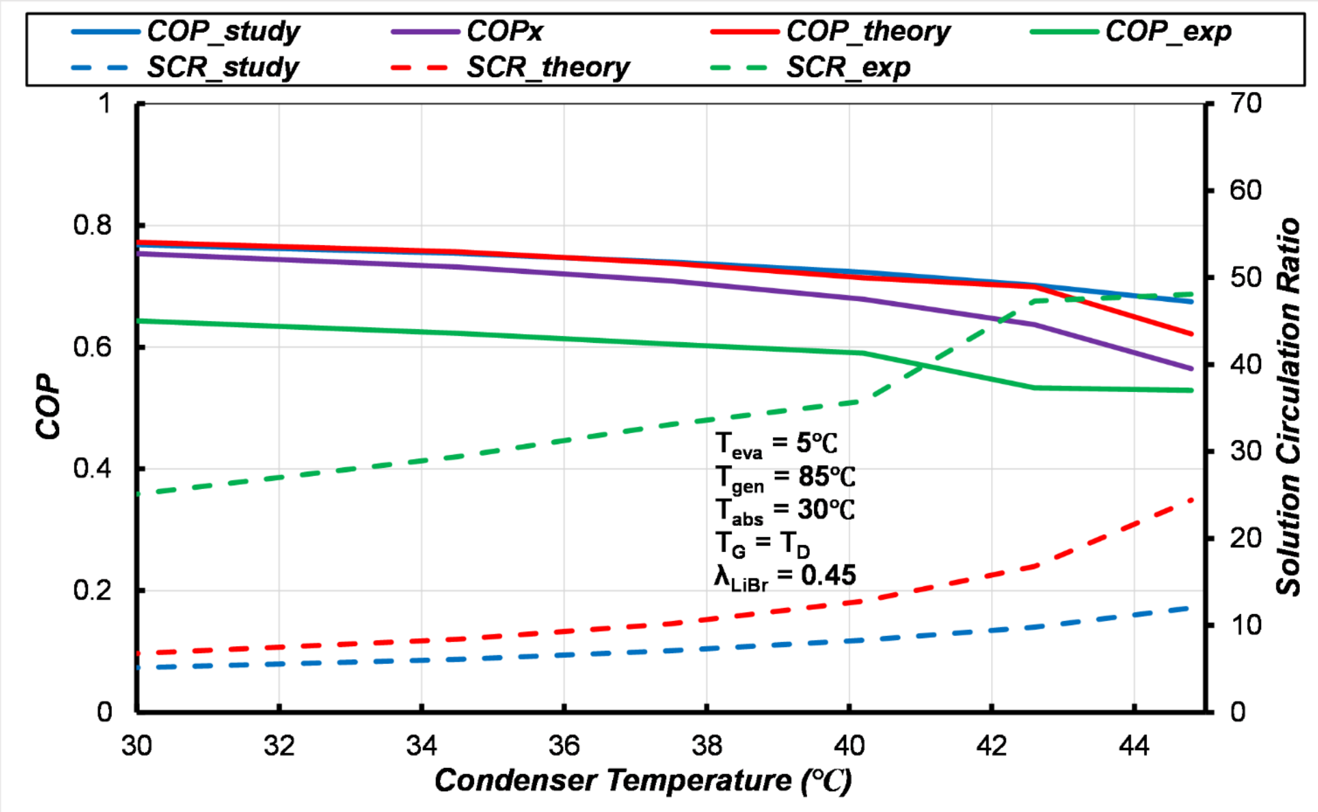

Fig 84: Comparison of [175] with the LiBr simulation at different condenser temperatures.

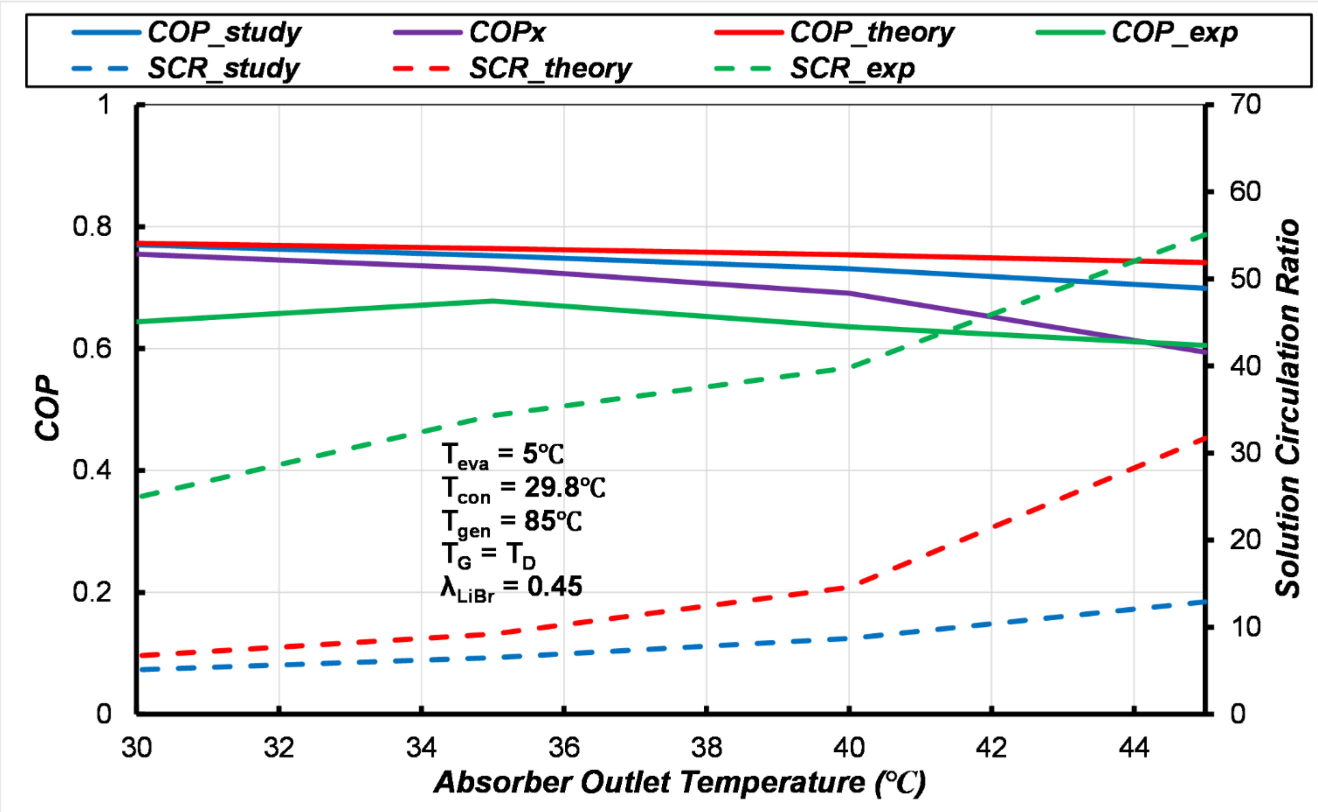

Fig 85: Comparison of [175] with the LiBr simulation at different absorber temperatures.

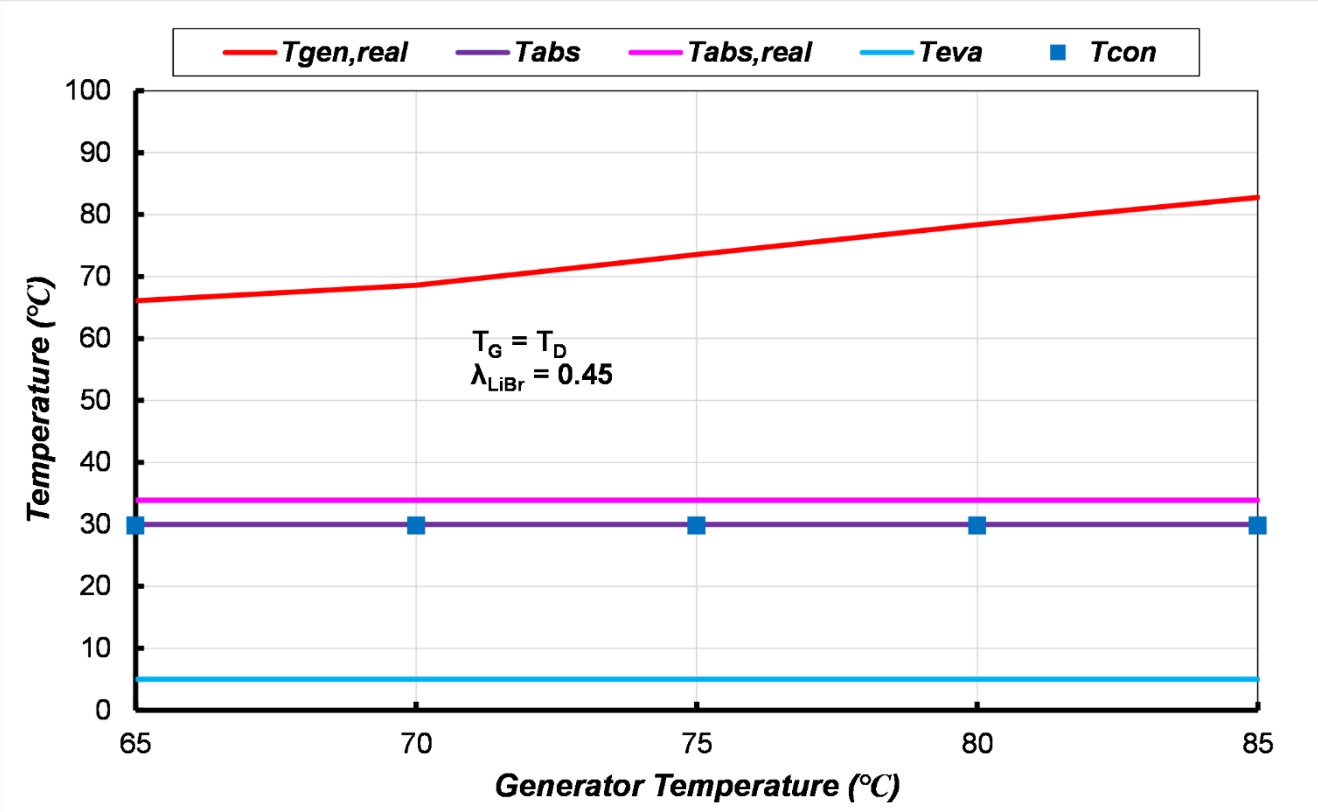

Fig. 86: Comparison of [175] with the LiBr simulation at different generator temperatures. [Temperature based]

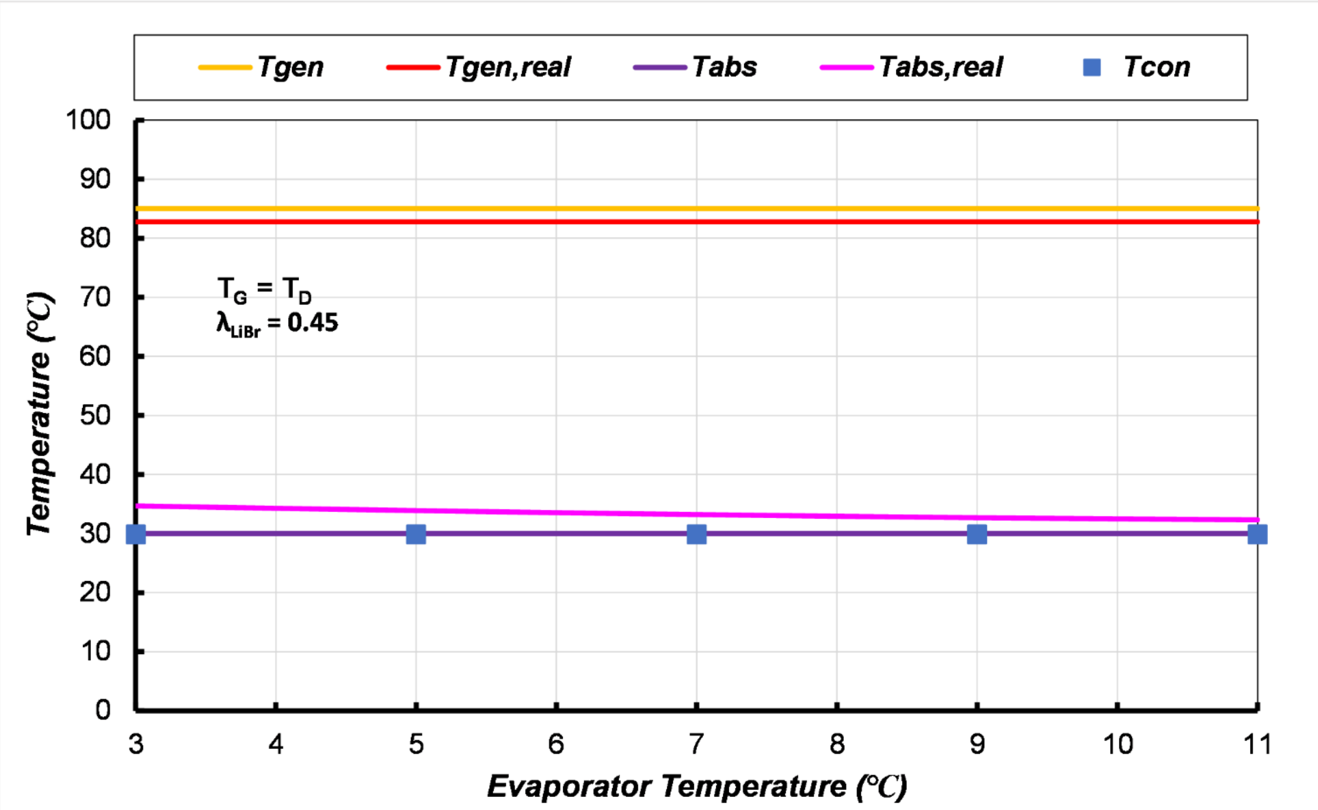

Fig. 87: Comparison of [175] with the LiBr simulation at different evaporator temperatures. [Temperature based]

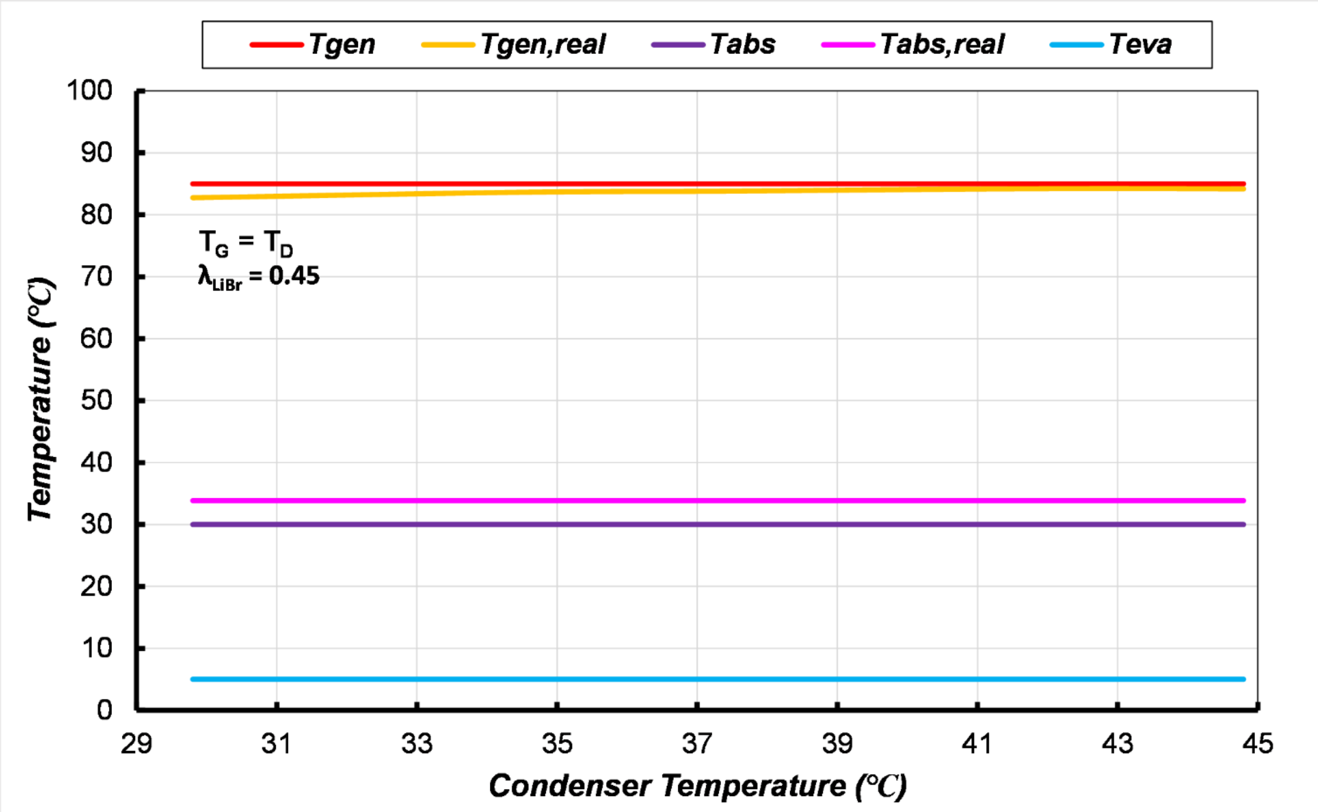

Fig. 88: Comparison of [175] with the LiBr simulation at different condenser temperatures. [Temperature based]

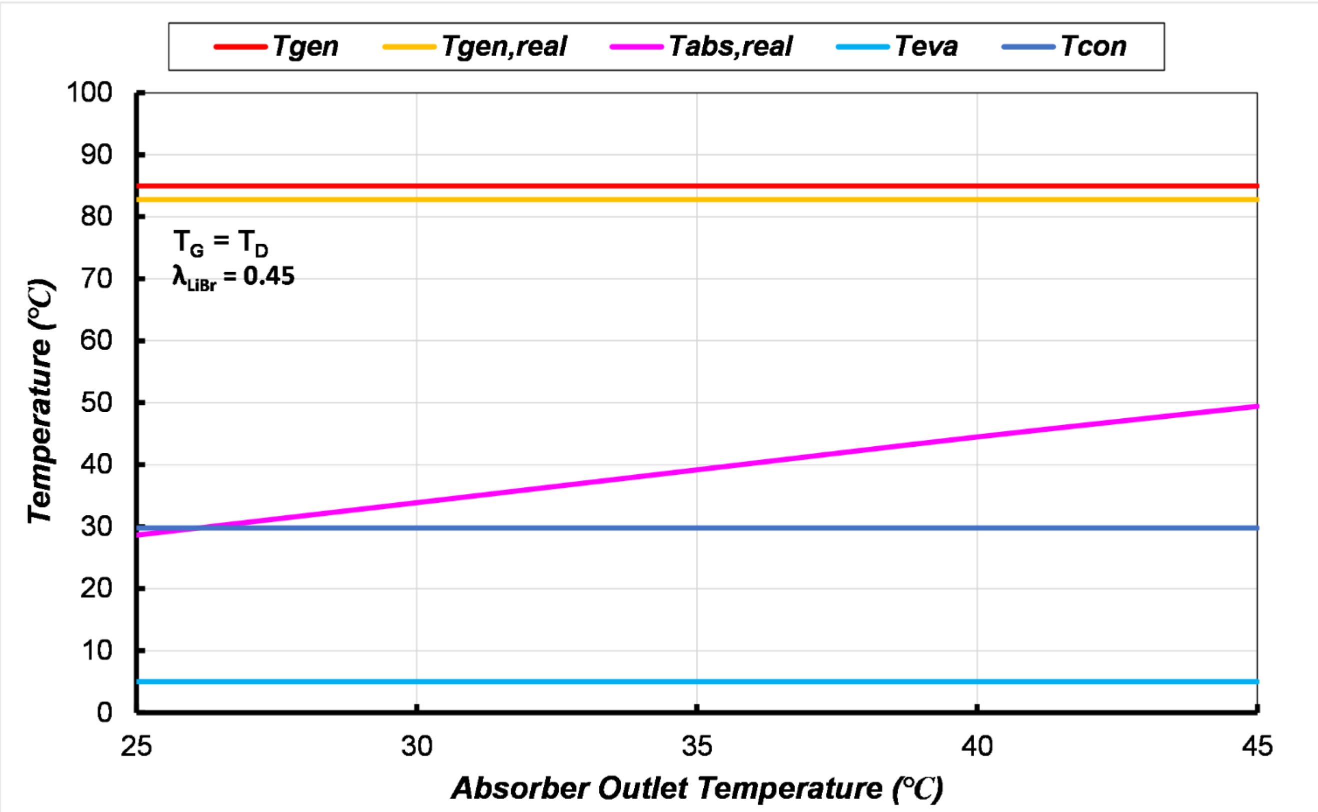

Fig. 89: Comparison of [175] with the LiBr simulation at different absorber temperatures. [Temperature based]

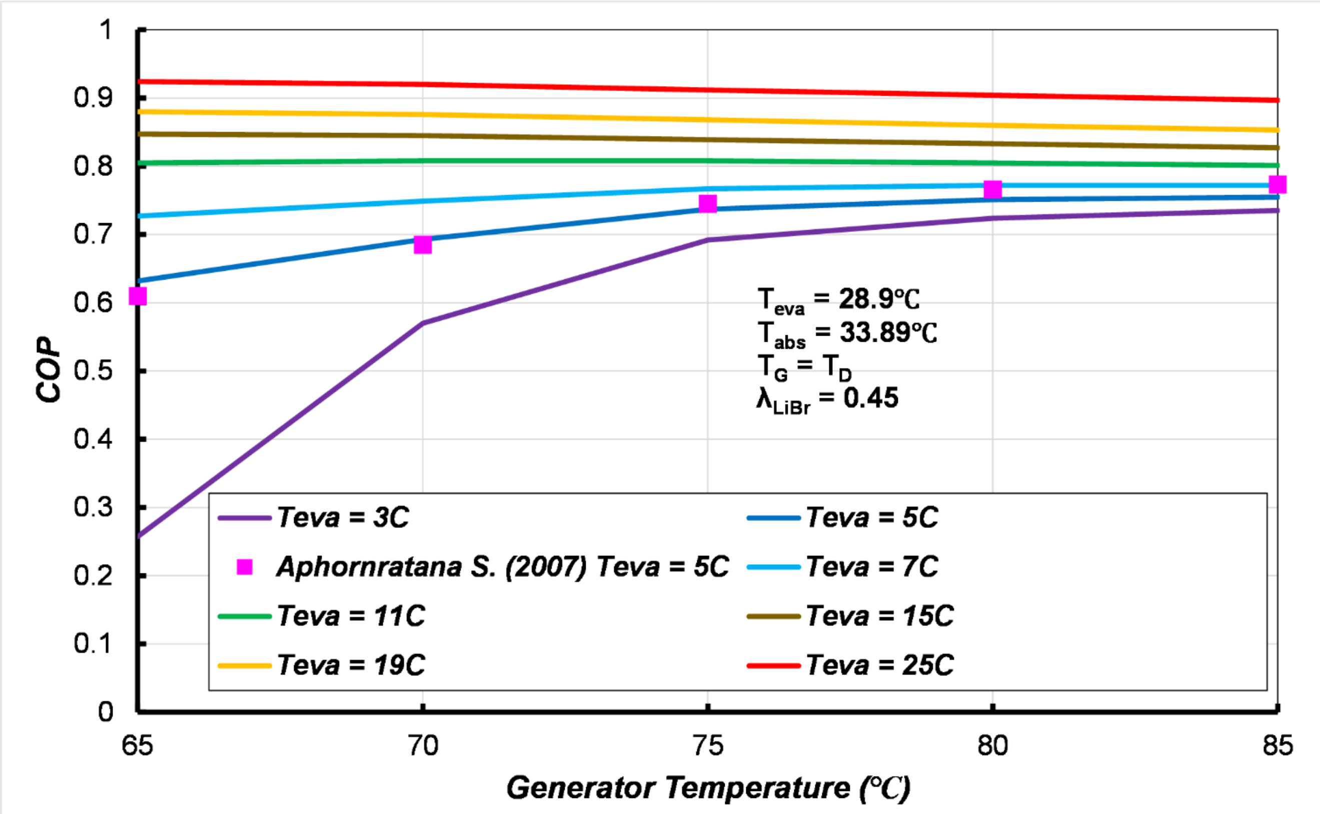

Fig. 90: Parametric analysis of normal LiBr cycle based on generator temperature

3.2. Modeling the LiBr to be integrated with SCDC

After the validation of the results, the LiBr cycle was modified to be used beside the SCDC. Fig. 91 shows the results. The absorber and condenser outlet temperatures are suggested to be similar because the size and economical value of the systems are increased. 32°C is selected based on [176]. The large size model for the generator was selected.

Fig. 90 and Fig.91 show a unique trend. At high evaporation temperatures, the optimum generator inlet temperature decreased. It is valuable when the LiBr is wanted to be coupled with the systems that only planned to be cooled down the fluid a few degrees under the ambient temperature and the high-temperature waste heat source is not available.

Fig. 92 illustrates the optimum COP and generator inlet temperature versus evaporation temperature. This data is used as a library to linearize the optimization algorithm. Fig. 93 is the widest operational range of the LiBr cycle in this study. As it can be seen crystallization is not going to be observed.

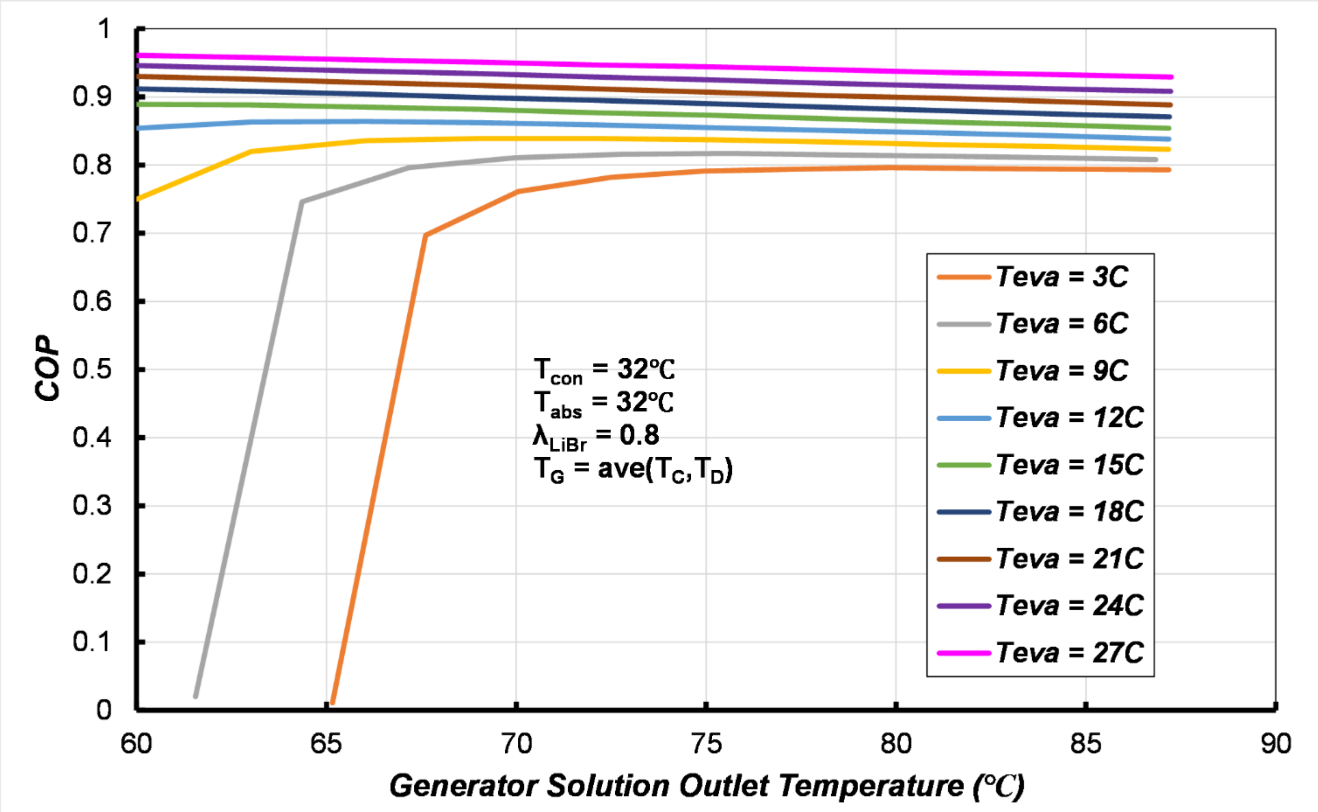

Fig. 91: Parametric analysis of LiBr cycle based on Generator

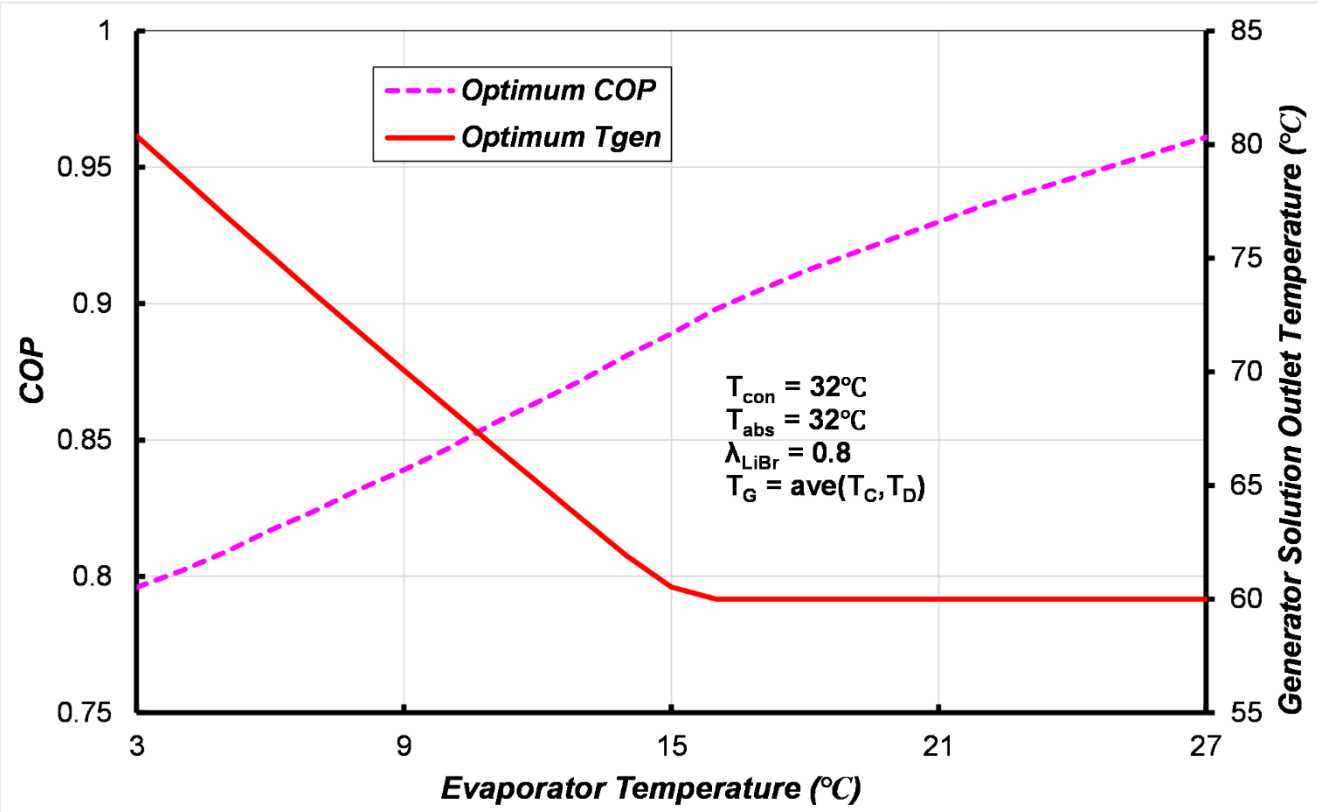

Fig. 92: COP and optimum generation temperature of LiBr cycle by evaporator temperature

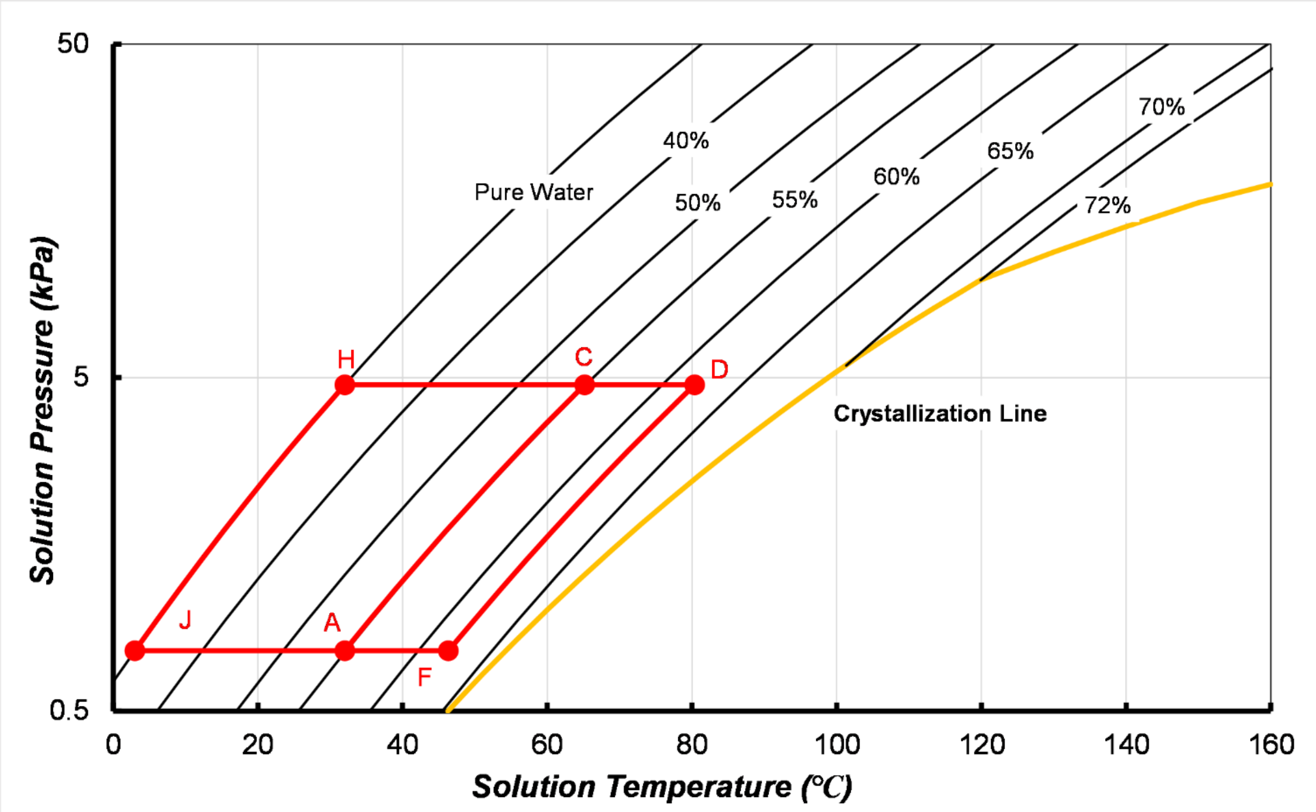

Fig. 93: Düring Diagram of LiBr cycle

3.3. Optimization algorithm and design parameter assumptions

The lowest possible temperature inside the cycles by means of natural cooling is 305.15 K. The maximum temperature inside the cycle is changing between 823.15 K to 1100 K. Maximum pressure is 25 MPa. The isentropic efficiencies of turbines and compressors and pumps are 0.93, 0.9, and 0.9[176]. The effectiveness of heat exchangers is 0.95 and the minimum approach temperature of 8 k[176]. Approach temperatures for forced cooler and generator are 5 degrees and for other places are 2.5 degrees. Two modes for LiBr were assumed. In full power mode, all possible heat is absorbed by the generator and maximum heat is harvested by the forced cooler. This mod is useful when the forced cooler is in the 2-phase region and full power can be utilized without upsetting the temperature profiles. In controlled power mod, the system tries to find optimum COP and avoids negative temperature slopes.

Fig. 94 and Fig. 95 are the program flowcharts of layout A and layout B respectively. The thermophysical properties of carbon dioxide were calculated was recalculated by calling REFPROP [89] libraries in Phyton. The “Conjugate Directions” method was chosen. This method seemed to be smoother and faster than other available methods.

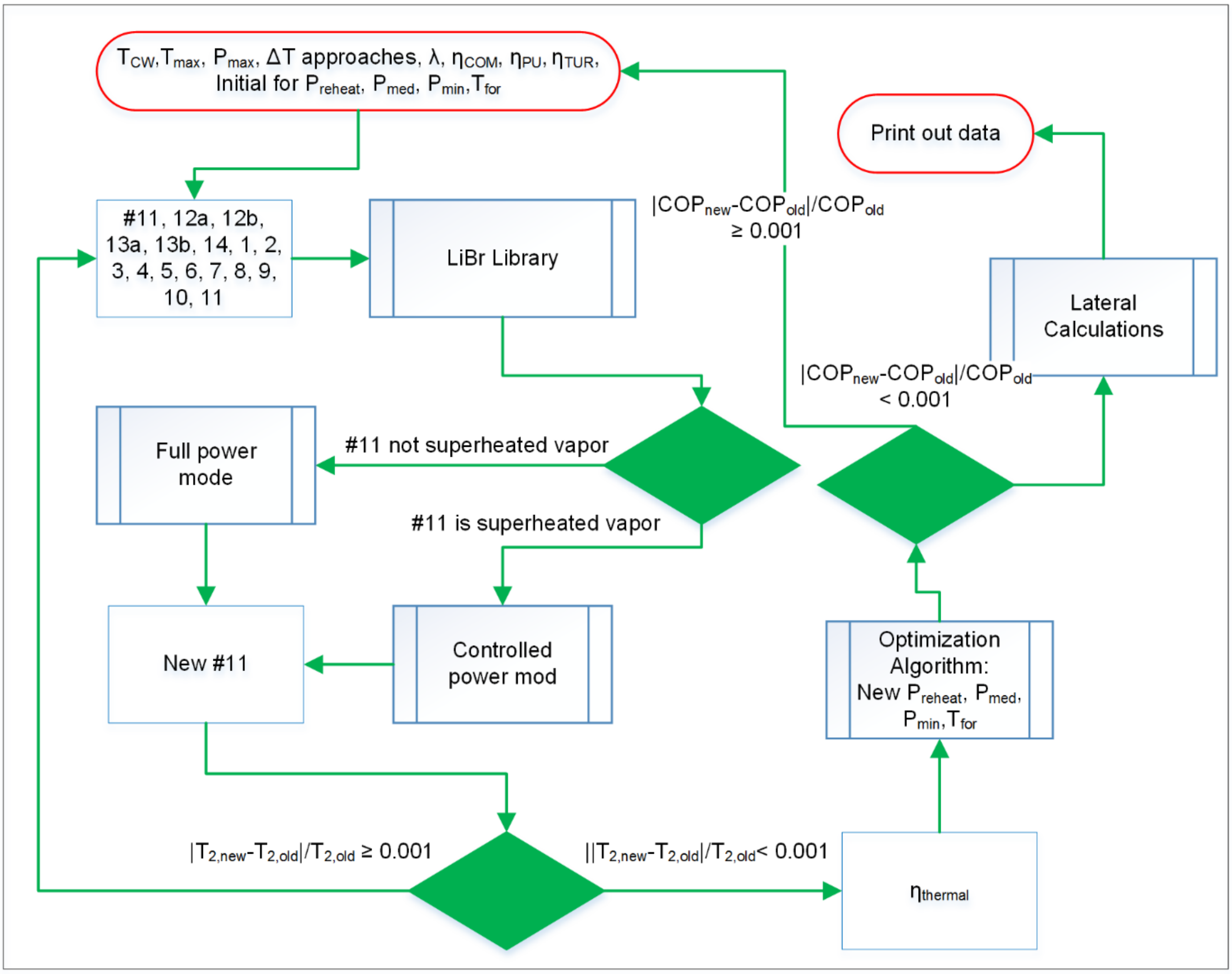

Fig. 94: programming flowchart of layout A

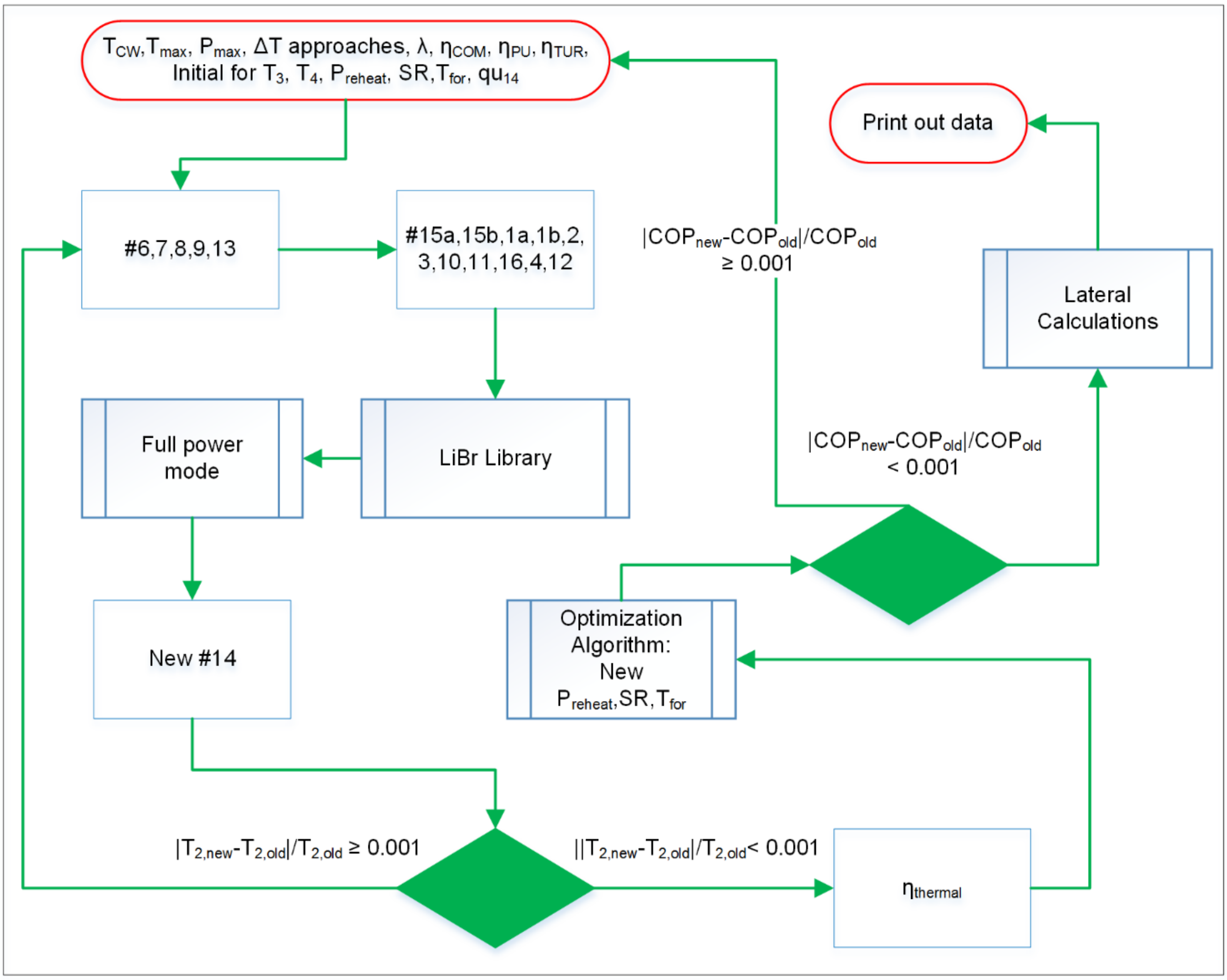

Fig. 95: programming flowchart of layout B

3.4. Layout A

Table 16 shows the thermodynamic properties of layout A with LiBr. The T-s and P-v diagram of Fig. 98 and Fig. 99 is based on table 16. The result for heater temperature of 823.15 is optimized.

Fig. 96 and Fig. 97 are the T-s and P-v diagrams of the single cycle (Fig. 78) with the same assumptions but different optimized values.

Fig. 100 shows the changes of thermal efficiency of the hybrid layout A to the maximum temperature of the cycle. The thermal efficiency of the single cycle and data from [172] are included. The results show that integration will significantly increase the performance of the cycle. This increase in performance is slightly reduced at high temperatures. The COP of LiBr remains constant because it works at its least possible temperature (3°C) and in all of the points the condensation of CO_2 happens.

Fig. 101 shows the mass flow rates of the cycle in hybrid layout A. Adding LiBr can slightly reduce the mass flow rate. Also, the mass flow rates of the LiBr are not noticeable. It can interpret that LiBr is not going to add large extra volume to the system.

Table 16: The thermodynamic properties of points in layout A with LiBr

State #	Specific Entropy (kJ/kg.K)	Temperature (K)	Specific Volume (m^3/kg)	Pressure (MPa)	Specific Enthalpy (kJ/kg)	Phase or Vapor quality
1	1.707	305.15	0.0045	6.795	413.2	Superheat
2	1.721	405.06	0.0021	25	470.3	Supercritical
3	2.336	618.47	0.0046	25	776.0	Supercritical
4	2.693	823.15	0.0065	25	1031.8	Supercritical
5	2.705	723.53	0.0122	11.296	922.0	Supercritical
6	2.860	823.15	0.014	11.296	1041.8	Supercritical
7	2.875	699.70	0.0329	4.021	903.9	Superheat
8	2.319	420.28	0.0186	4.021	598.2	Superheat
9	2.087	339.05	0.0137	4.021	510.6	Superheat
10	1.959	305.15	0.0112	4.021	469.5	Superheat
11	1.715	278.65	0.0076	4.021	399.8	0.8721
12a	1.813	278.66	0.0086	4.021	427.1	Saturated Vapor
12b	1.048	278.67	0.0011	4.021	213.8	Saturated Liquid
13a	1.820	318.56	0.0058	6.795	448.4	Superheat
13b	1.049	281.46	0.0011	6.795	217.2	Sub-cooled
14	1.725	306.72	0.0047	6.795	418.8	Superheat

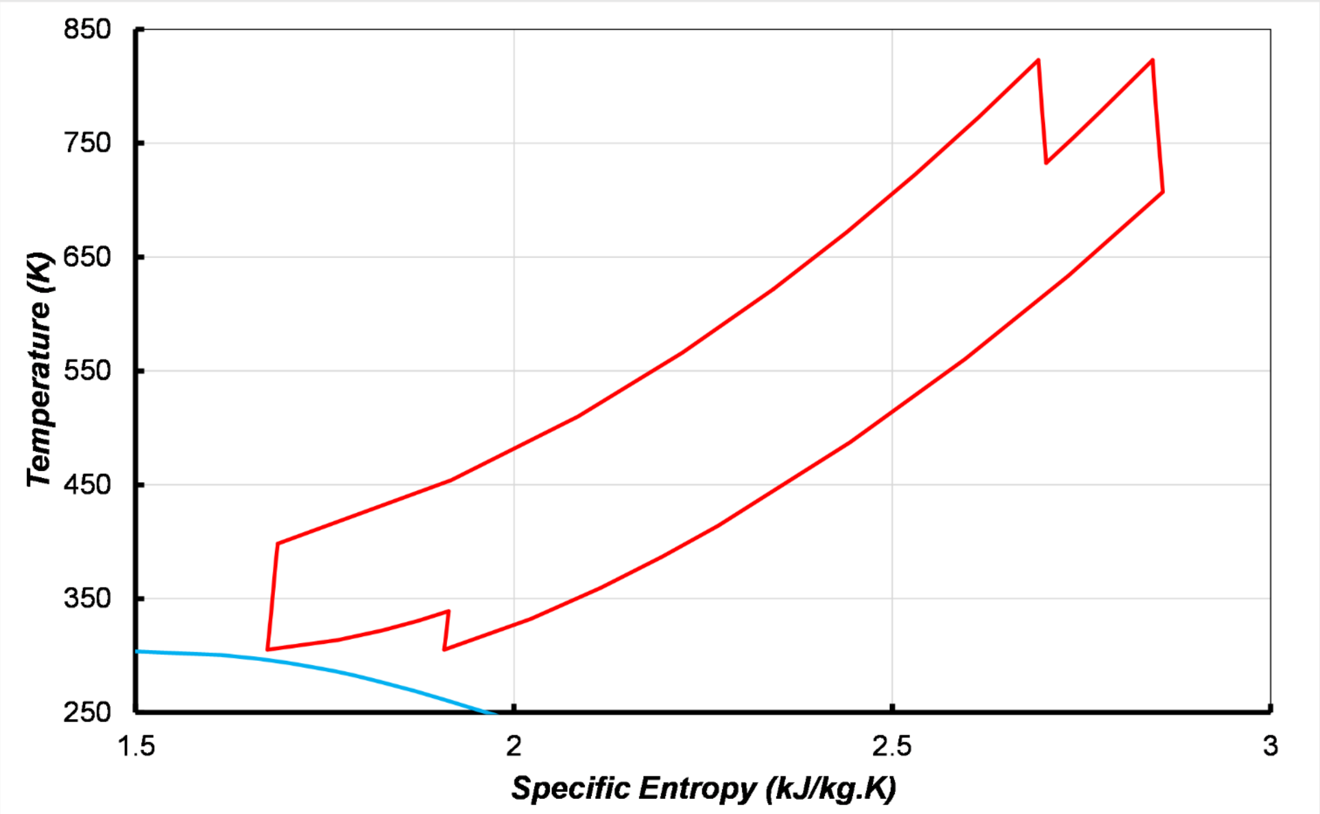

Fig. 96: Temperature-Specific entropy of single layout A

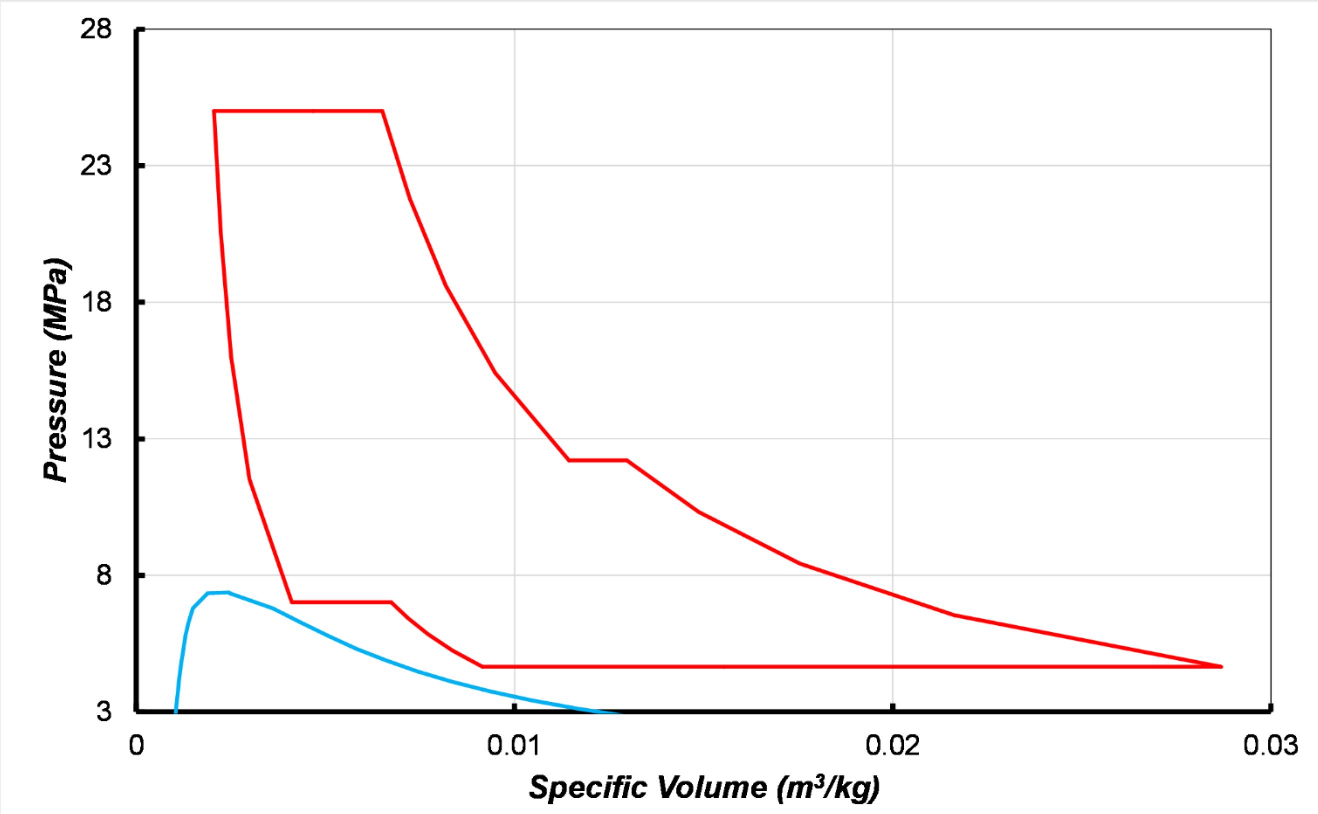

Fig. 97: Pressure-Specific entropy of single layout A

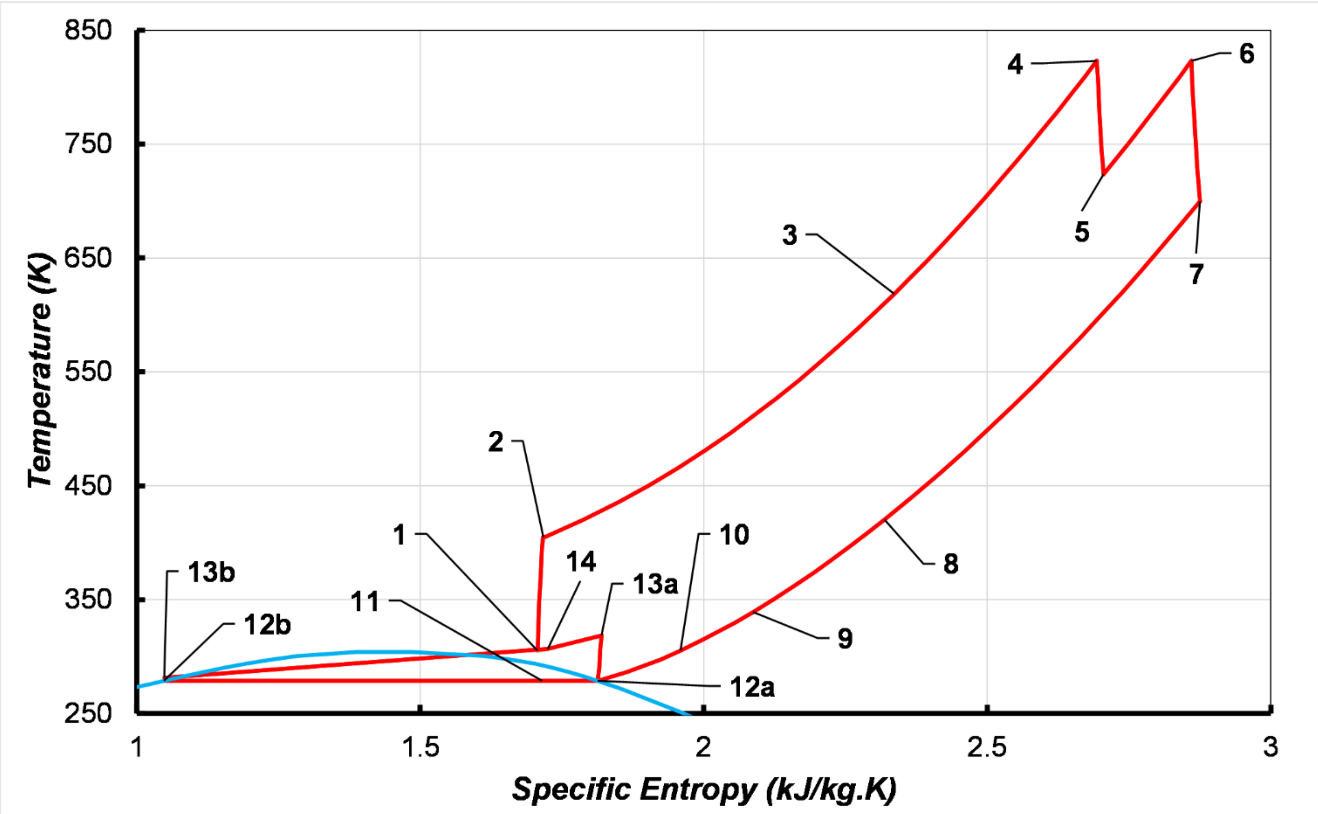

Fig. 98: Temperature-Specific entropy of hybrid layout A

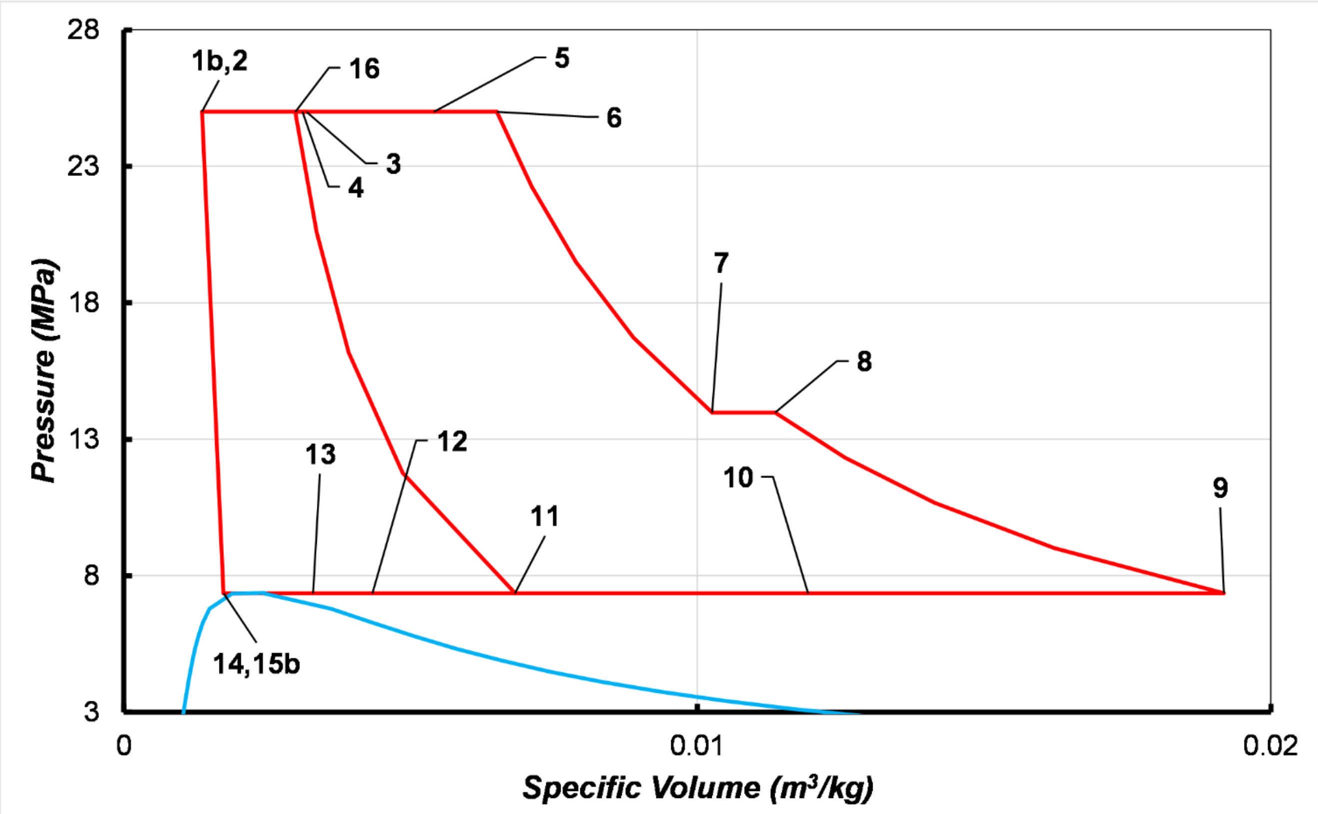

Fig. 99: Pressure-Specific entropy of hybrid layout A

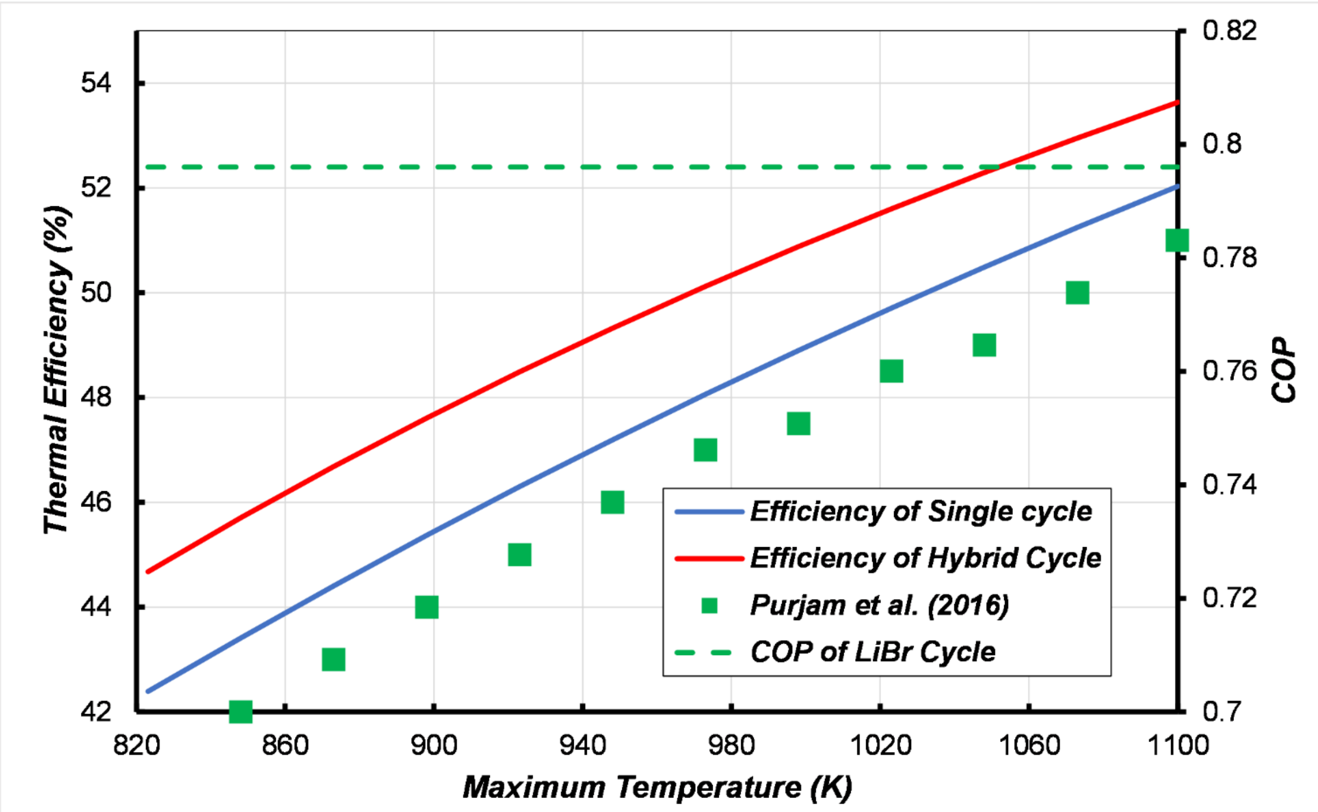

Fig. 100: Parametric analysis of layout A (thermal efficiency)

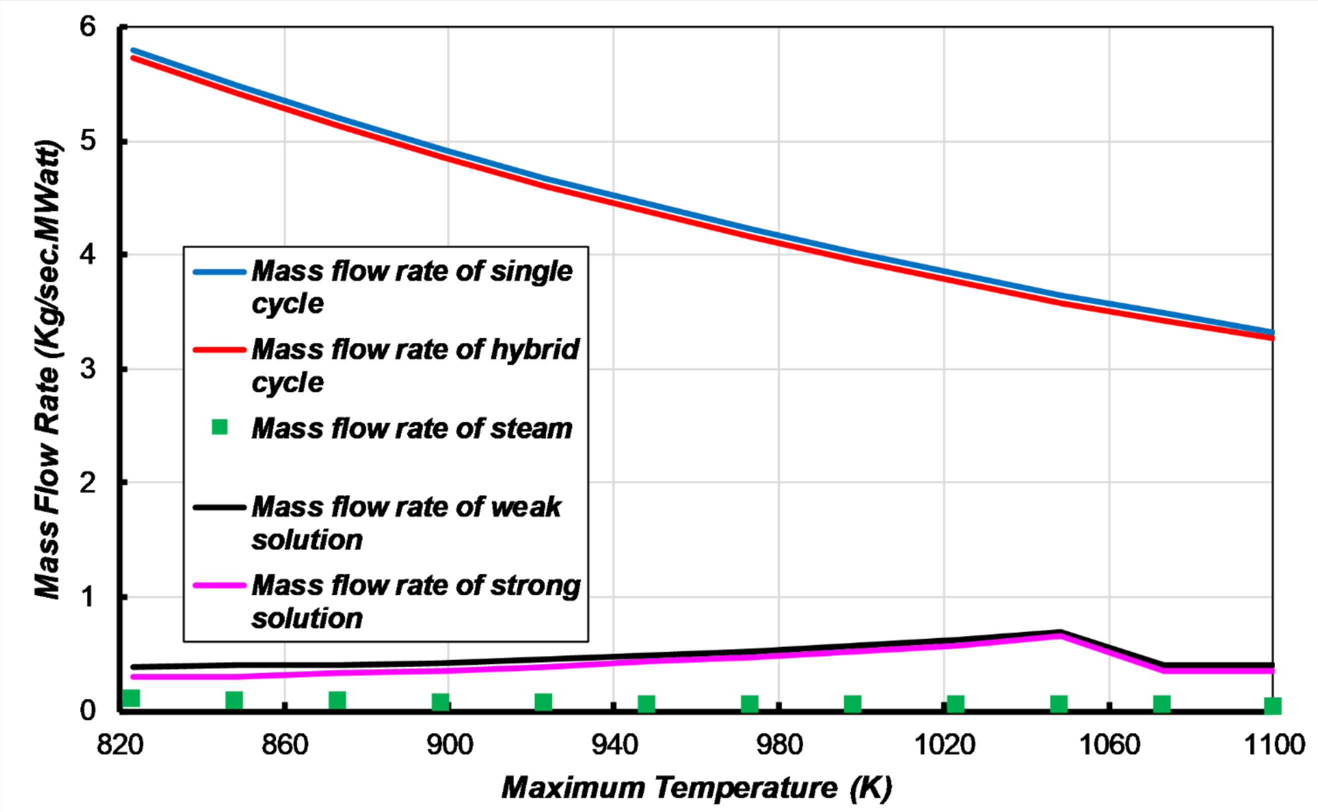

Fig. 101: Parametric analysis of layout A (Mass flow rates)

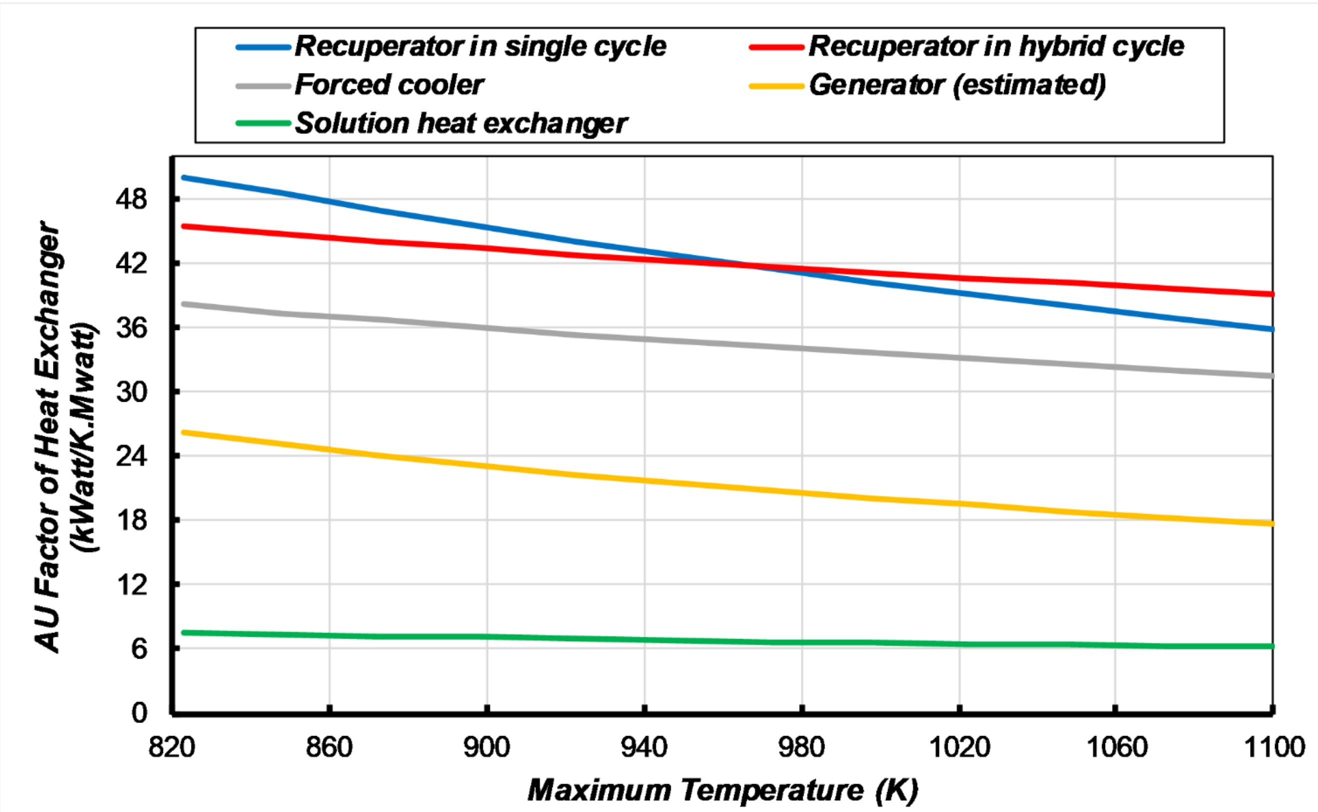

Fig. 102: Parametric analysis of layout A (Recuperator AU factor)

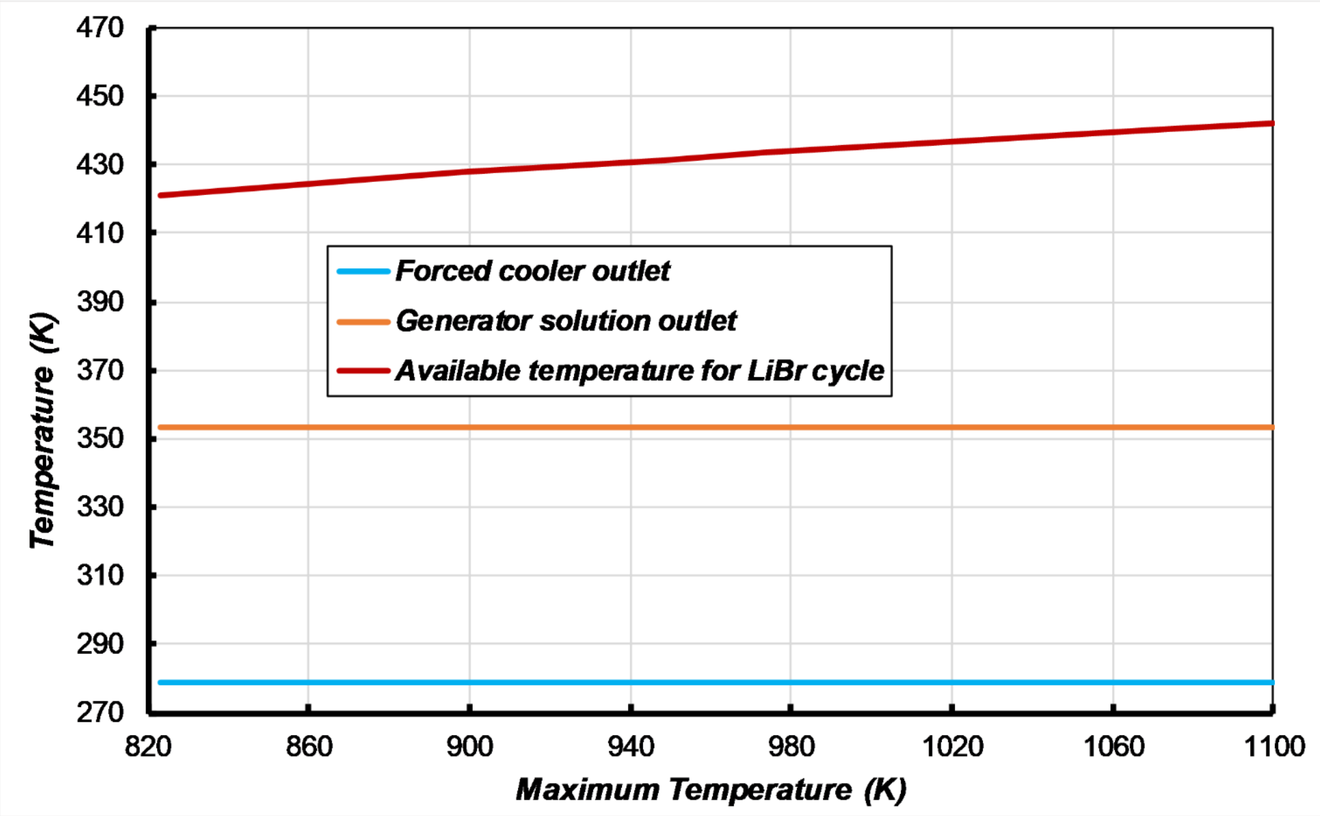

Fig. 103: Parametric analysis of layout A (Temperature profile in generator and absorber)

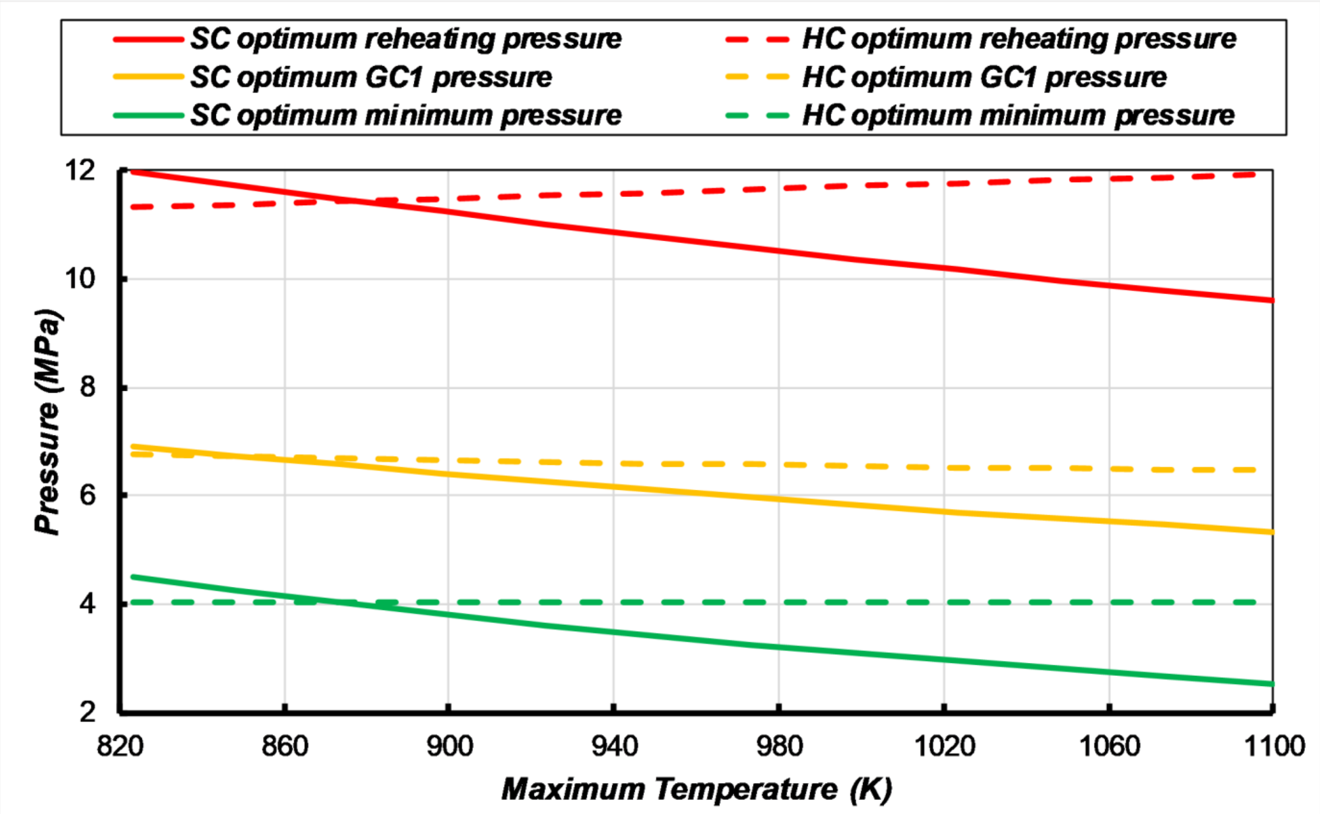

Fig. 104: Parametric analysis of layout A (Optimum Pressures)

Fig. 102 is the UA factor of the heat exchanger of the cycle. They follow the same trend as Fig. 101. Fig. 103 proves that the temperature profiles of the cycle were satisfied. Fig. 104 illustrates the main 3 optimization variables in both single and hybrid cycles.

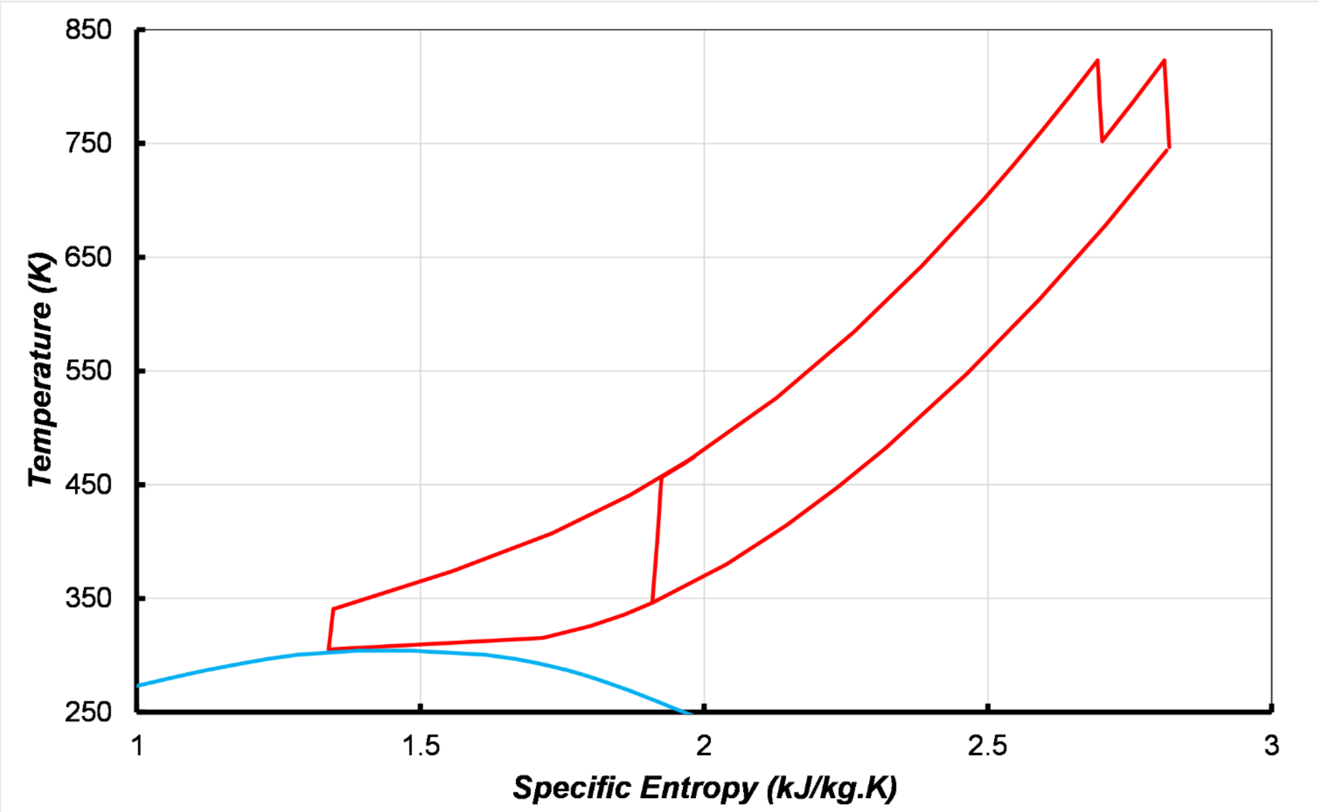

Fig. 105: Temperature-Specific entropy of single layout B

3.5. Layout B

Table 17 shows the thermodynamic properties of layout B with LiBr. The T-s and P-v diagram of Fig. 107 and Fig. 108 is based on table 17. The result for heater temperature of 823.15 is optimized.

Fig. 105 and Fig. 106 are the T-s and P-v diagrams of the single cycle (Fig. 80) with the same assumptions but different optimized values.

Fig. 109 shows the changes of thermal efficiency of the hybrid layout A to the maximum temperature of the cycle. The thermal efficiency of the single cycle and data from [176][177] are included. The results show that integration will not noticeably increase the performance of the cycle. This increase in performance is slightly reduced at high temperatures. The COP of LiBr mostly remains constant and it works at its highest possible temperature (28°C) and in all of the points the condensation of CO_2 happens.

Fig. 110 shows the mass flow rates of the cycle in hybrid layout B. Adding LiBr can slightly reduce the mass flow rate.

Fig. 111 is the UA factor of the heat exchanger of the cycle. They follow the same trend as Fig. 110. Fig. 112 proves that the temperature profiles of the cycle were satisfied. Fig. 113 illustrates the main 3 optimization variables in both single and hybrid cycles.

Table 17: The thermodynamic properties of points in layout B with LiBr

State #	Spesific Entropy (kJ/kg.K)	Temperature (K)	Specific Volume (m^3/kg)	Pressure (MPa)	Specific Enthalpy (kJ/kg)	Phase or Vapor quality
1a	1.401	348.96	0.0014	25	350.1	Supercritical
1b	1.368	343.8	0.0014	25	338.6	Supercritical
2	1.368	343.8	0.0014	25	338.6	Supercritical
3	2.009	483.18	0.0032	25	597.4	Supercritical
4	1.993	477.64	0.0031	25	589.4	Supercritical
5	2.491	699.94	0.0054	25	877.9	Supercritical
6	2.693	823.15	0.0065	25	1031.8	Supercritical
7	2.701	749.05	0.0103	13.977	949.6	Supercritical
8	2.816	823.15	0.0114	13.977	1039.6	Supercritical
9	2.825	743.75	0.0192	7.360	950.7	Superheat
10	2.352	491.18	0.0119	7.360	662.2	Superheat
11	1.943	349.79	0.0068	7.360	493.0	Superheat
12	1.712	311.38	0.0043	7.360	417.4	Superheat
13	1.599	305.15	0.0033	7.360	382.7	Superheat
14	1.359	303.92	0.001741	7.360	309.8	Sub-cooled
15a	1.479	304.03	0.0024	7.360	346.1	Saturated Vapor
15b	1.36	303.92	0.0017	7.360	309.8	Sub-cooled
16	1.961	467.40	0.003	25	574.3	Supercritical

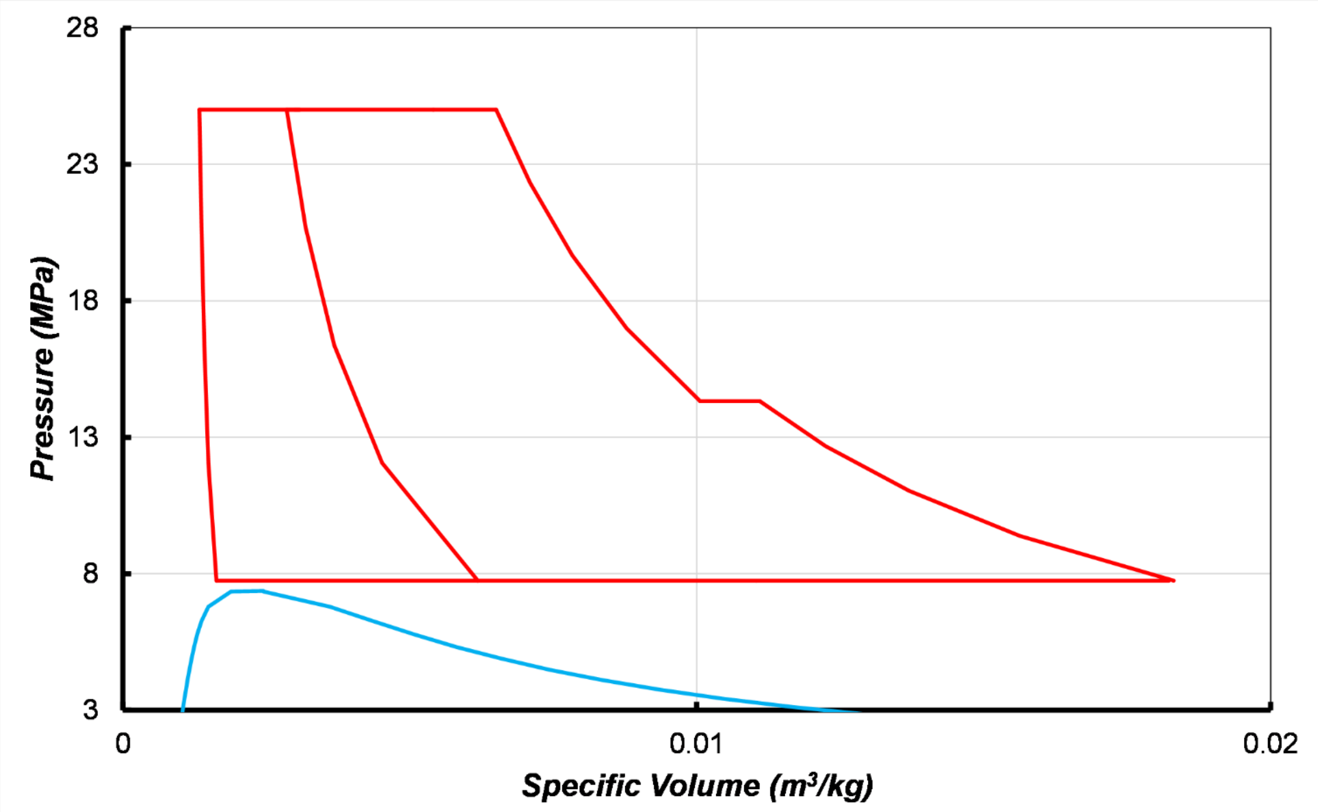

Fig. 106: Pressure-Specific entropy of single layout B

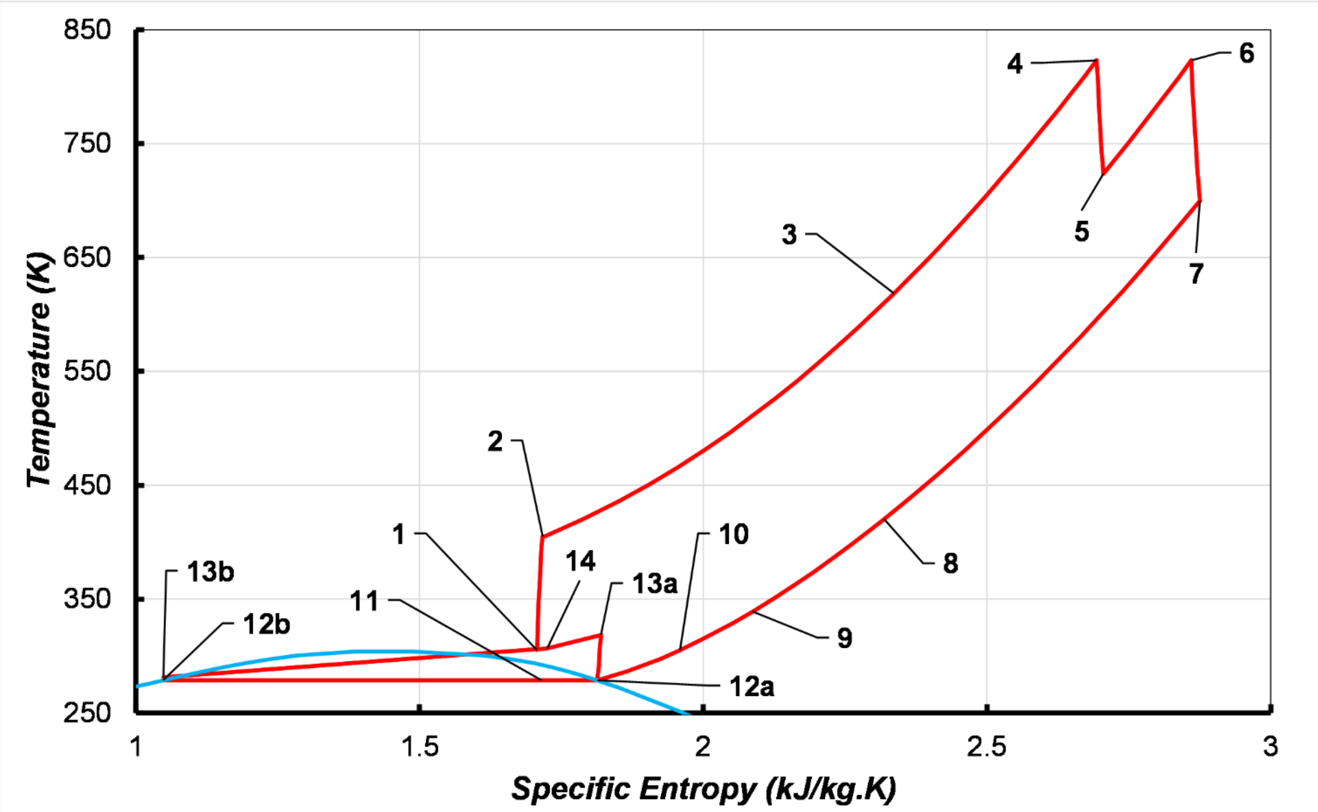

Fig. 107: Temperature-Specific entropy of hybrid layout B

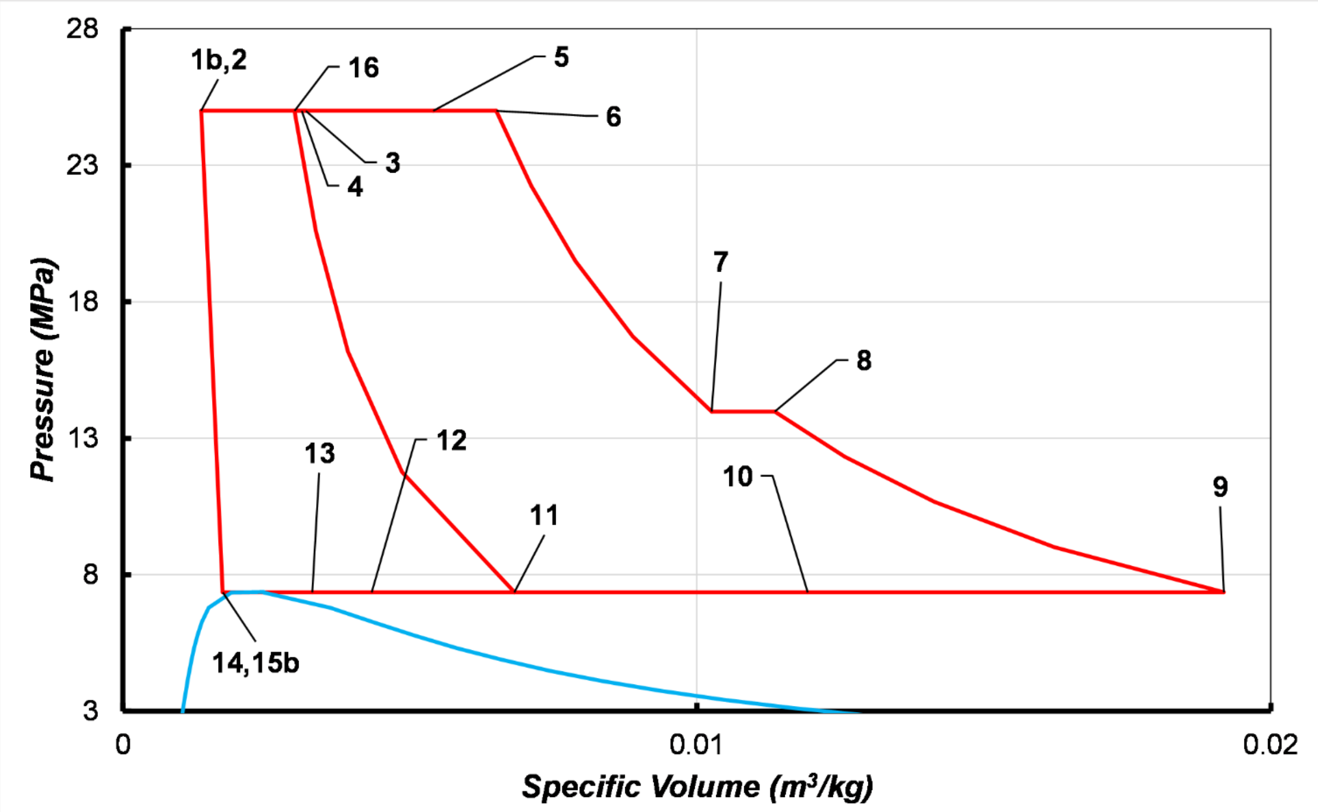

Fig. 108: Pressure-Specific entropy of hybrid layout A

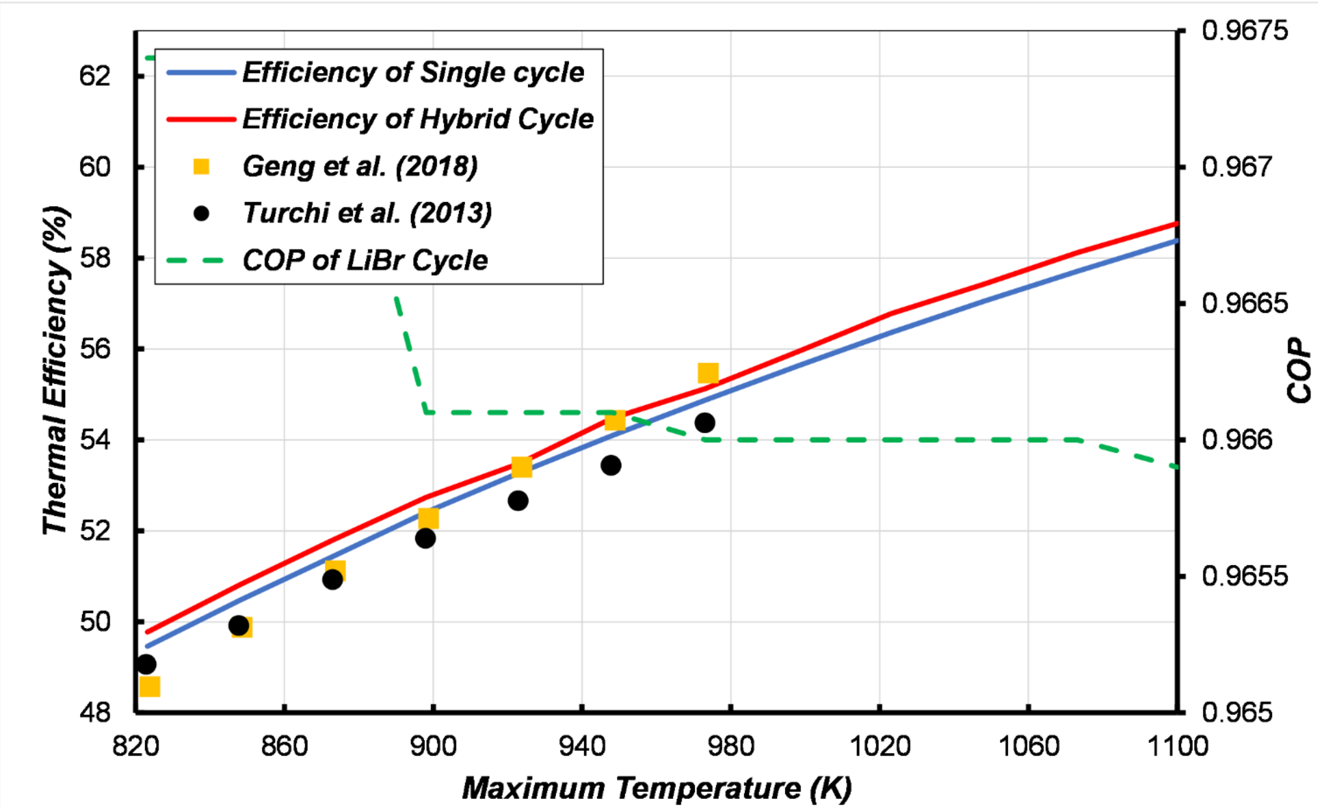

Fig. 109: Parametric analysis of layout B (thermal efficiency)

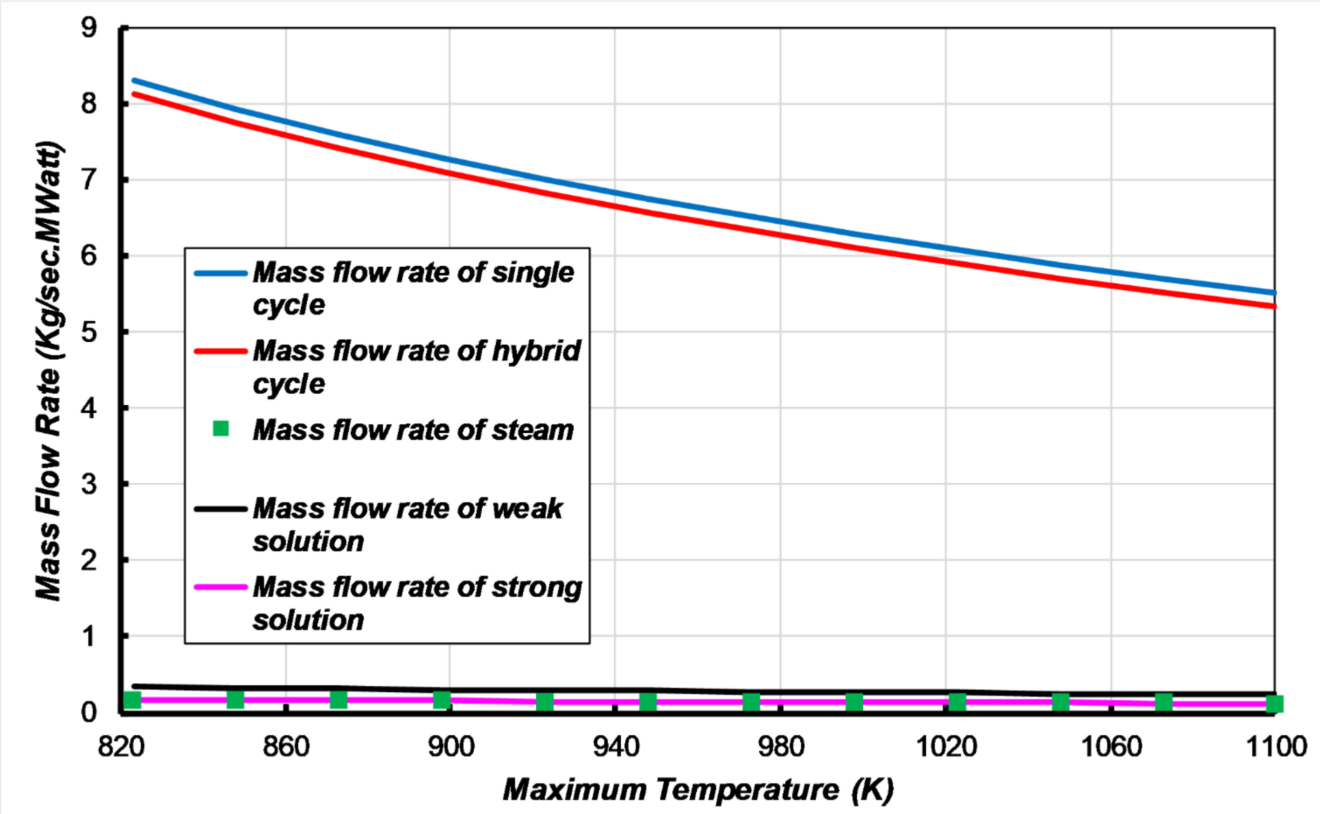

Fig. 110: Parametric analysis of layout B (Mass flow rates)

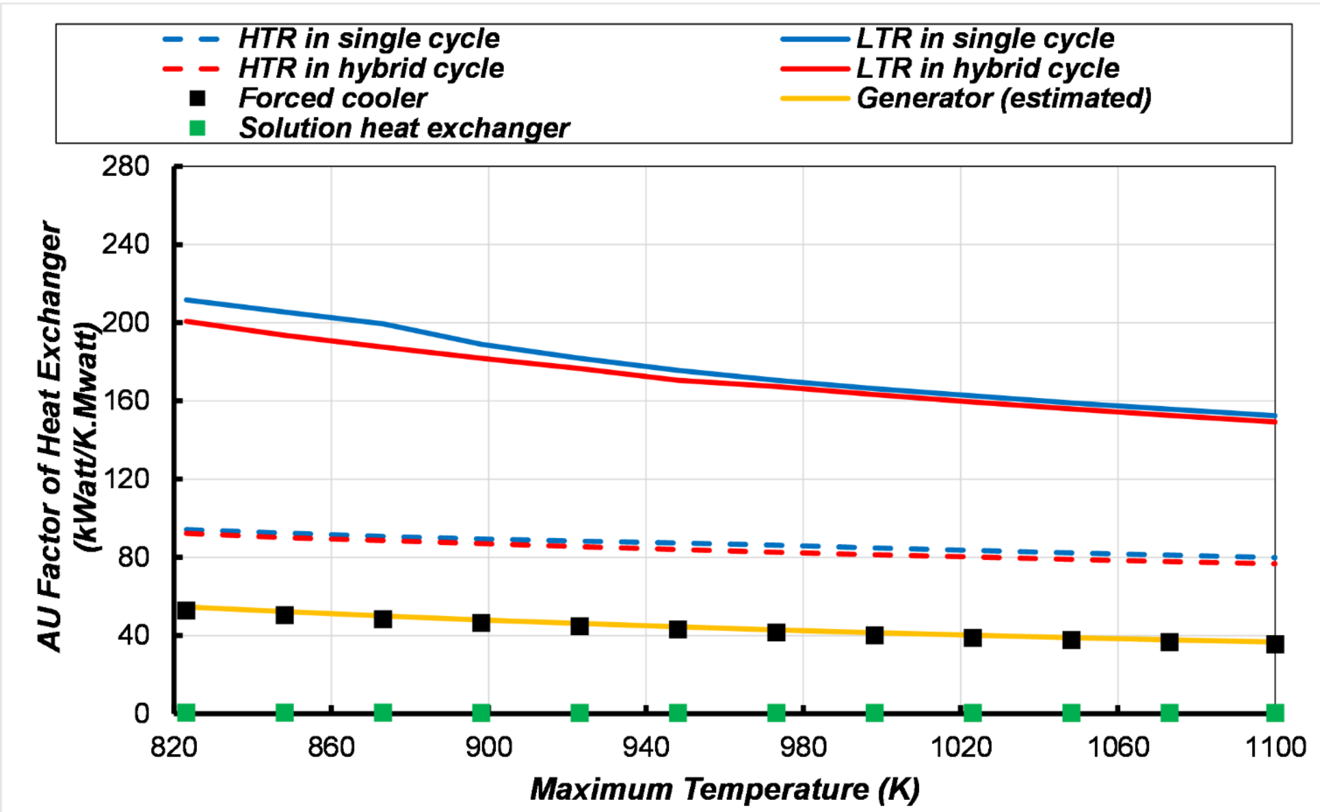

Fig. 111: Parametric analysis of layout B (Recuperator AU factor)

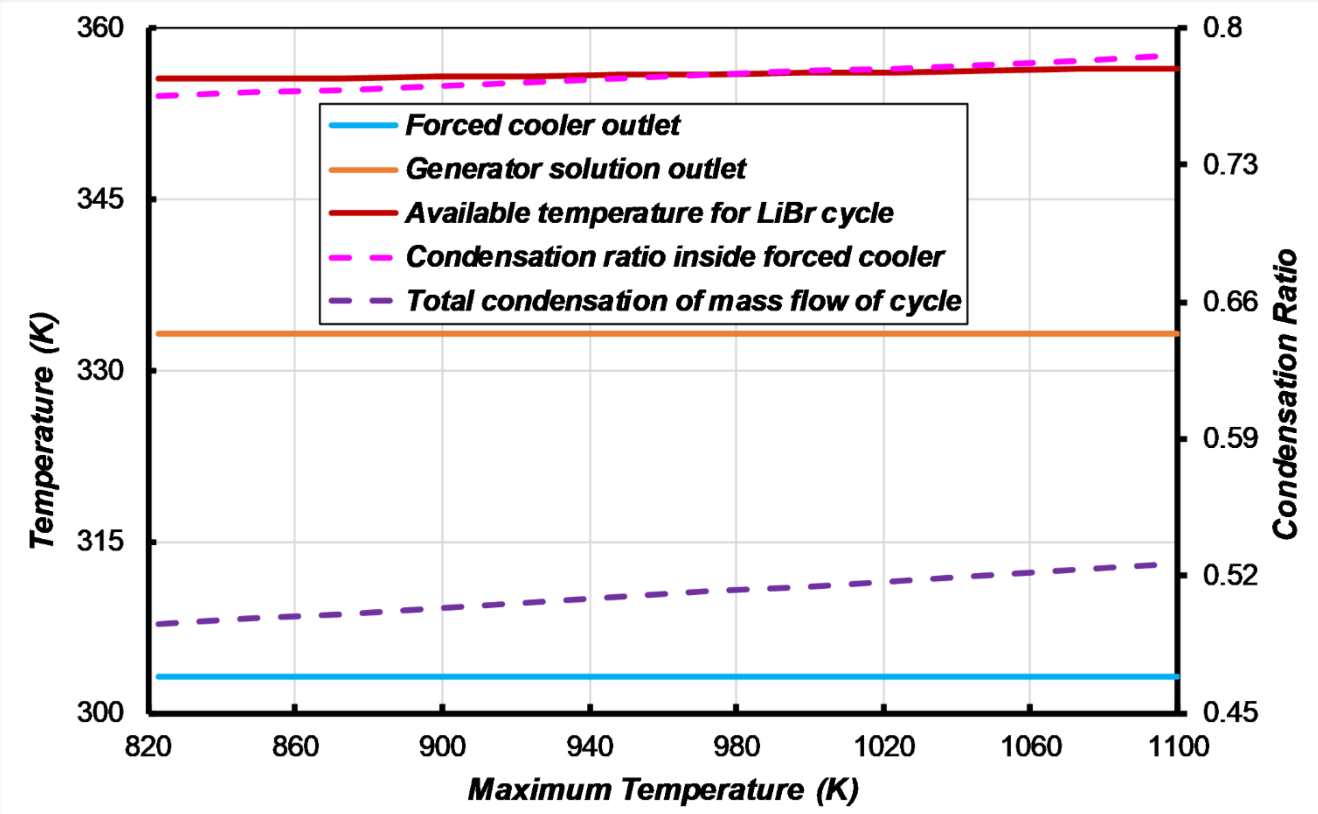

Fig. 112: Parametric analysis of layout B (Temperature profile in generator and absorber)

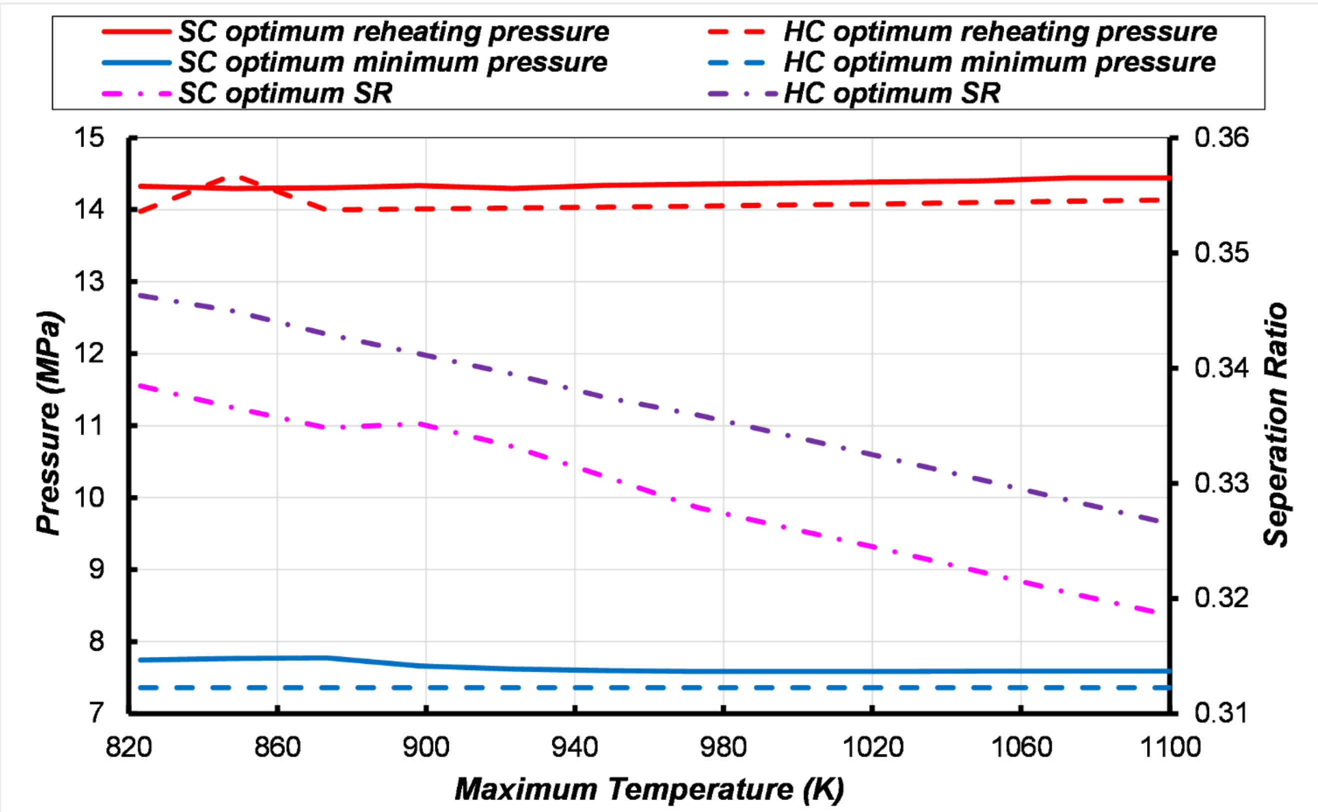

Fig. 113: Parametric analysis of layout B (Optimum Pressures)

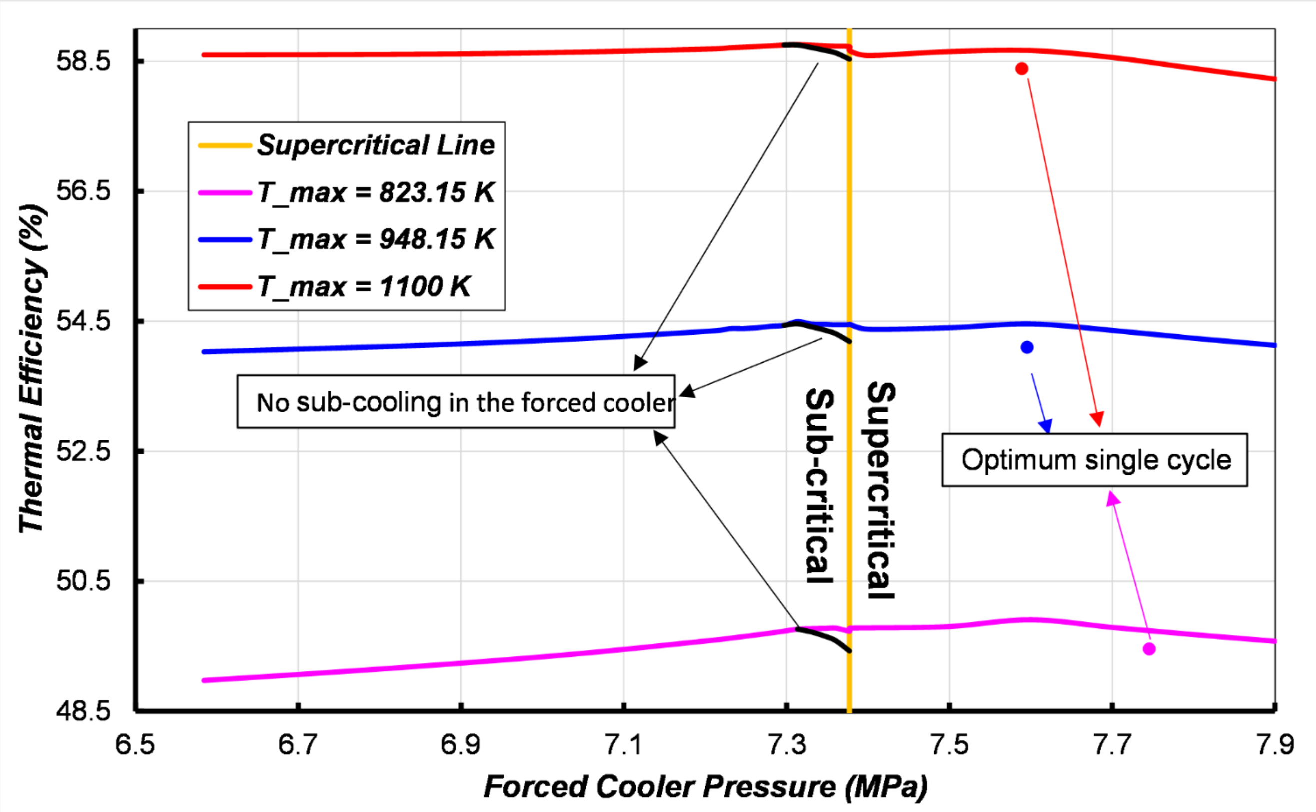

Fig. 114: Layout B parametric analysis vs forced cooler pressure (thermal efficiency)

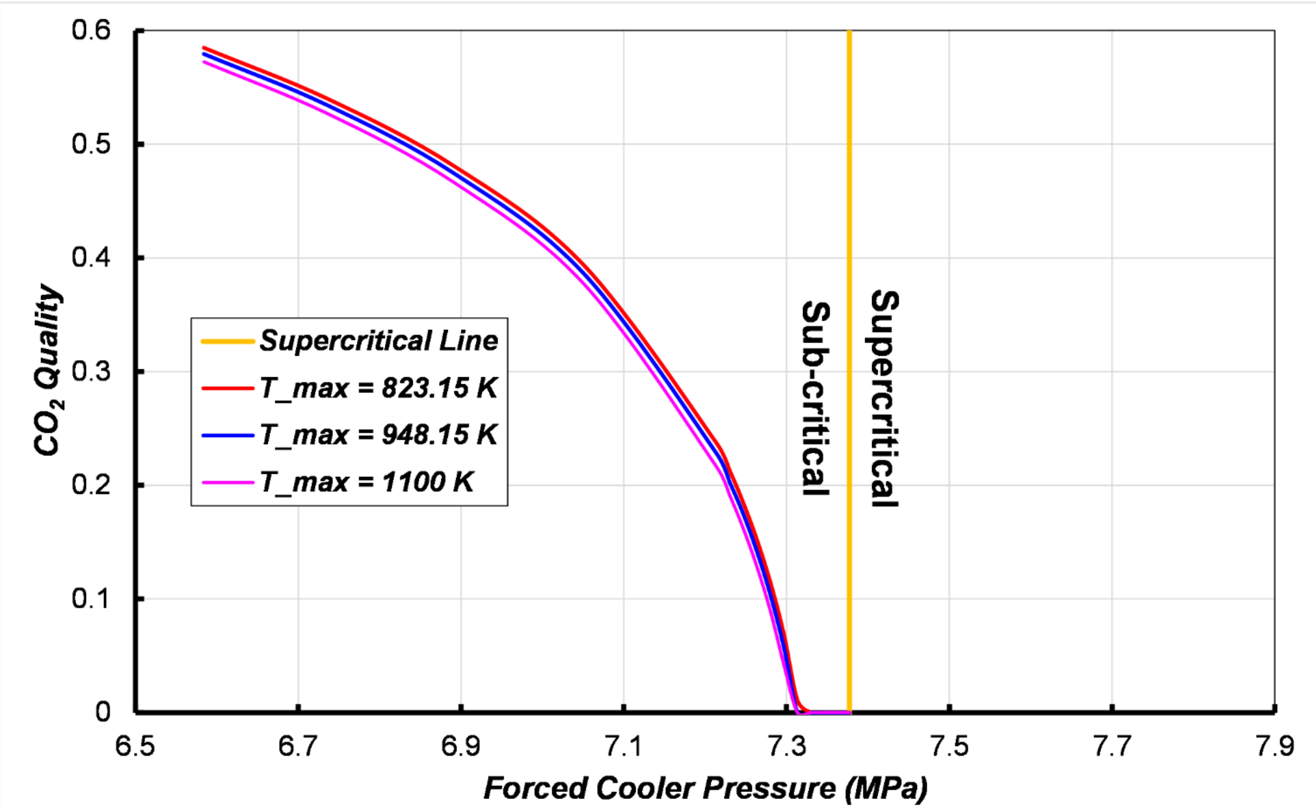

Fig. 115: Layout B parametric analysis vs forced cooler pressure (vapor quality in the forced cooler)

Fig. 114 and Fig. 115 show the effect of forced cooler pressure in the optimization. Forced cooling in the sub-critical region has better performance and sub-cooling the liquid increases the efficiency.

Using LiBr in Both layouts can increase their efficiency without adding significant weight. Layout A benefits better from the LiBr cycle because it has more waste heat to be utilized.

For capturing high-density CO_2 at warm ambient temperature both cycles provide more than enough condensate, but layout B has the advantages to also remove all of the impurities from the system.

4. Conclusion

Supercritical Carbon Dioxide Power Cycle (SCDC) has many potentials which makes it a preferable candidate for various applications. SCDC has high flexibility and tolerance for new types of energy resources like fusion, high-temperature reactors, and high-temperature concentrated thermal solar receivers. SCDC is also the best candidate for pre-combustion and the only candidate for oxy-fuel combustion systems.

Using refrigeration cycles to improve the performance of the power cycle is an accepted method. Absorption refrigeration cycles are renowned systems for this purpose. However, until now the research about coupling an absorption refrigeration cycle to an SCDC for the purpose of efficiency improvement is unknown. To bridge this gap, two SCDC layouts were selected and integrated with Lithium Bromide-Water refrigeration cycles (LiBr). Layout A is a modified intercooler single reheat cycle that shows great potential for an efficiency boost. Layout be is a recompression cycle with single reheat which did not show a great improvement, but the results illustrated that coupling LiBr with recompression cycle may have co-benefits for oxy-fuel combustion and carbon capture and storage.

A brief 1^{st} law parametric analysis was conducted. It was found that LiBr usually reduces the mass flow rate of the single cycle and at the lower temperature of the heat source the room for improvement is larger. The calculation and optimization of data were done by linearized methods.

Nomenclature

Abbreviations
COM: Compressor
EJE: Ejector
EVA: Evaporator
EXP: Expansion device or turboexpander
Exp.: Experimental
Sim.: Simulation
FC: Flash chamber
GC: Gas cooler
WR: Work recovery
ORC: Organic Rankine cycle
PU: Pump
TUR: Turbine
CON: Condenser
HX: Heat exchanger
LiBr: Lithium Bromide-Water refrigeration cycle
SCDC: Supercritical carbon dioxide cycle

Variables
a: Specific exergy of flow (kJ/kg)
COP: Coefficient of performance (-)
C: Speed of sound (m/s)
C_p: Isobaric specific heat capacity (kJ/kg. K)
C_v: Isochoric specific heat capacity (kJ/kg. K)
$\dot{E}$: Rate of exergy (kW)
h: Specific enthalpy (kJ/kg)
$\dot{m}$: Mass flow rate (kg/s, gr/s)
e: specific exergy (kJ/kg)
M: Mach number
P: Pressure (MPa)
q: Specific heat energy (kW/kg)
Q: Heat power (kW)
R: Entrainment Ratio (-)
RT: Ton of Refrigeration (3.5168 kW)
s: Specific entropy (kJ/kg.K)
T: Temperature (K, °C)
V: Speed of flow (m/s)
w: Specific Work (kW/kg)
W: Power (kW)
CCB: Cooling capacity boost (%)
RW: Recovered work (%)
x: Quality of vapor (kg/kg)
CR: Compression ratio (MPa/MPa)
SR: separation ratio
SCR: Solution circulation Ratio

Greek symbols
α: Void fraction (m^3/m^3)
γ: Specific heats ratio (-)

ε: Exergy efficiency (-)
η: Efficiency (-)
ρ: Density (kg/m^3)
ψ: Share of exergy flow (%)
λ: Effectiveness of heat exchanger (-)
Γ: heat transfer ratio inside LiBr

Subscripts
0: Reference state
1 ~ 10: State points number
d: Diffuser
D: Destroyed
a, b, c, d: State points inside the ejector
A, B, C, D: State points in ORC cycle or LiBr
id: Ideal
is: Isentropic
II: 2nd law
l: Liquid
m: Mixing chamber (inside ejector)
n: Nozzle
v: Vapor
pri: Primary flow into ejector
purge: Purged flow after ejector
sec: Secondary flow into ejector
RS: refrigerated space

References

[1] IPCC, Annex III: Glossary [Planton, S. (ed.)], Clim. Chang. 2013 Phys. Sci. Basis. Contrib. Work. Gr. I to Fifth Assess. Rep. Intergov. Panel Clim. Chang. (2013) 1447–1466.

[2] L.O. Bengtsson, C.U. Hammer, eds., Geosphere-Biosphere Interactions and Climate, Cambridge University Press, 2001. https://doi.org/10.1017/CBO9780511529429.

[3] FAQ 1.3 - AR4 WGI Chapter 1: Historical Overview of Climate Change Science, (n.d.). https://archive.ipcc.ch/publications_and_data/ar4/wg1/en/faq-1-3.html (accessed February 4, 2021).

[4] J. Huang, B. Mendoza, J.S. Daniel, C.J. Nielsen, L. Rotstayn, O. Wild, Anthropogenic and natural radiative forcing, Clim. Chang. 2013 Phys. Sci. Basis Work. Gr. I Contrib. to Fifth Assess. Rep. Intergov. Panel Clim. Chang. 9781107057 (2013) 659–740. https://doi.org/10.1017/CBO9781107415324.018.

[5] Global Warming Potentials (IPCC Second Assessment Report) | UNFCCC, (n.d.). https://unfccc.int/process/transparency-and-reporting/greenhouse-gas-data/greenhouse-gas-data-unfccc/global-warming-potentials (accessed February 4, 2021).

[6] M.M. Hurwitz, E.L. Fleming, P.A. Newman, F. Li, E. Mlawer, K. Cady-Pereira, R. Bailey, Ozone depletion by hydrofluorocarbons, Geophys. Res. Lett. 42 (2015) 8686–8692. https://doi.org/10.1002/2015GL065856.

[7] Y. Cengel, M. Boles, M. Kanoglu, Thermodynamics: An Engineering Approach, 9th ed., McGraw-Hill Education, OH, United States, 2018.

[8] U. Nations, Montreal Protocol on Substances that Deplete the Ozone Layer Montreal, United Nations Treaty Collect. C (1989). https://treaties.un.org/pages/ViewDetails.aspx?src=TREATY&mtdsg_no=XXVII-2-a&chapter=27&lang=en.

[9] T. Gerden, The adoption of the kyoto protocol of t he united nations framework convention on climate change, Prisp. Za Novejso Zgodovino. 58 (2018).

[10] C.V. Martin, Potential of near-surface geothermal heating on houses in Graz with graphic charts, Graz, 2014.

[11] I. V. Muralikrishna, V. Manickam, Air Pollution Control Technologies, in: Environ. Manage., Elsevier, 2017: pp. 337–397. https://doi.org/10.1016/B978-0-12-811989-1.00014-2.

[12] J. Lorentzen, Gustav, Pettersen, A new , efficient and environmentally benign system for car Un nouveau syst6me de conditionnement d ’ air automobile efficace et sans nuisance sur l ’ environnement, Int. J.. Refrig. 16 (1993) 4–12.

[13] Engineering – A18 | Tech Design Bureau, (n.d.). https://azul18.net/engineering/ (accessed February 5, 2021).

[14] BP, Statistical Review of World Energy globally consistent data on world energy markets . and authoritative publications in the field of energy The Statistical Review world of World Energy and data on world energy markets from is The Review has been providing, (2020) 66. https://www.bp.com/content/dam/bp/business-sites/en/global/corporate/pdfs/energy-economics/statistical-review/bp-stats-review-2020-full-report.pdf.

[15] Our World in Data, (n.d.). https://ourworldindata.org/ (accessed February 5, 2021).

[16] C. Kunze, H. Spliethoff, Assessment of oxy-fuel, pre- and post-combustion-based carbon capture for future IGCC plants, Appl. Energy. 94 (2012) 109–116. https://doi.org/10.1016/j.apenergy.2012.01.013.

[17] Z. Zhu, Y. Chen, J. Wu, S. Zhang, S. Zheng, A modified Allam cycle without compressors realizing efficient power generation with peak load shifting and CO2 capture, Energy. 174 (2019) 478–487. https://doi.org/10.1016/j.energy.2019.01.165.

[18] Toshiba Successfully Achieves First Fire of 50MWth Commercial-scale Combustor at the NET Power Demonstration Plant | TOSHIBA ENERGY SYSTEMS & SOLUTIONS CORPORATION, (n.d.). https://www.toshiba-energy.com/en/info/info2018_0615.htm (accessed February 5, 2021).

[19] F. Crespi, G. Gavagnin, D. Sánchez, G.S. Martínez, Analysis of the Thermodynamic Potential of Supercritical Carbon Dioxide Cycles: A Systematic Approach, J. Eng. Gas Turbines Power. 140 (2018) 1–10. https://doi.org/10.1115/1.4038125.

[20] J. Syblik, L. Vesely, S. Entler, J. Stepanek, V. Dostal, Analysis of supercritical CO2 Brayton power cycles in nuclear and fusion energy, Fusion Eng. Des. 146 (2019) 1520–1523. https://doi.org/10.1016/j.fusengdes.2019.02.119.

[21] J. McTigue, P. Farres-Antunez, K. Ellingwood, T. Neises, A. White, Pumped thermal electricity storage with supercritical CO2 cycles and solar heat input, Vii Int. Young Res. Conf. – Physics, Technol. Innov. 2313 (2020) 190024. https://doi.org/10.1063/5.0032337.

[22] N. Tauveron, E. Macchi, T. Tartière, D. Nguyen, C. Colin, F. Lacroix, Study of a Massive Electricity Storage System Based on CO 2 Transcritical Heat-Pump and Power Cycle and a Geothermal Heat Transfer Process, 438786151 (n.d.) 1–11.

[23] V. Dostal, P. Hejzlar, M.J. Driscoll, High-performance supercritical carbon dioxide cycle for next-generation nuclear reactors, Nucl. Technol. 154 (2006) 265–282. https://doi.org/10.13182/NT154-265.

[24] A. Ayub, N.A. Sheikh, R. Tariq, M.M. Khan, C.M. Invernizzi, Exergetic optimization and

comparison of combined gas turbine supercritical CO2 power cycles, J. Renew. Sustain. Energy. 10 (2018). https://doi.org/10.1063/1.5038333.

[25] G. Lorentzen, Revival of carbon dioxide as a refrigerant, Int. J. Refrig. 17 (1994) 292–301. https://doi.org/10.1016/0140-7007(94)90059-0.

[26] C. Aprea, A. Maiorino, An experimental evaluation of the transcritical CO2 refrigerator performances using an internal heat exchanger, Int. J. Refrig. 31 (2008) 1006–1011. https://doi.org/10.1016/j.ijrefrig.2007.12.016.

[27] S. Bhattacharyya, S. Mukhopadhyay, A. Kumar, R.K. Khurana, J. Sarkar, Optimization of a CO2-C3H8 cascade system for refrigeration and heating, Int. J. Refrig. 28 (2005) 1284–1292. https://doi.org/10.1016/j.ijrefrig.2005.08.010.

[28] M. Purjam, K. Goudarzi, High efficiency sub-critical carbon dioxide supplementary heat pump for low temperature climates (energy and exergy analysis), Renew. Energy. (2019). https://doi.org/10.1016/j.renene.2018.10.024.

[29] D.M. Robinson, E.A. Groll, Efficiencies of transcritical CO2 cycles with and without an expansion turbine: Rendement de cycles transcritiques au CO2 avec et sans turbine d'expansion, Int. J. Refrig. 21 (1998) 577–589. https://doi.org/10.1016/S0140-7007(98)00024-3.

[30] J.S. Baek, E.A. Groll, P.B. Lawless, Piston-cylinder work producing expansion device in a transcritical carbon dioxide cycle . Part I : experimental investigation ´ tente et re ´ cupe ´ ration de travail par piston dans un cycle De ´ rimentale transcritique au dioxyde de carbone . Partie I :, Int. J. Refrig. 28 (2005) 141–151. https://doi.org/10.1016/j.ijrefrig.2004.08.006.

[31] Y. Hwang, P. D, A. Celik, R. Radermacher, C. Park, Performance of Co 2 Cycles With a Two-Stage Compressor, Refrig. Air Cond. (2004) 1–8.

[32] H. Fritschi, F. Tillenkamp, R. Löhrer, M. Brügger, Efficiency increase in carbon dioxide refrigeration technology with parallel compression, Int. J. Low-Carbon Technol. 12 (2017) 171–180. https://doi.org/10.1093/ijlct/ctw002.

[33] Z. Zhang, L. Tong, X. Wang, Thermodynamic analysis of double-stage compression transcritical CO<inf>2</inf> refrigeration cycles with an expander, Entropy. 17 (2015) 2544–2555. https://doi.org/10.3390/e17042544.

[34] J. Sarkar, Cycle parameter optimization of vortex tube expansion transcritical CO2 system, Int. J. Therm. Sci. 48 (2009) 1823–1828. https://doi.org/10.1016/j.ijthermalsci.2009.01.016.

[35] R. Llopis, R. Cabello, D. Sánchez, E. Torrella, Energy improvements of CO<inf>2</inf> transcritical refrigeration cycles using dedicated mechanical subcooling, Int. J. Refrig. 55 (2015) 129–141. https://doi.org/10.1016/j.ijrefrig.2015.03.016.

[36] J. Sarkar, Performance optimization of transcritical CO 2 refrigeration cycle with thermoelectric

subcooler, Int. J. Energy Res. 37 (2013) 121–128. https://doi.org/10.1002/er.1879.

[37] D. Li, E.A. Groll, Transcritical CO2 refrigeration cycle with ejector-expansion device, Int. J. Refrig. 28 (2005) 766–773. https://doi.org/10.1016/j.ijrefrig.2004.10.008.

[38] J. qiang Deng, P. xue Jiang, T. Lu, W. Lu, Particular characteristics of transcritical CO 2 refrigeration cycle with an ejector, Appl. Therm. Eng. 27 (2007) 381–388. https://doi.org/10.1016/j.applthermaleng.2006.07.016.

[39] S. Elbel, Historical and present developments of ejector refrigeration systems with emphasis on transcritical carbon dioxide air-conditioning, Int. J. Refrig. 34 (2011) 1545–1561. https://doi.org/10.1016/j.ijrefrig.2010.11.011.

[40] K. Banasiak, A. Hafner, T. Andresen, Experimental and numerical investigation of the influence of the two-phase ejector geometry on the performance of the R744 heat pump, Int. J. Refrig. 35 (2012) 1617–1625. https://doi.org/10.1016/j.ijrefrig.2012.04.012.

[41] Y. Zhu, Y. Huang, C. Li, F. Zhang, P.X. Jiang, Experimental investigation on the performance of transcritical CO2 ejector-expansion heat pump water heater system, Energy Convers. Manag. 167 (2018) 147–155. https://doi.org/10.1016/j.enconman.2018.04.081.

[42] J. Sarkar, Optimization of ejector-expansion transcritical CO2 heat pump cycle, Energy. 33 (2008) 1399–1406. https://doi.org/10.1016/j.energy.2008.04.007.

[43] C. Lucas, J. Koehler, Experimental investigation of the COP improvement of a refrigeration cycle by use of an ejector, Int. J. Refrig. 35 (2012) 1595–1603. https://doi.org/10.1016/j.ijrefrig.2012.05.010.

[44] Y. He, J. Deng, F. Yang, Z. Zhang, An optimal multivariable controller for transcritical CO2 refrigeration cycle with an adjustable ejector, Energy Convers. Manag. 142 (2017) 466–476. https://doi.org/10.1016/j.enconman.2017.03.070.

[45] G. Lorentzen, Throttling, the internal haemorrhage of the refrigeration process, Proc. Inst. Refrig. 80. (1983) 39–47.

[46] G.A. Kemper, C.A., Harper, G.F., Brown, Multiple-phase ejector refrigerating system, 3,277,660, 1966.

[47] K. Braimakis, A. Mikelis, A. Charalampidis, S. Karellas, Exergetic performance of CO2 and ultra-low GWP refrigerant mixtures as working fluids in ORC for waste heat recovery, Energy. 203 (2020) 117801. https://doi.org/10.1016/j.energy.2020.117801.

[48] K. Goudarzi, M. Keshtgar, Improving the engine cooling system using a power generation cycle for low-temperature heat source (heat losses in engine) instead of radiator, Appl. Therm. Eng. 120 (2017) 196–202. https://doi.org/10.1016/j.applthermaleng.2017.03.119.

[49] A. Mota-Babiloni, M. Mastani Joybari, J. Navarro-Esbrí, C. Mateu-Royo, Á. Barragán-Cervera,

M. Amat-Albuixech, F. Molés, Ultralow-temperature refrigeration systems: Configurations and refrigerants to reduce the environmental impact, Int. J. Refrig. 111 (2020) 147–158. https://doi.org/10.1016/j.ijrefrig.2019.11.016.

[50] K. Sumardi, N. Nahadi, M. Mutaufiq, Experimental study of hydrocarbon refrigerant (R-1270) to replace R-32 in residential air conditioning system, J. Phys. Conf. Ser. 1469 (2020) 0–5. https://doi.org/10.1088/1742-6596/1469/1/012174.

[51] Industrial refrigeration and heating process | GEA, (n.d.). https://www.gea.com/en/refrigeration-heating/index.jsp (accessed February 6, 2021).

[52] Global Industrial Refrigeration Market 2017-2021: Industry Analysis and Top Application Segments by Technavio | Business Wire, (n.d.). https://www.businesswire.com/news/home/20170714005482/en/Global-Industrial-Refrigeration-Market-2017-2021-Industry-Analysis-and-Top-Application-Segments-by-Technavio (accessed February 6, 2021).

[53] Z. Sun, Q. Wang, Z. Xie, S. Liu, D. Su, Q. Cui, Energy and exergy analysis of low GWP refrigerants in cascade refrigeration system, Energy. 170 (2019) 1170–1180. https://doi.org/10.1016/j.energy.2018.12.055.

[54] M. Yari, S.M.S. Mahmoudi, Thermodynamic analysis and optimization of novel ejector-expansion TRCC (transcritical CO2) cascade refrigeration cycles (Novel transcritical CO2 cycle), Energy. 36 (2011) 6839–6850. https://doi.org/10.1016/j.energy.2011.10.012.

[55] K. Megdouli, N. Ejemni, E. Nahdi, A. Mhimid, L. Kairouani, Thermodynamic analysis of a novel ejector expansion transcritical CO2/N2O cascade refrigeration (NEETCR) system for cooling applications at low temperatures, Energy. 128 (2017) 586–600. https://doi.org/10.1016/j.energy.2017.04.073.

[56] Z. Sun, Y. Liang, S. Liu, W. Ji, R. Zang, R. Liang, Z. Guo, Comparative analysis of thermodynamic performance of a cascade refrigeration system for refrigerant couples R41/R404A and R23/R404A, Appl. Energy. 184 (2016) 19–25. https://doi.org/10.1016/j.apenergy.2016.10.014.

[57] A. Da Silva, E.P. Bandarra Filho, A.H.P. Antunes, Comparison of a R744 cascade refrigeration system with R404A and R22 conventional systems for supermarkets, Appl. Therm. Eng. 41 (2012) 30–35. https://doi.org/10.1016/j.applthermaleng.2011.12.019.

[58] J. Fernández-Seara, J. Sieres, M. Vázquez, Compression-absorption cascade refrigeration system, Appl. Therm. Eng. 26 (2006) 502–512. https://doi.org/10.1016/j.applthermaleng.2005.07.015.

[59] R. Llopis, C. Sanz-Kock, R. Cabello, D. Sánchez, L. Nebot-Andrés, J. Catalán-Gil, Effects

caused by the internal heat exchanger at the low temperature cycle in a cascade refrigeration plant, Appl. Therm. Eng. 103 (2016) 1077–1086. https://doi.org/10.1016/j.applthermaleng.2016.04.075.

[60] R. Llopis, D. Sánchez, C. Sanz-Kock, R. Cabello, E. Torrella, Energy and environmental comparison of two-stage solutions for commercial refrigeration at low temperature: Fluids and systems, Appl. Energy. 138 (2015) 133–142. https://doi.org/10.1016/j.apenergy.2014.10.069.

[61] A. Kilicarslan, M. Hosoz, Energy and irreversibility analysis of a cascade refrigeration system for various refrigerant couples, Energy Convers. Manag. 51 (2010) 2947–2954. https://doi.org/10.1016/j.enconman.2010.06.037.

[62] R. Cabello, D. Sánchez, R. Llopis, J. Catalán, L. Nebot-Andrés, E. Torrella, Energy evaluation of R152a as drop in replacement for R134a in cascade refrigeration plants, Appl. Therm. Eng. 110 (2017) 972–984. https://doi.org/10.1016/j.applthermaleng.2016.09.010.

[63] A.H. Mosaffa, L.G. Farshi, C.A. Infante Ferreira, M.A. Rosen, Exergoeconomic and environmental analyses of CO2/NH3 cascade refrigeration systems equipped with different types of flash tank intercoolers, Energy Convers. Manag. 117 (2016) 442–453. https://doi.org/10.1016/j.enconman.2016.03.053.

[64] M.V.A. Queiroz, V.H. Panato, J. Alberto, R. Parise, Experimental comparison of a cascade refrigeration system operating with R744 / R134a and R744 /, Int. Refrig. Air Cond. Conf. Pap. 1785. Http//Docs.Lib.Purdue.Edu/Iracc/1785. (2016) 1–8.

[65] J.A. Dopazo, J. Fernández-Seara, Experimental evaluation of a cascade refrigeration system prototype with CO2 and NH3 for freezing process applications, Int. J. Refrig. 34 (2011) 257–267. https://doi.org/10.1016/j.ijrefrig.2010.07.010.

[66] W. Bingming, W. Huagen, L. Jianfeng, X. Ziwen, Experimental investigation on the performance of NH3/CO2 cascade refrigeration system with twin-screw compressor, Int. J. Refrig. 32 (2009) 1358–1365. https://doi.org/10.1016/j.ijrefrig.2009.03.008.

[67] S. Eini, H. Shahhosseini, N. Delgarm, M. Lee, A. Bahadori, Multi-objective optimization of a cascade refrigeration system: Exergetic, economic, environmental, and inherent safety analysis, Appl. Therm. Eng. 107 (2016) 804–817. https://doi.org/10.1016/j.applthermaleng.2016.07.013.

[68] Y. Chen, W. Han, H. Jin, Proposal and analysis of a novel heat-driven absorption–compression refrigeration system at low temperatures, Appl. Energy. 185 (2017) 2106–2116. https://doi.org/10.1016/j.apenergy.2015.12.009.

[69] P. KASI, Simulation of Thermodynamic Analysis of Cascade Refrigeration System With Alternative Refrigerants, J. Impact Factor. 6502 (2014) 150–157.

[70] A.M. Dubey, S. Kumar, G. Das Agrawal, Thermodynamic analysis of a transcritical

CO2/propylene (R744-R1270) cascade system for cooling and heating applications, Energy Convers. Manag. 86 (2014) 774–783. https://doi.org/10.1016/j.enconman.2014.05.105.

[71] H.M. Getu, P.K. Bansal, Thermodynamic analysis of an R744-R717 cascade refrigeration system, Int. J. Refrig. 31 (2008) 45–54. https://doi.org/10.1016/j.ijrefrig.2007.06.014.

[72] A.D. Parekh, P.R. Tailor, Thermodynamic Analysis of Cascade Refrigeration System Using R12-R13 , R290-R23 and R404A-R23, 395007 (2014) 1351–1356.

[73] T.S. Lee, C.H. Liu, T.W. Chen, Thermodynamic analysis of optimal condensing temperature of cascade-condenser in CO2/NH3 cascade refrigeration systems, Int. J. Refrig. 29 (2006) 1100–1108. https://doi.org/10.1016/j.ijrefrig.2006.03.003.

[74] A.D. Parekh, P.R. Tailor, Thermodynamic Analysis of R507A-R23 Cascade Refrigeration System, Int. J. Mech. Mechatronics Eng. 5 (2011) 1919–1923. https://doi.org/10.5281/zenodo.1054847.

[75] F. YILMAZ, R. SELBAŞ, Energy and Exergy Analyses of CO2/HFE7000 Cascade Cooling System, Süleyman Demirel Üniversitesi Fen Bilim. Enstitüsü Derg. 21 (2017) 854. https://doi.org/10.19113/sdufbed.58140.

[76] C. Sanz-Kock, R. Llopis, D. Sánchez, R. Cabello, E. Torrella, Experimental evaluation of a R134a/CO2 cascade refrigeration plant, Appl. Therm. Eng. 73 (2014) 41–50. https://doi.org/10.1016/j.applthermaleng.2014.07.041.

[77] X.F. Liu, J.H. Liu, H.L. Zhao, Q.Y. Zhang, J.L. Ma, Experimental study on a-60 °c cascade refrigerator with dual running mode, J. Zhejiang Univ. Sci. A. 13 (2012) 375–381. https://doi.org/10.1631/jzus.A1100107.

[78] Nasruddin, S. Sholahudin, N. Giannetti, Arnas, Optimization of a cascade refrigeration system using refrigerant C3H8 in high temperature circuits (HTC) and a mixture of C2H6/CO2 in low temperature circuits (LTC), Appl. Therm. Eng. 104 (2016) 96–103. https://doi.org/10.1016/j.applthermaleng.2016.05.059.

[79] H. Kruse, H. Rüssmann, The natural fluid nitrous oxide-an option as substitute for low temperature synthetic refrigerants, Int. J. Refrig. 29 (2006) 799–806. https://doi.org/10.1016/j.ijrefrig.2005.11.007.

[80] S. Bhattacharyya, A. Garai, J. Sarkar, Thermodynamic analysis and optimization of a novel N2O-CO2 cascade system for refrigeration and heating, Int. J. Refrig. 32 (2009) 1077–1084. https://doi.org/10.1016/j.ijrefrig.2008.09.008.

[81] B. Yilmaz, Thermodynamic Analysis and Optimization of Cascade Condensing Temperature of a CO2 (R744)/ R404A Cascade Refrigeration System, Int. Refrig. Air Cond. Conf. Purdue, July 14-17, 2014. 2 (2014) 1–10.

[82] K. Megdouli, B.M. Tashtoush, E. Nahdi, M. Elakhdar, L. Kairouani, A. Mhimid, Thermodynamic analysis of a novel ejector-cascade refrigeration cycles for freezing process applications and air-conditioning, Int. J. Refrig. 70 (2016) 108–118. https://doi.org/10.1016/j.ijrefrig.2016.06.029.

[83] D. Aghazadeh Dokandari, A. Setayesh Hagh, S.M.S. Mahmoudi, Thermodynamic investigation and optimization of novel ejector-expansion CO2/NH3 cascade refrigeration cycles (novel CO2/NH3 cycle), Int. J. Refrig. 46 (2014) 26–36. https://doi.org/10.1016/j.ijrefrig.2014.07.012.

[84] V. Jain, D. Colorado, Thermoeconomic and feasibility analysis of novel transcritical vapor compression-absorption integrated refrigeration system, Energy Convers. Manag. 224 (2020) 113344. https://doi.org/10.1016/j.enconman.2020.113344.

[85] K. Mohammadi, M.S. Efati Khaledi, K. Powell, A novel hybrid dual-temperature absorption refrigeration system: Thermodynamic, economic, and environmental analysis, J. Clean. Prod. 233 (2019) 1075–1087. https://doi.org/10.1016/j.jclepro.2019.06.130.

[86] S.M.H. Mohammadi, Theoretical investigation on performance improvement of a low-temperature transcritical carbon dioxide compression refrigeration system by means of an absorption chiller after-cooler, Appl. Therm. Eng. 138 (2018) 264–279. https://doi.org/10.1016/j.applthermaleng.2018.04.006.

[87] Y. Liu, J. Liu, J. Yu, Theoretical analysis on a novel two-stage compression transcritical CO2 dual-evaporator refrigeration cycle with an ejector, Int. J. Refrig. 119 (2020) 268–275. https://doi.org/10.1016/j.ijrefrig.2020.08.002.

[88] Klein SA., Engineering Equation Solver, (2019).

[89] E.W. Lemmon, I.H. Bell, M.L. Huber, and M.O. Mclinden, REFPROP 10, (2018).

[90] J. Alberto Dopazo, J. Fernández-Seara, J. Sieres, F.J. Uhía, Theoretical analysis of a CO2-NH3 cascade refrigeration system for cooling applications at low temperatures, Appl. Therm. Eng. 29 (2009) 1577–1583. https://doi.org/10.1016/j.applthermaleng.2008.07.006.

[91] S.M. Liao, T.S. Zhao, A. Jakobsen, Correlation of optimal heat rejection pressures in transcritical carbon dioxide cycles, Appl. Therm. Eng. 20 (2000) 831–841. https://doi.org/10.1016/S1359-4311(99)00070-8.

[92] Y. Hou, C.H. Liu, J.L. Ma, S.T. Chen, Design and Setup of the Micro-Turboexpander Transcritical CO2 System, Int. Refrig. Air Cond. Conf. Pap. 1521. (2014) 2531 (1–7).

[93] L. Hays, A.T.C.O. Turbine-compressor, A Transcritical CO2 Turbine-Compressor, (2004).

[94] D.L. Nguyen, E.R.F. Winter, M. Greiner, Sonic velocity in two-phase systems, Int. J. Multiph. Flow. 7 (1981) 311–320. https://doi.org/10.1016/0301-9322(81)90024-0.

[95] G. Kuehner, Behavior of the Embedded Phase in a Shock- Driven Two-Phase Flow, The

University of New Mexico, 2014.

[96] J. Smolka, Z. Bulinski, A. Fic, A.J. Nowak, K. Banasiak, A. Hafner, A computational model of a transcritical R744 ejector based on a homogeneous real fluid approach, Appl. Math. Model. 37 (2013) 1208–1224. https://doi.org/10.1016/j.apm.2012.03.044.

[97] M. Yazdani, A.A. Alahyari, T.D. Radcliff, Numerical modeling of two-phase supersonic ejectors for work-recovery applications, Int. J. Heat Mass Transf. 55 (2012) 5744–5753. https://doi.org/10.1016/j.ijheatmasstransfer.2012.05.071.

[98] M. Palacz, J. Smolka, A.J. Nowak, K. Banasiak, A. Hafner, Optimisation de forme d'un éjecteur diphasique pour les systèmes frigorifiques au CO2, Int. J. Refrig. 74 (2017) 210–221. https://doi.org/10.1016/j.ijrefrig.2016.10.013.

[99] M. Palacz, M. Haida, J. Smolka, A.J. Nowak, K. Banasiak, A. Hafner, HEM and HRM accuracy comparison for the simulation of CO2 expansion in two-phase ejectors for supermarket refrigeration systems, Appl. Therm. Eng. 115 (2017) 160–169. https://doi.org/10.1016/j.applthermaleng.2016.12.122.

[100] K. Banasiak, M. Palacz, A. Hafner, Z. Buliński, J. Smołka, A.J. Nowak, A. Fic, A CFD-based investigation of the energy performance of two-phase R744 ejectors to recover the expansion work in refrigeration systems: An irreversibility analysis, Int. J. Refrig. 40 (2014) 328–337. https://doi.org/10.1016/j.ijrefrig.2013.12.002.

[101] F. Liu, Review on Ejector Efficiencies in Various Ejector Systems, 15th Int. Refrig. Air Cond. Conf. (2014) 1–10.

[102] S. Elbel, P. Hrnjak, Effect of Internal Heat Exchanger on performance of transcritical CO2 systems with ejector, Int. Refrig. Air Cond. Conf. Purdue. R166 (2004) 1–8. http://docs.lib.purdue.edu/iracc/708.

[103] E.B. Ksayer, D. Clodic, Enhancement of CO2 Refrigeration Cycle Using an Ejector : 1D Analysis, Int. J. Refrig. Air Cond. Conf. - Purdue Univ. R058 (2006) 1–8.

[104] S. Elbel, P. Hrnjak, Experimental validation of a prototype ejector designed to reduce throttling losses encountered in transcritical R744 system operation, Int. J. Refrig. 31 (2008) 411–422. https://doi.org/10.1016/j.ijrefrig.2007.07.013.

[105] S. Fangtian, M. Yitai, Thermodynamic analysis of transcritical CO2 refrigeration cycle with an ejector, Appl. Therm. Eng. 31 (2011) 1184–1189. https://doi.org/10.1016/j.applthermaleng.2010.12.018.

[106] F.E. Manjili, M.A. Yavari, Performance of a new two-stage multi-intercooling transcritical CO 2 ejector refrigeration cycle, Appl. Therm. Eng. 40 (2012) 202–209. https://doi.org/10.1016/j.applthermaleng.2012.02.014.

[107] G. Angelino, Carbon dioxide condensation cycles for power production, (1968).

[108] E.G. Feher, The supercritical thermodynamic power cycle, Energy Convers. 8 (1968) 85–90. https://doi.org/10.1016/0013-7480(68)90105-8.

[109] J.P. Dievot, The sodium-CO2 fast breeder reactor concept, in: Int. Conf. Sodium Technol. Large Fast React. Des. Argonne Natl. Lab., 1968.

[110] R.A. Strub, A.J. Frieder, Paper 5: HIGH PRESSURE INDIRECT CO2 CLOSED-CYCLE GAS TURBINES, in: Nucl. Gas Turbines, Thomas Telford Publishing, 1970: pp. 51–61.

[111] M.A. Pope, Reactor physics design of supercritical CO_2-cooled fast reactors, (2004).

[112] N.A. Carstens, P. Hejzlar, M.J. Driscoll, Control system strategies and dynamic response for supercritical CO2 power conversion cycles, Cent. Adv. Nucl. Energy Syst. (2006).

[113] V. Dostal, M. Kulhanek, Research on the supercritical carbon dioxide cycles in the Czech Republic, in: Czech Tech. Univ. Prague, Symp. SCO2 Power Cycles, 2009.

[114] A. Moisseytsev, J.J. Sienicki, Development of a plant dynamics computer code for analysis of a supercritical carbon dioxide Brayton cycle energy converter coupled to a natural circulation lead-cooled fast reactor., Argonne National Laboratory (ANL), Argonne, IL, 2007.

[115] A. Moisseytsev, J.J. Sienicki, Transient accident analysis of a supercritical carbon dioxide Brayton cycle energy converter coupled to an autonomous lead-cooled fast reactor, Nucl. Eng. Des. 238 (2008) 2094–2105. https://doi.org/10.1016/j.nucengdes.2007.11.012.

[116] A. Moisseytsev, J.J. Sienicki, Investigation of alternative layouts for the supercritical carbon dioxide Brayton cycle for a sodium-cooled fast reactor, Nucl. Eng. Des. 239 (2009) 1362–1371. https://doi.org/10.1016/j.nucengdes.2009.03.017.

[117] S.A. Wright, R.F. Radel, M.E. Vernon, G.E. Rochau, P.S. Pickard, Operation and analysis of a supercritical CO2 Brayton cycle, Sandia Report, No. SAND2010-0171. (2010).

[118] J. Pasch, T. Conboy, D. Fleming, G. Rochau, Supercritical CO2 Recompression Brayton Cycle: Completed Assembly, Sandia Report, SAND. 9546 (2012) 2012.

[119] Y. Kato, T. Nitawaki, Y. Muto, Medium temperature carbon dioxide gas turbine reactor, Nucl. Eng. Des. 230 (2004) 195–207. https://doi.org/10.1016/j.nucengdes.2003.12.002.

[120] Y. Ahn, S.J. Bae, M. Kim, S.K. Cho, S. Baik, J.I. Lee, J.E. Cha, Review of supercritical CO2 power cycle technology and current status of research and development, Nucl. Eng. Technol. 47 (2015) 647–661. https://doi.org/10.1016/j.net.2015.06.009.

[121] Y. Ahn, J. Lee, S.G. Kim, J.I. Lee, J.E. Cha, S.W. Lee, Design consideration of supercritical CO2 power cycle integral experiment loop, Energy. 86 (2015) 115–127. https://doi.org/10.1016/j.energy.2015.03.066.

[122] O. Olumayegun, M. Wang, Dynamic modelling and control of supercritical CO2 power cycle

using waste heat from industrial processes, Fuel. 249 (2019) 89–102. https://doi.org/10.1016/j.fuel.2019.03.078.

[123] H. Li, Y. Zhang, M. Yao, Y. Yang, W. Han, W. Bai, Design assessment of a 5 MW fossil-fired supercritical CO2 power cycle pilot loop, Energy. 174 (2019) 792–804. https://doi.org/10.1016/j.energy.2019.02.178.

[124] H. Li, Y. Zhang, Y. Yang, W. Han, M. Yao, W. Bai, L. Zhang, Preliminary design assessment of supercritical CO2 cycle for commercial scale coal-fired power plants, Appl. Therm. Eng. 158 (2019) 113785. https://doi.org/10.1016/j.applthermaleng.2019.113785.

[125] M.J. Li, J.L. Xu, F. Cao, J.Q. Guo, Z.X. Tong, H.H. Zhu, The investigation of thermo-economic performance and conceptual design for the miniaturized lead-cooled fast reactor composing supercritical CO2 power cycle, Energy. 173 (2019) 174–195. https://doi.org/10.1016/j.energy.2019.01.135.

[126] J. Xu, E. Sun, M. Li, H. Liu, B. Zhu, Key issues and solution strategies for supercritical carbon dioxide coal fired power plant, Energy. 157 (2018) 227–246. https://doi.org/10.1016/j.energy.2018.05.162.

[127] T. Neises, C. Turchi, A comparison of supercritical carbon dioxide power cycle configurations with an emphasis on CSP applications, Energy Procedia. 49 (2014) 1187–1196. https://doi.org/10.1016/j.egypro.2014.03.128.

[128] I. Pioro, Handbook of generation IV nuclear reactors, Woodhead Publishing, 2016.

[129] T. Abram, S. Ion, Generation-IV nuclear power: A review of the state of the science, Energy Policy. 36 (2008) 4323–4330. https://doi.org/10.1016/j.enpol.2008.09.059.

[130] T.M. Conboy, M.D. Carlson, G.E. Rochau, Dry-cooled supercritical CO2 power for advanced nuclear reactors, in: Turbo Expo Power Land, Sea, Air, American Society of Mechanical Engineers, 2014: p. V03BT36A001.

[131] P. Wu, C. Gao, Y. Huang, D. Zhang, J. Shan, Supercritical CO2 Brayton cycle design for small modular reactor with a thermodynamic analysis solver, Sci. Technol. Nucl. Install. 2020 (2020).

[132] B.S. Oh, Y.H. Ahn, H. Yu, J. Moon, S.G. Kim, S.K. Cho, Y. Kim, Y.H. Jeong, J.I. Lee, Safety evaluation of supercritical CO2 cooled micro modular reactor, Ann. Nucl. Energy. 110 (2017) 1202–1216. https://doi.org/10.1016/j.anucene.2017.08.038.

[133] A. Mazzetti, M. Gianotti Pret, G. Pinarello, L. Celotti, M. Piskacev, A. Cowley, Heat to electricity conversion systems for moon exploration scenarios: A review of space and ground technologies, Acta Astronaut. 156 (2019) 162–186. https://doi.org/10.1016/j.actaastro.2018.09.025.

[134] J. Davison, Performance and costs of power plants with capture and storage of CO2, Energy. 32

(2007) 1163–1176. https://doi.org/10.1016/j.energy.2006.07.039.

[135] S.D. Supekar, S.J. Skerlos, Reassessing the efficiency penalty from carbon capture in coal-fired power plants, Environ. Sci. Technol. 49 (2015) 12576–12584.

[136] B.O. Oboirien, B.C. North, T. Kleyn, Techno-economic assessments of oxy-fuel technology for South African coal-fired power stations, Energy. 66 (2014) 550–555. https://doi.org/10.1016/j.energy.2013.12.032.

[137] R. Scaccabarozzi, M. Gatti, E. Martelli, Thermodynamic analysis and numerical optimization of the NET Power oxy-combustion cycle, Appl. Energy. 178 (2016) 505–526. https://doi.org/10.1016/j.apenergy.2016.06.060.

[138] C.C. Cormos, Oxy-combustion of coal, lignite and biomass: A techno-economic analysis for a large scale Carbon Capture and Storage (CCS) project in Romania, Fuel. 169 (2016) 50–57. https://doi.org/10.1016/j.fuel.2015.12.005.

[139] P. Gładysz, A. Ziebik, Life cycle assessment of an integrated oxy-fuel combustion power plant with CO2 capture, transport and storage - Poland case study, Energy. 92 (2015) 328–340. https://doi.org/10.1016/j.energy.2015.07.052.

[140] M. Kanniche, R. Gros-Bonnivard, P. Jaud, J. Valle-Marcos, J.M. Amann, C. Bouallou, Pre-combustion, post-combustion and oxy-combustion in thermal power plant for CO2 capture, Appl. Therm. Eng. 30 (2010) 53–62. https://doi.org/10.1016/j.applthermaleng.2009.05.005.

[141] P.S. Pak, Y.D. Lee, K.Y. Ahn, Characteristics and economic evaluation of a power plant applying oxy-fuel combustion to increase power output and decrease CO2 emission, Energy. 35 (2010) 3230–3238. https://doi.org/10.1016/j.energy.2010.04.006.

[142] J. Hong, R. Field, M. Gazzino, A.F. Ghoniem, Operating pressure dependence of the pressurized oxy-fuel combustion power cycle, Energy. 35 (2010) 5391–5399. https://doi.org/10.1016/j.energy.2010.07.016.

[143] S. Peng, H. Hong, H. Jin, Z. Wang, An integrated solar thermal power system using intercooled gas turbine and Kalina cycle, Energy. 44 (2012) 732–740. https://doi.org/10.1016/j.energy.2012.04.063.

[144] Z. yu Zhao, H. Yan, Assessment of the biomass power generation industry in China, Renew. Energy. 37 (2012) 53–60. https://doi.org/10.1016/j.renene.2011.05.017.

[145] Y. Chen, Z. Guo, J. Wu, Z. Zhang, J. Hua, Energy and exergy analysis of integrated system of ammonia-water Kalina-Rankine cycle, Energy. 90 (2015) 2028–2037. https://doi.org/10.1016/j.energy.2015.07.038.

[146] Z. Zhu, Z. Zhang, Y. Chen, J. Wu, Parameter optimization of dual-pressure vaporization Kalina cycle with second evaporator parallel to economizer, Energy. 112 (2016) 420–429.

https://doi.org/10.1016/j.energy.2016.06.108.

[147] M.T. Luu, D. Milani, R. McNaughton, A. Abbas, Dynamic modelling and start-up operation of a solar-assisted recompression supercritical CO2 Brayton power cycle, Appl. Energy. 199 (2017) 247–263. https://doi.org/10.1016/j.apenergy.2017.04.073.

[148] F. Crespi, G. Gavagnin, D. Sánchez, G.S. Martínez, Supercritical carbon dioxide cycles for power generation: A review, Appl. Energy. 195 (2017) 152–183. https://doi.org/10.1016/j.apenergy.2017.02.048.

[149] E. Cayer, N. Galanis, H. Nesreddine, Parametric study and optimization of a transcritical power cycle using a low temperature source, Appl. Energy. 87 (2010) 1349–1357. https://doi.org/10.1016/j.apenergy.2009.08.031.

[150] J.D. Osorio, R. Hovsapian, J.C. Ordonez, Effect of multi-tank thermal energy storage, recuperator effectiveness, and solar receiver conductance on the performance of a concentrated solar supercritical CO2-based power plant operating under different seasonal conditions, Energy. 115 (2016) 353–368. https://doi.org/10.1016/j.energy.2016.08.074.

[151] N. Zhang, N. Lior, Two novel oxy-fuel power cycles integrated with natural gas reforming and CO2 capture, Energy. 33 (2008) 340–351. https://doi.org/10.1016/j.energy.2007.09.006.

[152] R.J. Allam, M.R. Palmer, G.W. Brown, J. Fetvedt, D. Freed, H. Nomoto, M. Itoh, N. Okita, C. Jones, High efficiency and low cost of electricity generation from fossil fuels while eliminating atmospheric emissions, including carbon dioxide, Energy Procedia. 37 (2013) 1135–1149. https://doi.org/10.1016/j.egypro.2013.05.211.

[153] R. Allam, S. Martin, B. Forrest, J. Fetvedt, X. Lu, D. Freed, G.W. Brown, T. Sasaki, M. Itoh, J. Manning, Demonstration of the Allam Cycle: An Update on the Development Status of a High Efficiency Supercritical Carbon Dioxide Power Process Employing Full Carbon Capture, Energy Procedia. 114 (2017) 5948–5966. https://doi.org/10.1016/j.egypro.2017.03.1731.

[154] T. Zhang, Z. Liu, H. Hao, L. Chang, Application research of intake-air cooling technologies in gas-steam combined cycle power plants in China, J. Power Energy Eng. 2 (2014) 304–311.

[155] E. Kakaras, A. Doukelis, A. Prelipceanu, S. Karellas, Inlet air cooling methods for gas turbine based power plants, (2006).

[156] A. De Sa, S. Al Zubaidy, Gas turbine performance at varying ambient temperature, Appl. Therm. Eng. 31 (2011) 2735–2739.

[157] I. Dincer, M.A. Rosen, M. Rosen, A. Bejan, Thermal Energy Storage: Systems and Applications, Wiley, 2002. https://books.google.co.jp/books?id=ktFSAAAAMAAJ.

[158] A.K. Shukla, O. Singh, Effect of Compressor Inlet Temperature & Relative Humidity on Gas Turbine Cycle Performance, Int. J. Sci. Eng. Res. 5 (2014) 664–671.

[159] M. Ameri, S.H. Hejazi, The study of capacity enhancement of the Chabahar gas turbine installation using an absorption chiller, Appl. Therm. Eng. 24 (2004) 59–68. https://doi.org/10.1016/S1359-4311(03)00239-4.

[160] B. Mohanty, G. Paloso, Enhancing gas turbine performance by intake air cooling using an absorption chiller, Heat Recover. Syst. CHP. 15 (1995) 41–50. https://doi.org/10.1016/0890-4332(95)90036-5.

[161] D. BIES, U. JOHANNTGEN, J. SCHARFE, TS-23 Optimised Cooling of the Compressor Intake Air: A New Way for the Improvement of Power and Efficiency in Gas Turbine Plants (Session A-6: Performance 3), in: Int. Gas Turbine Congr. B. Abstr., 公益社団法人日本ガスタービン学会, 1999: pp. 429–436.

[162] D. Hu, Reduce the effect of inlet temperature on output capacity of gas turbine, Ind. Technol. (2009).

[163] A.E.M. Nasser, M.A. El-Kalay, A heat-recovery cooling system to conserve energy in gas-turbine power stations in the Arabian Gulf, Appl. Energy. 38 (1991) 133–142.

[164] S. Boonnasa, P. Namprakai, T. Muangnapoh, Performance improvement of the combined cycle power plant by intake air cooling using an absorption chiller, Energy. 31 (2006) 2036–2046. https://doi.org/10.1016/j.energy.2005.09.010.

[165] M.R.M. Yazdi, M. Aliehyaei, M.A. Rosen, Exergy, economic and environmental analyses of gas turbine inlet air cooling with a heat pump using a novel system configuration, Sustainability. 7 (2015) 14259–14286.

[166] J.R. Khan, W.E. Lear, S.A. Sherif, J.F. Crittenden, Performance of a novel combined cooling and power gas turbine with water harvesting, J. Eng. Gas Turbines Power. 130 (2008).

[167] G. Fan, H. Li, Y. Du, S. Zheng, K. Chen, Y. Dai, Preliminary conceptual design and thermo-economic analysis of a combined cooling, heating and power system based on supercritical carbon dioxide cycle, Energy. 203 (2020) 117842. https://doi.org/10.1016/j.energy.2020.117842.

[168] Y. Liang, Z. Sun, M. Dong, J. Lu, Z. Yu, Investigation of a refrigeration system based on combined supercritical CO2 power and transcritical CO2 refrigeration cycles by waste heat recovery of engine, Int. J. Refrig. 118 (2020) 470–482. https://doi.org/10.1016/j.ijrefrig.2020.04.031.

[169] H. Li, W. Su, L. Cao, F. Chang, W. Xia, Y. Dai, Preliminary conceptual design and thermodynamic comparative study on vapor absorption refrigeration cycles integrated with a supercritical CO2 power cycle, Energy Convers. Manag. 161 (2018) 162–171.

https://doi.org/10.1016/j.enconman.2018.01.065.

[170] Y. Yang, Z. Wang, Q. Ma, Y. Lai, J. Wang, P. Zhao, Y. Dai, Thermodynamic and exergoeconomic analysis of a supercritical CO2 cycle integrated with a LiBr-H2O absorption heat pump for combined heat and power generation, Appl. Sci. 10 (2020). https://doi.org/10.3390/app10010323.

[171] H.A. Muhammad, G. Lee, J. Cho, U.H. Bhatti, Y.J. Baik, B. Lee, Design and optimization of CO2 pressurization system integrated with a supercritical CO2 power cycle for the CO2 capture and storage system, Energy Convers. Manag. 195 (2019) 609–619. https://doi.org/10.1016/j.enconman.2019.05.029.

[172] M. Purjam, K. Goudarzi, M. Keshtgar, A New Supercritical Carbon Dioxide Brayton Cycle with High Efficiency, Heat Transf. - Asian Res. 46 (2017). https://doi.org/10.1002/htj.21225.

[173] J. Pátek, J. Klomfar, A computationally effective formulation of the thermodynamic properties of LiBr-H2O solutions from 273 to 500 K over full composition range, Int. J. Refrig. 29 (2006) 566–578. https://doi.org/10.1016/j.ijrefrig.2005.10.007.

[174] D.A. Boryta, Solubility of lithium bromide in water between -50.deg. and +100.deg. (45 to 70% lithium bromide), J. Chem. Eng. Data. 15 (1970) 142–144. https://doi.org/10.1021/je60044a030.

[175] S. Aphornratana, T. Sriveerakul, Experimental studies of a single-effect absorption refrigerator using aqueous lithium-bromide: Effect of operating condition to system performance, Exp. Therm. Fluid Sci. 32 (2007) 658–669. https://doi.org/10.1016/j.expthermflusci.2007.08.003.

[176] C. Geng, Y. Shao, W. Zhong, X. Liu, Thermodynamic Analysis of Supercritical CO2 Power Cycle with Fluidized Bed Coal Combustion, J. Combust. 2018 (2018). https://doi.org/10.1155/2018/6963292.

[177] C.S. Turchi, Z. Ma, T.W. Neises, M.J. Wagner, Thermodynamic study of advanced supercritical carbon dioxide power cycles for concentrating solar power systems, J. Sol. Energy Eng. Trans. ASME. 135 (2013) 1–7. https://doi.org/10.1115/1.4024030.